Author:
Taylor, Hannah C

Title:
Exploring communication and collective behaviour between spatially organised inorganic protocell communities

Exploring communication and collective behaviour between spatially organised inorganic protocell communities

By

HANNAH CLAIRE TAYLOR

School of Chemistry

UNIVERSITY OF BRISTOL

A dissertation submitted to the University of Bristol in accordance with the requirements of the degree of DOCTOR OF PHILOSOPHY in the Faculty of Science.

MARCH 2023

WORD COUNT: 54,800

ABSTRACT

A living system profoundly relies on mass, information and energy interactions through cell-cell and cell-environment networks. As a step towards understanding such interactions, it is beneficial to design and create bottom-up artificial living systems from non-living components, with a specific focus on synergistic interactivity between artificial cells (protocells) and their local environment. Although there are several routes for fabricating protocellular systems, we recognise key challenges associated with a) developing protocellular models with high levels of organisational tunability, b) achieving cell-environment bilateral communication, and c) realising autonomous self-assembly and regulation of protocell systems. The aim of this thesis is thus to review some matrix-based and matrix-free methods of inorganic protocell (colloidosome) 3D-spatial organisation, as judicious system designs capable of cell-cell and cell-environment communication, collective behaviours, and dynamic self-assembly, in close relation with local environments.

The first experimental chapter details assembly of colloidosomes within hydrogel or coacervate-based matrices. A droplet microfluidic technique is employed as a novel method for encapsulating segregated colloidosome colonies within alginate hydrogel microspheres. The technique exploits high tunability for customisable size, ratio, microscale geometry, and 3D-patterning parameters.

Benefiting from the versatility associated with such matrix-based systems, the second experimental chapter develops 3D-organised colloidosomes for collective signalling and emergent behaviours. Notably, spatially segregated colonies show proximity-mediated chemical communication with increased kinetics compared to analogous homogenous arrangements. This proximity-enhanced colloidosome signalling is exploited, alongside segregated ionic/covalent crosslinking transitions in the environment, to obtain simultaneous structural degradation and resilience of hydrogel hemispheres as a programmable mechanism for protocell ejection. Colloidosomes are also employed as simple signalling hotspots within coacervate-matrix systems.

The final experimental chapter aims to re-imagine colloidosome organisation into a matrix-free system, capable of dynamic self-assembly and self-sorting via electrostatically-active membrane appendages. Alginate-coated and chitosan-coated colloidosomes are either co-assembled or self-sorted, in response to varied pH environments. Again, these systems are highly coordinated with their environment and as such, can be spatially pattered according to temporal pH changes through endogenous enzyme catalysis. Furthermore, a spatiotemporal effect on the rate of colloidosome communication in the presence of a hostile guest molecule is demonstrated.

DEDICATION AND ACKNOWLEDGEMENTS

I would like to thank everybody who has contributed towards this PhD. I would like to extend a special thank you to Professor Stephen Mann for this incredible opportunity, for your resources, your guidance, and your inspirational intellect. I would also like to thank Dr Avinash Patil and Dr Mei Li for supporting me within the Mann group over the last few years. Avinash, your ideas have been stimulating and constructive. Mei, thank you for project support and for entrusting me with the website.

I would like to express a huge thank you to Dr Ning Gao, who has helped me throughout the entirety of my PhD. His experimental wisdom, ideas, knowledge, and encouragement have been instrumental to this work. Ning, I could not have done this without you! I also thank you for trying to help me speak Chinese, for funny conversations and football bets. I would like to extend another huge thank you to Dr Ananya Mishra, for guiding me with experiments and project designs. Ananya, your help with the final chapter was inspiring and motivating. I would like to extend a big thank you to everyone in the Mann group.

I would explicitly like to thank my two wonderful housemates over the last 3 years. To Dr Ella Carter, for navigating 'week on, week off with me', for numerous lock-down walks, dressing up home-parties, and Friday night curries! My PhD will forever remind me of you and all the time spent walking to Uni together, sitting next to each other, working on the lab bench next to each other and having lunch together! To Chloe, for making home such a relaxed and lovely environment. Thank you to all my amazing friends in Bristol, to Louisa, Sarah, Alexia, Flo, Amber, Beth, Eveline, Dan & Rach, CHH boys, Mary, Justin and Antonia. And to my besties not in Bristol, Jess and Lau! You guys always keep me happy and confident!

I would like to say a humongous thank you to my best friend and fiancé, Adam Brace. You make every day so joyful and special, regardless of my lab endeavours. You have been with me every step of the way, supporting me, encouraging me, believing in me, and making my life in Bristol so perfect. I cannot wait to start post-PhD life completely with you.

Finally, I would like to say the biggest thank you to my family. Especially to my mum, dad, sister, and grandparents, who have always encouraged me to enjoy learning, who have fuelled my mild tea addiction (thank you to whoever supplies milk in the postgrad kitchen), and who have kept me being weird. I am especially grateful for all your love and support over the years. I would also like to give a special dedication to my grandpa Keith Bowskill, for passing on the chemistry genes!

AUTHOR'S DECLARATION

I declare that the work in this dissertation was carried out in accordance with the requirements of the University's *Regulations and Code of Practice for Research Degree Programmes* and that it has not been submitted for any other academic award. Except where indicated by specific reference in the text, the work is the candidate's own work. Work done in collaboration with, or with the assistance of, others, is indicated as such. Any views expressed in the dissertation are those of the author.

SIGNED: ……HANNAH TAYLOR…… DATE: ……15/03/2023……..

PUBLICATIONS

H. Taylor, N. Gao, S. Mann.
Chemical Communication and Protocell-Matrix Dynamics in Segregated Colloidosome Micro-Colonies.
Angewandte Chemie - International Edition, 62 (24): 2023.

TABLE OF CONTENTS

LIST OF FIGURES

LIST OF TABLES

LIST OF SCHEMES

LIST OF EQUATIONS

CHAPTER 1

INTRODUCTION

A living system comprises complex networks of interactive subsystems, which together define the self-sustaining and open organisation, capable of living functionalities. A living cell constitutes the primary level of a living system, within a nested hierarchy of different living subsystems.[1] Intrinsic to the living cell, there are estimated to be 20 process-systems that require mass, energy, and information flows, to be sustained. For example, the reproductive process system relies on mass, energy and information exchange in the form of DNA/RNA molecules to realise genetic material replication and cell division.[2] Similarly, the boundary process system delivers mass, energy and information through stimuli-responsive membrane filters and membrane receptors to control ion channels, offer cell protection, ingest inputs and extrude waste products.[3] Evidently such processes exploit mass, energy and information networks through a close relationship between the cell and the cell environment.

Cells that form closely related communities (tissues) have a major influence on the operation and complexity of a universal living system. A tissue is defined as an organised consortia of primary component living cells, that lies in the gap between cell and organ subsystems. The behaviour of a tissue cannot be understood as simply the accumulation of component-cell phenomena, as there are emergent structures and process that arise from a higher number of components with complicated interactive relationships. This increased capacity means that tissues often respond to more varied and dynamic cell-environment interactions.[1]

Evidently, a living system is inherently complicated. Non-linear mass, energy, and information interactions are increasingly complex upon each hierarchical subsystem (cell – tissues – organ) and cannot be understood by adding constituent behaviours. Therefore, to gather an understanding of how a living system works, it is incredibly useful to mimic facets of a living system in a greatly simplified way. Logically, researchers have developed artificial cells to give insight into the primary cell unit, which has been closely followed by artificial tissues, as a step towards understanding cell-cell interactions and organ behaviour. Moreover, it has been recently suggested that the creation of simplified cells might give insight into the origin of living systems.[4]

As a strategy for mimicking living cells, researchers have fabricated cell-like entities called protocells, which exploit key facets of living cells without maintaining their living status. This provides an efficient platform aiming to investigate specific life behaviours. Protocell models have been achieved via top-down, bottom-up and side-on approaches, that each produce cell-mimics with varying levels of internal complexity and control.[5]

Currently, a bottom-up approach offers the highest level of tunability and thus provides a popular platform for studying fundamental processes within living cells therein mimicking mass, energy and information interactions to explain subsystem phenomena. In single cell systems such interactions have been used to mimic membrane gating,[6] motility,[7] structural reconfiguration,[8] selective uptake,[9] and photo-responsiveness.[10] Researchers have also developed tissue-mimicking structures (prototissues) to study similar interactions within organised hierarchical networks. Although some subsystem processes, such as contractile motions and electric pathways, have been successfully mimicked within prototissues, a lack of organisational tunability has prevented further sophistication in subsystem mimicries. In an attempt to develop more interactive and sophisticated processes between different cell communities, behaviours such as predator-prey relationships,[11] phagocytosis[12] and translocation[13] have been achieved. Despite these cell-cell interactions successfully exploiting mass, energy, and information flows to initiate collective behaviours, a key challenge is to incorporate environment-cell interactions, especially within organised architectures.

Beyond creating new living process-mimics through protocell chemistries, the scientific community desires a deep understanding of mechanisms that drive protocell behaviours, to infer how a living system might operate. This has been developed to some extent, for example through an in-depth review of division mechanisms and genetic expression within protocells, to study reproductive interactions.[14] Moreover, living boundary interactions have been understood through protocell membrane studies.[15] Understanding these processes remains a key challenge, and further knowledge

could lead to more sophisticated behaviours, especially relating to the design of autonomous systems.

Current protocell models help us to understand basic living system processes, especially through controlling mass, energy, and information flows. Protocell and prototissue research has delivered promising application in drug delivery, biomedical chemistries, biomimetic microbots and cytomimetic materials. Developing this research, in particular through more complex and organised protocell communities, is therefore key to understanding how a living system works, can give insight into living system origins, and could have potentially ground-breaking application in bio-inspired medicine and engineering.

OBJECTIVE

This thesis endeavours to deepen our understanding of living system behaviours whilst part-unveiling the route through which contemporary life forms might have emerged from likely-simple matter. A strategy is employed using cell-like entities (protocells) to model life-like phenomena and to gain insight into original cell behaviours through the mimicry of one or more cell functionalities within such artificially made constructs. It is proposed that by exploring how cell consortia work together and thus by creating protocellular systems, deeper insight into living cell behaviours and primitive evolutionary occurrences towards multicellular life can be perceived. Furthermore, spatial organisation of protocell constructs can mimic higher order and more sophisticated biological systems, providing us with additional control for exploring cell-cell and cell-environment interactive behaviours. The aim of this thesis is therefore to study how the collective behaviour of spatially organised protocells can lead to emerging behaviours that mimic life-like phenomena, enhance chemical communication pathways, and generally improve our understanding of cell-cell behaviours within more organised structures. This introduction communicates the significance and history of protocell research, describes strategies for organising cells and introduces key materials used throughout the work.

1.1 Protocells

1.1.1 Origin of the protocell

In order to comprehend how something operates, it is often helpful to understand how something is fundamentally made. Living systems are intrinsically complicated and thus it can be beneficial to study the possible origins of a living system, as a route to understanding how it operates.

As yet, the origin of a living system is undetermined. On account of heated debates between prominent scientists and philosophers, current 'Origin of Life' theory suggests that under certain conditions, simple life probably emerged from non-living matter (abiogenesis).[16] Understanding and exploring how such simple non-living molecules might have assembled into the first living structure, is an ongoing 'hot topic' in the scientific world.

In 1967 Bernal suggested that the 'Origin of Life' phenomenon could be split into 3 stages.[17]

1. *Origin of biological monomers*
2. *Origin of biological polymers*
3. *Evolution from molecules to cells*

The following thesis ignores stages 1 and 2, pro tempore, assuming simple biological monomers and polymers to be present and available. Instead, the work focuses on stage 3, aiming to understand the emergence and behaviours of a basic living cell and basic cell systems.

The concept of a 'basic living cell' is complicated, since the definition 'living' is in many ways debated. Therefore, to help tackle the evolution of cells from molecules (stage 3), researchers have designed simplistic entities that mimic living cells, but are not themselves living. These entities are called protocells and they bridge a gap between non-living biological molecules and a 'basic living cell', aiming to get ever closer to the latter.

To understand this ultimate 'goal' for a protocell model, it is important to be clear about what a 'basic living cell' means. Biologically speaking 'living' can now defined as an entity that, within boundaries created by its own making, is capable of self-maintenance from components produced by the system itself.[18] Referring briefly to the days of Aristotle's nature/living things debates, it is evident that there is nothing basic about a living system and thus the concept is in some ways an oxymoron.[19] A living cell can, however, despite these philosophical debates and under the definition presented above, be underlined by some fundamental principles that are key to the properties of modern life. These are summarised in table 1.1.

Table 1.1. *Key features that are deemed necessary for a living system.*[5]

Feature	Function
Systems interface	Compartmentalisation to induce spatial coupling of genotype and phenotype
	Protection against parasitic attack
	Exchange of materials and energy with the external environment
	Signalling
Internal network system	Energy generation and storage
	Metabolism
	Replication
	Evolutionary capacity

The features and functions presented in table 1.1 incorporate a range of interactive systems that require novel chemistries and concepts to replicate and study. To satisfy the term 'basic', a primitive cell is therefore designed to encompass only a few of the necessary functions presented. The self-assembly of simple molecules to form compartmentalised capsules that perform *some* primitive life operations is thus proposed as the principle behind protocell design in the laboratory, with a general aim to help understand how living systems function from determining how they might have originated ('Origin of Life').[5]

Typically, the protocell model demonstrates a bottom-up approach to creating life-like cells. A bottom-up approach is defined by the self-assembly of abiogenic building blocks, to achieve complexity and higher order structure.[20] This approach provides a stark contrast to the more traditional top-down approach, which involves removing cell functionalities from modern living cells to study primitive cell formation. A bottom-up approach often provides increased freedom for exploring different 'Origin of Life' theories and concepts. Both bottom-up and top-down strategies are important and can work together towards the bigger primitive cell picture. An example of this was recently reported in literature through a side-on approach to creating bacteriogenic protocells.[21]

1.1.2 Overview of the protocell

The foundation of modern protocell research was established by Oparin[22], who put forward the hypothesis that cell-like entities could emerge as a consequence of a different prebiotic atmosphere, allowing the gradual progression of inorganic precursors into organic molecules and self-contained structures with increasing complexity and life properties. There is now a plethora of protocell designs (figure 1.1), most commonly categorised by type of membrane. As a most obvious mimic to contemporary cells surrounded by a self-assembled membrane of amphiphilic lipid molecules, lipid or fatty acid-based vesicles have a well-established reputation.[23,24] However these designs are not perfect when considering primitive models, as phospholipids suffer from low permeability and, being complex structures, it is plausible that phospholipid ingredients were not readily available under prebiotic conditions.[25] Fatty acids on the other hand, seem prebiotically plausible candidates but have decreased vesicle stability due to low hydrophobicity.[26] Membranes formed by other candidates, such as from protein-polymer nanoconjugates (proteinosomes)[27,28], inorganic nanoparticles (colloidosomes)[6,12,29] and polymer amphiphiles (polymersomes)[30], whilst perhaps being more distant replicas of a contemporary cell, show a range of improved functions and life-mimicking properties. Furthermore, membrane-free (coacervates)[31,32] and hybrid[33,34] protocells have established themselves as good models for mimicking living cellular processes. In all cases, a semipermeable barrier compartmentalises chemical processes, delivering *some* key functions of living systems, as summarised in table 1.1. Most importantly, this barrier is necessary to separate internal processes from the environment, to protect them against parasitic attack, to keep molecules spatially connected thus allowing for an evolutionary effect and to regulate the internal cell environment.[5] Although each protocell model possesses distinct advantages and disadvantages, this thesis will focus on the inorganic protocell model (colloidosomes), primarily due to its robustness.

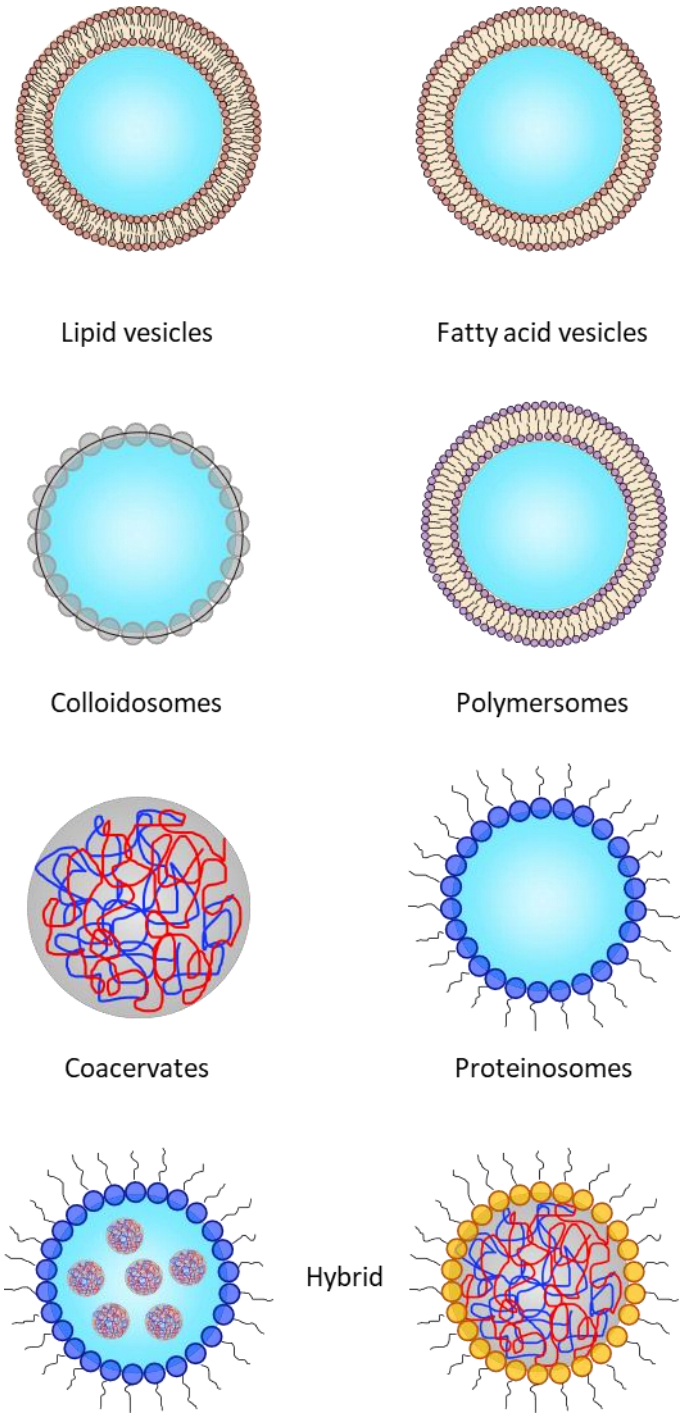

Figure 1.1. Different types of protocell models.

1.1.3 Colloidosomes

Colloidal particles are small particles (typically ranging from 1 nm to 10 μm) that are dispersed within a liquid or gas phase.[35] Colloidosomes are microcapsules with shells comprising of colloidal particles. They are produced by the self-assembly of colloidal particles at the interface between two immiscible liquid phases to form a Pickering emulsion, driven by a decrease in free energy.[36] The category of Pickering emulsion is governed by how each colloidal particle sits at the fluid interface. Either more of the particle is submerged in the water phase, more of the particle is submerged in the oil phase or exactly half the particle is submerged in each phase (figure 1.2). A key parameter called the contact angle, is used to measure how much of the particle is submerged in each phase (convention is to measure through the more polar liquid) and thus defines the type of Pickering emulsion. The contact angle measurement depends on the interfacial tension between the particle and oil (γ_{po}), the particle and water (γ_{pw}) and the oil and water (γ_{ow}), according to Young's equation.

$$\cos(\theta) = \frac{\gamma_{po} - \gamma_{pw}}{\gamma_{ow}} \qquad \textbf{Equation 1.1}$$

For more hydrophilic particles where $\gamma_{po} > \gamma_{pw}$, the contact angle θ will be $< 90°$ and an oil in water (O/W) emulsion will be realised. For more hydrophobic particles where $\gamma_{po} < \gamma_{pw}$ the contact angle $> 90°$ and a W/O emulsion will be realised.[37, 38]

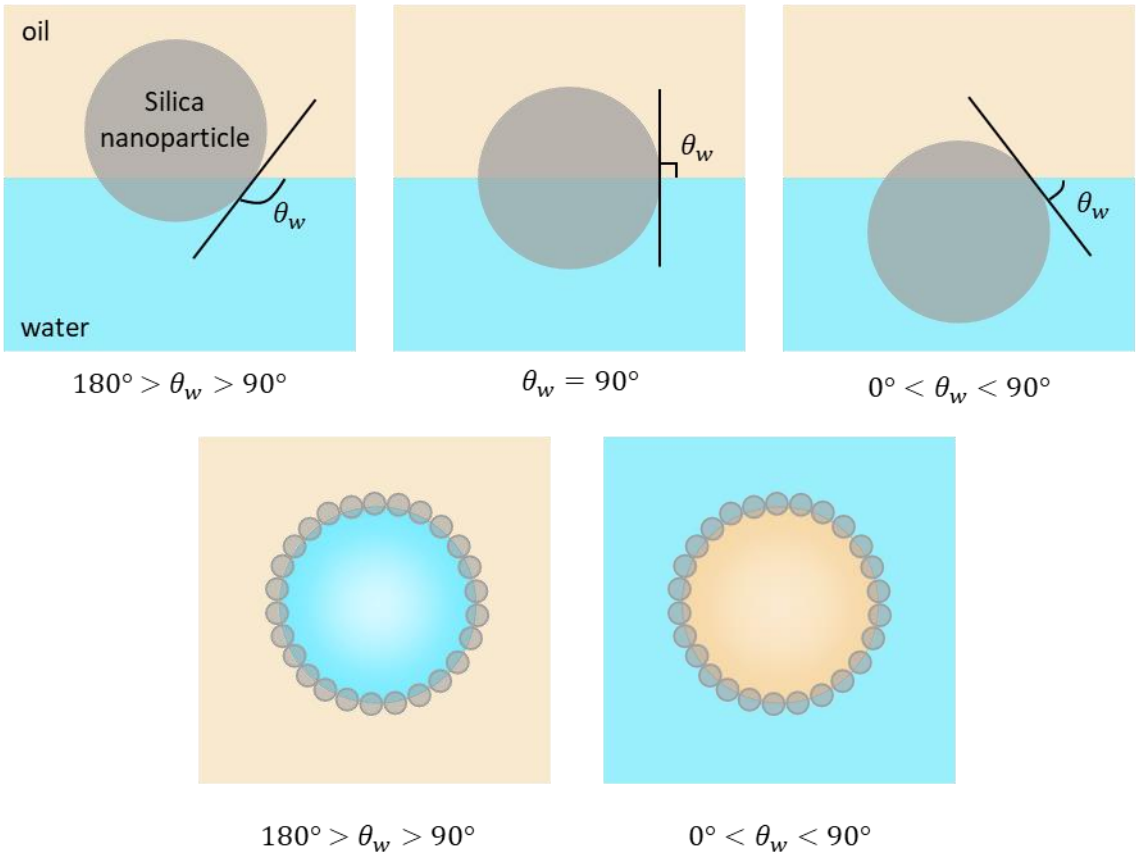

Figure 1.2. Wettability of colloidal particles and resulting type of emulsion.

With regards to colloidosome protocells, a water in oil (W/O) Pickering emulsion is desirable. This is because the colloidosome core aims to mimic a living cell, which would be an aqueous environment. The Pickering emulsion is highly stable due to a large reduction in free energy (ΔG) when the colloidal particles move from free solution to the W/O interface.[39] In typical emulsions, surfactant molecules bind at the interface with $\Delta G \approx 5\ K_bT$ enabling molecules to hop on and off. In a Pickering emulsion, particles tend to be adsorbed with $\Delta G \approx 10^4\ K_bT$ for a 90° contact angle and $\Delta G \approx 10^2\ K_bT$ for a 30° contact angle.[40] This is considerably greater than a typical emulsion and means that the membrane particles are bound more strongly. The colloidal shells have interstitial gaps which form pores, allowing for selective permeability across the membrane. They are often locked into place by a crosslinking process so that the capsules can be transferred into a different medium, often resembling the inside core (figure 1.3), whilst retaining structural integrity and encapsulated material inside the core. Overall, colloidosomes afford a high level of control over membrane permeability, which is altered by colloidal particle size, the extent of crosslinking and the strength of binding at the interface.[41] A range of colloidosomes have been prepared using a variety of inorganic colloidal materials such as silica[42], clay[43], $CaCO_3$[44], Fe_3O_4[12] and gold nanoparticles[45], to name a few.

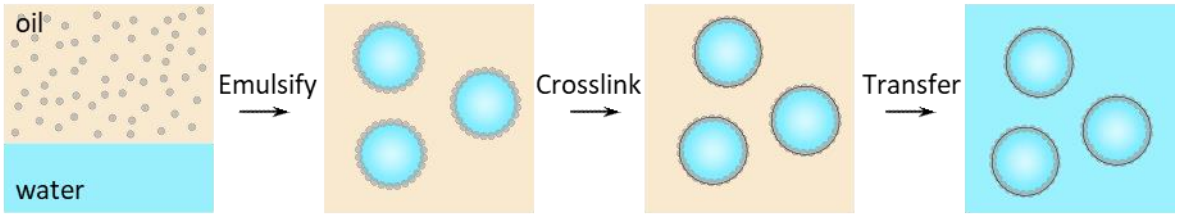

Figure 1.3. Preparation of colloidosomes. *Colloidosomes prepared by forming a water in oil Pickering emulsion followed by crosslinking of the colloidal shell and subsequent transferal to water.*

In literature, partially hydrophobic silica colloidal nanoparticles have been used to stabilise water droplets, to form a Pickering emulsion. Silica nanoparticles are treated with salinising agent dichlorodimethylsiliane in the presence of water, to change silanol groups ($-O_3SiOH$) to dimethylsilane ($-O_2Si(CH_3)_2$) groups of varying extent, as a method of fine-tuning the hydrophobicity of the silica.[42] Work by Binks *et al*.[46] showed that varying the hydrophobicity of silica therein varied the contact angle and thus the stabilisation of water foam by silica nanoparticles. At present, it is difficult to determine the contact angle of silica nanoparticles at the surface of the fluid interface. However, from Binks' work it can be assumed that a 100% SiOH particle has a 20° contact angle whereas a < 20% SiOH particle has contact angle 130°.[47] In this thesis we use approximately 50% SiOH silica nanoparticles which have a contact angle just below 90°.

As previously discussed, protocells are compartmentalised platforms with the ability to perform one or more biological process, as a mimic of a living system. In literature, colloidosomes loaded with simple biological materials have been shown to demonstrate life-like behaviours such as cell-free gene expression[42], enzyme mediated catalysis, and growth and division[48]. Colloidosome communities have also been employed as primitive models for the early stages of proto communication, signalling, and collective behaviour, for example in phagocytosis inspired behaviour[12] and in enzyme signalling pathways.[43]

1.1.4 Coacervate microdroplets

Colloidosomes, along with most other protocell models, harness membrane assembly into the formation of platforms for synthetic cellularity. Despite these membrane-bound platforms having technological merit and showing promise for biomedical/bioengineering applications, they are poor candidates for the 'first cell' and are in fact quite peripheral to the question of 'Origin of Life'. Even lipid vesicles, which are most akin to contemporary cells, have significant limitations regarding pH and ionic strength sensitivity and low encapsulation efficiencies.[25] In the 1930s Oparin noted that the spontaneous formation of compartmentalised entities through liquid-liquid phase separation was a likely step in the early life process, thus declaring complex coacervates as having strong relevance in 'Origin of Life' research. Furthermore, membrane-less compartments were first spotted within living cells in 1830s and have since shown diversity in subcellular locations and functions.[49] Such membrane-less organelles are therefore a relevant mimic to living cell compartments and are thus important to develop and explore, in terms of understanding a living system.

Complex coacervates are formed from spontaneous liquid-liquid phase separation via electrostatic interactions between macromolecules or polymers. This produces membrane-free microdroplets with a chemically rich interior within a chemically deficient aqueous phase. Many coacervate entities have been achieved, mostly using larger macromolecules and high molecular weight polymers. Breakthrough coacervate protocell experiments were achieved by the spontaneous formation of low molecular weight mononucleotides and simple cationic peptides.[31] Mann *et al.* were able to make coacervate liquids using small molecules, which displayed physical properties different enough from the bulk to give interesting functionalitites.[50] Many biomolecular substrates, proteins, RNA, chloroplasts have been sequestered into coacervates to achieve various biological functions. Behaviours such as metamorphosis[8], gene expression[51], selective uptake and protein refolding[9], light-induced chemistries[52,53] , enzyme and ribozyme activities[54,55] have been displayed.

Coacervates have also been significant in the development of hybrid protocells. Coacervate tendency to coalesce is a disadvantage and sometimes an absence of membrane is a drawback in their design. These challenges can be addressed through forming a membrane around the coacervate interior. Examples of different membranes including fatty acids[56], lipid membrane fragments[57], gold nanoparticles/PEG[58], proteins[59] and surfactants.[60] Even the coacervates themselves can form part of a membrane structure around an aqueous lumen[61]. Alternatively, coacervates can be nested within other protocell models as organelle-like structures[62], or they can reconfigure into vesicle-like structures.[63]

1.2 Protocell communication

1.2.1 Motivation for protocell communication

Despite new protocell designs being somewhat necessary for discerning primitive life forms, it seems clear that another important step in the transition between non-living and living matter, and for understanding living processes, is the communication and systems interaction between these basic protocells. A paper by A. M. Brizard proposes a 4-step strategy to the formation of a complete artificial cell.[34]

1. *Biomimetic containers*
2. *Construction mimic*
3. *Communication and exchange*
4. *Metabolic process mimic*

Whilst new synthetic protocell designs aim to advance steps 1 and 2, studying the communication and collective behaviour between protocell models is vital in stage 3 and for the possibility of achieving stage 4. The challenge is therefore to use existing protocell models to explore how protocells could work together to form hierarchical structures such as tissues, and how chemical signalling could create environments in which protocells might autonomously develop and evolve.

Protocell communication defines the transferral of a signal (usually a chemical molecule) from a sender protocell or protocell community to a receiver protocell or protocell community, to initiate a quantitative response. Protocell communication, as a mimic of living cell communication, can help better understand cell-cell interactions, better mimic complex emergent cell processes and eventually lead to the development of biological behaviours such as differentiation, chemotaxis and cell division.[64] Generally, chemical communication between protocells (and living cells) can be categorised by proximity as either contact-dependent (juxtacrine), through-space (paracrine, endocrine) or nested/within itself (autocrine).[65] Proximity plays an important role in the mass, energy and information exchange between protocells, thus influencing any resulting life-like behaviour. Communication protocell models are built by harnessing different protocell communities into populations and then linking them through chemical networks such as enzyme cascades[43,66], DNA[67,68,69]or in vitro gene expressions.[70,71,72] Controlling individual chemical networks can offer a step towards understanding living system interactions.

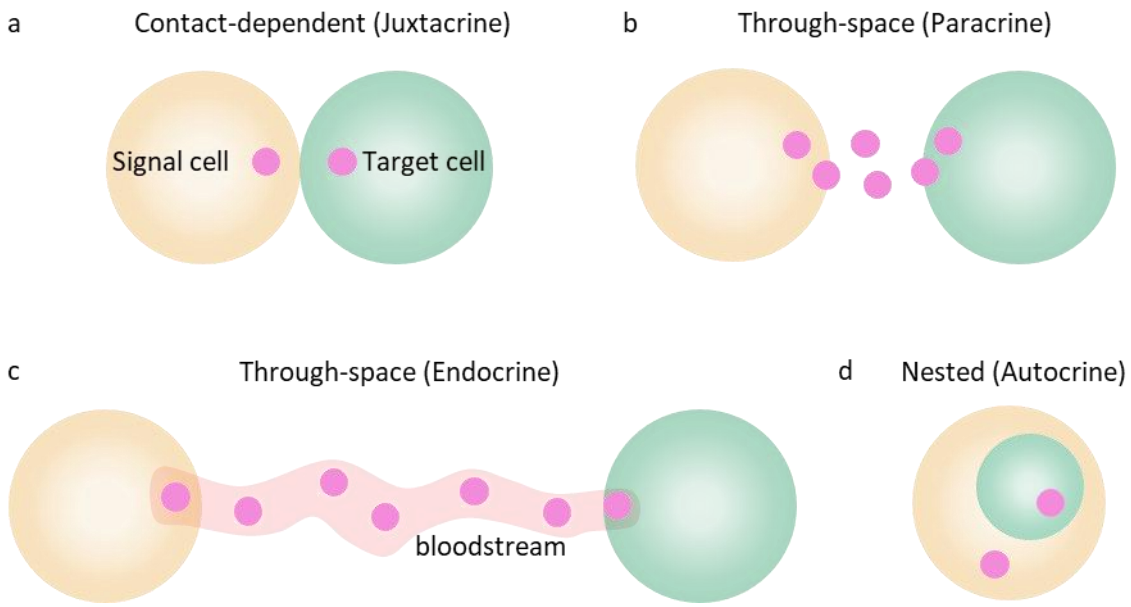

Figure 1.4. Four types of chemical signalling between cells. ***a****, Contact-depended (Juxtacrine) signalling.* ***b****, Through-space (Paracrine) signalling.* ***c****, Through-space (Endocrine) signalling.* ***d****, Nested or internalised (Autocrine) signalling.*[64,65]

1.2.2 Living cell communication

A living system relies on the interaction and communication between living cells and between living cells and their environment in order to perform specially designed functions and to promote environmental adaption.[73] In multicellular organisms, cells communicate to become specialised (differentiation), as a step to forming higher-order structures such as tissues and organs. In single cell systems, communication leads to cells working together to perform emergent functions such as swarming. The communication pathways within and between living cells is extremely complex, thus it is beneficial to use protocells as simplified models for exploring how communication can lead to specialisation and collective behaviours.

Communication between living cells occurs via specialised cell-to-cell or environment-to-cell signalling processes, which can be categorised as mechanical, light-induced, temperature-induced, electrical or, most commonly, as chemical. Chemical communication in most biological cells relies on signalling molecules that are released from one cell and received by another cell wherein the signal molecules are processed to generate a quantifiable response, function or output.[74] For example in synaptic transmission, neurotransmitters are released from a neuron, travel across the synapse and are then received by, say, a muscle cell with a target neuron, which responds by changing.[75] Importantly, these response-driven functions cannot be achieved by a single population of cells.

Chemical signalling processes have been studied by synthetic biologists and resultingly, artificial cell-cell communication has been developed in striped down, yet still complicated, living cell systems.[76] Unfortunately, these systems are difficult to work with as cell components are diverse and synthesising gene networks is particularly challenging. On the contrary, cell-cell communication between minimal protocell communities could offer easier levels of control and tunability.

1.2.3 Protocell communication

Due to extensive research into various types of soft compartmentalised microsystems, there is now a plethora of protocell models available for the construction of networked systems capable of signalling pathways. There have been several reviews publicising current protocell communication research, which recognise challenges and opportunities, especially related to higher order organised systems.[64,65,77] Communication between protocells relies on the production and conveyance of molecules that originate from sender protocells, are transferred to receiver protocells via contact-dependent, through-space or nested means, and then are generated into quantifiable responses or outputs. From these communication modes it can be noted that the extent of separation between protocells, and the nature of protocell interfaces are perhaps the most significant factors which determine how fast or easy a communication pathway can be achieved. Further detail into these modes will be described in chapters 4 and 5. Importantly within each mode, complexity and higher order functionality can be achieved by three system changes; increasing the integration of different synthetic cell varieties, increasing signal type complexity and by increasing the level of spatial organisation or hierarchical patterning.[64]

Typically, chemical signalling between protocells is implemented by through-space (paracrine and endocrine – mimicking) induction and activation of chemical activity via coupled enzyme reactions, in vitro gene expression or DNA strand development. Enzyme coupling reactions are often the easiest networks to achieve in through-space systems, for example the communication between glucose oxidase (GOx) and horseradish peroxidase (HRP)-containing protocells. In these examples communication is often achieved by a glucose input, hydrogen peroxide signal and Amplex red-derived resorufin output. This coupled enzyme-induced communicative system has been implemented in both randomly arranged[78] and spatially organised[79] through-space systems.

Beyond coupled enzyme cascades, the implementation of cell-free gene expression systems within vesicle-based protocells has been utilised for diffuse, through-space signalling and communication. Typically, membrane-impermeable signalling molecules are transferred through the use of gene circuitry to endogenously synthesise signal molecules. Examples of such signalling include the construction of multiple gene cascades under the control of external signals and communication,[71] and the genetic/enzyme coupling communication between vesicles and proteinosomes.[72] To afford a higher level of programmability, and as a higher complexity technique, the encapsulation of DNA and the integration of DNA nanotechnology has been employed to construct protocell-protocell communication networks by through-space communication modes. For example, proteinosomes with encapsulated DNA have been shown to send, process and respond to DNA based messages.[69] Through-space communication between various protocell models has been well studied. System complexity is increased by either the integration of different protocell models, programmability (for example using DNA), the integration of different communication proximity/modes, and by implementing spatial organisation with corresponding localised signalling. Increased complexity leads to a closer mimic of real living interactive systems.

As a different strategy for better mimicking the complexity of a living system, communication between artificial and living cells has been explored. As with protocell-protocell communication, protocell-living communication can be categorised into three proximity modes: through-space populations, contact-dependent and nested populations. Within through-space populations there are a range of studies, typically where a protocell biochemical signal induces a change in bacterial, and to a lesser extent, eukaryotic cells. A simple example is the synthesis of sugars in a lipid protocell to engage in quorum sensing of marine bacterium.[80] Within contact-dependent networks of cells there are steps towards creating interfacially connected artificial-biological tissues to achieve immune responses.[64] Within nested populations there are rudimentary examples of endocytosis wherein synthetic cells are ingested by living cells, and more advanced examples of signals between sender living cells (entrapped) to the contents of the host protocells.[81]

1.2.4 Collective behaviour between protocells

As discussed, protocell communication has received breakthrough attention in the past 5 years, such that signalling networks between various types of protocells have been established. Despite relatively complex signalling networks, protocell communication remains the starting point for mimicking life-like, complex biological processes. Signalling networks can be creatively designed and

programmed to achieve life-like emerging behaviours. In a natural progression from protocell communication, there have been several studies that look at the collective behaviour between protocell communities. Collective behaviours occur when the communication between cells initiates a response in more than one protocell, ideally in a community of several, that cannot occur from a singular protocell. This response, carried out in several protocells, determines an overall behaviour in the system. The variety of behaviours is thus phenomenal, and the type of behaviour depends on the number of protocells involved, the type of protocells involved and the type of signalling. As with signalling networks, these collective processes can be categorised into contact-dependent, through-space and nested modes.

Most examples of collective behaviour have been demonstrated in randomly arranged populations of protocells. Between contact-dependent communities of protocells tissue mimicking contractions and expansions[82], phagocytosis inspired behaviour[12] and buoyancy[83] (especially within nested protocell communities) have been demonstrated. Between through-space communities translocation[13] and morphological differentiation[84] have been achieved. Some collective protocell systems rely of both types of signalling, such as reconfiguration[8] and predator-prey[11] mimicking relationships. These collective processes have had an impact on developing synergistic sensing systems, biomimetic engineering applications and tissue engineering.

1.2.5 Prototissues

The collective assembly of protocell building blocks into higher order structures can lead to the formation of 3D interconnected networks that mimic tissue structures (prototissues).[85] Prototissues are becoming an increasingly popular stream of 'Origin of Life' research, as they develop insight into the basis of multicellularity as an important evolutionary transition from singular cells towards more sophisticated and complex life forms.[86] In addition to advancing fundamental scientific ideas, prototissues have a probable impact in areas of biomedical science, environmental science and soft robotics. As a potentially highly programmable, biocompatible and life-mimicking material, prototissues therefore provide an excellent matrix for protocell community design. The ability to organise protocell communities by prototissue construction is a key motivation for prototissue research, especially throughout this thesis.

Within natural tissues, cells are often organised into spatial patterns to afford specific functionality.[85] Being able to mimic such organisation within prototissues, could therefore constitute extremely advanced and evolved life-like functions. The most advanced method for creating spatially coded

prototissues is using picolitre droplets connected via droplet interface bilayers (DIBs) fabricated using a 3D printing device. Tissues created with this method are capable of several functionalities such as, electrical communication and shape change, protein synthesis and light controlled protein expression.[87,88] However, such tissues exist in an oil phase and have a short half-life of only a few hours. Another method for prototissue formation involves the magnetophoresis of GUVs into spatially coded prototissue-like arrays that can display basic communications between community arrangements. However, these tissues are formed in a $MnCl_2$ solution and succumb to deconstruction when the magnetic field is turned off. The challenge therefore is to create free standing, spatially organised protocells in an aqueous phase, capable of functionalities hinged upon their spatial arrangement.[89]

As a step towards this endeavour, free standing prototissues in an aqueous environment have been developed in spheroid, bio-orthogonally connected proteinosome systems.[82] Such tissues are capable of contractile functionalities and communication. Furthermore, a floating mould assembly technique has led to such tissues possessing some basic level of spatial control.[90] However, there is still abundant opportunity for developing spatially organised prototissues capable of advanced functionalities and communication pathways. A new model of prototissue, fabricated in an aqueous phase within minutes, has been fabricated using coacervate building blocks. Coacervate micro drops with gold (Au)/polyethylene glycol (PEG) nanoparticles at the interface, facilitate bidentate PEG-mediated bridging of jammed membranes to realise a robust prototissue capable of communication, self-healing and selective disassembly.

In all cases, cell spatial organisation has not been fully exploited and prototissue communities comprising different cell-types have not been explored.

1.3 Protocell organisation techniques

1.3.1 Spatially arranged protocell models

Spatial organisation is ubiquitous across all levels of a living system. The spatial patterning of protocell communities can therefore lead to more realistic mimics of living systems and provide a platform for higher order, collective, cell-like behaviours. To-date, the spatial grouping of protocells has been used to mimic tissue structures[89,90] and to exploit synergistic and cumulative interactions for more complex communication pathways between various types of protocells.[69] Protocell patterning can have the added benefit of creating anisotropy within systems, which could be used to mimic embryo development and further advance collective behaviours. However, some key challenges have not yet been addressed. These challenges include the development of organised protocell-environment communication, ordered collective processes and dynamic protocell organisation. Thus far, several techniques have been used to drive the organisation of protocells including microfluidics, acoustic trapping, magnetic fields, 3D printing, layer by layer tissue formation and electrostatic interactions. In this background microfluidics is reviewed in some depth, as the technique is central throughout the thesis. This is followed by a brief overview of acoustic trapping and a small overview covering 3D printing, magnetophoresis and electrostatic interactions.

1.3.2 Microfluidics

Microfluidics is the science of fluid control and manipulation on a microscale,[91,92] typically using networks of channels (tens to hundreds of micrometers) that are intricately designed to carry and contain small (10^{-9} to 10^{-18} litres) volumes of fluid.[93,94,95] The value of microfluidics comes from its small size, and consequential unique fluid physics.[96] The small size means that low volumes of precious reagents are required, that analysis times are rapid, and that mass-transfer is highly efficient, leading to quick and resourceful chemical reactions.[97] As the size of channels, through which a fluid flows, decreases, the dominant forces on that fluid change significantly from what is observed in the macroscale. Thus, in microfluidics, dominant effects are no longer governed by gravity but rather by laminar flow, diffusion, specific surface area and surface tension.[98] These dominant effects mean that diffusion and mixing can be precisely predicted and controlled, and that various types of microparticles can be formed.

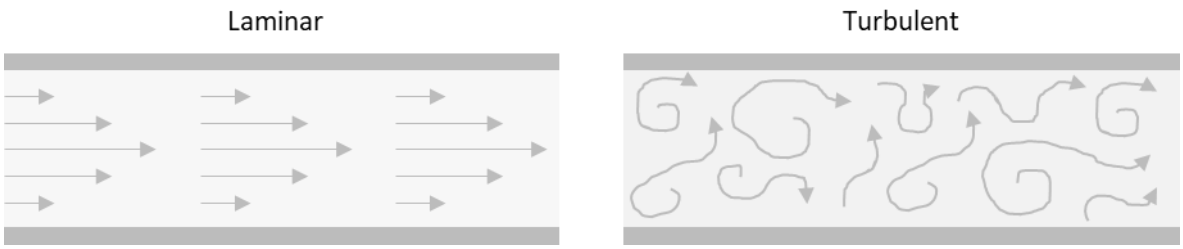

Figure 1.5. Laminar and turbulent flow systems.

1.3.2.1 History of microfluidics

The first microfluidic device is regarded to be the oscillograph, published by Sweet *et al.* in 1965.[99] This device emerged following a sequence of events driven by microelectronic research and the desire for improved telecommunication. The invention of the transistor in 1947 kick started these events, leading to the creation of the first integrated circuit (IC) and the onset of a revolutionary 'silicon age'. As the silicon age advanced, lithography and micro processing techniques pioneered by Kilby (following his IC invention), were popularised, and became more complex.[100] This ultimately led to the oscillograph (inkjet printing device) published by Sweet becoming the first microfluidic device. However, work published by Terry *et al.* in 1979, which described the fabrication of a microscale gas chromatography system, is believed to be the first 'Lab on a chip' style microfluidic device and it was this work which really established microfluidics as a field of its own.[101] Continuing along this microfluidic timeline, the invention of 3D printing in the 80s[102], the introduction of PDMS as a suitable material for microfluidic devices[103] and the increasing demand of bioinspired applications, were all notable milestones, culminating in the field of microfluidics today. The 21st century has revealed a generation of new microfluidic devices with a range of functionalities including droplet microfluidics, 3D printed devices, the 'organ on a chip'[104], open microfluidics, paper analytical devices[105] plus many more. The timeline of microfluidics is presented below in figure 1.6.

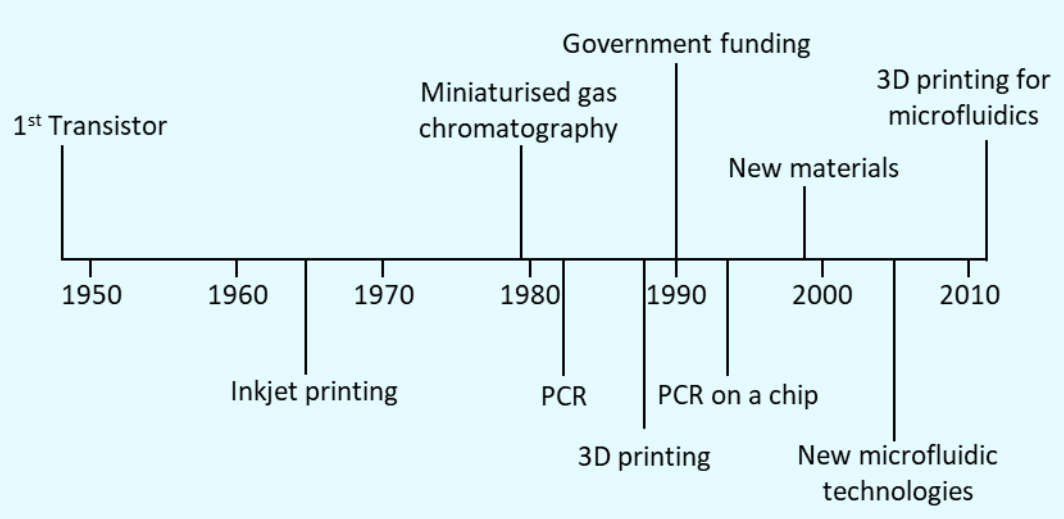

Figure 1.6. 30-year timeline of microfluidics.[100]

1.3.2.2 Droplet-based microfluidics

Droplet-based microfluidics is a subcategory of microfluidics which has been recognised by its distinctive ability to produce homogenous, monodisperse microdroplets. The technique is incentivised by a goal to create 'lab on a chip' technologies and the will to miniaturise systems for efficient chemical and biological analysis.[106] Microspheres are especially useful as independent flow reactors to enable rapid mixing of reagents, and for individual drop analysis.[107] As examples, droplet-based microfluidics in PCR has been shown to increase efficiency by eliminating reagent dispersion and adhesion to device surfaces, and droplet-based microfluidics in protein crystallisation has been used as a fast individual screening technique.[108] Importantly, microspheres prepared by droplet-based microfluidics can provide ideal boundary conditions for the isolation and protection of materials. As such, droplet-based microfluidics is used to compartmentalise biological entities and encapsulate biomedical material for use in drug delivery systems, biopharmaceuticals, and cell mimics.[109,110,111]

Droplet-based microfluidics usually involves two main steps: droplet generation and droplet solidifying. Solidifying commonly takes place by chemical, photochemical or physical processes. The next section discusses droplet generation.

1.3.2.3 Drop formation

In all types of microfluidic systems, physical flow dynamics at the microscale differ from the macroscale, bringing about dominant viscous (internal friction) over inertial (fluid momentum) forces and dominant surface tension over gravity.[112] The fluid dynamics are therefore characterised by a set of dimensionless numbers that are calculated by the fluid properties and device parameters. In physics, dimensionless numbers are used to compare the importance of different physical properties. In droplet microfluidics there are three important dimensionless numbers, the Reynolds number (Re), the Webber number (We) and the Capillary number (Ca).[113] Such numbers are presented in table 1.2.

Droplets are formed by a shearing action when two immiscible phases flowing inside the microchannels are exposed to dominant forces. Immiscible fluid phases are driven into a microchannel using an external measurable and controllable driving force. This is typically a syringe pump which applies a steady force to an injection syringe that is programmed to maintain specific flow rates. Pumps are favourable over other driving forces such as air pressure or gravity, as they are easier to control, variable and considerably faster.[114] The immiscible phases meet in a confined microchannel wherein the geometry of the device dictates how the interacting phases break up into droplets. Unique control over the size and shape of droplets is afforded through tuneable dominant force restraints, resulting in high levels of monodispersity with high throughput and reproducibility. Emulsion droplets are formed one-at-a-time inside the microfluidic device due to a balance of the inertial force, viscosity, interfacial tension and buoyancy acting upon the fluid flow. In most instances buoyancy is negligible due to a small volume, channel size and slow velocity. Thus, droplet break-up depends on quantities primarily related to interfacial tension and viscous drag.

Table 1.2. *A comparison of dimensionless numbers that are used to understand droplet formation in droplet-based microfluidics.*[115]

Dimensionless number	Symbol	Equation	Forces compared
Reynolds	Re	$\frac{\rho v L}{\mu}$	Inertial and viscous
Webber	We	$\frac{\rho v^2 L}{\sigma}$	Inertial and surface
Capillary	Ca	$\frac{\mu v}{\sigma}$	Viscous and surface

where ρ= mass density, μ= dynamic viscosity, v= mean velocity of fluid, L= characteristic length scale, σ= interfacial tension

As previously established, droplet generation arises from fluid instabilities caused by tensions when one immiscible fluid is introduced into another. Depending on the balance of forces, droplets can be formed in different regimes and characterised by different dimensionless numbers. The regimes are most commonly either the dripping (where viscous forces dominate) or jetting (where inertial forces dominate). In microfluidic devices, Re is between 10^{-6} and 10, so viscous forces dominate inertia forces yielding a laminar flow. Mostly the capillary number is used to help predict droplet formation as it compares the two prominent and relevant forces, viscous and interfacial surface.[116,110] For most regimes We < 1 as inertial force is small, however when inertial forces become more prominent as in the jetting regime, the Webber number becomes larger and can be used to characterise the droplet formation process. Droplet break-up is also determined by the geometry of the device itself. There are three common geometries: co-flow, cross-flow and flow focusing, as shown in figure 1.7. Each geometry expresses different advantages and disadvantages over the extent of droplet internal mixing, droplet sizes and droplet encapsulation. The three geometries are discussed in more detail.

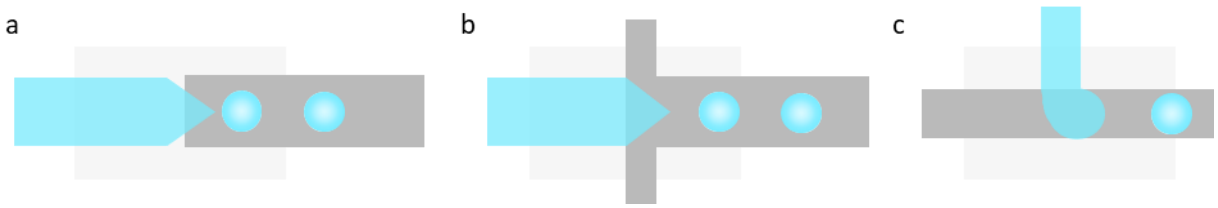

Figure 1.7. Droplet microfluidic geometries. *Droplet-microfluidic (**a**) co-flow (**b**) flow-focusing (**c**) T-junction geometries.*[117]

- *Co-Flow*

  A Co-flow geometry is formed by coaxial alignment of immiscible phases. These phases break into droplets through contact at an orifice. As an example, Tan *et al.*[118] described a microfluidic device fabricated from 3D glass capillaries which was used to study how the size of an alginate droplet depended upon flow rates, viscosity, and fluid properties. Co-flow systems have also been used to study the transition between dripping and jetting regimes, concluding that at some value related to the capillary number (Ca), droplet break up goes from absolute instabilities in the dripping phase, to convective instabilities in the jetting phase.[119] A co-flow microfluidics device is often favoured for applications involving multiple emulsions or cell encapsulation due to the 3D capillaries forming a symmetrical flow and a potential inner phase being able to avoid contact with device walls.

- *Flow focusing*

  Flow focusing geometry is reported in many journals due to the geometry being easy to mould in popular PDMS devices. In flow focusing, the two immiscible phases flow coaxially through a contracted region, which aids the break-up of droplets. An advantage of this system is that droplets smaller than the orifice size can be formed. Xu *et al.* demonstrated a novel flow-focusing device for creating sodium alginate droplets with *in situ* crosslinking.[120] Flow focusing devices can also be placed in sequence to form more complex double and triple emulsions, as seen by the work of Seo *et al.* [121]

- *Cross-Flow*

  The most common cross-flow devices feature a T-junction geometry (figure 7c) however, V- and K-junctions have also been reported in the literature.[122,123] In such cross-flow devices, one immiscible phase meets the other at an angle, and a droplet is subsequently formed due to a pressure drop and shearing force that occurs because one phase is partially blocked by the other. The size of the droplet thus depends highly on the shear stress.[124] Interestingly a microfluidic T-junction device has been employed to create monodisperse alginate spheres that were crosslinked using an off-device method. The alginate spheres, when mixed in the aqueous solution of nanoparticles, were shown to encapsulate Ag and AuNPs.[125] The off-device crosslinking method was adapted for this thesis however, droplets were not made using a T-junction device due to increased internal mixing.

- *Thesis device geometry*

  There are many literature examples of droplets (notably alginate droplets) formed via droplet-based microfluidics. Upon reviewing these geometries, a co-flow glass capillary device was used throughout the thesis as the droplet size and internal patterning could be easily controlled by device parameters and an off-device crosslinking method could be implemented

1.3.2.4 Device materials

Droplet based microfluidic devices can be made from a variety of materials such as silicon, PDMS, glass capillaries, quartz and PMMA. Original devices were made from silicon due to microfluidics stemming from the silica age of microelectronics. However, fabrication of silica moulds is time consuming, making them less desirable in the face of new, faster technologies. PDMS has quickly revolutionised the microfluidics industry due to moulds being relatively quick and cheap to manufacture. Glass is often a good material for device fabrication that can be left untreated however, the production of capillary-based devices is often manual, time consuming and difficult to reproduce. 3D printing is a newer technique that offers quick mould fabrication and easy design variation. However, because the process is new it remains less reliable. A variety of fluid materials can be injected into microfluidic devices as the dispersed phase to form droplets. Typically, these include natural and synthetic polymers. [91,92,114]

1.3.2.5 Microfluidics and protocells

Droplet based microfluidics has been used in artificial cell research as a technique for compartmentalising biological molecules into cell-like structures (polymersomes[126], liposomes[127] and coacervate-in-liposomes hybrid protocells[128]) and recently for encapsulating protocells into micro filaments.[13] Although the technique has shown promise in these areas, it has not been fully explored as a method for spatially organising protocells. Spatial organisation can be afforded through microfluidics by trapping protocells in a gel-matrix or by physically trapping protocells in a device. Although microfluidics has great potential for spatially organising protocells, higher-order patterns are often difficult to achieve. Other methods, such as acoustic trapping, can sometimes offer easier routes to complex protocell patterning.

1.3.3 Acoustic trapping

Acoustic trapping involves the immobilisation of cells and particles by ultrasonic wave formation. The phenomenon was first observed by Faraday in 1831, through the patterning of sand on a vibrating Chladni plate.[129] In the 1860s, Kundt cleverly utilised acoustic trapping to measure the speed of sound in different gasses and solid materials.[130] He noticed that a vibrating metal tube accumulated fine powder at specific intervals. These intervals related to the nodal positions of the acoustic standing wave and were positioned with half-wavelength spacing. The speed of sound was therein calculated through the relationship between half-wavelength spacing and propagating medium. Kundt followed this work by developing the acoustic trapping of particles in a liquid. Since the 1930s

acoustic trapping of particles has become increasingly researched and in 1971 the biological impact of acoustic cell manipulation was published by Dyson *et al*. who were able to stop the flow of red blood cells with ultrasound.[131] Since then, acoustic trapping of particles has been used for applications such as acoustic tweezers, enriching low concentration samples, washing or fractioning cell populations, acoustic levitation and particle-based bioassays.[132] One main advantage of this technique is that the device is not in contact with the trapped objects and thus provides non-invasive control of particle motion.

Acoustic trapping relies on the acoustic radiation force experienced by particles when a standing wave is established. As an acoustic wave propagates through a medium with suspended particles, it hits the particles and produces a force on the particles (called the acoustic radiation force[133]) which tends to move these particles to areas of low/high pressure and velocity depending on their relative density and compressibility.[134] Cells with higher densities and lower compressibility than the suspending medium, tend towards area of low pressure, corresponding to the nodes in a standing wave (figure 1.8).

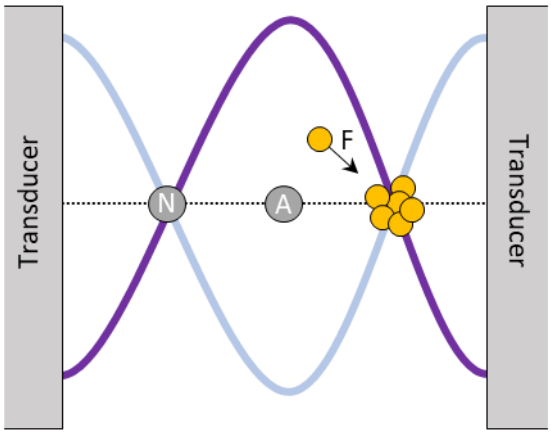

Figure 1.8. Standing wave formation between two transducers, assuming no reflection. *Diagram shows waves (light blue and dark blue) from each transducer. Node and antinode denoted by N and A in a grey circle. Acoustic radiation force (F) tends particles towards the node of the waves.*

Acoustic trapping has been implemented into protocell research for the localisation and spatial control of protocell communities. Tian *et al.* demonstrated spatiotemporal sensing between trapped coacervate arrays[79], and coacervate differentiation within acoustically trapped arrays.[84] Parallel catalytic processing was also demonstrated using similar devices.[135] Protocells and living cells have been localised together in acoustic trapping devices, such as GUVs with E. coli[136] and GUVs with red-

blood cells.[137] More permanent patterning has been achieved via hydrogelation of coacervates to trap enzymes into patterned arrays.[138]

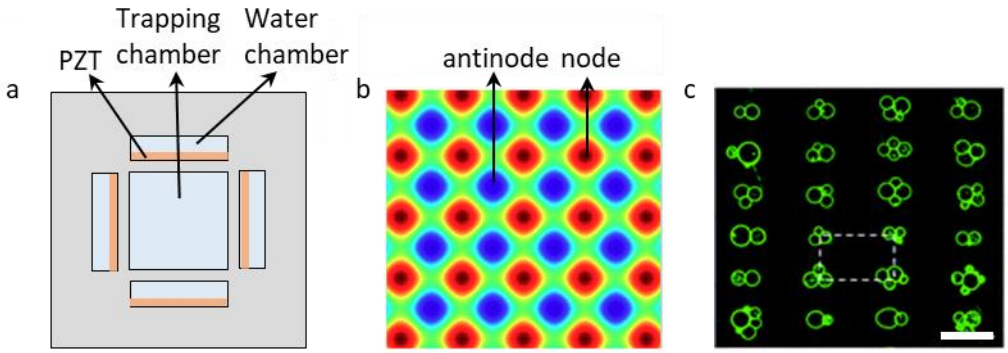

***Figure 1.9. Acoustic trapping devices for protocells**. **a**, Diagram showing the acoustic chambers and piezoelectric transducers (PZT) elements that generate the acoustic waves. **b**, Computerised nodal (red, low pressure) and antinodal (blue, high pressure) pattern of acoustic waves. Reproduced with permission.[137] **c**, Acoustically assembled GUVs. Scale bar, 100 µm. Reproduced with permission.*[136]

Although acoustic trapping can spatially organise protocells/protocell communities into a variety of complex patterns, the distance between each node is relatively far. Other spatial organisation techniques, such as 3D printing, have therefore been implemented to organise protocells into close-proximity contacting arrays.

1.3.4 3D printing

3D printing is a relatively recent technology, with the first 3D printer being made in 1988 by Charles Hull of 3D systems.[139] In general, 3D printing is the software-programmed addition of material, layer-by-layer into a 3D object. A category of such, 3D bioprinting, is the layer-by-layer addition of biomaterials and living cells into pre-determined 3D architectures that resemble tissue constructs. The technique has been developed since the 1990s by laser-based 3D cell patterning. Bayley *et al.* have designed a system which uses aqueous droplets as a bio ink (figure 1.10). The droplets are joined by a single lipid bilayer to create a software-defined 3D protocell network. Thus far these 3D printed prototissues have been used to realise electrical communication, shape change, enzyme cascades[140] and synthetic/living hybrid functionalities.[85]

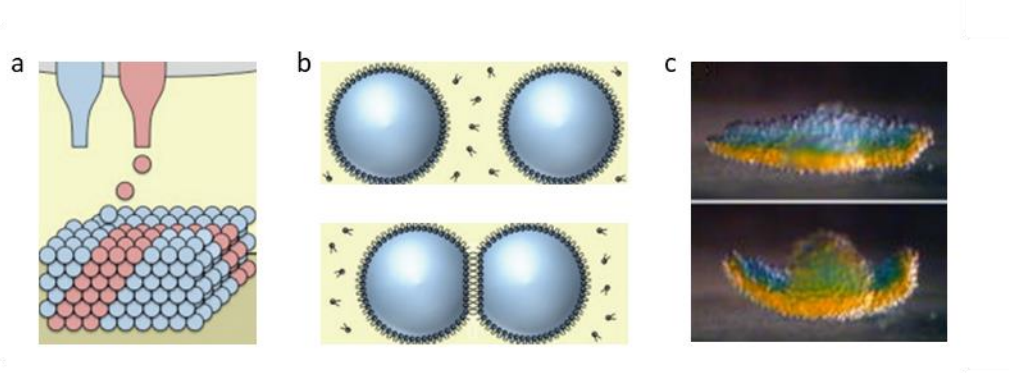

Figure 1.10. 3D printing of lipid droplets. a, *Schematic of 3D droplet printing from glass capillary nozzles that are each connected to a chamber interfaced with a piezoelectric disk, to enable the picolitre droplet printing of aqueous droplets into an oil bath.* ***b,*** *Aqueous droplets connected by a droplet interface bilayer of lipids.*[87] ***c,*** *4-petal, 3D printed, spatially organised arrangements of droplets with different osmolaries.*[88] *All images reproduced from paper by M. Booth and H. Bayley with permissions.*[87]

1.3.5 Magnetophoresis and layer-by-layer

There are a few, less common, techniques that have been exploited for spatial control over protocell communities. These include magnetic manipulation and layered assembly. In general, these techniques endeavour to pack protocell communities into tight arrays so that they resemble prototissues and are capable of life-like behaviours.

Magnetophoresis is the contactless migration of particles within a magnetic field. It can be categorised as positive or negative migration relating to whether the particles move towards area of maximum field intensity (positive) or towards an area of minimum intensity (negative). The magnetic susceptibility of a particle and its surrounding medium is crucial for controlling magnetophoresis. Positive magnetophoresis occurs with magnetic particle samples, whereas negative magnetophoresis occurs with objects having lower magnetic susceptibility than the surrounding medium. Both traditional magnetophoresis types require high magnetic field intensities to move the objects. However, a subcategory of negative magnetophoresis, called the magneto-Archimedes effect can be achieved by a weaker magnetic field.[141] The magneto-Archimedes effect is observed when particles of low magnetic susceptibility are dispersed in a paramagnetic medium. In such a case, the externally applied inhomogeneous magnetic field attracts the surrounding paramagnetic medium towards the area of a field maximum, pushing the material with a smaller magnetic susceptibility the minimum magnetic field.[142]

Layer by Layer assembly is a widely used technique for the engineering of materials and coatings. Early uses of the technique involved assembly from graphite oxides, clay sheets and nanoparticles. More recently the technique has been used for energy materials, complex self-assembly and biomimetic components.[143] Layer by layer spatial organisation of protocells has thus far been studied in proteinosome prototissue moulds[90] and in hydrogel-protocell assemblies.[144]

1.3.6 Intermolecular interactions to drive spatial organisation

This thesis endeavours to spatially organise protocells by using an electrostatic interaction driving force. The technique is dynamic and thus patterning can be changed by external stimuli (most likely pH). One example of exploiting electrostatic interactions within protocell systems is the spatial positioning of coacervates inside proteinosomes by tuning the electrostatic interaction of encapsulated coacervate and negative proteinosome membrane.[62] A predator-prey relationship has also been established using a selective electrostatic interaction to initiate a killing mechanism.[145]

1.4 Hydrogels

1.4.1 Hydrogel overview

Throughout this thesis hydrogels have been used as a compartmentalising extra protocellular scaffold. Hydrogels are classified as water-swelling 3D polymeric networks that maintain structure through the crosslinking of their polymeric chains.[146] This unique water-swelling property, along with soft structure, biocompatibility and molecular transport capabilities, appeals to various biological applications such as drug delivery, tissue engineering, wound healing, biosensing, bacterial culture and immunotherapy.[147] In the 1960s, Wichterle and Lim discovered crosslinked poly hydroxyethyl methacrylate (pHEMA) for use in contact lenses. This discovery pioneered the current hydrogel research field, immediately highlighting usefulness for biomedical applications.[148] There are several ways to form hydrogel networks, such as through covalent click bonding, enzymatic covalent reactions, photo optical polymerisation, ionic bonding, mechanical bonding, and supramolecular chemistry. Differently formed hydrogels give rise to varying properties, especially with relation to how the material responds to external environment. For example, temperature- and pH- dependent crosslinking is directly related to variation in temperature and pH environments, removal of ions can undo ionic crosslinking and reversal of reactions can undo covalent crosslinking. In this thesis, the

individual response of covalent and ionically crosslinked hydrogels, to environmental conditions is exploited.

When a hydrogel responds in a controlled way to external stimuli such as pH, temperature, and chemical environment, it is classified as a 'smart material'.[149] Responses can be programmed by the modification of polymer chains to alter crosslinking or other polymeric interactions. As an example, PNIPAAm is often incorporated into hydrogel polymeric chains as it has a transition temperature of ~32°C (perfect for bio-applications) and can be used as a polypeptide mimic. When heated above this temperature, water molecules are released from between the polymer chains and it shrinks, whereas below the transition temperature, polymer chains have strong hydrophilic interactions with surrounding water molecules, and the gel is swollen. Further modifications to PNIPAAm hydrogels include the addition of other hydrophilic or hydrophobic groups to change the phase transition temperature, as this can be useful for controlled release applications in drug delivery and tissue engineering.[150]

1.4.2 Swelling

Hydrogels are water-swollen 3D polymeric networks that can intake water up to a thousand times their dry weight. The water inside hydrogels can act as a medium for the diffusive transport of certain solute molecules, whilst the 3D polymeric network holds the structure together. The swelling property of a hydrogel is characteristic, and the extent of swelling can determine the degree of solute diffusion. This could, for example, determine the amount of nutrients that might reach a cell within the hydrogel.[151] The mechanism of hydrogel swelling is relatively complex. Starting with a dried hydrogel, water first enters the matrix and hydrates hydrophilic groups in the polymer chains. This is called the primary bound water. Following this, the network swells and water begins to surround newly exposed hydrophobic groups, causing attractive interactions with the primary bound water. This is called secondary bound water. Once all sites have been taken, the hydrogel continues to swell as additional water is absorbed by the networks due to the osmotic driving force of network chains to dilution. This is called bulk water. Crosslinking of polymer chains opposes this osmotic pressure and results in an elastic resilience force that leads to an equilibrium swelling.[152]

In general, hydrogels are classified into either synthetic or natural polymer categories. Synthetic hydrogels for example can be made from polyethylene glycol, polyacrylamide and polyvinyl alcohol. Natural hydrogels often come from polysaccharides and include sodium alginate, chitosan, cellulose

or agarose.[153] Natural polysaccharides have been chosen for this work due to them being easy to extract/acquire, having biological relevance and potential health benefits.

1.4.3 Sodium alginate

Sodium alginate is a naturally occurring polysaccharide derived from brown algae (phaeophyceae). The co-polymer chain contains β-D mannuronate blocks (M blocks) and β-L guluronate blocks (G blocks) with 1,4 linkage. The larger network structure is comprised of random sequences of these MMM and GGG or MGMG residues and the residue combination depends on the natural source of the polymer.[154] The combination of the blocks can affect material behaviour, for example increasing GGG blocks can lead to a stiffer hydrogel, which is discussed later. The polymer chains are crosslinked by divalent cations to form the 3D network, which is able to swell and uptake water due to the highly hydrophilic chains. Most commonly Ca^{2+} is used to bind the polymer chains together. This is achieved by the displacement of Na^{+} ions by the divalent Ca^{2+} and ionic interaction between carboxyl groups on neighbouring chains in an 'egg box' fashion as shown in figure 1.11.[155]

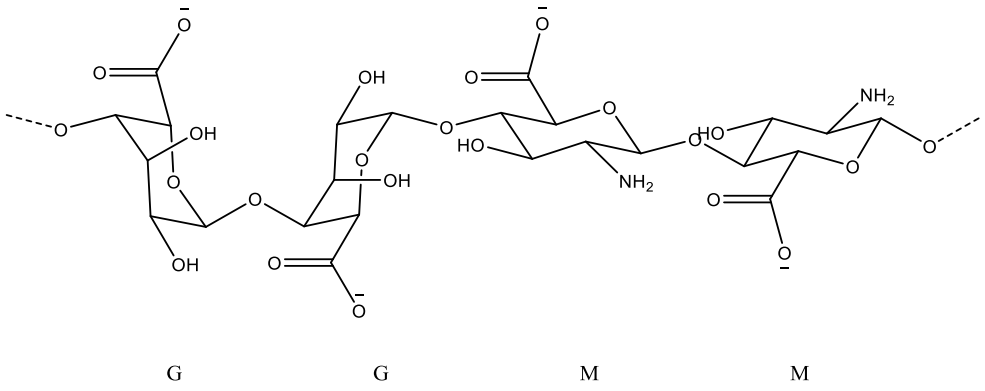

Figure 1.11. The chemical structure of G and M blocks in sodium alginate polymer chain.

The degree of crosslinking thus depends on the electrostatic interaction and coordination function of the Ca^{2+} as a chelating centre. Other divalent ions have been shown to crosslink alginate chains together. Sr^{2+} and Ba^{2+} form more rigid hydrogels as they are larger ions and thus have greater coordination opportunity and so crosslinking is stronger and chains are pulled tighter together. It is also seen that the crosslinking ions will preferentially bind G blocks together in the egg box arrangement before linking M blocks together. This can be explained by the pre-organised arrangement of side groups that are in the optimal position for binding in the G blocks. The carboxyl group is pointing inwards and other OH groups are also pointing towards the gap and can be involved

in weaker binding to the divalent ions as seen in figure 1.12. This is also the reason GGG blocks tend to be stiffer than MMM blocks.

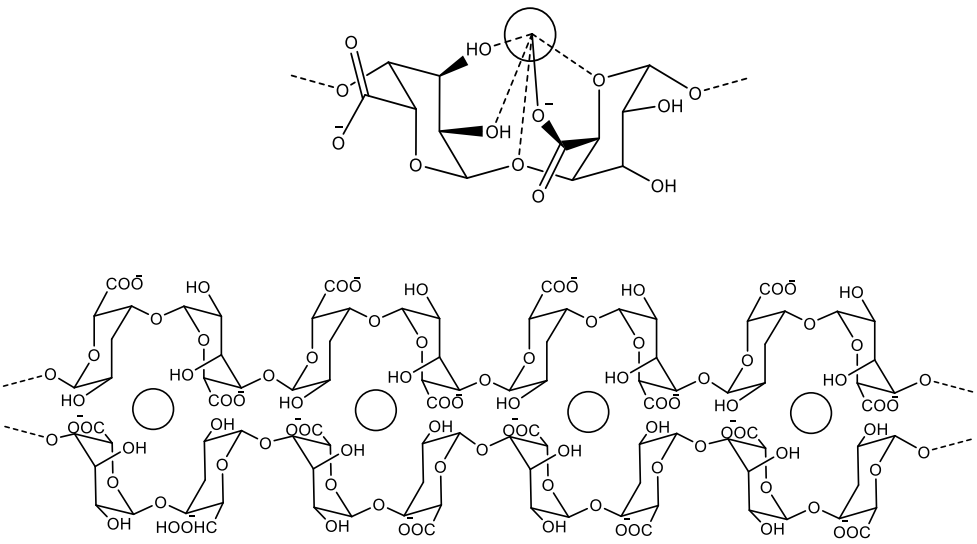

Figure 1.12. Egg box ionic crosslinking of alginate chains.

1.4.4 Chitosan

As with alginate, chitosan is a naturally occurring polysaccharide. It is produced from the deacetylation of chitin, which is found and extracted from the outer skeleton of crustaceans such as crab, lobster, and shrimp. This linear biopolymer chain is made up of majority D-glucosamine units with a few N-acetyl-D-glucosamine units remaining from incomplete deacetylation processes (figure 1.13). The degree of each unit thus results from the degree of deacetylation (DD) which varies according to the origin of the biopolymer and the deacetylation method. Most commonly the DD is in the 60-98% range.[156] Chitosan forms strong intermolecular hydrogen bonds through the amine and hydroxyl groups at the C2, C3 and C6 positions, leading to its insolubility in water. Due to this insolubility, applications of chitosan can be limited and thus chitosan is often modified at the amine or hydroxyl sites. The cationic amine groups can also react with several multi-valent anions, enabling chitosan to form a hydrogel network. Like alginate, chitosan is biocompatible, non-toxic and biodegradable. These properties of chitosan therefore make it increasingly important in drug delivery and tissue engineering applications.[157]

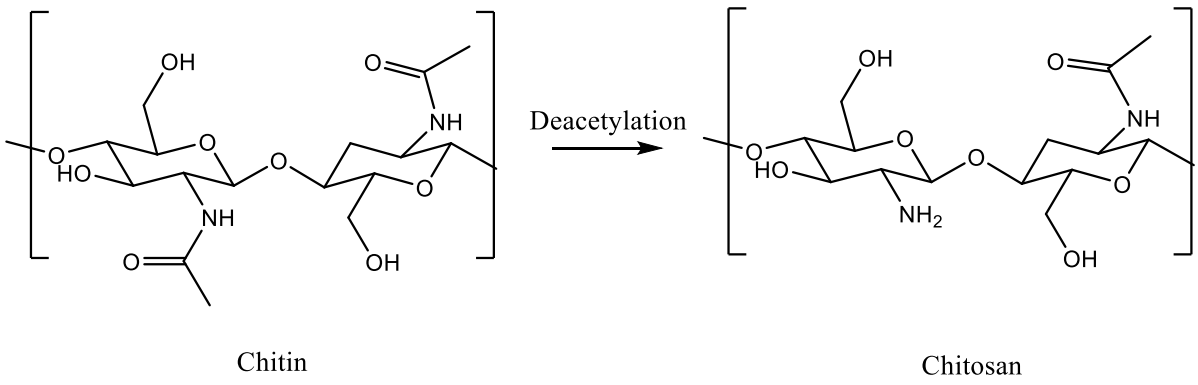

Chitin Chitosan

Figure 1.13. Deacetylation of chitin to chitosan.

1.4.5 Hydrogel applications

Historically, hydrogels have been used in a variety of industries including agriculture, food, pharmaceutical, hygiene product, tissue engineering and biomedical.[155] More specifically, sodium alginate hydrogels have been used in various food applications as a stabiliser, emulsifier or gelling agent[158] and in agriculture for soil additives that increase the ability of soil to retain water.[159] In the biomedical industry sodium alginate has been widely used for therapeutics, dental impressions and as wound dressings. Alginate is a particularly good wound dressing because it is highly hydrophilic, thus promoting the absorption of wound exudate, whilst also being used as a delivery platform for controlled release of drugs around the wound.[160] Alginates as drug delivery systems are favourable as they are often gelled via a non-intrusive ionic crosslinking mechanism. This gentle gelling process means that cell or drug encapsulation of various substances can occur with minimal trauma, thus enabling them to become some form of delivery platform. The release of drugs can also be stimulated by external factors and 'smart' properties of the hydrogel such as pH.[161] Most drug release mechanisms rely on a diffusion barrier whereby the nature of drug release depends upon the interaction between the drug and the alginate. For example, hydrophilic drugs will diffuse quickly whilst hydrophobic drugs more slowly through the gel network.

Hydrogels have been featured in protocell research previously published by the Mann research group. In this context, hydrogels have been used for both an ECM mimicking environment [138] (with protocell compartments) and as an internal protocell medium.[162] Specific examples related to these phenomena will be discussed in chapter 3. The potential application of hydrogels in 'Origin of Life' studies and cell mimicking applications is prominent however, the full breadth of advantages in using hydrogels in this work has not been fully explored.

1.5 Introduction conclusions

Living systems comprise complex networks of interacting subsystems that are maintained through mass, energy, and information flows. There is a strong desire to understand how these systems function and how these systems might have originated. However, living systems are extremely complex and thus protocell chemistries have been developed as simple methods for mimicking the composition and behaviour of living cells. There are several different protocell designs, each with unique advantages that make them either a closer mimic to contemporary cells or a more simplified and robust primitive cell design. It has been recognised that, a detailed understanding of how protocell communities interact with each other and with their environment is crucial to primitive cell research and for mimicking living, emergent behaviours. To-date, communication has been developed within spatially organised and randomly distributed arrangements of protocells, via through-space, nested, or contact-dependent signalling networks. A range of collective behaviours, that mimic living processes, have also been developed within protocell arrangements however, such behaviours are scarce in spatially organised communities. Nevertheless, several techniques have been used to spatially organise cells and protocells, primarily into tissue-like constructs. In particular, droplet microfluidics provides an excellent technique for the manipulation and control of cell-like particles.

Despite growing research in communication between protocell communities, there are key challenges associated with organised protocell functionalities, cell-environment interactions and dynamic or autonomously regulated communities. This background has given an overview of protocell chemistry, focusing on colloidosomes, protocell communication pathways and techniques for protocell spatial organisation, with a focus on microfluidics. The key materials (alginate and chitosan) used throughout this thesis have also been outlined and hydrogels are highlighted as a useful biocompatible material, ideal for biomedical engineering applications and for protocell scaffolding.

CHAPTER 2

MATERIALS AND METHODS

This chapter describes the materials and experimental methods used to complete this thesis. The chapter begins with a brief overview of common procedures and techniques used across all thesis chapters. This is followed by a more detailed account of specific experimental methods, categorised sequentially by each thesis chapter.

2.1 General materials and techniques

2.1.1 Materials

Throughout this thesis all chemicals were purchased and used as received. The following enzymes were purchased from Sigma Aldrich; GOx (50-100 kU g^{-1}), HRP (179.2 kU g^{-1}), urease (URS, 50-100 kU g^{-1}), β-glucosidase (β-Glu, > 6 kU g^{-1}), catalase (Cat, 3000 kU g^{-1}), alcohol oxidase (AOx, 10-40 kU g^{-1}) and invertase (INV, > 300 kU g^{-1}). Dyes rhodamine B isothiocyanate (RITC) and fluorescein isothiocyanate (FITC) were also purchased from Sigma Aldrich, whereas DyLight™ 405 NHS Ester (Dy405) was purchased from Thermo Fisher Scientific. Enzyme substrates including ethanol, d-glucose, sucrose, ortho-phenylenediamine (o-PD), gluconolactone (GDL) and fluorescein di-β-D-glucopyranoside (FDGlu) were purchased from Sigma Aldrich whereas urea was purchased from Merk Millipore and Amplex red was purchased from Thermo Fisher Scientific. Sodium alginate (medium viscosity) was purchased from MP Biomedicals LLC. HDK H30 silica nanoparticles were purchased from IMCD UK Ltd. Tetramethyl orthosilicate (TMOS), (3-glycidyloxypropyl) trimethoxy silane (GLYMO), dodecane, bis(trimethoxysilyl)hexane (BMOSH), chitosan (high viscosity), PEG-silicate, calcium bromide ($CaBr_2$), decanol, sodium citrate, H_2O_2 (30% v/v), 1-ethyl-3-(3-dimethylaminopropyl)carbodiimide hydrochloride (EDC), N-Hydroxysulfosuccinimide sodium salt (NHSS), polyallylamine hydrochloride (PAH), azobenzene-3-carbozylic acid (AzoCOOH) and succinyl α-cyclodextrin (CD) were purchased from Sigma Aldrich. Tyramine hydrochloride was purchased from Acros Organics. Dialysis bags with molecular weight cut off (MWCO, 12-14k) were purchased from Millipore.

2.1.2 Data analysis

Numerical data was analysed in Excel and plotted in Origin software. Microscope images were analysed or processed using Fiji (Image J) and videos were processed using VSDC video editing software.

2.1.3 Microscopy

2.1.3.1 Optical microscopy

Quick optical microscopies were performed on an Olympus BX53 top-down microscope equipped with a camera connected to an Olympus cellSens Standard software. Optical and fluorescence microscopies were performed on a Leica DM13000 B manual inversed fluorescence microscope with Leica EL6000 light source attached. A fluorescence filter with excitation wavelengths at 515-560 nm,

450-490 nm and 355-435 nm was used (table 2.1) to observe fluorescent dyes RITC, FITC and Dy405 respectively.

Optical microscopy works by reflecting light through a series of lenses which, due to having different refractive indexes, bend the light to make an image appear magnified.[163] Fluorescence microscopy works by irradiation of a sample with a specific band of wavelengths which causes specific electrons to be excited into higher energy level bands. The electrons subsequently fluoresce to lower energy levels releasing a different wavelength of light, that is detected by the microscope. The light emitted from the sample is separated from the light exciting the sample by a series of optical filters.[164]

Table 2.1. *Optical filters available on Leica DM13000 B manual inversed fluorescence microscope.*

Value	Fluorescence	Excitation /nm	Excitation cut-off /nm
I3	Blue	450-490	510
N2.1	Green	515-560	580
D	Violet	355-435	455
A	UV	340-380	400

2.1.3.2 Confocal microscopy

A Leica SP5-II confocal laser scanning microscope with 50 mW laser (405 nm), 150 mW Ar laser (488 nm) and 20 mW solid state yellow laser (561 nm) attached to a Leica DMI 6000 inverted epifluorescence microscope was used for detailed imaging and analysis. A confocal microscope, in contrast to a standard fluorescence microscope, measures one point of a sample at a time, thus creating an image by scanning across the sample. The advantage of only scanning one point at a time is that the emitted light can be focused through a pinhole and therefore scattering from other points in the sample are discarded.[165] Images taken by the Leica SP5-II confocal laser scanning microscope were then processed with the LEICA LAS X software.

2.1.3.3 Light sheet microscopy

A Zeiss Z.1 light sheet system was used to take images and 3D animations of colloidosome-encapsulated Janus hydrogel microspheres. Hydrogel microspheres were embedded in 1% low melting agarose before being entered into the light sheet. Automated imaging was taken through Zeiss Zen software and data was analysed on a second workstation with advanced 3D/4D rendering

through Arivis Vision4D software. In light sheet microscopy (also known as single plane illumination microscopy; SPIM) a laser beam is focused in one direction into a light sheet which illuminates a very thin strip of sample, exciting electrons within certain energy levels. Electrons are then emitted and observed in a plane perpendicular to the laser sheet through a normal optical microscope objective. Due to only illuminating a thin strip that is being observed, photodamage of the sample is significantly reduced and thus a clear 3D image can be more easily obtained.[166]

2.1.3.4 Wide field microscopy

A Leica LAS-X microscope attached to a Leica DM IRBE inverted epifluorescence microscope with phase-contrast was used for widefield microscopy. A widefield microscope illuminates the entire thickness of a sample which can create a blur from areas out of focus, above and below the image plane.[164] In this case, wide field microscopy was used to obtain lower magnification images as the confocal microscope was not equipped with low enough magnification lenses.

2.1.3.5 Microscope slide preparations

Channelled slides were used to image solutions and suspensions more clearly. These were prepared using cover slips and glass microscope slides, affixed using UV cured glue (figure 2.1a). For imaging of matrix-based constructs and enzyme cascade reactions, slides with individual wells were prepared (figure 2.1b). Glass cover slips were fixed using UV adhesive, onto a glass slide with pre-drilled holes to create wells to hold ca. 60 µl solution.

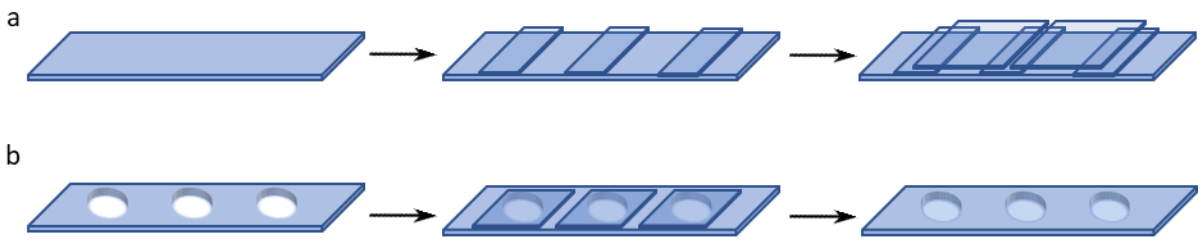

***Figure 2.1. Microscope slide preparation. a**, Channel slide preparation using microscope slide and coverslips fixed together using UV cured glue. **b**, Well slide preparation using pre drilled microscope slides and coverslips fixed together using UV cured glue. Hole diameter, 70 mm.*

2.1.3.6 Scanning and transmission electron microscopy

Scanning electron microscopy (SEM) analysis was carried out on a Jeol IT300 system. Colloidosomes were dispersed into deionised water and dried at room temperature onto a carbon coated Cu grid for analysis. Transmission electron microscopy (TEM) and scanning transmission electron microscopy-darkfield (STEM-DF) images were undertaken on a Jeol TEM 2100. Again, colloidosome solutions were dispersed in deionised water and dried at room temperature onto a carbon coated Cu grid for analysis. EDX analysis of Ca^{2+} loaded, uncoated and alginate coated colloidosomes was also performed on individual colloidosome samples.

SEM analysis requires an electron source to generate a stream of electrons towards a sample. These high energy electrons interact with the sample to generate secondary electrons (electrons that have been knocked off the sample), backscattered electrons, and X-rays. As the electron beam is scanned across the sample, these scattered electrons are detected to give an image.[167,168] TEM analysis involves electrons being transmitted through a sample, interacting with the sample internal structure, and then arriving at a detector below to create an image.[169]

2.1.4 Spectroscopy

2.1.4.1 Ultraviolet-visible spectroscopy

Ultraviolet-visible spectroscopy (UV-Vis) experiments were undertaken on a Perkin-Elmer Lambda 750 Spectrometer. Samples were prepared in 1 cm wide quartz cuvettes and a background spectrum of deionised water was always taken.

UV-Vis spectroscopy is used to quantify the amount of discrete light being absorbed by a sample. This is achieved by measuring the intensity of incident light and transmitted light through a sample at each wavelength, in comparison to a reference sample. Electrons in a sample can be excited from the highest occupied molecular orbital- (HOMO) to the lowest unoccupied molecular orbital- (LUMO) energy level by absorbing light. The bigger the energy gap is then the lower the wavelength of light needed to excite the electrons in the sample and thus the greater the absorbed of light at that wavelength. Different electron environments change the size of this HOMO-LUMO energy gap, meaning that samples with different composition show different absorbance spectra.[170]

2.1.4.2 Fourier transform infrared spectroscopy

Fourier transform infrared spectroscopy (FT-IR) was conducted on dry samples using a Perkin Elmer-Spectrum One FT-IR Spectrometer. Colloidosome samples were pipetted onto a glass slide where they were left to air dry before being gathered up and placed on the spectrometer.

Typically FT-IR spectroscopy detects absorption or transmission of light in the infrared region of the electromagnetic spectrum, after interacting with a sample. This technique does not interact with electrons in a sample (like UV-Vis) but instead resonates with molecular vibrations. The frequency of infrared light absorbed must match the intrinsic vibration of a molecular bond which can be categorised into symmetric stretches, asymmetric stretches or bending. The strength of a bond and the mass of atoms either end of the bond determines the vibrational frequency and thus the absorbance/transmission in an FT-IR spectrum. FT relates to the Fourier transformation technique used to turn raw data into an absorbance/transmission spectrum.[171,172]

2.1.4.3 Nuclear magnetic resonance spectroscopy

Nuclear magnetic resonance (NMR) spectra were collected using a Varian 500a NMR spectrometer. All samples were dissolved in deuterated water (D_2O) at a concentration between 2.5-10 mg ml^{-1}.

NMR is a technique used to characterise chemical molecular structure (in great detail) based on the interaction of an external magnetic field with atomic nuclei. All atomic nuclei have an intrinsic spin property. If a nucleus spin is not zero, then the nucleus has a small magnetic moment and so can behave as a tiny magnet. In the absence of an external magnetic field the magnet-like nucleus is randomly orientated however, as soon as an external magnetic field is applied, the nucleus lines up with either low energy or high energy. To make analysis more straightforward, NMR techniques typically analyse atoms with spin state ½, as this gives just two energy levels. Spins can flip at an exact quantum of energy. NMR therefore measures the frequency of radio waves required to flip spin states in different atoms. Importantly every atom is surrounded by electrons that shield the nucleus from the external magnetic field therein changing the effect on energy levels between spin states. This means that different frequencies of radio waves are required to flip spins in different atoms.[173]

2.1.5 Dynamic light scattering and zeta potential

Dynamic light scattering (DLS) and zeta potential (ZP) measurements were taken using a Malvern Nano series Zetasizer. Samples for DLS were placed in a 1cm wide quartz cuvette, whilst ZP samples were placed in a Malvern DTS1070 cell. All samples were run at room temperature and left to equilibrate for 120 s inside the device.

DLS is a technique used to determine the size of small particles. All particles randomly move when suspended in a solvent, according to Brownian motion caused by particle-solvent collisions. Smaller particles move faster than larger particles due to the collisions having a greater effect on them. The speed of a moving particle can be related to the particle hydrodynamic diameter using Stokes-Einstein equation.[174,175]

$$D = \frac{K_b T}{6\pi\eta R_H} \qquad \textbf{Equation 2.1}$$

where D is translational diffusion coefficient 'speed', K_b is Boltzmann constant, T is temperature, η is viscosity of solvent and R_H is hydrodynamic diameter.

In DLS, light is scattered by the moving particles and measured over time at a certain angle. Faster (smaller) particles show faster fluctuations in scattered light over time and thus this measurement can be used to determine particle velocity.

Zeta potential measurements can be used to infer the surface charge of a particle suspended in solution. When colloids are dispersed in a solution, they are surrounded by a double layer of charged ions (from the surrounding medium). The inner layer 'stern layer' is a tightly bound ring of strongly ionic interacting ions. The second layer 'slipping plane' consists of more loosely interacting ions which can exchange with the surrounding medium. A zeta potential is taken as the electric potential between the slipping plane and a point in the bulk medium. By applying an external electric field, a measure of the electrophoretic mobility can be recorded, which can subsequently be used by Henry's equation to calculate the zeta potential.[176]

$$U_e = \frac{2\varepsilon_{rs}\varepsilon_0}{3\eta}\,\zeta\, f(ka) \qquad \textbf{Equation 2.2}$$

where U_e is the electrophoretic mobility, $\mathcal{E}$ is the dielectric constant, η is viscosity of solvent, ζ is the zeta potential and $f(ka)$ is Henry's function.[177]

2.2 General methods

2.2.1 Making small silica colloidosomes

Partially hydrophobic silica nanoparticles (20 mg) were mixed with dodecane (2 ml) for 1 min by sonication in an ultrasound bath. Gentle pipetting was used to further disperse large aggregates of silica nanoparticles. 30 µl of enzyme aqueous solution was added to the oil/silica suspension and then vigorously shaken by hand for 1 min to form a Pickering emulsion. This was followed by sonication for 4 min with gentle pipetting within the sonication bath. TMOS (15 µl) was added to the Pickering emulsion which was then rotated on a Stuart tube rotator at 25 rotations per min (rpm) for 24 h. Colloidosomes were then transferred to water via a series of washing steps. The colloidosomes in oil were washed with a solution of 7 : 3 (v : v) ethanol : water before being centrifuged for 2 min at 2000 rpm. Subsequent washing steps were 2x 7 : 3 (v : v) ethanol : water 1x 1 : 1 (v : v) ethanol : water, 1x water.

2.2.2 Fluorescent labelling of proteins

In general, enzymes (20 mg) were dissolved in 10 ml sodium carbonate buffer (100 mM, pH 8.5) followed by addition of 100 µl fluorescent dye, FITC/RITC/Dy405 (2 mg ml^{-1} DMSO) which was added dropwise. The solution was stirred in the fridge for 12 h, purified by dialysing against milli-Q water for 3 days and then freeze-dried.

2.2.3 Fluorescent labelling of alginate

Sodium alginate (0.9 g, 1 wt.% aq. solution) was dissolved in acetate buffer (pH 5.18) for 90 min with continuous stirring. The dissolved alginate was subsequently mixed with EDC/NHSS (4 mg/2.5 mg) and stirred for 30 min to activate carbonyl groups on the alginate. 1,6 diaminohexane (70 mg) was dissolved in acetate buffer (5 ml) and added dropwise to the bulk reaction solution. The reaction was left at room temperature for 4 h to allow the amine to react with the activated carbonyl on the alginate. The mixture was precipitated in isopropanol twice to remove unreacted amine and dried overnight in the oven. The alginate-amine derivative (180 mg) was dissolved in sodium bicarbonate (10 ml, pH 8.5) and deionised water (10 ml) then reacted with either RITC or FITC (0.003g, 1 ml DMSO) for 4 h (scheme 2.1). The solution was dialysed against milli-Q water, then freeze-dried.[178,179,180]

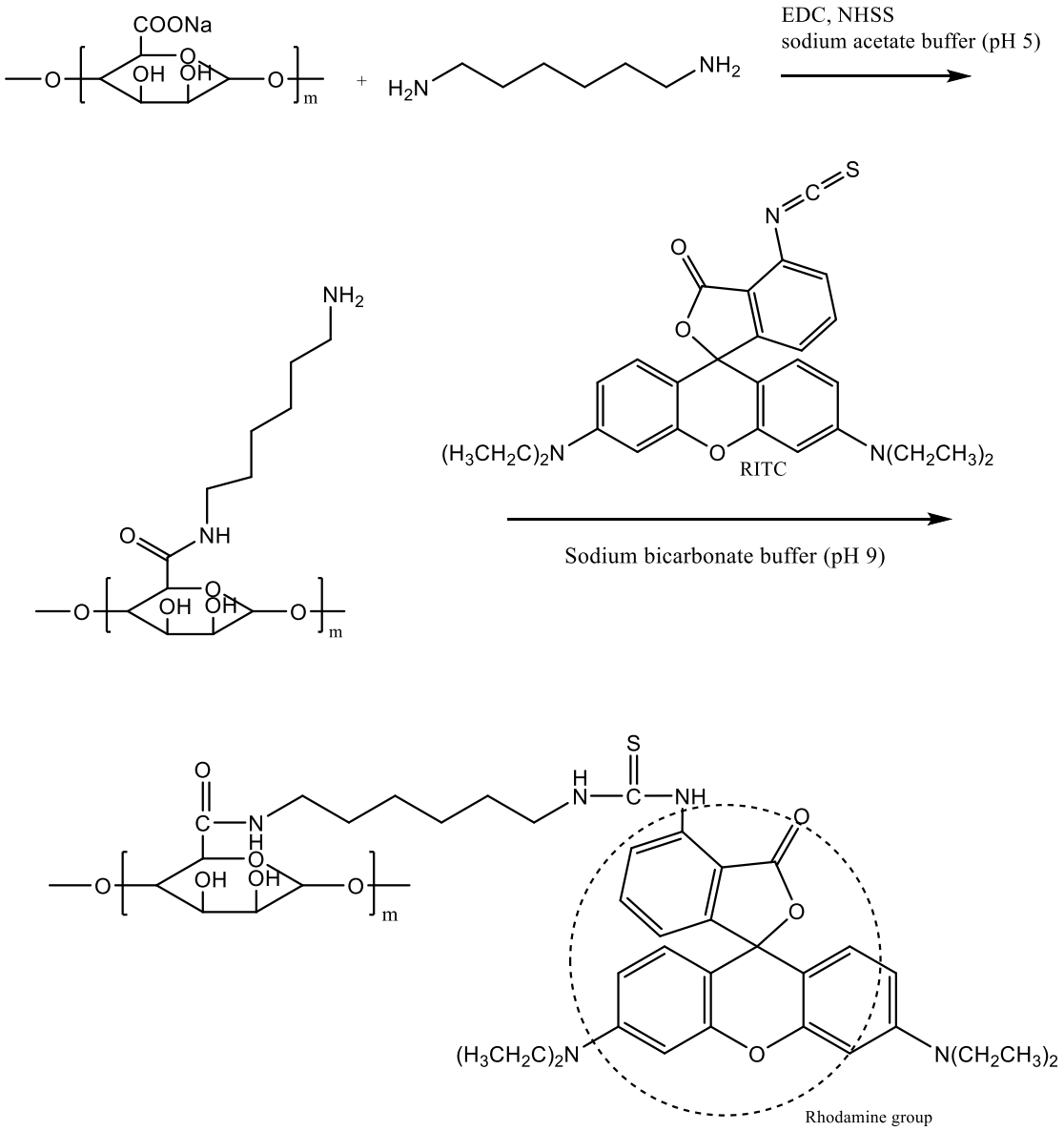

Scheme 2.1. Synthesis of RITC-sodium alginate. *The same procedure was followed with FITC in place of RITC.*

2.2.4 Fluorescent labelling of chitosan

Chitosan (310-375 kDa, 50 mg) was dissolved in 0.1 M acetic acid (5 ml). Methanol (5 ml) was added to the solution, followed by slow addition of FITC (6 mg, 2.5 ml methanol) under continuous stirring. The reaction was left stirring at room temperature for 4 h. After 4 h the reaction mixture was poured into NaOH (50 ml, 0.5 M) then centrifuged (10 min, 3000 rpm). NaOH was removed, and the solid product washed with 7 : 3 (v : v) methanol : water solution three times. The washed solid was dissolved in acetic acid (10 ml, 0.1 M) before being dialysed in the dark against milli-Q water (4 days) and then freeze-dried.[181]

2.3 Chapter 3 experimental methods

2.3.1 Microfluidic device manufacture

2.3.1.1 Materials

The following borosilicate capillaries were supplied by World Precision Instruments Inc. and CM Scientific; theta capillary (inner diameter (ID), 1.02 mm; outer diameter, 1.5 mm), collection capillary (ID, 1.02 mm; OD, 1.55 mm), small round capillary (ID, 0.58 mm; OD, 1.00 mm), square capillary (ID, 2.00 mm $\pm$ 6%; wall thickness, 0.400 mm), small square capillary (ID, 1.05 mm; OD, 1.5 mm) and three-barrel capillary (ID, 1.00 mm; OD, 0.75 mm). 5-minute epoxy resin was supplied by Thorlabs and polypropylene hub dispensing needles, GA20 (ID 0.6 mm; OD 0.89 mm; length 12.7 mm) were supplied by Onecall.

2.3.1.2 Device for spherical hydrogel microspheres

A round capillary (ID, 0.58 mm) was tapered using a P-97 Flaming/Brown type micropipette puller. Tapered capillaries were subsequently hand-grafted using Grit 5000 sandpaper to produce an orifice size ca. 80 µm in diameter. The orifice was observed and measured using quick microscopy on the Olympus SC50 light microscope and Olympus cellSens Standard system. The tapered and grafted theta capillaries were flushed with ethanol and dried using compressed air to remove debris from the sanding process. A square capillary (ID, 1.05 mm) was fixed to a glass microscope slide with 5-minute Epoxy and the tapered capillary was inserted inside. This was coaxially aligned with a collection tube (ID, 0.58 mm) and sealed using 5-minute Epoxy. A hypodermic needle with polypropylene hub was attached between the injection and the square capillary to introduce the outer phase.

2.3.1.3 Device for spherical hydrogel microspheres with Janus internal patterning

A theta septum borosilicate capillary was tapered using a P-97 Flaming/Brown type micropipette puller. Tapered capillaries were subsequently hand-grafted using Grit 5000 sandpaper to produce an orifice size ca. 200-350 µm in diameter. The tapered and grafted theta capillaries were flushed with ethanol and dried using compressed air to remove debris from the sanding process. A square capillary (ID, 2 mm, length 2 mm) was fixed to a glass microscope slide with 5-minute Epoxy and the tapered theta tube was inserted inside. This was coaxially aligned with a collection tube (ID, 1.02 mm) and sealed using 5-minute Epoxy. A smaller round capillary (ID, 0.58 mm) was pulled using a flame torch to form bent capillaries with narrow orifices (ca. 100-150 µm). These were inserted into each

side of the theta capillary and sealed with 5-minute Epoxy. A hypodermic needle with polypropylene hub sealed the join of the injection tube and the square capillary (scheme 2.2).

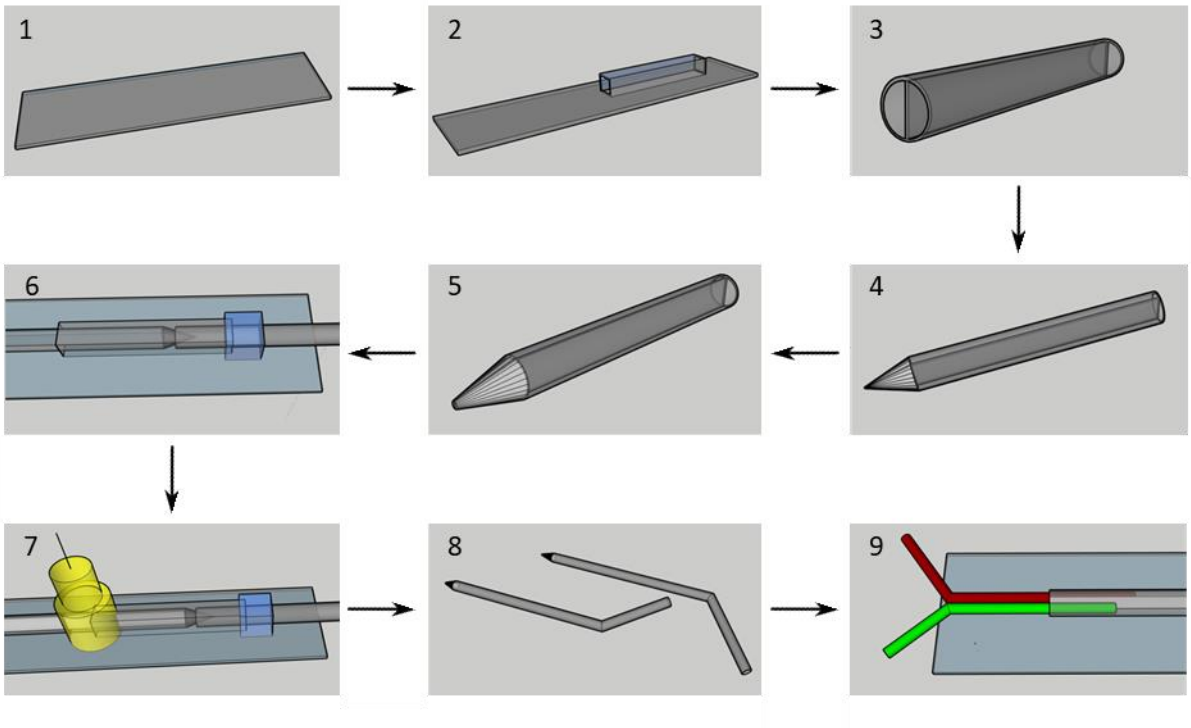

Scheme 2.2. *F**abrication of a theta co-flow glass capillary microfluidic device.** (**1**) The glass slide. (**2**) Square capillary fixed to the glass slide. (**3**) The theta septum capillary. (**4**) The tapered theta capillary. (**5**) The grafted theta capillary. (**6**) Coaxially aligned theta capillary and collection capillary. (**7**) Attachment of hypodermic needle to introduce the outer phase. (**8**) The bent capillaries created by pulling straight capillaries using a flame torch. (**9**) Positioning of bent capillaries within the theta capillary. Red and Green colours representing the two different inner phases introduced through these capillaries.*

2.3.1.4 Device for spherical hydrogel microspheres with ternary internal patterning

A three-bore borosilicate capillary was tapered using the P-97 Flaming/Brown type micropipette puller. Tapered capillaries were subsequently hand-grafted using Grit 5000 sandpaper to produce an orifice size ca. ~300-450 µm in diameter. The tapered and grafted three-bore capillaries were flushed with ethanol and dried using compressed air to remove debris from the sanding process. A square capillary (ID, 2 mm, length 20 mm) was fixed to a glass microscope slide with 5-minute Epoxy and the tapered three-bore tube was inserted inside. This was coaxially aligned with a collection tube (ID, 1.02 mm) and sealed using 5-minute Epoxy. Smaller round capillaries (ID, 0.58 mm) were pulled using a flame torch to form bent capillaries with narrow orifices (ca. 100-150 µm). These were

inserted into each side of the three-bore capillary and sealed with 5-minute Epoxy. A hypodermic needle with polypropylene hub sealed the join of the injection tube and the square capillary.

2.3.1.5 Device for rod-shaped hydrogel microspheres with Janus internal patterning

A theta borosilicate capillary was tapered using the P-97 Flaming/Brown type micropipette puller. Tapered capillaries were subsequently hand-grafted using Grit 5000 sandpaper to produce an orifice size ca. 400 µm in diameter. The tapered and grafted theta capillaries were flushed with ethanol and dried using compressed air to remove debris from the sanding process. Two glass microscope slides were glued together (short ends adjoined). A square capillary (ID, 2 mm, length 20 mm) was fixed to one slide and a square capillary (ID, 1.05 mm, length 20 mm) was fixed, horizontally aligned, on the other slide. The tapered theta tube was inserted inside the large square capillary and was coaxially aligned with a collection tube (ID,0.58 mm) which was inserted at the other end into the small square capillary at a length that ended halfway through the square capillary. A smaller round capillary (ID, 0.58 mm) was pulled using a flame torch to form bent capillaries with narrow orifices (ca. 100-150 µm). These were inserted into each side of the theta capillary and sealed with 5-minute Epoxy. Two hypodermic needles with polypropylene hub sealed each join of the injection tube and the square capillaries. An extension capillary tube (with zigzag path) was inserted into the small square capillary and fixed leaving a 1 mm gap between the end of the collection tube. This extension capillary restricted microdroplets into a rod-shaped morphology and increased the residence time through the device allowing some crosslinking to take place.

2.3.2 Fabrication of basic hydrogel microspheres

A standard microfluidic device with single round capillary (ID, 0.58 mm) was connected to 1 ml and 10 ml syringes via polyethylene tubing. An inner phase comprising RITC labelled alginate (Alg, 2 wt.%) was injected into the device from the 1 ml syringe (V_{in} = 0.2 ml h^{-1}) and an outer phase comprising decanol was injected from the 10 ml syringe (V_{out} = 4 ml h^{-1}) via the hypodermic needle. Droplets were collected in $CaBr_2$ (3 mM, decanol). Droplets were left at room temperature to crosslink for 24 h before being transferred to an aqueous environment via washing steps. 2x 7 : 3 (v : v) ethanol: water 2x 1 : 1(v : v) ethanol: water 1x water.

2.3.3 Fabrication of hydrogel microspheres through theta orifice

A theta microfluidic device was connected from the injection capillaries, via polyethylene tubing, to two syringes (1 ml) with dispensing needles. The syringes were filled with an aqueous inner phase and were connected to two different syringe pumps (Havard Apparatus model 11 Elite). Tubing also connected the microfluidic device to a 10 ml syringe filled with decanol outer phase. The inner aqueous phases were pumped through the device at V_{in} ranging from 0.005-0.25 ml h^{-1} and the outer phase was pumped through the device at V_{out} ranging from 5-100 ml h^{-1}. Droplets were collected in a petri dish filled with the 1-decanol outer phase and $CaBr_2$ crosslinker. Droplets were left at room temperature to crosslink for 24 h before being transferred to an aqueous environment via washing steps (2x 7 : 3 (v : v) ethanol: water 2x 1 : 1 (v : v) ethanol: water 1x water).

2.3.4 Hydrogel microspheres with segregated binary alginate populations

Hydrogel microspheres comprising a Janus-like distribution of fluorescently labelled sodium alginate were fabricated using the theta microfluidic device. Two independent aqueous inner phases, FITC-Alg (3.5 wt.%) and RITC-Alg (3.5 wt.%), were injected into the device through two syringes. Each syringe was connected to the injection capillaries inserted within the theta capillary and each with a V_{in} = 0.05 ml h^{-1}. A decanol outer phase was injected at a V_{out} = 30 ml h^{-1}. The microspheres were collected immediately in a 5 mM crosslinking solution and left for 20-24 h. Following transfer to water by repeated washing steps, images of the hydrogel microspheres were taken using CLSM. Microsphere diameters and fluorescence intensity were measured and analysed using Fiji software.

2.3.5 Different microsphere sizes by varying inner and outer phase velocities

Hydrogel microspheres were prepared using the theta septum glass capillary microfluidic device. Two independent RITC-Alg (3.5 wt.%) inner phases were injected into the device through a theta capillary each with V_{in} = 0.12 ml h^{-1}. A decanol outer phase was injected at various V_{out} = 10 ml h^{-1} to 100 ml h^{-1}. The microspheres were collected immediately in crosslinking solution for different time lengths so that the final concentration of $CaBr_2$ remained constant (5 mM). After 24 h crosslinking, the spheres were transferred to water. Hydrogel microspheres were prepared with each inner phase simultaneously injected at various V_{in} = 1.2 to 0.012 whilst the outer phase kept a constant V_{out} = 20 ml h^{-1}. The microspheres were collected immediately in a 5 mM crosslinking solution over a 1.5 min

time period, left to crosslink for 24 h, and then transferred to water. Microscope images were taken and then diameters were measured.

2.3.6 Changing $CaBr_2$ concentration

Hydrogel microspheres were prepared using the theta septum glass capillary microfluidic device. Two independent RITC-Alg (3.5 wt.%) inner phases were injected into the device through a theta capillary each with V_{in} = 0.05 ml h^{-1}. A decanol outer phase was injected at V_{out} = 25 ml h^{-1}. The microspheres were immediately collected in various concentrations of $CaBr_2$ ranging from 1-11 mM, left overnight and then transferred to an aqueous environment. The coefficient variance (CV) of a collection of hydrogel microspheres was calculated by mean diameter/standard deviation.

2.3.7 Changing microfluidic device orifice size

Several theta septum glass capillary microfluidic devices were manufactured, each with a hand-grafted orifice of ca. 200, 250, 300, 350 µm respectively. Two independent RITC-Alg (3.5 wt.%) inner phases were injected into the device through a theta capillary each with V_{in} = 0.1 ml h^{-1}. A decanol outer phase was injected at V_{out} = 25 ml h^{-1}. The microspheres were immediately collected in a petri dish containing decanol.

2.3.8 Hydrogel microspheres with Janus colloidosome populations

Hydrogel microspheres comprising a Janus-like distribution of a binary population of colloidosome-based protocells were prepared using the theta septum glass capillary microfluidic device. Colloidosomes were dispersed into Alg using pipette mixing. Two independent colloidosome-Alg (3.5 wt.%) inner phases (RITC-GOx colloid. and Dy405-HRP colloid.) were injected into the device through a theta capillary each with V_{in} = 0.15 ml h^{-1}. A decanol outer phase was injected at V_{out} = 30 ml h^{-1}. The microspheres were collected in 3 mM $CaBr_2$ before transferral to water.

2.3.9 Hydrogel microspheres with free enzymes

Hydrogel microspheres were prepared using the theta septum glass capillary microfluidic device. Two independent enzyme-Alg (3.5 wt.%) inner phases (RITC-GOx and Dy405-HRP, 2 mg ml^{-1}) were injected into the device through a theta capillary each with V_{in} = 0.1 ml h^{-1}. A decanol outer phase was injected at V_{out} = 30 ml h^{-1}. The microspheres were immediately collected in various concentrations of $CaBr_2$ = 3, 4, 5, 6, 7 mM, left overnight and then transferred to an aqueous environment.

2.3.10 Hydrogel microspheres with different volume ratios of segregated colloidosome populations

Hydrogel microspheres were fabricated using Alg (3.5 wt.%) and $CaBr_2$ (3 mM) crosslinker. Different V_{in} values for the two inner phases were used to produce spatially segregated micro-colonies with different protocell volume ratios. For example, at V_{in} = 0.1-0.25 ml h^{-1} and V_{out} = 100 ml h^{-1}, a 70% volume ratio of GOx-containing colloidosomes was achieved at a 5 : 2 (0.25 : 0.1 ml h^{-1}) RITC-labelled GOx : Dy405-labelled HRP velocity ratio; this volume ratio was reduced to 60, 50 or 25% by changing the velocity ratio to 5 : 3 (0.2 : 0.12 ml h^{-1}), 3 : 5 or 2 : 5, respectively.

2.3.11 Hydrogel microspheres with three segregated colloidosome populations

Hydrogel microspheres were prepared using the three-bore glass capillary microfluidic device. Three independent colloidosome-Alg inner phases (RITC-GOx colloid., FITC-GOx colloid., Dy-HRP colloid.) were injected into the device through the three-bore capillary each with V_{in} = 0.2 ml h^{-1}. A decanol outer phase was injected at V_{out} = 100 ml h^{-1}. Hydrogel microspheres were collected in 5 mM $CaBr_2$, left overnight and then transferred to an aqueous environment.

2.3.12 Rod-shaped hydrogel microparticles with segregated colloidosome populations

Rod shaped hydrogel microparticles comprising a Janus-like distribution of a binary population of colloidosome-based protocells were fabricated using a theta septum microfluidic device with smaller collection tube (ID, 0.58 mm) to spatially compress the microparticles into rod-like shapes. $CaBr_2$ was

introduced into the device downstream, to initiate the microparticle crosslinking process. Two independent colloidosome-Alg (3.5 wt%) inner phases (RITC-GOx colloid. and Dy405-HRP colloid.) were injected into the device through a theta capillary each with V_{in} = 1 ml h^{-1}. A decanol outer phase was injected at V_{out} = 10 ml h^{-1} and a $CaBr_2$ (25 mM) outer phase injected at V_{out} = 10 ml h^{-1}. Spheres were collected in decanol, left to crosslink and then transferred to aqueous phase via standard washing steps.

2.3.13 Preparation of Au nanoparticles

100 µl $HAuCl_4$ aqueous solution (100 mg ml^{-1}) was added to a 250 ml aqua regia-treated round bottom flask with 80 ml deionised water. The solution was heated to 60 °C. Sodium citrate (0.049 g), tannic acid (0.01 g) and K_2CO_3 (0.0036 g) were dissolved in 20 ml deionised water and also heated to 60 °C. After 15 min of heating at 60 °C the sodium citrate/tannic acid/K_2CO_3 solution was quickly transferred to the $HAuCl_4$ solution and reacted under magnetic stirring (400 rpm) for 10 min at 60 °C. The temperature was then further increased (ca. 100 °C) so that the reaction boiled for 5 min before being cooled to room temp.

2.3.14 Preparation of caged coacervate droplets

A coacervate phase was prepared by mixing 400 µl PDDA (400 mM, PBS 10 mM pH 7.4) with 900 µl CM-dextran (370 mM, PBS 5 mM pH 7.4) and isolating by centrifugation (6000 rpm, 3 min). Caged coacervate droplets were then fabricated under vortex mixing following the addition of Au nanoparticles (100 µl) and TA-PEG 20k-TA (5 µl) to the coacervate phase (10 µl). Fluorescently labelled coacervate droplets were prepared by adding 10 µl FITC-labelled CM-dextran to the coacervate preparation phase.[58]

2.3.15 Preparation of coacervate-based prototissue

Caged coacervate droplets were prepared as above, then centrifuged (1000 rpm, 3 min) to form a PEG-Au nanoparticle coated coacervate prototissue.

2.3.16 Small PEG-coated colloidosomes

Small colloidosomes were made according to the method in section 2.2.1. However, after the addition of TMOS and 20 h rotation overnight, PEG silicate (10 µl) was added to the solution and the colloidosomes were further rotated for 3 h. Colloidosomes were then transferred to water via the normal procedure.

2.3.17 Large PEG-coated colloidosomes

Partially hydrophobic silica nanoparticles (15 mg) were mixed with dodecane (2 ml) for 1 minute by sonication in an ultrasound bath whilst being continuously pipetted. 100 µl of an aqueous solution of enzyme (30 mg ml^{-1}, pH 8.5 sodium bicarbonate buffer) was added to the oil/silica suspension and then vigorously shaken by hand for 1 minute to form a Pickering emulsion. Bis(trimethoxysilyl)hexane (BMOSH, 15 µl) was added to the Pickering emulsion which was then rotated on a Stuart tube rotator at 25 rotations per minute (rpm) for 20 h. After 20 h, PEG silicate (10 µl) was added to the solution and the colloidosomes were further rotated for 24 h.

2.3.18 Coacervate prototissue with dispersed colloidosome population

Caged coacervate droplets were fabricated under vortex mixing following the addition of Au nanoparticles (100 µl) and TA-PEG 20k-TA (5 µl) to a FITC-labelled coacervate phase (10 µl). PEG-coated colloidosomes (2-10 µl) were added to the caged coacervate solution and mixed by pipetting for 20 seconds. The solution was then centrifuged (1000 rpm, 3 min).

2.3.19 Coacervate prototissue with segregated colloidosome populations

Colloidosome-coacervate prototissues were fabricated with RITC-GOx colloidosome and FITC-GOx colloidosome populations respectively. The prototissues were placed on top of each other inside an Eppendorf and 50 µl of caged coacervate droplets were added. Upon centrifugation (1000 rpm, 3 min) the two prototissues were joined together.

2.4 Chapter 4 experimental methods

2.4.1 Enzyme cascades within colloidosome-embedded microspheres

All microspheres were prepared using [Alg] = 3.5 wt.%, [$CaBr_2$] = 3 mM.

2.4.1.1 Enzyme cascade within segregated hydrogel microparticles with Janus colloidosome populations

Hydrogel microspheres with spatially segregated populations of RITC-GOx (30 mg ml^{-1})-containing colloidosomes and Dy405-HRP (30 mg ml^{-1})-containing colloidosomes were transferred to a microscope slide well, followed by the removal of excess water using a pipette. D-glucose (50 µl, 1 M) and o-Phenylenediamine o-PD (10 µl, 10 mM) were added to the well simultaneously. CLSM images were taken at regular time intervals over a 40-min period to observe the appearance of 2,3-DAP. Control experiments, in the absence of d-glucose input, were conducted with the addition of deionised water (50 µl) to the microscope well along with o-PD (10 µl, 10 mM). The input d-glucose concentration was also varied from 0-1 M by dilution with deionised water before microscope well addition.

2.4.1.2 Enzyme cascade with BSA and either GOx or HRP colloidosome community

Hydrogel microspheres with spatially segregated populations of RITC-GOx (30 mg ml^{-1})-containing colloidosomes and Dy405-BSA (10 mg ml^{-1})-containing colloidosomes were prepared. Similarly, hydrogel microspheres with spatially segregated populations of RITC-BSA (5 mg ml^{-1})-containing colloidosomes and Dy405-HRP (30 mg ml^{-1})-containing colloidosomes were prepared. A fresh batch of microspheres with spatially segregated populations of RITC-GOx (30 mg ml^{-1})-containing colloidosomes and Dy405-HRP (30 mg ml^{-1})-containing colloidosomes were also fabricated. 10 spheres of one type of microsphere were transferred to a microscope well. D-glucose (8.4 M) and o-PD (17 mM) were added to the well simultaneously and CLSM images were taken at 5 min time intervals over a 25 min period. The process was then repeated for each microsphere population.

2.4.1.3 Comparison between Janus and homogeneous colloidosome arrangements

Hydrogel microspheres with Janus spatially segregated populations of RITC-GOx (30 mg ml^{-1})-containing colloidosomes and Dy405-HRP (30 mg ml^{-1})-containing colloidosomes were fabricated. The inner phases comprising colloidosome-Alg, were then mixed together to form the inner phases

for homogeneous spheres. Hydrogel microspheres containing a homogeneous population of RITC-GOx (30 mg ml^{-1})-containing colloidosomes and Dy405-HRP (30 mg ml^{-1})-containing colloidosomes were therefore created. In each experiment ca. 40 spheres of one type of either Janus or homogeneous microsphere were placed in the microscope well. A d-glucose/o-PD mixture (35 µl, 0.84 M/17 mM) was added to the external solution and images were taken at 5 min intervals over a 30 min period.

2.4.1.4 Enzyme cascade within rod-shaped microparticles

Rod-like hydrogel microparticles comprising a Janus-like distribution of a binary population of RITC-GOx (30 mg ml^{-1})-containing colloidosomes and Dy405-HRP (30 mg ml^{-1})-containing colloidosomes were transferred to a microscope well. D-glucose (1.2 M) and o-PD (14 mM) were added to the well and CLSM images were taken at 5 min time intervals over 30 min.

2.4.1.5 Enzyme cascade within ternary segregated microspheres

Hydrogel microparticles comprising a ternary distribution of Dy405-Inv (30 mg ml^{-1})-containing, RITC-GOx (30 mg ml^{-1})-containing and HRP (30 mg ml^{-1})-containing colloidosomes were transferred to a microscope well (ca. 15 spheres). A sucrose/o-PD mixture (35 µl, 0.84 M/17 mM) was added to the well at t = 0 min and CLSM images were taken at 5 min time intervals over 20 min.

2.4.1.6 Enzyme cascade within different volume ratios of segregated colloidosomes

Hydrogel spheres comprising spatially segregated micro-colonies with different protocell volume ratios were prepared. Specifically, three types of hydrogel microsphere with RITC-GOx (30 mg ml^{-1})-containing colloidosome populations (70 %, 50% and 30%) and Dy405-HRP (30 mg ml^{-1})-containing colloidosome populations (30 %, 50% and 70%) were fabricated. 20 microspheres were transferred to a well followed by simultaneous addition of d-glucose (1.2 M) and o-PD (14 mM). A control experiment wherein glucose was replaced with deionised water was also performed.

2.4.1.7 Fluorescence intensity measurements

Microscope setting were as follows; Dylight405 λ_{ex}= 405 λ_{em}= 415-460 nm, RITC λ_{ex}= 561 λ_{em}= 571-630 nm 2,3-DAP λ_{ex}= 458 λ_{em}= 470-540 nm. Unless otherwise stated, fluorescence intensity measurements were obtained using FIJI software to measure the green intensity across the whole of

a single hydrogel microparticle at each timepoint. This data was then plotted in Origin. Error bars were obtained by repeating the experiment three times and then calculating the standard deviation.

2.4.2 Urease-mediated hydrogel microsphere disassembly

Ca. 50 hydrogel microspheres comprising a homogeneous population of URS-containing colloidosomes (45 kU ml^{-1}) were transferred to the well of a microscope slide. Following this, excess water was removed. Urea (35 µl, 1 M) was added to the well and bright field and fluorescent microscopy images were taken at regular time intervals over a 3 h period. Control experiments were conducted whereby the hydrogel spheres were left in deionised water for the same duration of time. Hydrogel microspheres comprising a homogeneous population of RITC-URS (45 kU ml^{-1}) containing colloidosomes were also fabricated as a method of visualising the release of colloidosomes from the hydrogel matrix.

2.4.3 Tyramine-labelled alginate synthesis

Sodium alginate (0.1 g, 0.5 wt.% aq. solution) was dissolved in pH 6 MES buffer (0.1 M, 20 ml) for 2 h with continuous stirring. EDC (0.048 g) and NHSS (0.027 g) were subsequently added, and the reaction stirred for 30 min to activate the carbonyl groups. Tyramine hydrochloride (0.9 g) was added and left to stir at room temperature for 24 h. The solution was dialysed for 3 days, then freeze-dried.[182]

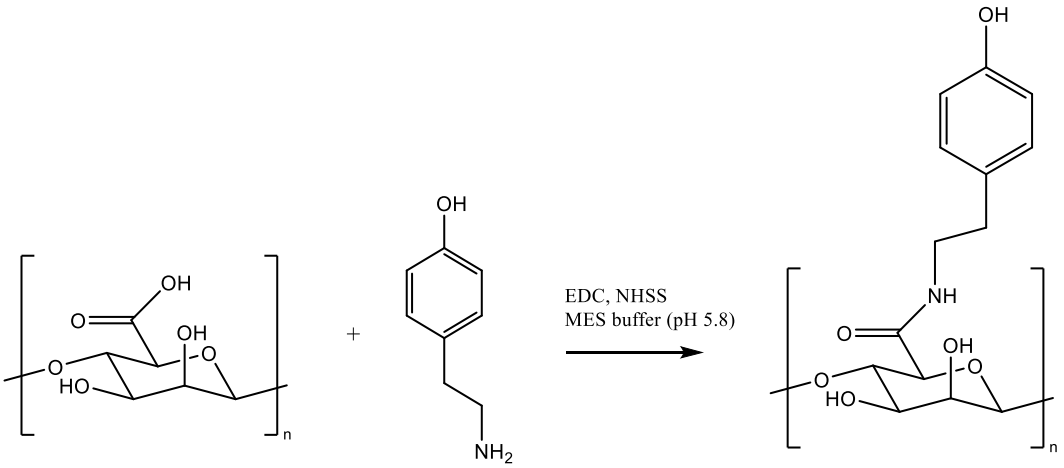

Scheme 2.3. Synthesis of tyramine labelled alginate (ty-Alg).

The percentage of tyramine was calculated using UV-Vis spectroscopy. A calibration curve which measured the absorbance of tyramine at 275 nm over concentrations ranging from 0.00005 – 0.0011 wt.% was created. The absorbance of tyramine functionalised alginate (ty-Alg, 0.02 wt.%) at 275 was measured (0.29) and the value was used with the calibration trend line to work out the tyramine concentration. This was then adjusted for dilutions (0.0004 wt.%). The substitution degree was therein worked out as 3%.

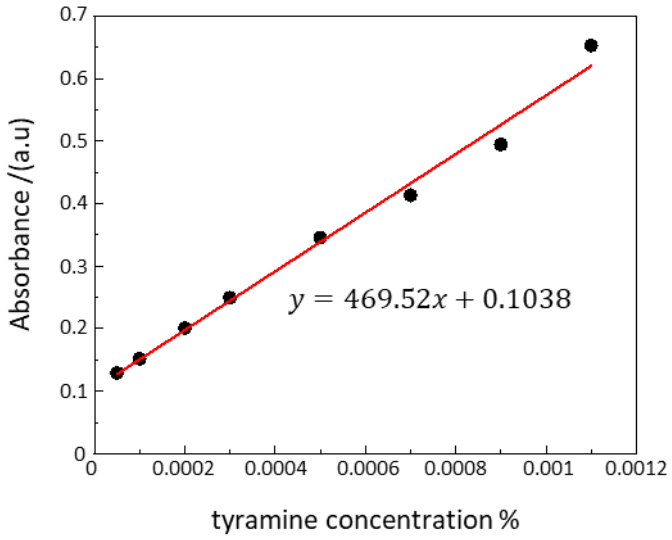

Figure 2.2. Calibration concentrations of tyramine. *Calibration plot showing the absorbance of tyramine at 275 nm for concentrations 0.00005-0.0011 wt.%.*

2.4.4 H_2O_2/HRP mediated covalent crosslinking of hydrogel microspheres

Hydrogel microspheres fabricated using ty-Alg (3.5 wt.%) inner phases were ionically crosslinked using $CaBr_2$ (3 mM) in decanol before being transferred to water. A mixture of H_2O_2 (400 µl, 0.9 mM) and HRP (40 µl, 450 U ml^{-1}) was added to a collection of ca. 50 microspheres and left to covalently crosslink for 3 h. These spheres were subsequently transferred to the well of a microscope slide where sodium citrate (0.5 %) was added. Microscope videos were taken over a 10 min period. Control experiments were conducted in the absence of either HRP or H_2O_2.

2.4.5 GOx/HRP mediated covalent crosslinking of hydrogel microspheres

Hydrogel microspheres containing FITC-GOx (20 mg ml^{-1}) loaded colloidosomes were prepared by microfluidics using tyramine functionalised alginate and crosslinked with $CaBr_2$ (3 mM) in decanol. Ca.

50 microspheres were transferred to the well of a microscope slide and excess water was removed. D-glucose (35 µl, 1M) and HRP (2.5 µl, 600 U ml^{-1}) were added to the well and left for a minimum of 3 h to produce a network of covalent crosslinks. The external solution was removed and sodium citrate (0.5 wt.%) was then added to remove the Ca^{2+} ionic crosslinks. Control experiments were conducted in the absence of glucose whereby deionised water (35 µl) and HRP (2.5 µl, 600 U ml^{-1}) were added to the well and left for the same duration of time. Bright field and fluorescence images were taken at regular time intervals after the addition of sodium citrate (0.5 wt.%).

2.4.6 Collective disassembly/resilience of hydrogel microspheres

Janus hydrogel microspheres with one domain containing RITC-Alg, unlabelled Alg and URS (130 KU ml^{-1})- containing colloidosomes and the other domain containing ty-Alg (25%), non-modified Alg (75%) and FITC-GOx-(30 mg ml^{-1}) loaded colloidosomes were prepared by microfluidics at an inner phase Alg : inner phase ty-Alg velocity ratio, 0.75 : 0.25 ml h^{-1}. These microspheres were ionically crosslinked off-device using $CaBr_2$ (3 mM) in decanol and microspheres were then transferred to aqueous environment after 24 h. The ionically crosslinked hydrogel microspheres were transferred to the well of a microscope slide (ca. x50). D-glucose (0.5 M), urea (0.5 M) and HRP (3 mg) were added simultaneously into the well and a coverslip placed over to seal it. Fluorescence and optical images were taken every 2 h. Control experiments were conducted whereby just deionised water was added to the well in place of d-glucose and urea, and just urea (1 M) in place of d-glucose.

2.4.7 Programmed disassembly of hydrogel microspheres

Hydrogel microspheres were made comprising a segregated community of URS-containing colloidosomes in unmodified-Alg and FITC-GOx-containing colloidosomes in ty-Alg. Four different collections of microspheres were made, each with URS-containing colloidosomes containing different concentrations of URS (10, 50, 100, 150 kU). 20 spheres were placed in a microscope well and a mixture of glucose (0.5 M), urea (0.5 M) and HRP (3 mg) was added. The spheres were monitored over 30 h, with microscope optical images being taken a t=0, t=6 and t=30. The ‘disassembly time’ was the required time for the entire URS-containing domain to completely degrade. Each experiment was repeated three times.

2.4.8 Collective disassembly/assembly of hydrogel microspheres

Control experiments were also performed with non-segregated colloidosome and hydrogel microsphere domains. Firstly, completely homogenous hydrogel microspheres with both domains containing ty-Alg (12.5 wt.%), RITC-labelled and non-modified alginate (87.5 wt.%), URS-loaded colloidosomes and FITC-GOx-loaded colloidosomes were prepared. Secondly, Janus hydrogel microspheres were prepared with a Janus population of hydrogel but a homogeneous population of colloidosomes. This meant that one domain (V_{in} = 25 ml h^{-1}) contained ty-Alg (25%), non-modified alginate (75%) and a non-segregated mixed community of URS-loaded colloidosomes and FITC-GOx-loaded colloidosomes. The other domain (V_{in} = 75 ml h^{-1}) contained RITC-labelled Alg, unlabelled Alg and a non-segregated mixed community of URS-loaded colloidosomes and FITC-GOx-loaded colloidosomes. In these experiments, d-glucose (0.48 M), urea (0.48 M) and HRP (30 mg ml^{-1}) were simultaneously added into the microscope well. More control experiments were conducted whereby urea (0.48 M) and HRP (30 mg ml^{-1}) were added in the absence of d-glucose.

2.4.9 Jettisoning hydrogel microspheres

Janus hydrogel microspheres with one domain (V_{in} = 75 ml h^{-1}) containing unlabelled Alg and FITC-labelled GOx-(30 mg ml^{-1}) loaded colloidosomes and the other domain (V_{in} = 25 ml h^{-1}) containing ty-Alg (25%), RITC-Alg (75%) and URS (130 kU ml^{-1})-containing colloidosomes were prepared by microfluidics and ionically crosslinked off-device using $CaBr_2$ (3 mM) in decanol and then transferred to aqueous environment after 24 h. The ionically crosslinked hydrogel microspheres were transferred to the well of a microscope slide (ca. x50). D-glucose (0.5 M), urea (0.5 M) and HRP (3 mg) were added simultaneously into the well and a coverslip placed over to seal it. An image was taken at t=0 and t=24. Control experiments were conducted whereby just water was added to the well in place of d-glucose and urea and just urea (1 M) in place of d-glucose.

2.4.10 Enzyme cascades within colloidosome hotspots

Caged coacervate droplets were fabricated under vortex mixing following the addition of Au nanoparticles (100 µl) and TA-PEG 20k-TA (5 µl) to a coacervate phase (10 µl). Large PEG-coated RITC-GOx (30 mg ml^{-1})-loaded colloidosomes (4 µl) were added to the caged coacervate solution and mixed by pipetting for 20 seconds. The solution was then centrifuged (1000 rpm, 3 min). The tissue

was transferred to a microscope slide well and d-glucose (0.16 M), HRP (0.2 mg) and o-PD (0.01 mM) were simultaneously added to the outside of the tissue. CLSM images were taken at 1 min time intervals for a total of 15 min.

Experiments wherein large PEG-coated RITC-β-glucosidase (30 mg ml^{-1})-loaded colloidosomes were embedded inside the caged coacervate tissue were also conducted. The tissue was transferred to a microscope slide well and fluorescein di-β-D-glucopyranoside (FDGlu, 0.25 mg ml^{-1}) was added to the outside of the tissue. CLSM images were taken over a 20 min time-period.

2.4.11 Enzyme cascades between colloidosome hotspots

Caged coacervate droplets were fabricated under vortex mixing following the addition of Au nanoparticles (50 µl) and TA-PEG 20k-TA (2.5 µl) to a coacervate phase (5 µl). Small PEG-coated RITC-GOx (30 mg ml^{-1})-loaded colloidosomes (0.5 µl) were added to the caged coacervate solution and mixed by pipetting for 20 seconds. The solution was then centrifuged (1000 rpm, 3 min). Another caged coacervate tissue was fabricated with small DyHRP (30 mg ml^{-1})-loaded colloidosomes (0.5 µl) embedded inside. Each tissue (with GOx and HRP loaded colloidosomes) was transferred to a fresh solution of caged coacervates and was centrifuged (1000 rpm, 3 min). The tissue was transferred to a microscope slide well and d-glucose (0.16 M), and o-PD (0.01 mM) were simultaneously added to the outside of the tissue. CLSM images were taken at 1 min time intervals for a total of 15 min. Control experiments were conducted in the absence of d-glucose. The experiment was repeated 3 times.

2.5 Chapter 5 experimental methods

2.5.1 Attaching polymers to small silica colloidosomes

Colloidosomes were made according to section 2.2.1. Following the addition of TMOS, the colloidosomes were rotated for 4 h on a Stuart tube rotator at 25 rpm. GLYMO (15 µl) was subsequently added to the colloidosome suspension and left to rotate for a further 20 h. As with section 2.2.1, colloidosomes were then transferred to water via a series of washing steps, 2x 7 : 3 (v : v) ethanol : water, 1x 1 : 1 (v : v) ethanol : water, 1x polymer. During the final wash, an aqueous polymer solution was added (alginate or chitosan, 0.08 wt. %). The suspension was further rotated overnight for 20 h at 25 rpm.

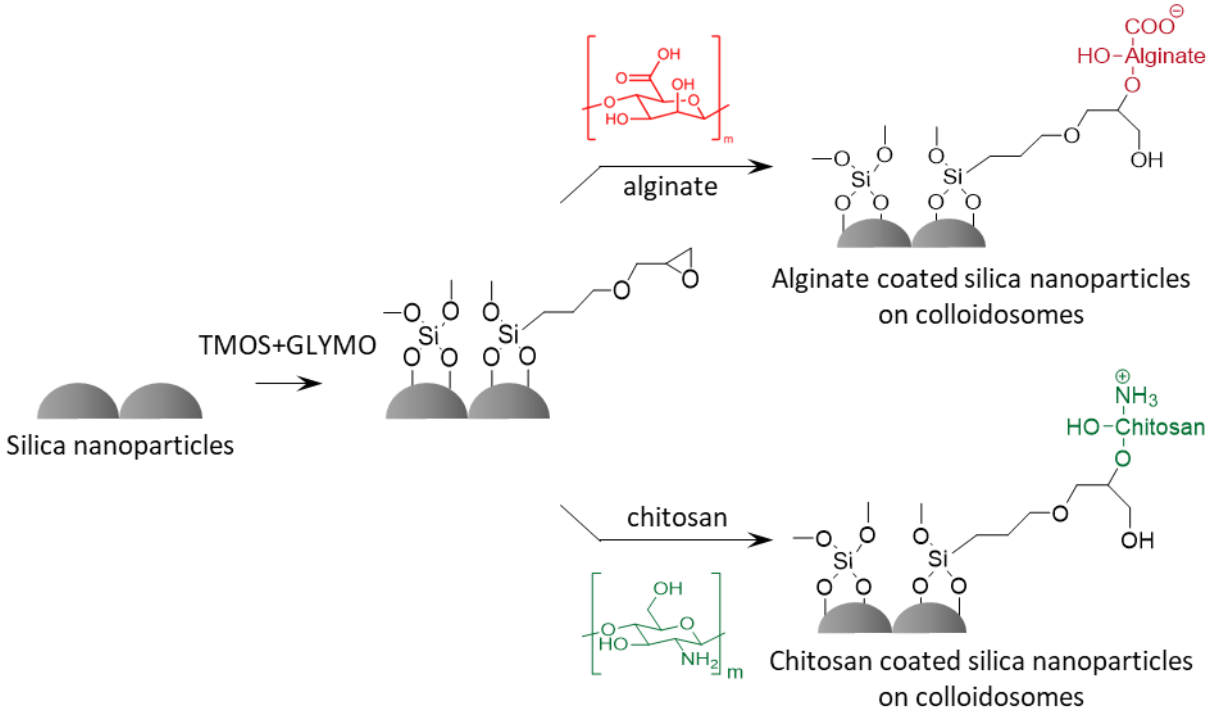

Scheme 2.4. Synthesis of polymer coated silica nanoparticle colloidosomes.

2.5.1.1 Preparation of RITC labelled alginate-coated colloidosomes

Colloidosomes were prepared according to the previous method (2.5.1). Specifically, FITC-labelled GOx (30 µl, 30 mg ml^{-1}) was added to a suspension of silica nanoparticles in dodecane to form a Pickering emulsion. 4 h after the addition of TMOS (15 µl), GLYMO (15 µl) was added to the colloidosomes and they were rotated overnight for ca. 20 h at 25 rpm. Colloidosomes were then transferred to an aqueous solution wherein the final wash consisted of an RITC-labelled alginate (0.08 wt.%) solution. Colloidosomes were collected by centrifugation (2000 rpm, 2 min) then dispersed in 0.5 ml deionised water to give a concentration of ca. 10 $x10^9$ colloidosomes ml^{-1} (section 2.5.1.3).

2.5.1.2 Preparation of FITC labelled chitosan-coated colloidosomes

Colloidosomes were prepared according to the previous method (2.5.1). Specifically, RITC-labelled GOx (30 µl, 30 mg ml^{-1}) was added to the suspension of silica nanoparticles in dodecane to form a Pickering emulsion. 4 h after the addition of TMOS (15 µl), GLYMO (15 µl) was added to the colloidosomes and they were rotated overnight for ca. 20 h at 25 rpm. Colloidosomes were then transferred to an aqueous solution wherein the final wash consisted of an FITC-labelled chitosan (0.08 wt. %). Colloidosomes were collected by centrifugation (2000 rpm, 2 min) then dispersed in 0.5 ml dialysed water to give a concentration of ca. 10 $x10^9$ colloidosomes ml^{-1} (section 2.5.1.3).

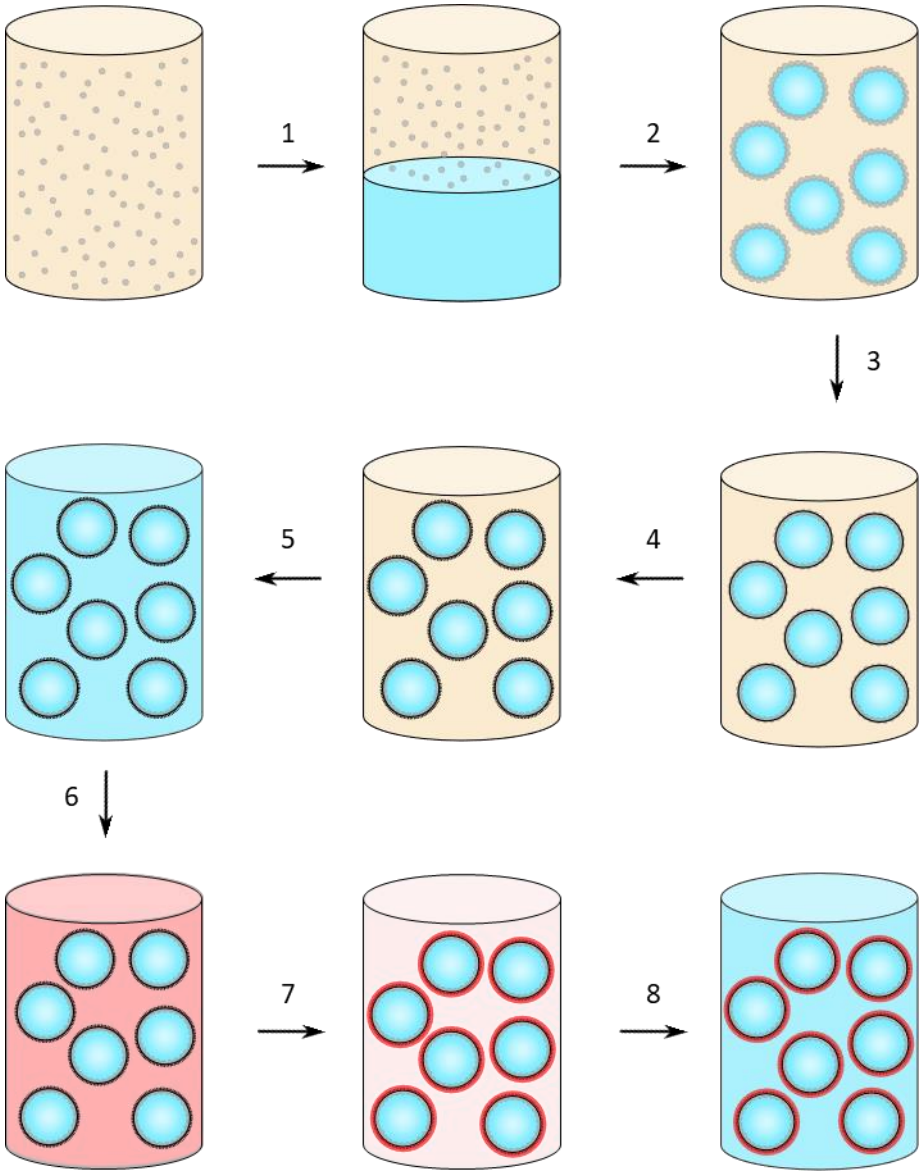

Scheme 2.5. Step by step vial synthesis of polymer-coated colloidosomes. *(**1**) Aqueous enzyme solution is added to a silica nanoparticle dispersion in oil. (**2**) Vigorous hand shaking makes Pickering emulsion. (**3**) TMOS is added to crosslink silica nanoparticles. (**4**) GLYMO is added to attach epoxide groups. (**5**) Colloidosomes are transferred to water environment. (**6**) Polymer is added to the environment. (**7**) Colloidosomes are rotated for 20 h. (**8**) Colloidosomes are washed with water.*

2.5.1.3 Calculation of colloidosome concentration in stock solution

Bulk colloidosome solutions were diluted (x20) and fluorescence microscope images were taken. A colloidosome number density was calculated within a 100 μm^2 area from the image. This number density was extrapolated into a 100 μm^3 dimension by assuming the average diameter of a colloidosome to be 5 µm and so by multiplying the number density in 100 μm^2 by 20. This was then multiplied to account for the dilution factor. The number density was then converted from no.

colloidosomes per μm^3 into no. colloidosomes per ml. The final concentrations were ca. 10 $x10^9$ colloidosomes ml^{-1}.

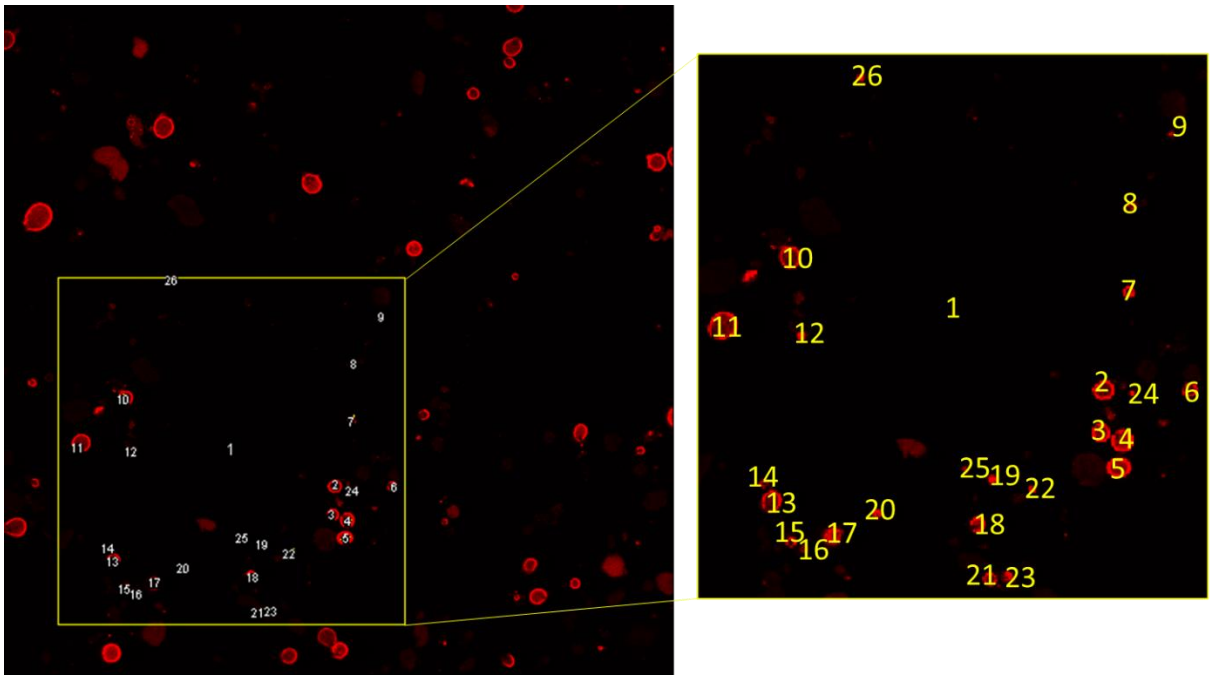

Figure 2.3. Colloidosome number density. *Fluorescence images of Ch coated RITC-GOx loaded colloidosomes diluted by a factor of 20. Scale bar, 25 µm. Square region (yellow box) showing a 100 μm^2 area, which is magnified to show the colloidosome number density.*

2.5.1.4 DLS and zeta potential measurements

1 ml PBS buffer (0.001M, pH 4.5) containing each uncoated, FITC-Alg and RITC-Ch coated colloidosomes (10 µl) were prepared for DLS and zeta potential analysis, to work out the size distribution and surface charge of the colloidosomes.

2.5.2 Colloidosomes without GLYMO

Colloidosomes were prepared according to a previous method (section 2.3.1). Specifically, FITC-labelled GOx (30 µl, 30 mg ml^{-1}) was added to a suspension of silica nanoparticles in dodecane to form a Pickering emulsion. TMOS (15 µl) was subsequently added, and the colloidosomes were rotated overnight for 20 h at 25 rpm. Colloidosomes were then transferred to an aqueous solution via a series of washes, 2x 7 : 3 (v : v) ethanol : water, 1x 1 : 1 (v : v) ethanol : water, 1x polymer. The final polymer wash consisted of a solution of RITC-labelled Alg (0.08 wt. %). The aqueous solution of colloidosomes was then rotated for a further 24 h at 25 rpm. Colloidosomes were collected by centrifugation (2000 rpm, 2 mins) then dispersed in 0.5 ml deionised water. This method was

repeated with RITC-labelled GOx (30 mg ml^{-1}) and the addition of FITC-labelled Ch. CLSM images were taken in the red and green channel to observe the absence of fluorescent polymer due to the lack of GLYMO step.

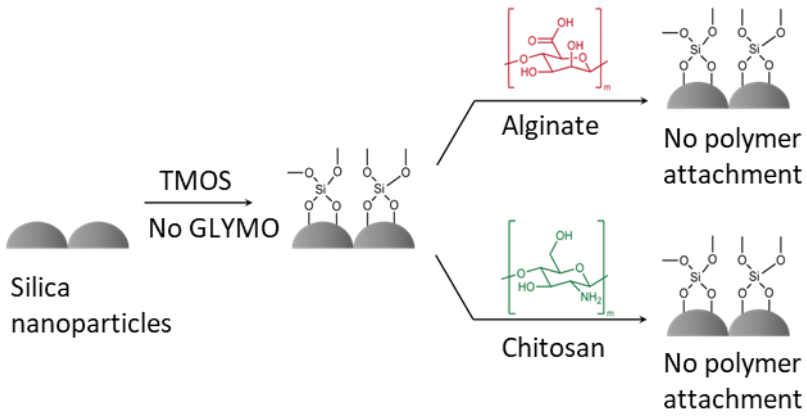

Scheme 2.6. Attempted attachment of polymers with no GLYMO step.

2.5.3 Colloidosome assembly experiments

0.5 ml PBS buffer (0.001M, pH 4.5) was added to a small glass vial. Alg-coated colloidosomes (6 µl) were dispersed into the PBS solution and gently stirred for 1 min at 100 rpm. A second 0.5 ml PBS solution (0.001M, pH 4.5) with Ch-coated colloidosomes (6 µl) was prepared. The Ch-colloidosome suspension (in vial 2) was injected into the Alg-coated colloidosome suspension (vial 1) and stirred at 5 min at 100 rpm. A Canon EOS 500D Digital SLR Camera with EF-S 60 mm macro lens was used to capture a video of the whole process. Snap shots of the video were taken at t=0 and 5 min. 40 µl samples of the solution were collected into glass channel slides for CLSM observations. Control experiments with uncoated colloidosomes were achieved by the same process.

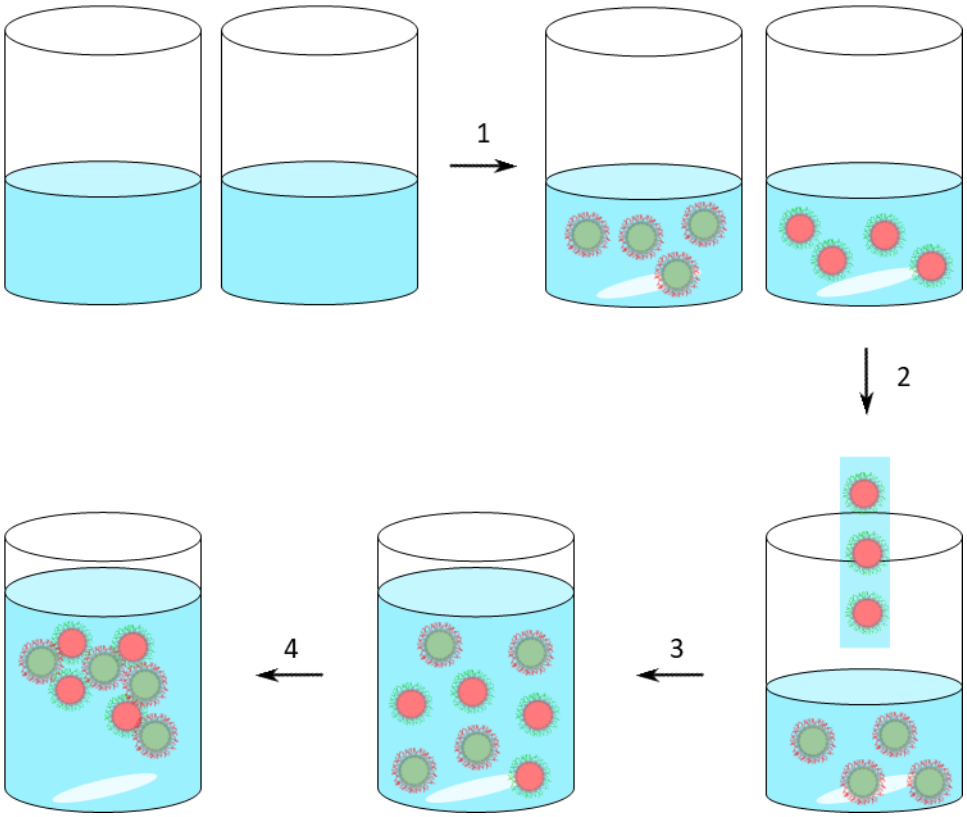

Scheme 2.7. Self-assembly of Alg and Ch coated colloidosomes. *(**1**) Addition of Alg-coated colloidosomes and Ch-coated colloidosomes to two PBS solution-containing vials respectively. (**2**) contents of the vial containing Ch-coated colloidosomes is syringed into the other vial. (**3**) Solution stirred at 100 rpm for 5 min. (**4**) Colloidosomes show visible self-assembly after 5 min.*

2.5.4 Zeta potential measurements of polymer-coated colloidosomes

RITC-Ch and FITC-Alg-coated colloidosomes were each diluted (x100) into 1 ml PBS buffer (0.001M) at various pHs (pH 2, 2.5, 3, 3.5, 4, 4.5, 6, 6.5, 7, 7.5, 8, 8.5 and 9). The suspensions were transferred into a Malvern DTS1070 cell, and zeta potential was measured by a Malvern Nano series Zetasizer.

2.5.5 pH-triggered self-assembly of Alg and Ch coated colloidosomes

PBS (0.001 M) solutions at pH 2, 4.5 and 7 were prepared. HCl and NaOH were used to alter the pH. 0.5 ml PBS solutions containing suspended colloidosomes were prepared according to table 2.2. Vial 2 was injected into vial 1 and stirred at 100 rpm for 5 min. Each combination was observed by CLSM imaging and a video was taken.

Table 2.2. *1 : 1 mixing of polymer-coated polymers.*

pH	Colloidosomes in Vial 1	Colloidosomes in Vial 2
4.5	Alg-coated FITC-GOx containing	Ch-coated RITC-GOx containing
4.5	Alg-coated FITC-GOx containing	Alg-coated FITC-GOx containing
4.5	Ch-coated RITC-GOx containing	Ch-coated RITC-GOx containing
7	Alg-coated FITC-GOx containing	Ch-coated RITC-GOx containing
7	Alg-coated FITC-GOx containing	Alg-coated FITC-GOx containing
7	Ch-coated RITC-GOx containing	Ch-coated RITC-GOx containing
2	Alg-coated FITC-GOx containing	Ch-coated RITC-GOx containing
2	Alg-coated FITC-GOx containing	Alg-coated FITC-GOx containing
2	Ch-coated RITC-GOx containing	Ch-coated RITC-GOx containing
4.5	RITC-GOx containing	FITC-GOx containing

2.5.6 Fluorescence activated cell sorting (FACS)

FACS analysis was carried out on a BD LSRFortessa X-20 sorting machine, operating at low pressure with a 100 µm sorting nozzle. A minimum of 10^6 particles were analysed to obtain 2D plots of the forward scattering (FSC) and side scattering (SSC) light. Time series of counting were obtained and FlowJo 7.6 software was used for all the data analysis. Samples for FACS analysis were prepared according to section 2.5.3. In brief, a total 12 µl colloidosomes were stirred in 1 ml PBS solutions (0.001M) at various pHs. These samples were then immediately drawn into the FACS machine.

2.5.7 Tissue formation

100 µl of Alg-coated colloidosomes were placed into a PDMS mould with a cut-out (l : w : h, 1 : 0.5 : 0.5 cm) placed on a microscope slide. 50 µl $CaCl_2$ (5 wt.%) was added to the cut-out and a coverslip placed over the opening and then left to rest overnight. The mould was then removed. 5 µL each of Alg and Ch-coated colloidosomes were transferred into a 1 ml PBS solution (0.001M, pH 4.5) and stirred to form aggregates. 2 µL of 100 mM $CaCl_2$ was added into the solution and the resulting aggregates left to settle and gel. Gelled tissues were imaged by CLSM z-stacking, through an optical microscope and by a camera.

2.5.8 Acoustic trapping

A custom-built acoustic trapping device based on a square arrangement of four piezoelectric transducers (Noliac, NCE 51, L15 x W2mm x T1 mm) was used. The opposing transducer pairs were wired in series, driven by two signal generators (Agilent 33220a-001), and connected to an oscilloscope (Agilent DSOX2014A). A glass coverslip was attached to the bottom of the device using an adhesive.

For *in situ* 2D array self-assembly of colloidosomes, 100 µl of polymer coated colloidosome solutions (total volume = 0.5 ml, 1 mM PBS, 4.5 pH) were added into the sample chamber at the orthogonal transducer pairs. Waves were produced at third harmonic frequency (7.00/7.01 MHz and 10 V). The solution was kept standing for 30 min to ensure homogeneous colloidosome assembly formation at a separation of 50 µm. The supernatant in the acoustic chamber was carefully removed and exchanged with deionised water three times, under the same acoustic force field. High contrast images against the background solution were obtained after one hour of *in situ* pattern formation. When the acoustic wave was switched off, after self-assembly, colloidosomes remained in position. Controls with uncoated colloidosomes showed the random dispersion of colloidosomes. For colloidosome co-assembly at different ratios, either Alg-coated or Ch-coated colloidosomes (varying ratios, total volume = 0.5 ml) were introduced into the sample chamber followed by supernatant replacement with deionised water. Then 50 µl of complementary polymer coated colloidosomes were added, supernatant was replaced, and the resulting assembly was observed under fluorescence microscope.

2.5.9 Region of interest (ROI) calculations

ROI calculations were obtained by importing a CLSM image into FIJI and manually drawing around each individual fluorescent region. The regions were then counted and plotted in Origin. ROIs for each fluorescence channel were calculated. When there was a mix of channels, all the regions were selected, if there was a red and green in a region, then it was counted for both counts. CLSM images of assembled or physically separated colloidosome solutions were also directly imported into Origin and converted to corresponding heatmap representation in pixels and analysed.

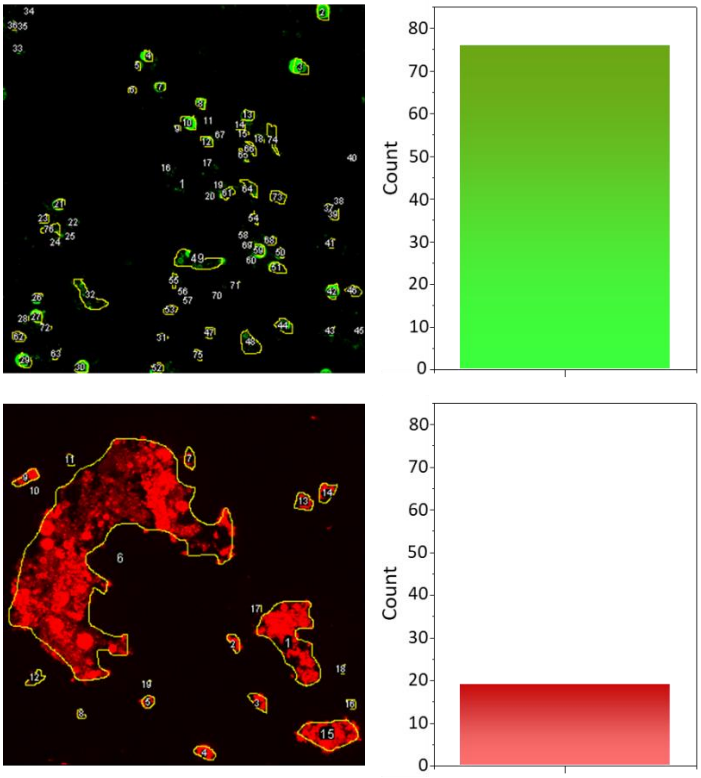

Figure 2.4. ROI measurements from image data. *As an example, CLSM images of Alg-coated colloidosomes (green) and Ch-coated colloidosomes (red) at pH 7. Hand-selected regions outlined by yellow were counted and plotted in corresponding bar charts.*

2.5.10 Turbidity measurements

The pH dependence on colloidosome self-assembly or disassembly was investigated by monitoring the changes in absorbance at a fixed wavelength (λ = 500 nm) from which the turbidity was calculated following the formula 100-%T (%T = % transmission = 100 $x10^{-A}$, and A = absorbance).

2.5.11 Enzyme induced colloidosome aggregation

D-glucose (300 µl, 1 M) was added to a PBS solution (1 ml, pH 7.75) to give an overall pH 7.5 solution. 30 µl of each Alg-coated FITC-GOx (30 mg ml^{-1}) and Ch-coated RITC-GOx (30 mg ml^{-1}) colloidosomes were added to the PBS solution and stirred continuously (100 rpm) the pH was measured at intervals over 23 h. Three aliquots (20 µl each) were taken from the solution at t = 0-2 h, three aliquots between 7-9 h and three aliquots between 21-23 h. CLSM images were taken immediately. This method was repeated for solutions 60 µl Alg-coated FITC-GOx (30 mg ml^{-1}) and 60 µl Ch-coated RITC-

GOx (30 mg ml^{-1}) colloidosomes respectively. A turbidity measurement of each sample was taken at 6 timepoints throughout the enzyme-induced pH drop.

2.5.12 Large colloidosome preparation

Silica nanoparticles (15 mg) were dispersed in 2 ml dodecane. The mixture was sonicated for 1 min to disperse the nanoparticles. An aqueous phase containing 20 µl RITC-GOx (30 mg ml^{-1}, pH 8.5 bicarbonate buffer) and 80 µl β-glucosidase (30 mg ml^{-1}, pH 8.5 bicarbonate buffer) was injected into the solution, which was shaken by hand for 1 min to create a Pickering emulsion. TMOS (20 µl) was added to the emulsion, and it was rotated for 4 h. GLYMO (20 µl) was then added to the emulsion, and it was left to rotate overnight for 20 h. Colloidosomes were transferred to water via washing steps, as stated in previous methods, and polymer (0.08 wt.%) was added. Large colloidosomes were further rotated overnight.

2.5.13 Detachment of small colloidosomes from big colloidosomes

Large Ch-coated RITC-GOx loaded colloidosomes and small Alg-coated FITC-GOx loaded colloidosomes were prepared. 6 µl of each colloidosome population was dispersed in a 1 ml PBS solution (0.001M, pH 4.5) and stirred (100 rpm) for 5 min. An aliquot (20 µl) of solution was taken and a CLSM z-stack image of the aggregates was captured. NaOH (to pH 7) was then added to the solution which was further stirred for 10 mins. Another aliquot (20 µl) of solution was taken and again, a CLSM z-stack image of the aggregates was captured.

2.5.14 Enzyme cascades

All colloidosomes were mixed at a 1 : 1 ratio. 6 µl each of Alg-coated, FITC-AOx (30 mg ml^{-1})-loaded colloidosomes and Ch-coated, Dy405-HRP (30 mg ml^{-1})-loaded colloidosomes were mixed in 1 ml PBS solution (0.01 M, pH 8) and stirred at 100 rpm in a cuvette. GDL (10 µl, 50 mM), o-PD (5 µl, 25 mM) and EtOH (10 µl, 20 mM) were injected into the colloidosome dispersion and stirred. The reaction was monitored over time in a UV-Vis spectrometer.

The same procedure was repeated with the addition of Cat (0.01 mg ml^{-1}) into the colloidosome dispersion at t=0. The absorbance at 420 nm was recorded and plotted against time. The pH was also monitored. Rate was calculated as dA/dt.

2.5.14.1 Effect of polymer coating on enzyme cascade rate

6 µl each of uncoated FITC-AOx (30 mg ml^{-1})-loaded and Dy405-HRP (30 mg ml^{-1})-loaded colloidosomes were mixed in 1 ml PBS solution (0.01 M) at pH 3, 5 and 7. o-PD (5 µl, 25 mM) and EtOH (10 µl, 20 mM) were injected into the colloidosome dispersion, which was stirred (100 rpm). The reactions were monitored by UV-Vis over 2 h. This procedure was repeated with the addition of Cat (0.01 mg ml^{-1}) into the colloidosome dispersion at t=0.

Similarly, 6 µl each of Alg-coated, FITC-AOx (30 mg ml^{-1})-loaded colloidosomes and Ch-coated, Dy405-HRP (30 mg ml^{-1})-loaded colloidosomes were mixed in 1 ml PBS solutions (0.01 M) at pH 3, 5 and 7. o-PD (5 µl, 25 mM) and EtOH (10 µl, 20 mM) were injected into the colloidosome dispersion, which was stirred (100 rpm). The reactions were monitored by UV-Vis over 2 h. This procedure was repeated with the addition of Cat (0.01 mg ml^{-1}) into the colloidosome dispersion at t=0.

2.5.14.2 Effect Cat. concentration on enzyme cascade

6 µl each of Alg-coated, FITC-AOx (30 mg ml^{-1})-loaded colloidosomes and Ch-coated, Dy405-HRP (30 mg ml^{-1})-loaded colloidosomes were mixed in 1 ml PBS solutions (0.01M) at pH 3, 5 and 7. At each pH, o-PD (5 µl, 25 mM) and EtOH (10 µl, 20 mM) were added to the colloidosome mixture, alongside catalase at concentrations 0.1, 0.05, 0.01 mg ml^{-1} respectively. The reactions were monitored by UV-Vis over 2 h.

2.5.15 Synthesis of CD-PAH

PAH (125 mg) was dissolved in deionised water (5 ml). EDC, NHS and succinyl-CD (60, 30 and 100 mg) were added to the aqueous solution simultaneously. The reaction was heated to 60°C and stirred for 48 h. Once reacted, the reaction was filtered to remove unreacted CD, and dialysed against Milli Q water for 5 days. The product was then freeze dried. ^{1}H NMR (500 MHz, D_2O): δ 1.5 (CH2 (PAH); 1.9 (CH (PAH)); 3 (CH2 (PAH)); 2.37-3.2 (CH6 (succinyl)); 3.5-4.15 (C2-6H (CD)); 5.01 (C1H (CD)).

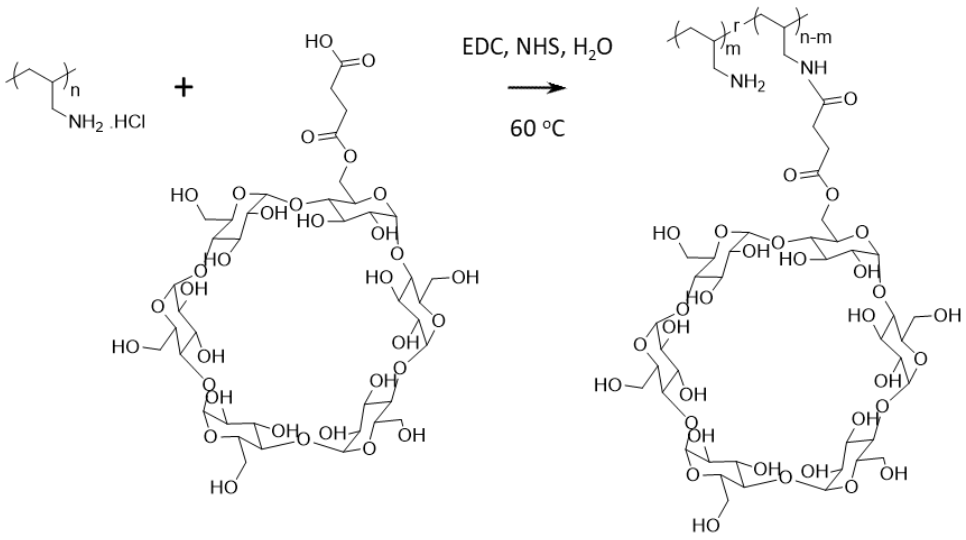

Scheme 2.8. Synthesis of CD-PAH.

2.5.16 Synthesis of Azobenzene-PAH

PAH (125 mg) was dissolved in deionised water (5 ml). Azobenzene-3-carboxylic acid (120 mg) was dissolved in DMSO (300 µl) and added dropwise to NaOH (aq, 0.5 M) at 60 °C. EDC, NHS and azobenzene-3-carboxylic acid solution (60 mg, 30 mg and 5 ml) was added to the aqueous solution simultaneously. The reaction was heated to 60 °C and stirred for 48 h. Once reacted, the reaction was filtered to remove unreacted azobenzene, and dialysed against Milli Q water for 5 days. The product was then freeze dried. ^{1}H NMR (500 MHz, D_2O): δ 1.13 (CH2 (PAH)); 1.70-2.32 (CH (PAH)); 2.90-3.18 (CH2 (PAH)); 7.48 (CH (Azo)).

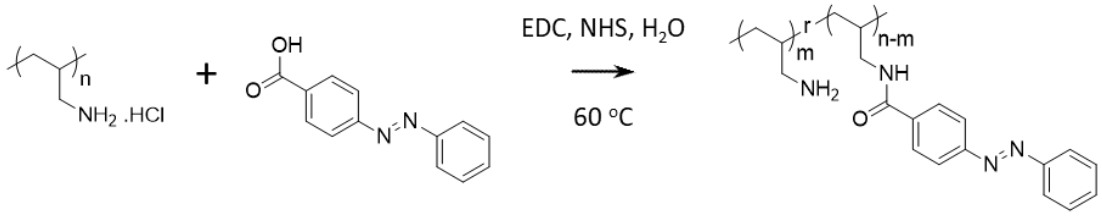

Scheme 2.7. Synthesis of azobenzene-PAH.

2.5.17 Co-assembly of CD-PAH-coated colloidosomes and azo-PAH-coated colloidosomes

CD-PAH coated FITC-GOx loaded and Azo-PAH coated RITC-GOx loaded colloidosomes (10 µl) were each dispersed in 0.5 ml PBS (0.001M) pH7 solution separately. Both colloidosomes gave a + 30 mV zeta potential due to the protonated PAH polymer. The solutions were mixed together and stirred for 10 min (100 rpm). Images were recorded by CLSM before and after 1 : 1 volume mixing.

2.5.18 Effect of pH on CD-PAH-coated colloidosomes and azo-PAH-coated colloidosome spatial organisation

CD-PAH coated FITC-GOx loaded colloidosomes (6 µl) were stirred (10 min) in 0.5 ml PBS buffer (0.001M) at pH environments 2, 7 and 10. Azo-PAH coated RITC-GOx loaded colloidosomes (6 µl) were also stirred (10 min) in 0.5 ml PBS buffer (0.001M) at pH environments 2, 7 and 10. A 1 : 1 volume ratio (total 12 µl) mixed colloidosome solution was also stirred under pH conditions 2, 7 and 10. Images were recorded by CLSM.

CHAPTER 3

MATRIX-BASED SPATIALLY ORGANISED COLLOIDOSOMES

This chapter describes in detail, two passive assembly methods for the spatial organisation of colloidosome colonies. Firstly, droplet-based microfluidics is used to create alginate hydrogel micro-platforms embedded with segregated populations of colloidosomes. Secondly, a prototissue assembly method is used to trap colloidosome colonies within a coacervate-based platform. Both techniques produce distinct scaffolds comprising immobilised spatially controlled colloidosome populations, as a mimic of living cells held within an extracellular or tissue-like matrix. Passive assembly techniques provide high levels of control over the colloidosome systems and can thus lead to complex organised patterning within various size and shape environments.

3.1 Background

Cells in closely related communities (tissues) are often supported and connected by a network of proteins and molecules called the extracellular matrix (ECM). This matrix has many roles including the structural and spatial organisation of cells. Therefore, to understand the link between cellular interactions and spatial organisation as important processes within a living system, the ECM must be studied. Again, due to the complexities of a native ECM, mimicking the ECM is often desirable. This background summarises the composition and role of the ECM and provides an overview of techniques and materials used to create ECM-mimicking scaffolds. Specifically, this background studies hydrogels as an ECM mimicking material and outlines important literature associated with protocell-containing hydrogel scaffolds. With a focus on alginate hydrogels, droplet microfluidics is reviewed as a technique to make alginate droplets, and the capacity for cell encapsulation and internal Janus organisation within these droplets is discussed. This background finally provides an overview of prototissues formed by interface bilayer-connected microdroplets, outlining literature examples and recognising the potential for such prototissues as a matrix-based scaffold for the encapsulation and organisation of other protocell communities.

3.1.1 Extra cellular matrix overview

The ECM is a complex water-based network of proteins, minerals, and other macromolecules, which constitutes the non-cellular component of living tissues. The ECM acts as a physical scaffold for cells within a tissue, providing anchoring and structural support.[183] This directs cell organisation and guides cell-community formation, to enable collective functionality for the development of tissue-like behaviours. The ECM also facilitates important cellular communication pathways guiding growth, differentiation, morphogenesis, and homeostasis.[184,185] Fundamentally, the ECM is composed of water, fibrous proteins, glycoproteins and proteoglycans[186] (figure 3.1a) however, ECM composition and function varies significantly between different types of tissue.

Mimicking the ECM can provide higher order control over cell communities, aid understanding of complex multicellular systems and function as a biomimetic interactive cell environment. When combined with protocell chemistries, an ECM-mimic can lead to advanced and complete prototissue designs. An ECM-mimic must uphold certain features akin to a native ECM, such as the ability to support cell growth, cell maintenance, gas exchange, nutrients transfer, metabolic waste removal and signal transduction.[187] Mechanical and biological characteristics of an ECM must also be sustained by any ECM-mimicking material.[188] Cell-laden hydrogels are suggested as suitable ECM-like

scaffolds that align with most of the physical characteristics of an ECM and have the ability to absorb large quantities of water and biological fluids due to hydrophilic porous architectures, enabling small molecule exchange and diffusion.[187]

A variety of synthetic and natural polymers have been used as hydrogel ECM-mimic building blocks. These include collagen, hyaluronic acid[189], fibrin, alginate[190], agarose, cellulose[191], silk and poly(ethylene) glycol.[192] Despite collagen being most widely used as it makes up ca. 30% of native ECM connective tissues, all hydrogels provide a simple ECM-mimicking bottom-up scaffold for applications such as self-repair (figure 3.1b). Microengineering techniques such as lithography, nano-/microfluidics and micro-moulding have been used to control hydrogel-cellular microenvironments to better mimic the inhomogeneous and anisotropic properties of native tissues.[187] This chapter partially explores microfluidics as a means for the microengineering of an alginate-based ECM mimicking environment for encapsulated protocell communities.

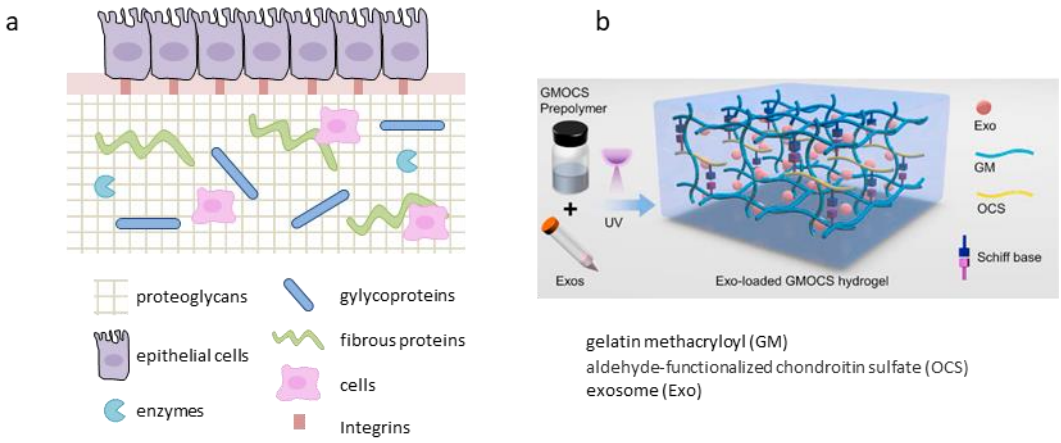

***Figure 3.1. ECM components. a**, Diagram representing the components in a native connective tissue extracellular matrix (ECM).*[185] ***b**, Diagram showing example components within a natural-polymer hydrogel ECM mimic. Reproduced as part of a figure without changes from paper by P. Guan et al. under CC BY-NC-ND 4.0.*[193]

3.1.2 Protocells within a hydrogel scaffold matrix

Immobilising micro-synthetic objects within a hydrogel scaffold offers a route towards tissue-like structures and engineering opportunities. Incorporating objects within a hydrogel-based network varies the overall material composition, leading to increased complexity and on-demand functionalities.[194] Significantly, establishing well-defined multicompartments within an external network can provide the opportunity for spatiotemporally controlled functions and life-like domains. In literature, nano/microparticles and enzymes have been trapped within hydrogel scaffolds for use as self-healing building blocks[195], sensors (figure 3.2a)[196] and biocatalysts[197]. As well as these objects, compartment-like entities have been trapped within a hydrogel medium to introduce cargoes or reactive sites (figure 3.2b).[198] A variety of cargos have been delivered into hydrogel matrices, but as a step towards the construction of cell-mimicking compartments, synthetic-like vesicles have been entrapped. This research was first realised through the agarose trapping of oil-coated liquid droplets, fused together through droplet bilayer interfaces (figure 3.2c).[199] Removal of the oil phase and thus the direct trapping of liposomes within a range of hydrogel structures has now been achieved (figure 3.2d).[200,201] The ambition to increase complexity and encourage life-mimicking behaviour in encapsulated microcompartments has led to the immobilisation of protocells within hydrogel-based scaffolds. A current example comprises protein-membranised vesicles (proteinosomes) trapped within a helical alginate, capable of signal induced movement and protocell-mediated actuation (figure 3.2e).[13] Coacervate protocells have also been immobilised within hydrogels (figure 3.2f), demonstrating communicative interactions and mimicking life-like processes such as nitric-oxide-induced vasodilation (figure 3.2g).[57] In general, hydrogel systems exhibit interpenetrated physical scaffolding for protocells, can facilitate interactive communication through the exchange/diffusion of chemicals, and can spatially organise and pattern protocell populations. In most instances, macro-sized moulds have been used as a preferred method to organise protocells within hydrogel constructs however, in such designs organisation is limited to the macroscale length and typically to modular assemblies. More recently microfluidics has been explored as a technique for micro-organisation of protocell communities within hydrogel matrices.

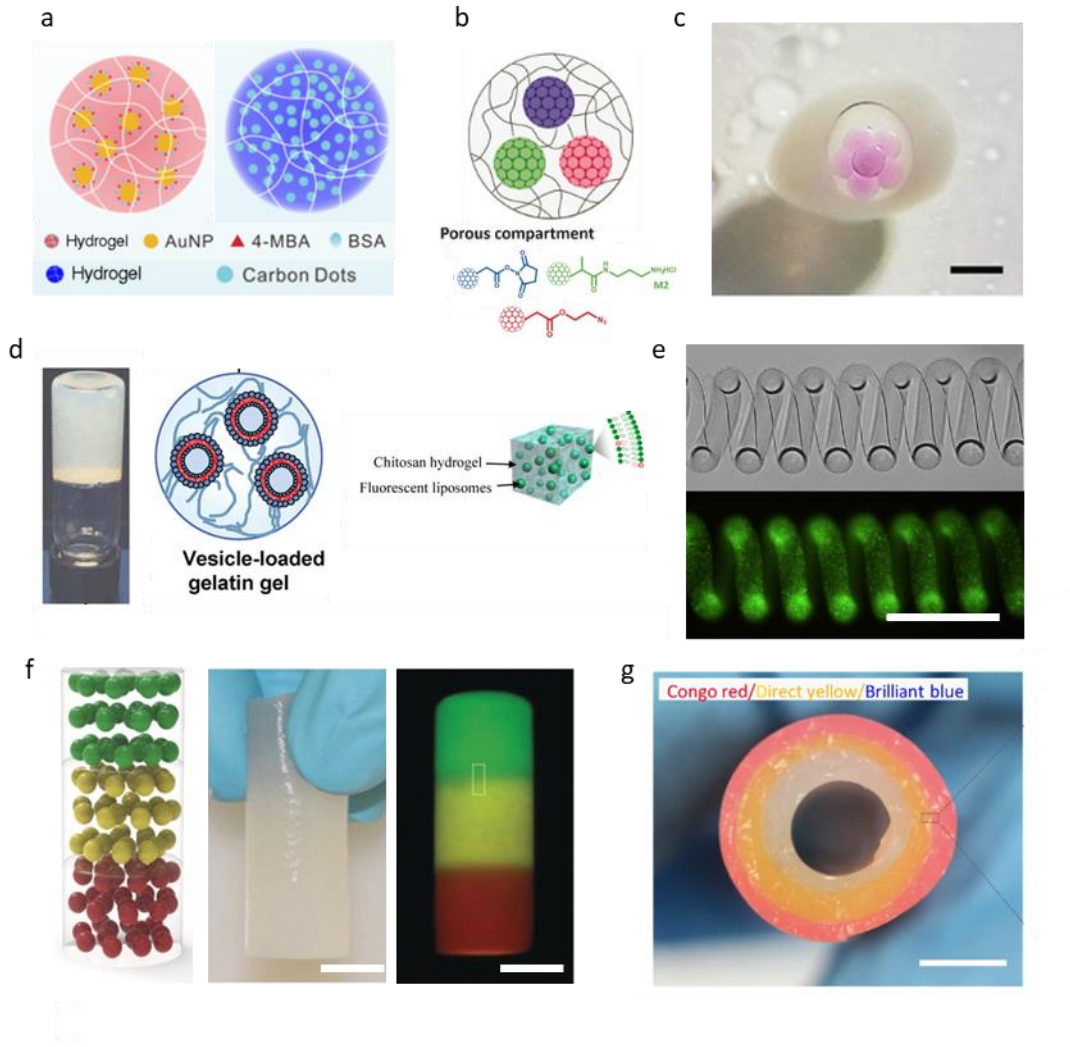

Figure 3.2. Towards hydrogel-immobilised protocells. ***a****, Functionalised nanoparticles entrapped within hydrogel microspheres. Reprinted (adapted) with permission from S. Yue et al. Copyright 2023 American Chemical Society.*[196] ***b****, Functionalised porous microcompartments immobilised within hydrogel sphere. Reproduced with permission from N. Gao.*[198] ***c****, Oil-coated lipid vesicles joined together through droplet interface bilayers encapsulated within an agarose hydrogel platform. Scale bar, 1 mm. Reproduced from paper by D. Baxani et al. under CC BY-NC 4.0.*[199] ***d****, Fatty acid vesicles trapped within hydrogel scaffolds. Reprinted (adapted) with permission from M. Dowling et al. Copyright 2023 American Chemical Society.*[200,201] ***e****, Proteinosomes encapsulated within helical hydrogel filament. Scale bar, 400 µm. Reproduced with permission.*[13] ***f****, Modular coacervate communities trapped within an agarose hydrogel. Scale bars, 10 mm. Reproduced with permission.*[144] ***g****, Coacervates embedded within an agarose hydrogel as a vascular system mimic. Reproduced from paper by S. Liu et al. under CC BY 4.0. Scale bars, 5 mm.*[57,202]

The work in this chapter expands on the proteinosome-in-alginate helix work of Gao *et al.* by exploring microfluidics as a technique for encapsulating spatially micro-organised colloidosomes within a hydrogel matrix. Alginate hydrogel matrix-based platforms are chosen for cell encapsulation since microfluidic-fabricated alginate systems are well explored. As previously mentioned, alginate

also offers a natural, biocompatible physical scaffold with the capacity for chemical information exchange.[203]

3.1.3 Microfluidics to form alginate spheres

As previously mentioned, sodium alginate provides a suitable medium for cell encapsulation, is well-known in the food industry and is a useful drug carrier with high potential in pharmaceutical applications.[154,204] Typically in these applications alginate is used in the form of micro-gelled beads, prepared using a variety of techniques such as simple dripping, spinning disk, emulsification, electrostatic potential, and droplet-based microfluidics. Droplet-based microfluidics is an excellent candidate for the fabrication of such micro-beads that yields highly monodisperse droplets, provides easy droplet size control/manipulation, and issues high droplet through-put rates and droplet shape-tunability.[205] Several publications describe the droplet-microfluidic fabrication of sodium alginate hydrogels.[206–208] Droplets with a coefficient variance (CV) < 5% are typically regarded as being monodisperse. Sodium alginate hydrogels, ionically crosslinked either by an internal or external ionic solution, often report a CV < 3% thus indicating high monodispersity.[209,210] Varying the flow rate of microfluidic injection channels and thus changing the two-phase flow ratio V_{out}/V_{in}, offers tuneable size control for alginate droplets.[120,211] Additionally, using different geometry injection channels and developing advanced methods of external crosslinking can lead to high levels of control over the alginate shape.[212]

3.1.4 Co-flow microfluidics

A co-flow geometry was used throughout this thesis to produce alginate microspheres and microrods. Glass capillary co-flow microfluidic devices were fabricated on-demand and on the bench top to afford extra customisability. In co-flow systems, drops are produced in either the dripping or the jetting regime.[213] The jetting regime produces irregular and polydisperse droplets at the end of a high-velocity dispersed phase jet, due to the Rayleigh-plateau principle. Instabilities are created by unequal forces on a liquid stream, causing different pressure points along the jet. High pressure areas at the troughs squeeze liquid into low pressure areas at the peaks, growing the instabilities. If the rate of this growth is greater than other effects, eventually a droplet will break off. In the dripping regime the instability is in a fixed location (at an orifice). A drip occurs at low inner phase

velocity, when the surface tension between the inner and outer phase is exceeded by the drag force of the outer phase (figure 3.3).[214,215]

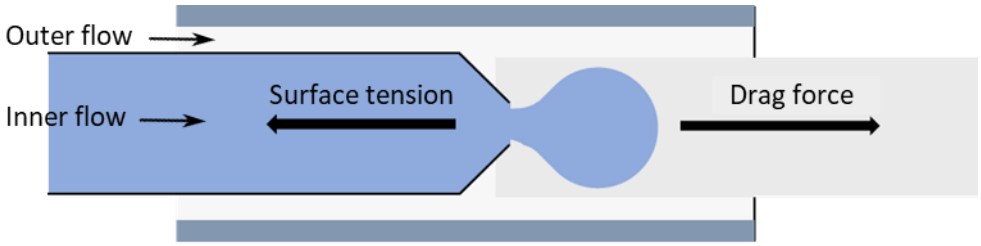

Figure 3.3. Droplet microfluidic forces. *Diagram which shows the drag force and surface tension acting on a droplet within a co-flow microfluidic system in the dripping regime.*

3.1.5 Encapsulation of cells via microfluidic techniques

Sodium alginate droplets provide excellent platforms for the encapsulation of biological cells, harbouring cell maintenance, proliferation, and cell culture. Droplet-based microfluidics allows easy cell-alginate integration through combining cells and alginate as an inner flow. Several studies show that cells within microfluidic-produced droplets successfully maintain their autopoietic status and biological functions. For example, M6C cells encapsulated within alginate hydrogel microspheres and incubated for 6 days, were able to show growth and demonstrate proliferation.[216] A similar technique was used to encapsulate mammalian cells (Jurkat) inside alginate droplets, again leading to maintained cell viability.[209] The encapsulation of living cells within hydrogel droplets advances cell delivery systems, generates specific environments for cells analysis and accelerates tissue-engineering endeavours. The encapsulation of protocells within hydrogel microparticles is thus predicted to deliver similar advantages in protocell delivery, controlled protocell analysis and prototissue engineering.

So far, this discussion has examined droplet-based co-flow microfluidics as a tool for creating monodisperse microdroplets that can encapsulate and support living cells. The discussion has focused on isotropic droplets. However, within native tissues and many biological systems cells are often arranged in anisotropic arrangements. It is therefore important to mimic anisotropic patterning within ECM-mimicking scaffold-like microdroplets. As a step towards anisotropy, Janus-patterned hydrogels are well-researched and fabricated by similar microfluidic methods.

3.1.6 Janus particles

Janus particles consist of two segments that are physically and chemically different from each other.[217] The term 'Janus' originates from ancient Roman mythology and is the name given to the God of beginnings and ends who is depicted as having two faces looking away from each other, at the past and towards the future.[218] Due to the two segregated segments in a Janus particle and thus the distinct chemical and physical environments coexisting within a single particle system, Janus particles have harnessed many unique applications in drug delivery, self-assembly, micromotors and display devices.[219] In biomedical drug delivery systems, Janus particles can combine incompatible drug molecules and improve targeted delivery, two concepts of vital importance. Modern techniques for producing Janus particles have originated from the spinning disk method. In this method two types of molten polymer flow onto different sides of a spinning disk, both flow to the disk ends and then form small jets which, due to the Rayleigh instability principle, break up into small droplets and solidify in the air.[220] Other fabrication methods include electrified jetting, deposition methods and sputtering. Unfortunately, these techniques produce highly polydisperse Janus particles and thus droplet-based microfluidic techniques have later been developed to improve monodispersity.

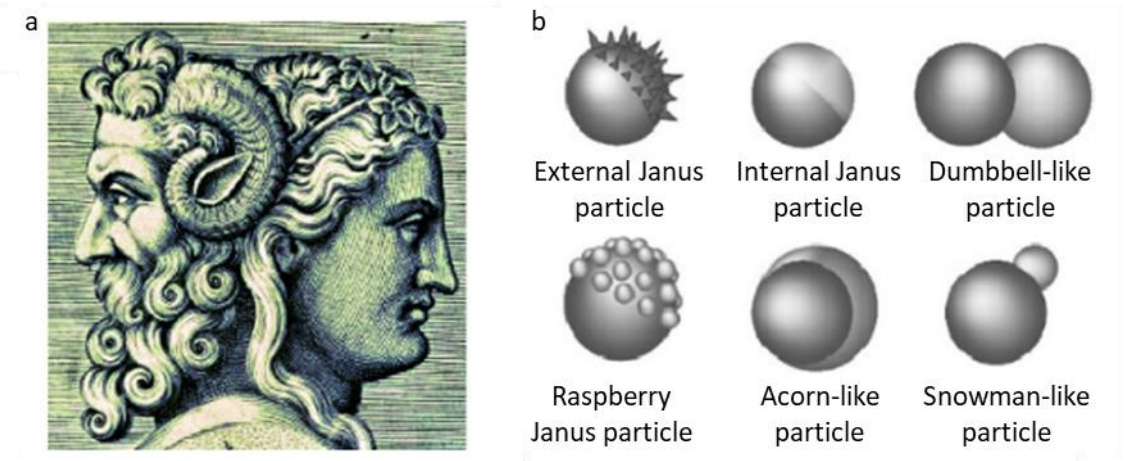

***Figure 3.4. Janus pattern. a**, The Roman God of beginnings and ends 'Janus'. **b**, Image depicting six different types of Janus particles. Reproduced with permission.*[220]

3.1.7 Using microfluidics to make Janus microdroplets

Janus droplets can be fabricated using three different microfluidic processes. Either, two separate droplets can be coalesced together, two different disperse phase streams can be merged to form one droplet[221] or, droplets can phase separate. Most internal Janus particles (figure 3.4) are produced by two segregated inner phases running in parallel to the point of droplet formation, upon which a droplet is formed comprising both miscible inner phases. This one-step method for producing individual Janus particles can be tuned according to flow rates, device dimensions or solidifying techniques. In literature, both a Y-channelled microfluidic device with a flow focused orifice and a 3D glass capillary microfluidic device with a co-flow orifice[222] have been used to fabricate Janus droplets via the merging of inner phase streams. It is of paramount importance when merging two inner phase miscible streams, that the geometry of the device is symmetrical, and thus T-junction geometries are often disregarded. Internal mixing can occur between such miscible inner phases post-droplet formation due to the convective and diffusive internal transport within the droplets, and thus the droplets must be crosslinked immediately after formation. UV solidification is a preferable technique, as crosslinking occurs quickly and can be achieved close to the orifice site. Despite this, other crosslinking methods such as ionic and thermal, have been successfully reported in literature.[223,224] Importantly, literature has shown that Janus droplets can be made using cross-linkable polymer precursors.[225] This is advantageous as material composition is separated from the particle gelation process, allowing modification of the material without causing an effect on gelation.[226] The miscible inner phases must also be injected at similar flow rates and constitute similar viscosities so that segregated hemispheres are obtained. If the two inner phases are not miscible then internal mixing is negligible and thus a non-symmetric T-junction device could be used. However, the three different interfacial tensions must be carefully controlled as this parameter will determine which type of Janus droplet is produced and the extent to which one dispersed phase is engulfed within the other.[227]

3.1.8 More advanced patterning in microdroplets

Droplet-based microfluidics enables manipulation and control over shape, composition, and patterning of microdroplets, which is especially useful for the fabrication of Janus particles.[222,228,229] Disk and rod-shaped hydrogels have been fabricated using flow focusing microfluidic devices, typically by altering the dimensions of the collection channel to spatially confine droplets. Monomers mixed with a photo initiator and crosslinked using UV are typically used to create such shapes as this enables the monomers to be crosslinked inside a confined space, helping to fix the desired shape.[230] It is difficult to control the shape of the hydrogel when crosslinked using external methods as demonstrated when making sodium alginate tear-drops through crosslinking droplets with an external solution of $CaBr_2$.[231] Advanced patterning within sodium alginate hydrogels has been realised using a centrifugal microfluidic method. Upon changing an inner capillary to capillaries with more complexed architectures comprising multiple channels, compartmentalised drops with 3-7 segregated compartments were fabricated. In this example, fluorescently labelled alginate was used to identify the multi-compartment pattern in the absence of encapsulated species.[232] Despite droplet-based microfluidics demonstrating shape and pattern tunability, the challenge of encapsulating cells into these more advanced architectures remains. There is also minimal work with regards to protocell encapsulation as a platform for prototissues, protocell delivery or controlled protocell reactions.

3.1.9 Prototissues based on interface bilayer-connected microdroplets

As discussed, hydrogels are a good rudimentary ECM mimic. However, designs can be biochemically uninteresting which generates a ceiling in tissue-related studies. Using 'biochemically interesting' protocell building blocks to create prototissues that mimic spatially interconnected living cells, is therefore a next step for understanding multicellular behaviour and in determining early processes on earth. Although these prototissues are also an incomplete picture without vital ECM components, this chapter explores how they could provide a platform for the encapsulation of protocells to develop collective behaviours and interactive tissue mimics.

As is the case with protocells, prototissues do not need to be an exact replica of a living tissue, however they must possess some key components/functions and be a simplified model. Under this definition, prototissues have been made from interconnected microdroplets, joined together by bilayer interface interactions.[86] Several examples of interconnected protocells have been designed to mimic a tissue and support multi-protocellular functions. GUVs[233,234], proteinosomes, polymersomes and water in oil droplets have all provided suitable candidates for the backbone of a prototissue. The first prototissues based on the concept of connected interface bilayers, were shown by Baley e*t al* (figure 3.5a).[88] The group used 3D printers to spatially organise lipid-coated water droplets designed to adhere at the interface. The assembly of GUVs into interconnected prototissues was first shown by Elani *et al.* whereby optical tweezers were used to assemble networks of vesicles (figure 3.5b)[235] and by Stur-hamsen *et al.* whereby GUVs were clustered by surface reactions (figure 3.5c).[236] Surface reaction chemistry was also employed by Gobbo *et al.* to create clustered proteinosomes by carefully designed crosslinkers (figure 3.5d).[82] Such interconnected bilayer constructs can exhibit collective behaviours, signalling, deformation, and gene expression, thus qualifying them as viable prototissues. However, these prototissues are relatively weak and suffer from a variety of restrictions related to mechanical strength, stability and size.

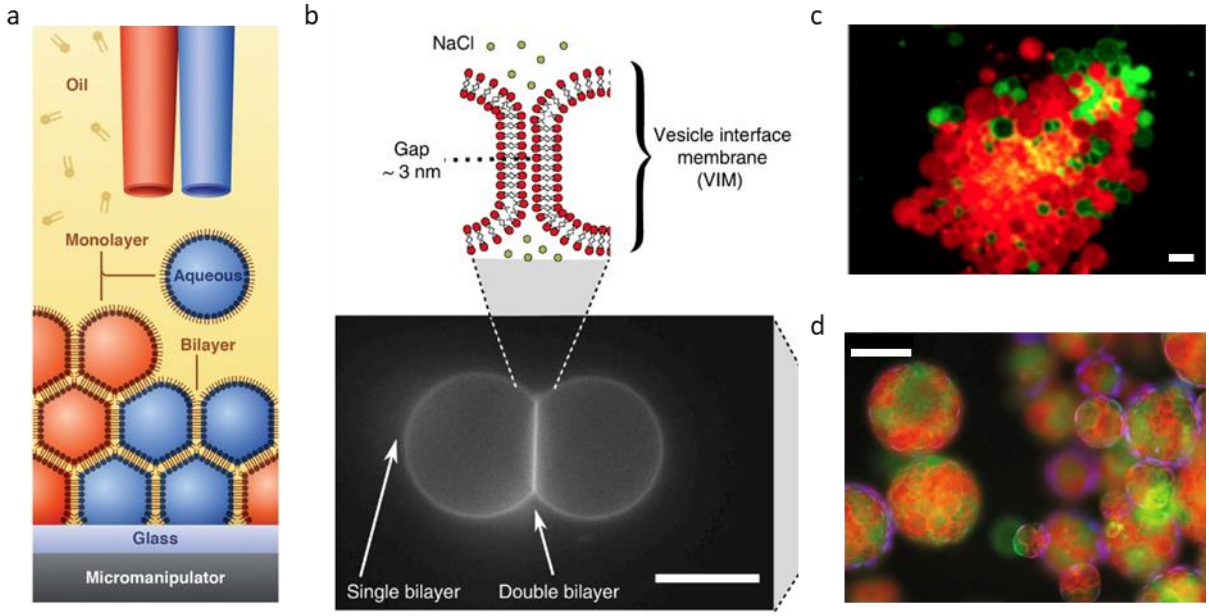

Figure 3.5. Interface bilayer-connected prototissues. ***a****, 3D printing of lipid vesicles, immobilised together through bilayer interface interactions. Reproduced from paper by M. Booth et al.*[88] ***b****, Inkjet technique used to assemble GUVs. Reproduced from paper by G. Bolognesi et al. under CC BY 4.0.*[235] ***c****, Clustering of GUVs using phenyl ester-hydrazine ligation surface chemistry bonding techniques. Reprinted (adapted) with permission from N. Stuhr-Hansen et al. Copyright 2023 American Chemical Society.*[236] ***d****, Microscope image of proteinosome-based prototissue. Reproduced with permission from P. Gobbo et al.*[82]

3.1.10 Background conclusions

In conclusion, the interaction between closely related cell communities relies on organisation within a structurally and chemically important matrix. To help understand such cell-cell and cell-environment interactions, this matrix can be mimicked by simple hydrogels or by interconnected protocells. Hydrogel-immobilised protocells have been studied as interactive protocell systems however, spatial organisation has only been achieved at the macroscale and cell-environment relationships have been neglected. Microfluidics has a rich history in making hydrogel droplets that have been used for the encapsulation of various cells and used to achieve complex anisotropic internal droplet patterning at the microscale. Thus, the technique has potential for microscale patterning of hydrogel-immobilised protocells, as a better mimic of living tissues. Prototissues based on interface bilayer-connected protocells provide a more biochemically interesting matrix that has the potential for better cell-environment interactivity.

This chapter studies the microfluidic preparation of alginate hydrogel microparticles as a platform for the encapsulation of colloidosome protocells. The work develops microscale spatial organisation through complex shapes and internal patterning. The chapter also studies coacervate prototissues as a more biochemically interesting platform for colloidosome encapsulation and spatial organisation.

3.2 Results and Discussion

The aim of this chapter is to study methods for trapping colloidosomes within matrix scaffolds, as a means for spatial organisation of protocell communities at the micro-scale. The motivation is to mimic extra-cellular or tissue matrix structures as a harbour for cells and a platform for their communication and collective behaviours. Two methods were chosen for the matrix-lead organisation of colloidosome communities; hydrogel-based trapping, controlled by microfluidic droplet generation, and coacervate-tissue trapping, controlled by layered assembly. The following results show that colloidosome communities can be successfully organised within matrix-based constructs, maintaining structural integrity and cell-mimicking capabilities. The ability to localise enzymes and thus reaction centres via colloidosome encapsulation is shown to exploit increasingly complex patterns and higher ordered interactions for more advanced multicellular models.

3.2a Hydrogel scaffold matrix

A droplet-based microfluidic technique was used to organise and immobilise colloidosomes within discrete microparticle alginate hydrogel scaffolds. Typically, this work was conducted in Janus spherical platforms however, later in the chapter more complex internal patterns and shapes were explored. Microfluidics was chosen as a good microengineering tool to control protocellular microenvironments and thus to construct matrices that could better mimic the inhomogeneous and anisotropic properties within native tissues. The technique enabled good control over the size and shape of each hydrogel platform and supported a categorical increase in the complexity of protocell organisation, resulting in aqueous viscoelastic scaffolds as decent mimics of cell-laden ECMs.

3.2a.1 Microfluidics to make sodium alginate droplets

Sodium alginate droplets were continuously formed at the orifice of a co-flow glass capillary microfluidic device. The glass capillary device was prepared according to the method in section 2.3.1 and was favoured over more commonly used designs, such as PDMS or 3D-printing, due to biocompatibility, cost, and ease of remodelling/redesigning. The slight hydrophobicity of the glass also aided W/O droplet formation, minimising alginate adhesion to the capillary wall. However, there were some drawbacks to the devices such that they were disposable, thus requiring a lot of manual labour and temporal sacrifice through making a new device for each experiment. This also reduced

droplet size reproducibility between experiments, as the droplet size depended upon the specific orifice size within the device. Thus when switching device, human error meant that the orifice size could not be exactly replicated and hence the droplet sizes were different.

The co-flow glass capillary microfluidic device was used to produce monodisperse spherical hydrogel platforms with an average diameter (d_A) of 111 ± 1 µm, as demonstrated by figure 3.6. A 2 wt.% RITC-Alg aqueous phase was broken into droplets within an immiscible 1-decanol outer phase to produce uniform sized spheres at the orifice of the device. The spheres were crosslinked via an external solution of $CaBr_2$ (3 mM) before being transferred to water. Microscope images of the microspheres in an aqueous environment were used to calculate a size distribution and coefficient variance (CV) based on each sphere's diameter measurement. The resulting microdroplets showed a highly monodisperse size distribution (CV, 1.6 with n=49).

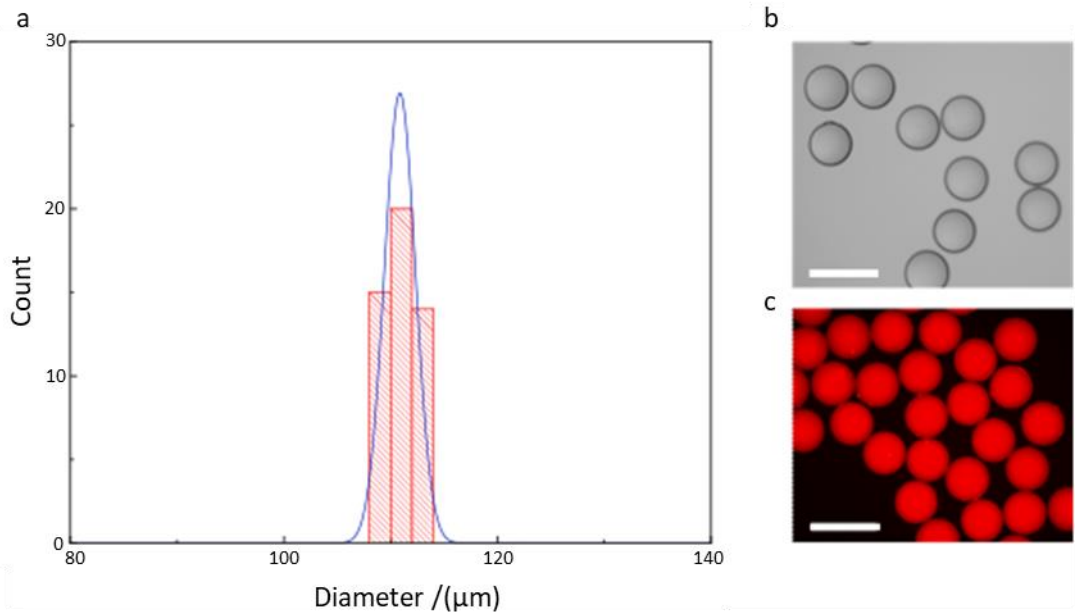

Figure 3.6. Droplet-based microfluidic preparation of RITC-Alg hydrogel microspheres. *Microspheres were crosslinked in an off-device solution of $CaBr_2$ (3.1 mM, decanol) and transferred to water.* ***a****, size distribution of 49 spheres. Bright field (****b****) and fluorescence (****c****) microscope images of hydrogel spheres in aqueous solution. Scale bars, 200 µm.*

Spatially segregated Janus internal patterning within the hydrogel microspheres was achieved by using a theta-septum microfluidic device as prepared in section 2.3.1.3. A monodisperse distribution of Janus hydrogel spheres comprising RITC-Alg (3.5 wt.%) and FITC-Alg (3.5 wt.%) inner phases (figure 3.7a) was achieved by injecting each inner phase through the theta-septum at the same velocity. The droplets were crosslinked with a concentration of 1-3 mM $CaBr_2$ before transferal to water and imaging via CLSM (figure 3.7b-d). The characteristic d_A of the hydrogel spheres in water was 264 ± 9 µm, and a CV of 3.6 % was calculated by dividing the standard deviation by the mean size (figure 3.7e). 3.6 % lies within the 3-5 % monodisperse category achieved by droplet-based microfluidics in the published literature. Thus, a monodisperse collection of microspheres is obtained. The fluorescence intensity of FITC and RITC was measured through the cross section of a single hydrogel sphere, confirming that a spatially segregated Janus pattern of each Alg population was achieved (figure 3.7f). The two Alg inner phases are miscible, and the sharpness of the interface thus depends on the extent of mixing pre-solidification, in this case ionic crosslinking. There is a time-dependent limit on the crosslinking process, as crosslinking too fast can lead to irregular shapes, whereas crosslinking at a slower pace can result in a significant amount of mixing between hemispheres and a gradual change in composition along the axis normal to the interface. A small degree of this mixing is seen by the fluorescence profile in figure 3.7f however, the existence of a sharp interface in this circumstance is not crucial. Increasing the viscosity of the inner phase from 1 wt.% to 3.5 wt.% aqueous sodium alginate was shown to decrease the extent of mixing (figure 3.7f-i), although this was counterbalanced with an increased risk of blocking the orifice.

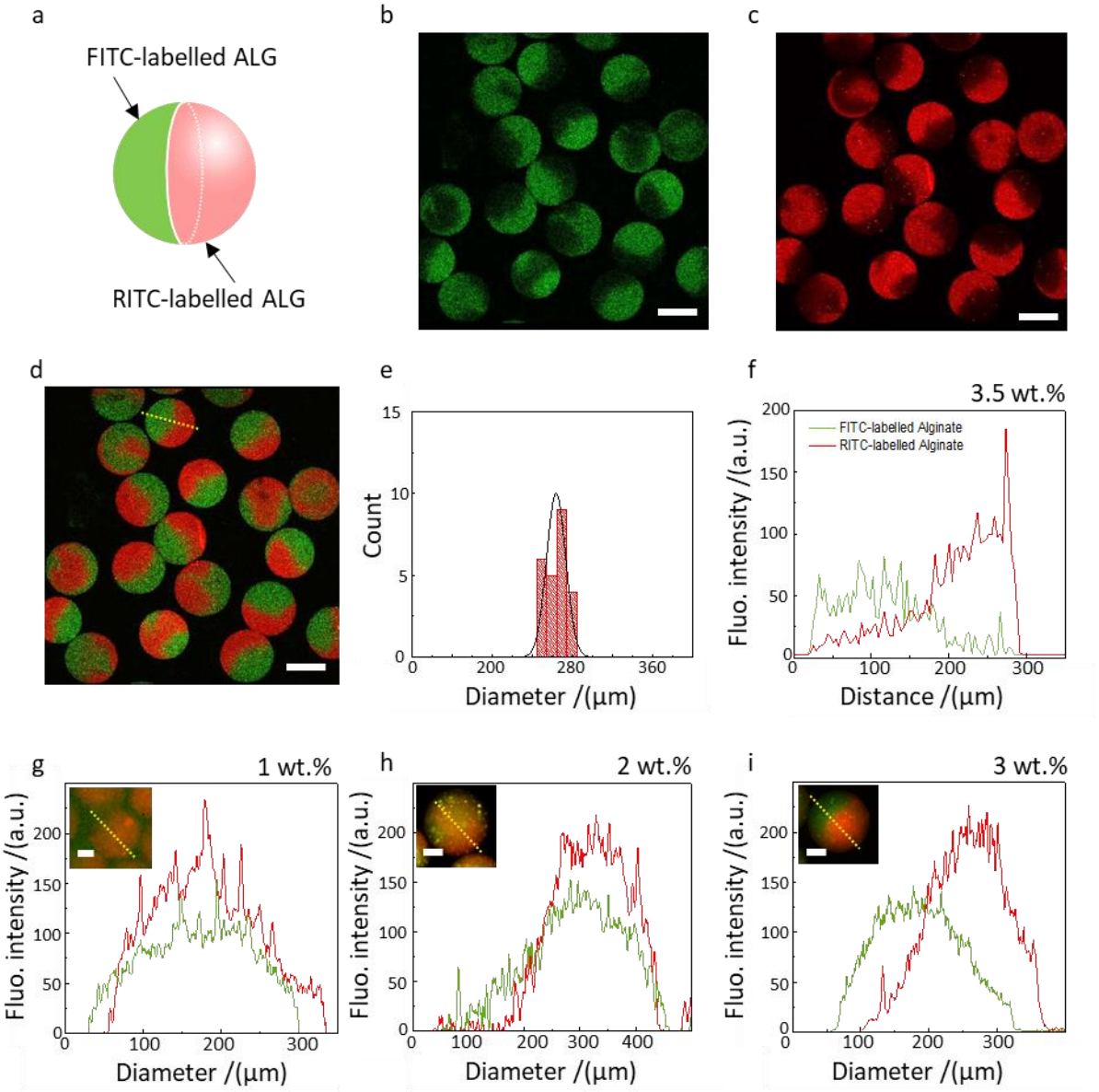

Figure 3.7. Microfluidic-prepared Janus fluorescently labelled hydrogel spheres. ***a****, diagram to show hydrogel sphere consisting of spatially segregated FITC-labelled (green) and RITC-labelled (red) 3.5 wt.% Alg hemispheres.* ***b****, CLSM image of FITC-labelled Alg (λ_{ext}= 488 nm and λ_{em}= 498-550 nm).* ***c****, CLSM image of RITC-labelled Alg (λ_{ext}= 561 nm and λ_{em}= 570-630 nm).* ***d****, CLSM image of FITC-labelled and RITC-labelled alginate. Scale bars = 200 µm.* ***e****, size distribution of Janus hydrogel spheres, calculated by measuring the population diameter in water.* ***f****, fluorescence intensity profile through the cross-section of a Janus hydrogel (yellow dotted line in* ***d****).* ***g****, fluorescence intensity profile through the cross-section of a Janus hydrogel (inset) made using 1 wt.% Alg.* ***h****, fluorescence intensity profile through the cross-section of a Janus hydrogel (inset) made using 2 wt.% Alg.* ***g****, fluorescence intensity profile through the cross-section of a Janus hydrogel (inset) made using 3 wt.% Alg. Scale bars (****g-i****) = 100 µm.*

The size of each hydrogel microsphere platform was controlled and tuned by several parameters both on and off the microfluidic device. Most obviously, changing the size of the inner capillary orifice on the device, proportionally changed the size of the resulting droplets (figure 3.8). Droplets fabricated by microfluidic devices with hand-sanded orifices of diameters 200, 250, 300, 350 µm and with controlled velocity parameters, were collected in a decanol bath. Droplet diameters were measured from optical microscope images, and plotted against orifice size, to show a direct proportionality.

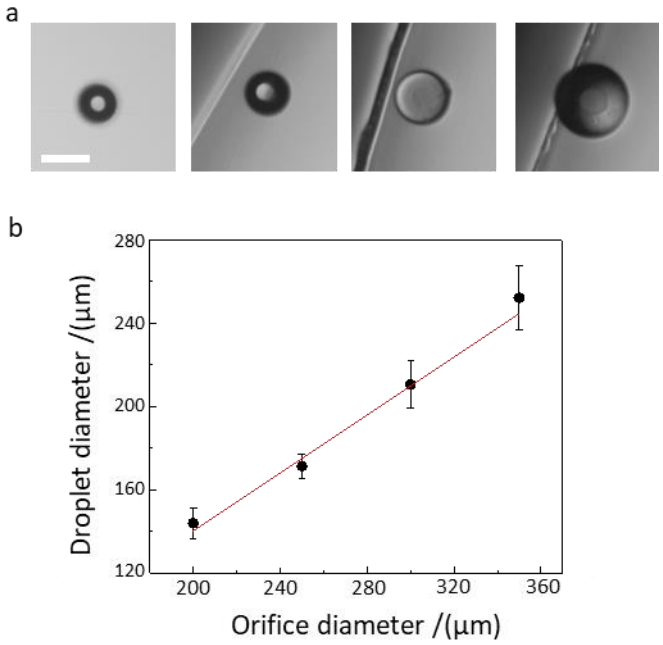

Figure 3.8. Controlling the size of the inner capillary orifice to adjust the alginate droplet diameter. ***a****, Bright field microscope images of a single alginate droplet in decanol, fabricated using dual microfluidic devices with 200, 250, 300 and 350 µm (left to right) orifice diameters. Scale bar, 200 µm.* ***b****, A graph showing the directly proportional increase in alginate droplet diameter, with increasing orifice size. Error bars represent standard deviation (n=3).*

Despite a clear relationship between orifice size and droplet diameter, it was more desirable to tune the droplet size by parameters off the microfluidic device, so that the same device could be used to fabricate an array of alginate microspheres with different diameters. The velocities at which both the inner and outer phases were injected through the device, had a significant effect on droplet size. In experiments where droplets were collected in a decanol bath (figure 3.9a) and where they were crosslinked in $CaBr_2$ before being transferred to water (figure 3.9b), an increase in the outer phase velocity (keeping inner phase velocity constant) decreased the droplet diameter. For droplets collected in decanol, the trend exponentially decreased with increasing outer phase velocity,

plateauing towards high V_{out}, whereby it was likely that the regime of the drop formation changed from a dripping to a jetting regime and thus the droplet diameter became limited by the orifice size. For hydrogel microspheres collected in water, the trend showed a linear decrease in diameter with increasing outer phase velocity. When hydrogel microspheres were transferred to water, they swelled significantly due to an influx of water. The size of the final swelled droplet therefore depended upon the degree of crosslinking in each droplet and the extent of swelling. As a consequence, the sensitivity of the results was decreased, resulting in a loss of the exponential trend. This was also represented by an increase in diameter error. At increased outer phase velocity, the capillary number is higher and thus there is a greater ratio of viscous force to surface tension at the capillary orifice. This makes the droplets smaller in size as they possess a greater tendency to break off from the orifice, ceasing droplet growth.

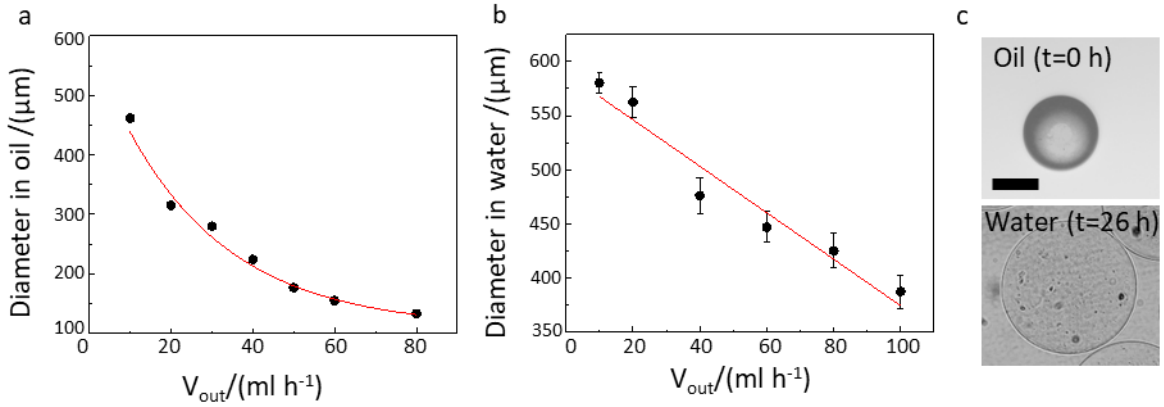

Figure 3.9. Outer phase velocity effect on sphere diameter. a,b, *Graphs to show how changing the outer phase velocity, at constant inner phase velocity, controls the size of the alginate droplets in oil (**a**) and crosslinked (**b**) droplets in water. Each inner phase was composed of 3.5 wt.% RITC-tagged alginate. Inner velocities kept constant, V_{in} = 0.15 ml h^{-1} [$CaBr_2$] = 5 mM. **c**, Bright field microscope images of a droplet formed at V_{out} = 20 ml h^{-1}. Top image recorded directly after collection in oil, bottom image recorded after crosslinking for 24 h and transferal to water. Scale bar, 200 µm. Error bars represent standard deviation (n=3).*

Changing the inner phase velocities, whilst maintaining a constant outer phase velocity, also effectuated a change in the droplet size, albeit showing a reduced effect in comparison to changing the outer phase velocity, and thus being more difficult to control. For example, in the decanol phase, changing the outer velocity by a factor of x5 from 10 to 50 ml h^{-1} resulted in a 285 µm change in droplet diameter whereas changing the inner velocity by a factor of x5 from 0.1 to 0.5 ml h^{-1} only resulted in an 86 µm change in droplet diameter. Water phases could not be compared due to a lack of control from the crosslinking solutions. Each inner phase velocity was increased from 0.01 ml h^{-1} to

1 ml h^{-1} (ratio 1 : 1, 2x RITC-Alg 3.5 wt.%) whilst the outer phase was kept constant at 40 ml h^{-1}. Droplets in both decanol (figure 3.10a) and water (figure 3.10b), showed a directly proportional trend between inner phase velocity and droplet diameter, at constant outer phase velocity. The concentration of $CaBr_2$ in this experiment, and thus crosslinking effect, was higher than the outer velocity experiment, resulting in less droplet swelling and thus smaller hydrogel microspheres compared to pre-crosslinked droplets in oil. Increasing the inner phase velocity, increases the significance of inner fluid inertia on the system, and thus the ratio of inertia to surface tension (Webber number). The rate of growth of droplet therefore increases and thus more liquid is channelled into the droplet before it breaks away from the orifice. However, this increase in inertial force also increases the rate at which droplets form and break away from the orifice, thus the overall increase in droplet size is determined by a balance between quicker droplet formation and increased droplet growth. These competing effects mean that using inner phase velocity to control the droplet size is significantly less effective than increasing outer phase velocity. At inner phase velocities greater than 1 ml h^{-1} a transition into a jetting regime was observed. This second type of dripping to jetting, observed at high inner flow rates, is controlled by the relative inertia of the dripping phase, pushing the dripping location downstream and resulting in a jet through the orifice.

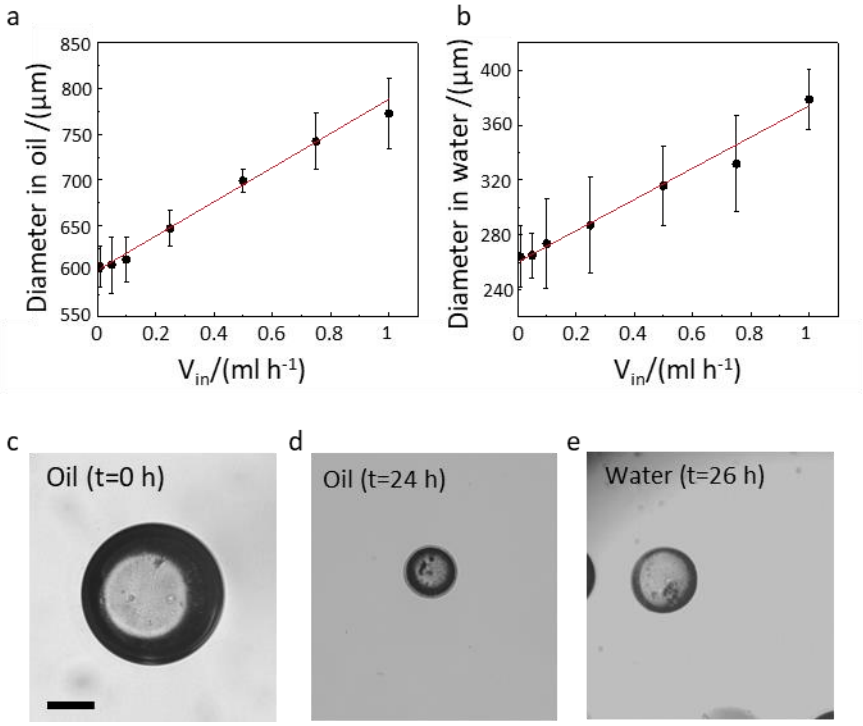

Figure 3.10. Inner phase velocity effect on sphere diameter. *Graphs to show how changing each inner phase velocity, at constant outer phase velocity, can control the size of the alginate droplets in oil and crosslinked droplets in water. Each inner phase was composed of 3.5 wt.% RITC-tagged Alg.* ***a,b****, Outer velocity kept constant,* V_{in} *= 40 ml* h^{-1} *[*$CaBr_2$*] = 8 mM.* ***c****, Bright field images of a droplet formed at* V_{in} *= 0.25 ml* h^{-1}*. Optical images showing Janus microsphere at different stages of fabrication.* ***c****, in oil immediately after collection and before crosslinking has occurred.* ***d****, in oil after 24hrs of crosslinking.* ***e****, transferred to water. Scale bar, 200 µm. Error bars represent standard deviation (n=3).*

As previously mentioned, the final size of hydrogel microspheres in water, is highly dependent on the concentration of crosslinker in the external collection solution. To observe this phenomenon hydrogel droplets were collected into various concentrations of $CaBr_2$ (1-11 mM) then left for 24 h before being transferred to water for diameter measurement. Increasing the concentration of $CaBr_2$ crosslinker decreased the size of the hydrogel spheres (figure 3.11) due to the alginate chains being held more tightly together by more Ca^{2+} ions and a concurrent reduction of water within the hydrogel matrix. The tightly packed and overlapping chains resulted in deformation of the spherical drop, thus changing the shape and monodispersity of droplets. A truly reflective diameter was therefore difficult to obtain in tightly crosslinked drops and, in this thesis, taken as the shortest diameter (figure 3.11c). At low concentration of $CaBr_2$ the hydrogel droplets absorbed large quantities of water, thus swelling them considerably and increasing the droplet diameter.

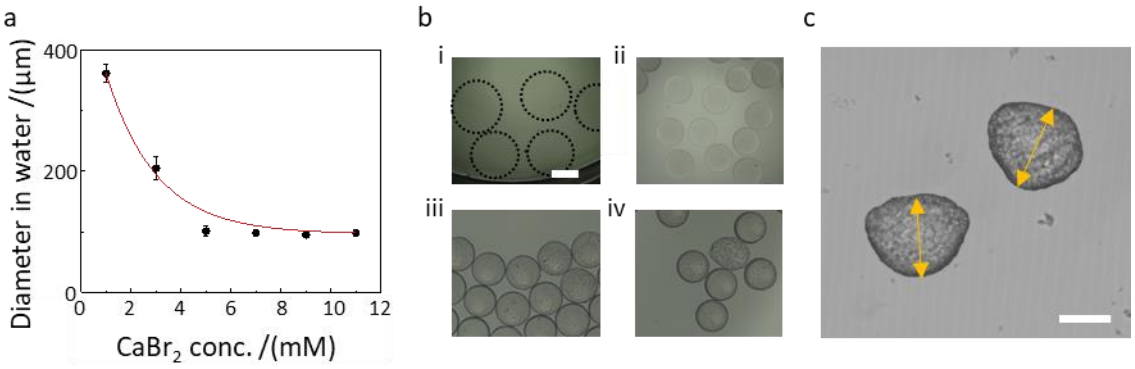

***Figure 3.11. Crosslinker concentration effect on sphere diameter**. **a**, Plot of $CaBr_2$ concentration vs hydrogel sphere diameter in water (inner phase, ALG 3.5 wt.%, V_{in} = 0.05 ml h^{-1}, V_{out} = 25 ml h^{-1}). **b**, Bright field images of hydrogel spheres prepared in (**a**) and crosslinked at concentrations (3, 5, 9, 11 mM from i-iv). Scale bar, 100 µm **c**, hydrogel microparticle diameter measurement across smallest diameter, prepared in (**a**) crosslinked with $CaBr_2$ (11 mM). Scale bar, 50 µm. Error bars represent standard deviation (n=3).*

The change in swelling and shape of the hydrogel microparticles, upon crosslinking and transferal to water, was determined by calculating the coefficient variance (CV) at each concentration of $CaBr_2$ crosslinker. Hydrogel spheres were prepared and crosslinked with $CaBr_2$ (1, 4, 8 and 10 mM, 24 h) before being transferred to water. Bright field microscope images were recorded and each microparticle diameter was measured to calculate the CV (figure 3.12). At the lowest concentration of $CaBr_2$ crosslinker, significant swelling was observed, and a CV, 9.4 was calculated. This CV value is significantly greater than the observed range for monodisperse droplets, meaning that hydrogel microspheres crosslinked with low levels of crosslinker (1 mM) are polydisperse. At the highest concentration of crosslinker (10 mM), a CV, 6.6 was calculated, again indicating polydisperse microparticles. Figure 3.12b categorises the shape and CV of hydrogel microparticles based on the experiments in figure 3.12a. At optimum concentration of crosslinker a monodisperse collection of spherical hydrogel microparticles is observed.

a

$CaBr_2$ conc. /(mol dm^{-3})	CV /(%)
1	9.4
4	1.6
8	5.5
10	6.6

b

$CaBr_2$ conc.	Low ◄ Optimum ► High		
Shape			
CV	>9%	0-5%	5-9%

Figure 3.12. Crosslinking concentration effect on shape and monodispersity. *How the concentration of $CaBr_2$ crosslinker controls the shape and monodispersity of hydrogel microspheres.* ***a****, Table comparing different concentrations of $CaBr_2$ with coefficient variance (CV).* ***b****, Table summarising how the shape and CV of microparticles changes depending on [$CaBr_2$].*

3.2a.2 Encapsulating colloidosomes within hydrogel platforms

Droplet-based microfluidics provides a highly tuneable technique for the fabrication of hydrogel microspheres through parameters such as orifice size, velocities, and crosslinking solution. At suitable crosslinking concentrations, alginate microspheres which displayed excellent monodispersity were created and velocities were programmed to achieve good control over microsphere size. The co-flow capillary microfluidic device, comprising two inner phase inlets, facilitated the intrinsic Janus patterning of alginate within the hydrogel microspheres to create distinct and spatially segregated hemispheres. The next step in developing this technique as a suitable platform for spatially organising protocells, was to encapsulate protocells through combining them with the alginate inner phases. Colloidosomes were chosen as a robust protocell that could be encapsulated without loosing their structure.

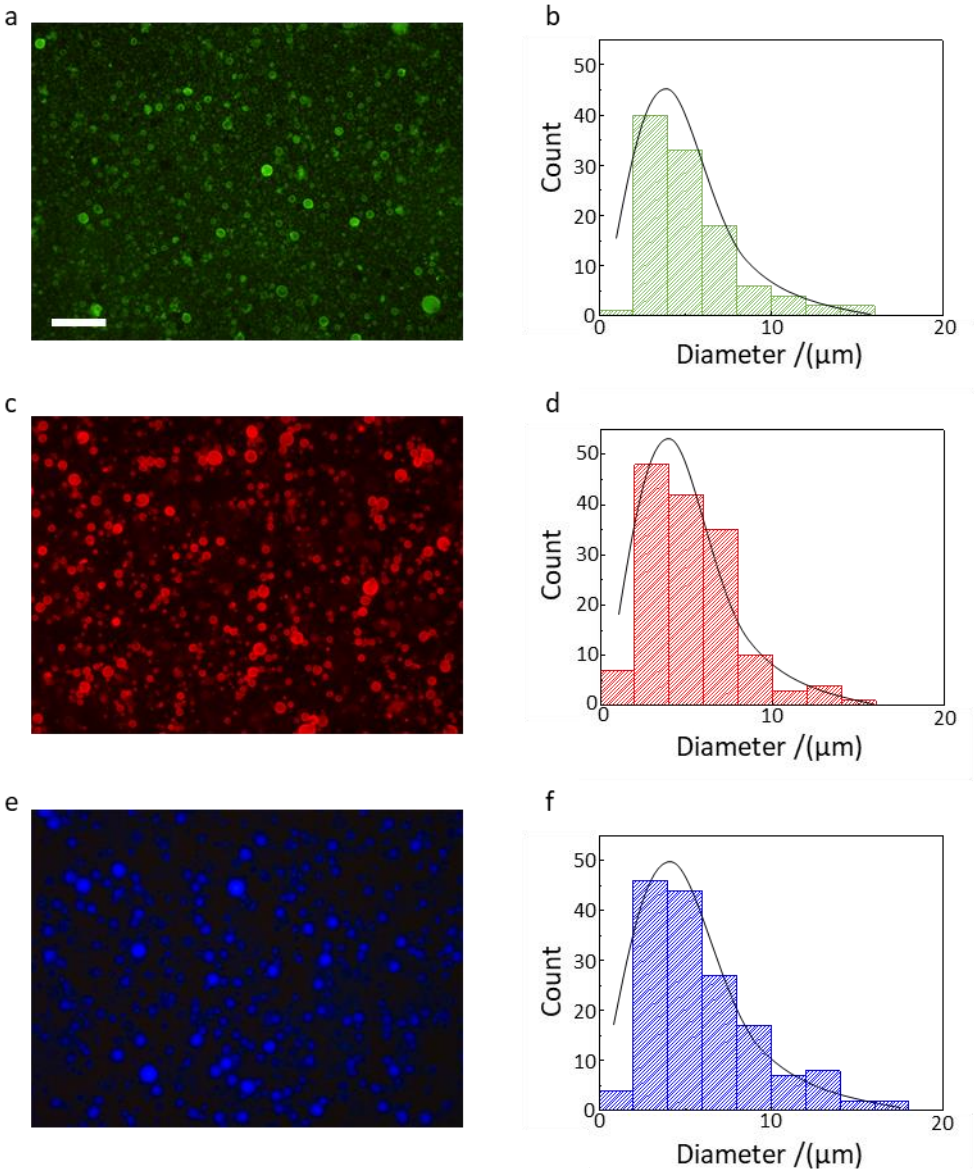

***Figure 3.13. Fluorescence images and size distribution of enzyme-loaded colloidosomes in water. a**, FITC-GOx loaded colloidosomes. **b**, Size distribution of colloidosomes in (**a**). **c**, RITC-GOx loaded colloidosomes. **d**, Size distribution of colloidosomes in (**c**). **e**, Dy405-HRP loaded colloidosomes. **f**, Size distribution of colloidosomes in (**e**). Scale bar, 50 μm.*

Silica colloidosomes with fluorescently labelled GOx cores were prepared according to method 2.2.1. Each population of colloidosomes FITC-GOx, RITC-GOx and Dy405-HRP had d_A of 5.61 ± 2.65 μm, 5.34 ± 2.6 μm and 6.09 ± 3.2 μm respectively (figure 3.13). Small colloidosomes were crucial for avoiding blockages within the capillaries of the microfluidic device. FITC/RITC-GOx displayed more affinity to the silica colloidosome membrane in comparison to Dy405-HRP, as seen by a fluorescent ring-like appearance rather than a homogeneous fluorescent sphere. Both enzymes showed similar overall charges according to their zeta potentials of -11.6 mV and -18.5 mV (RITC-GOx, Dy405-HRP). An original conclusion was that the more negative charge of Dy405-HRP meant that it repelled

further away from the silica surface, thus appearing more homogenous throughout the core of the colloidosome. However, this did not explain why GOx was being adsorbed to the silica membrane, given its negative charge -11.6 mV. Another conclusion was that the enzyme distribution was associated with the change in dye and thus groups within the dye structures and silica nanoparticles were interacting differently. However, experiments which compared Dy405-GOx and RITC-HRP (figure 3.14) showed that the dye was not influencing this enzyme distribution. From literature, although GOx is negatively charged, functional groups are unevenly distributed over the protein surface and thus, a positive region is exposed on the 'back' of GOx.[237] This enables it to be attracted and adsorbed to a negatively charged surface such as the silica nanoparticles on the membrane of colloidosomes. In contrast, the negative charge of HRP is well distributed across the protein surface and so the enzyme is repelled by the silica, not adsorbed to the surface, and distributed throughout the colloidosome interior. This is observed using CLSM images where both RITC-GOx and Dy405-GOx enzymes were observed to be adsorbed at the membrane of the colloidosome (figure 3.14a,b) whereas RITC-HRP and Dy405-HRP (figure 3.14c,d) were well dispersed.

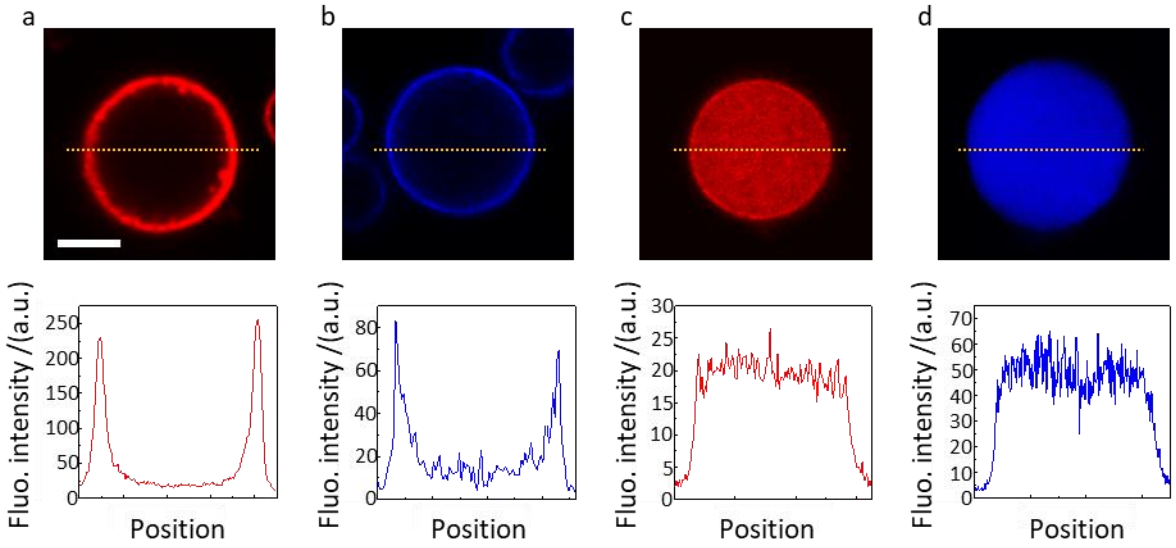

Figure 3.14. Spatial distribution of enzymes within colloidosomes loaded with RITC and Dy405 labelled GOx and HRP. *Fluorescence images and intensity profile across the cross section (yellow dotted line) of* ***a****, RITC-tagged GOx loaded colloidosome* ***b****, Dy405-tagged GOx loaded colloidosome* ***c****, RITC-tagged HRP loaded colloidosome d, Dy405-tagged HRP loaded colloidosome. Scale bar, 2 µm.*

Janus hydrogel spheres were used as distinct platforms for the spatial control and distribution of colloidosome communities, as a way of mimicking neighbouring cell communities within biological ECM-based systems. Colloidosomes (~5 μm ± 5) were dispersed into sodium alginate and used as a building block for the hydrogel matrix and thus a suitable inner phase for the microfluidic device. Two independent colloidosome-Alg inner phases were injected into the microfluidic device through a theta capillary, which led to droplet formation at the co-flow device orifice where an outer phase of decanol was injected. The droplets were collected immediately into a decanol (off-device) pool combined with $CaBr_2$ crosslinking solution (1-12 mM) and left for ~20 hrs. The crosslinked hydrogel spheres were subsequently transferred to water by various washing steps (figure 3.15a).

The binary population of spatially separated colloidosome communities within a spherical hydrogel platform (d_A, ~300-800 μm), was observed by CLSM images and corresponding fluorescence intensity measurements. Figure 3.15a,b clearly shows hydrogel spheres consisting of two distinct fluorescence regions. The fluorescence emission is derived from RITC-GOx loaded colloidosomes and Dy405-HRP loaded colloidosomes, which have been successfully localised and encapsulated in a spatially segregated Janus pattern within the hydrogel platform. Measuring the fluorescence intensity across the hydrogel platform (yellow dotted line) shows two distinct regions of fluorescence relating to the RITC and Dy405 fluorescent dyes (figure 15c). Janus spheres with encapsulated colloidosome communities, fabricated using droplet microfluidics, showed high monodispersity (CV, 1.4%).

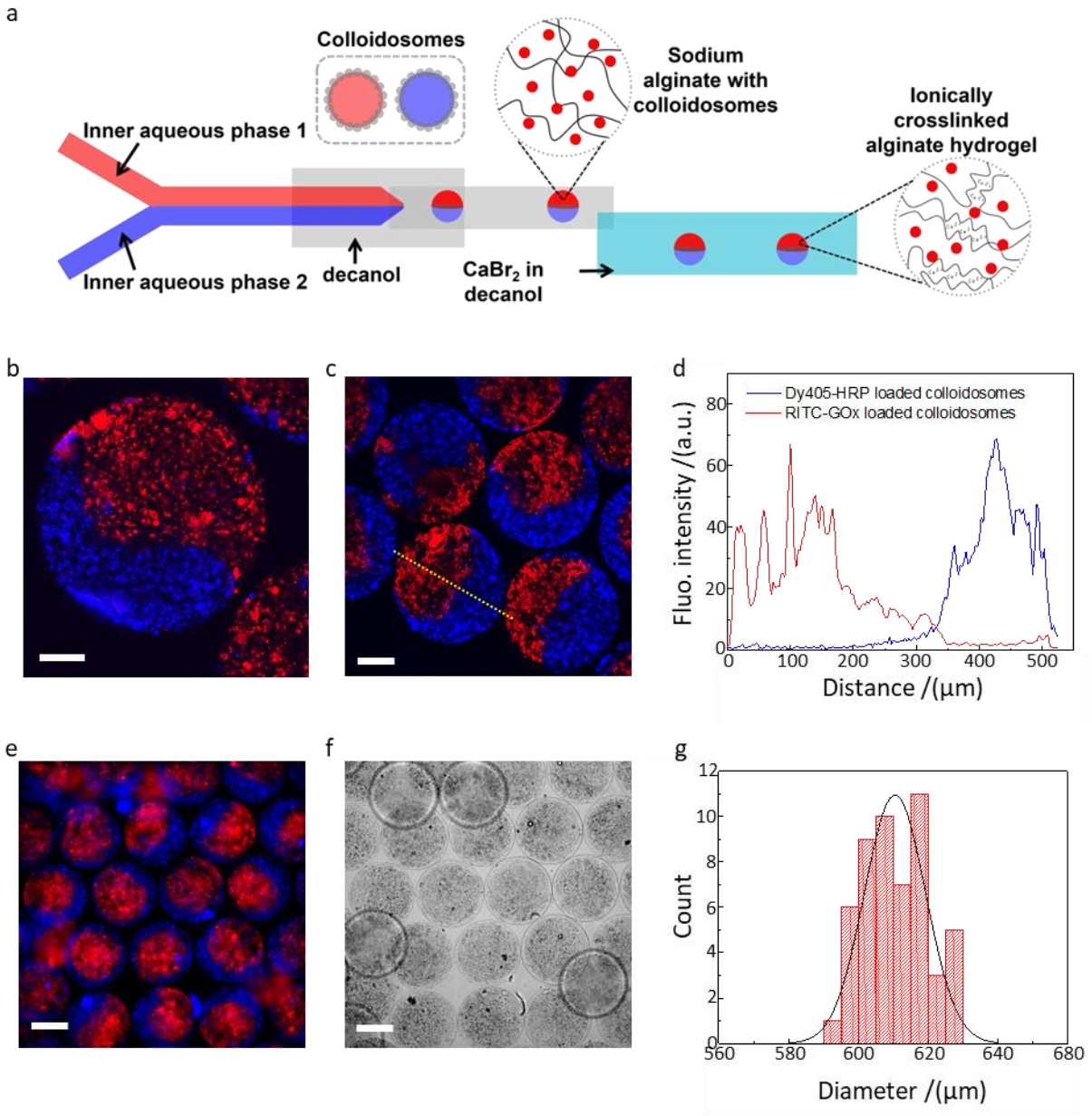

Figure 3.15. Microfluidic-prepared Janus hydrogel spheres comprising spatially segregated populations of RITC-GOx loaded and Dy405-HRP loaded colloidosomes. ***a****, Microfluidic-based segregation and immobilisation of a binary population of spherical colloidosomes (red, blue) within crosslinked hydrogel microspheres. Two independent inner phases consisting of aqueous sodium alginate with different single populations of spherical colloidosomes merge with a decanol outer phase (grey) and the resulting Janus droplets are collected and crosslinked in decanol/$CaBr_2$ (turquoise). CLSM image of single (**b**) and multiple (**c**) hydrogel spheres in water, made from ALG 3.5 wt.% alginate with segregated populations of RITC-GOx loaded colloidosomes (red) and Dy405-HRP loaded colloidosomes (blue). Scale bar, 200 µm.* ***d****, Fluorescence intensity profile through the cross-section of a single hydrogel sphere (yellow dotted line in (**c**)). Wide field fluorescence (**e**) and bright field (**f**) image featuring several hydrogel spheres as prepared in (**b**). Scale bars, 300 µm.* ***g****, Size distribution of hydrogel spheres in (**f**) n, 50.*

Colloidosomes comprise an inorganic shell which is crosslinked to provide extra rigidity. The TMOS-crosslinked silica colloidosomes prepared in this thesis are therefore excellent candidate protocells for encapsulating into alginate through relatively harsh techniques such as droplet-based microfluidics. Colloidosome structures are retained, and enzymes remain captured within the colloidosome interiors, as seen in figure 3.16. A sample was taken from the RITC-GOx loaded colloidosome-Alg inner phase and imaged (figure 3.16a). Fluorescence intensity profiles were measured across two individual colloidosomes to show clear localisation of RITC-GOx enzymes within the colloidosome boundary. An image was recorded from RITC-GOx loaded colloidosomes encapsulated within a crosslinked alginate microsphere. Again, fluorescence intensity profiles showed intact colloidosomes within the alginate matrix. Images taken by a x63 lens were used to get an even clearer image of single RITC-GOx and Dy405-HRP loaded colloidosomes within the crosslinked alginate microsphere. Again, GOx is attracted to the membrane of the protocell and HRP is evenly distributed throughout the colloidosome however, both colloidosomes maintain their spherical structure and the enzymes remain localised within the colloidosome as seen by fluorescence intensity measurements.

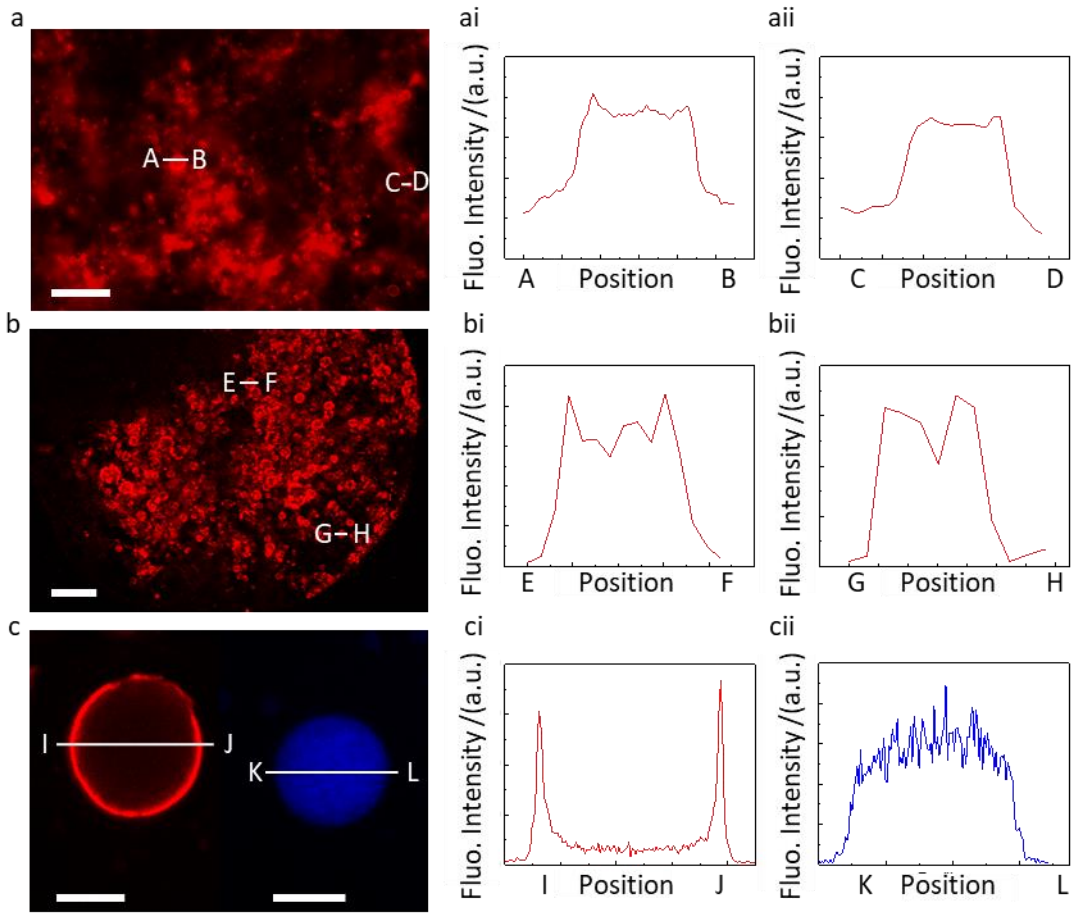

Figure 3.16. Retention of colloidosome structure after encapsulating within alginate and following microfluidic-based fabrication of hydrogel microspheres. a*, Fluorescence image of RITC-GOx loaded colloidosomes embedded within Alg (3.5 wt.%) used as inner phase for the microfluidic set-up. Scale bar, 20 µm.* ***ai*** *and* ***ii*** *show fluorescence profiles across two distinct colloidosomes within (****a****).* ***b****, Fluorescence image of RITC-GOx loaded colloidosomes embedded in crosslinked hydrogel microsphere (Alg, 3.5 wt.%). Scale bar, 20 µm.* ***bi*** *and* ***ii*** *show fluorescence profiles across two distinct colloidosomes within (****b****).* ***c****, Close-up fluorescence image of RITC-GOx and Dy405-HRP loaded colloidosomes embedded in crosslinked hydrogel microsphere (Alg, 3.5 wt.%). Scale bar, 10 µm.* ***ci*** *and* ***ii*** *show fluorescence profiles across each distinct colloidosomes within the alginate sphere.*

Spatially segregated communities of RITC-GOx loaded and FITC-GOx loaded colloidosomes imaged using 3D light sheet microscopy, showed that the interior Janus population of colloidosomes was extended throughout the entire crosslinked hydrogel sphere (figure 3.17). A 3D movie was also captured, to view the hydrogel sphere from several different angles, and images were isolated at different orientations. A small degree of colloidosome population mixing occurred due to unavoidable pre-crosslinking diffusion. This effect remained mostly insignificant, as the bulk colloidosomes communities clearly show a segregated Janus formation from several angles.

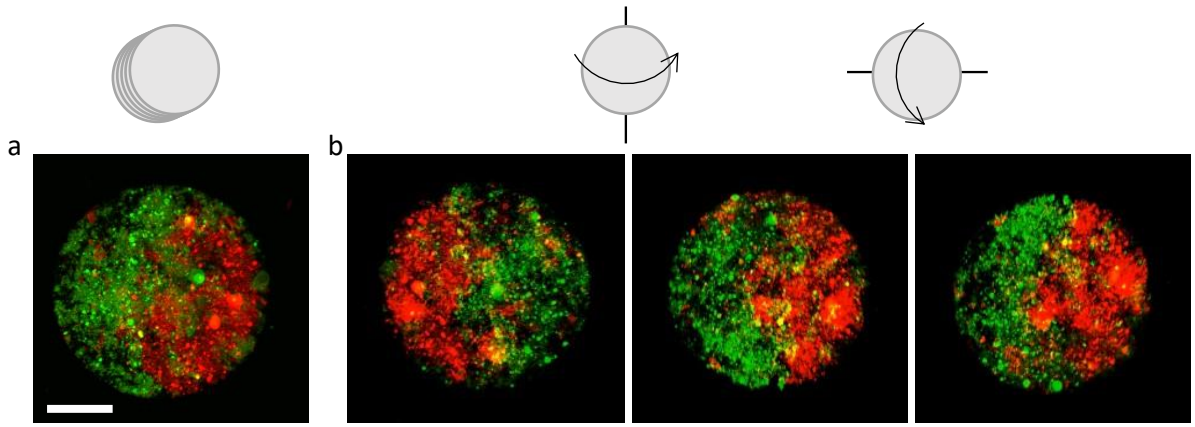

Figure 3.17. 3D light sheet images of colloidosome-embedded Janus hydrogel spheres comprising spatially segregated populations of FITC-GOx loaded and RITC-GOx loaded colloidosomes. a*, Stack of images superimposed on top of each other.* ***b****, Screenshots from a 3D projection of the hydrogel sphere rotated 180°around the vertical axis and 180° around the horizontal axis. Scale bar, 200 µm.*

As well as mimicking a basic living cell unit system, colloidosomes are crucial for the spatial positioning and localisation of enzymes within the alginate hydrogel microsphere. The colloidosomes are large enough that they become trapped within the crosslinked hydrogel matrix and can thus be spatially confined. When enzymes were not encapsulated within a colloidosome they were free to diffuse throughout the hydrogel matrix and thus could not be successfully trapped or spatially localised. RITC-GOx and Dy405-HRP enzymes were separately mixed with sodium alginate and used as each enzyme-Alg inner phases respectively, for the fabrication of hydrogel platforms via microfluidics. The platforms were crosslinked using 3 mM, 5 mM and 7 mM $CaBr_2$ crosslinker. It was clearly observed (figure 3.18) that a Janus pattern was not realised in any of these microspheres, showing that spatial segregation could not be achieved using free enzymes. At low concentration of crosslinker (3 mM) both enzymes diffused into the aqueous environment and were therefore not confined within the matrix. This was due to hydrogel swelling, which created large pores in the hydrogel matrix enabling the enzymes to freely diffuse in and out of the microsphere until equilibrium is reached. At concentrations 5 mM and 7 mM crosslinker, the enzymes are trapped within the hydrogel platforms, however a Janus pattern has not been achieved. Due to more tightly bound alginate chains by increased crosslinking, enzymes are trapped within the hydrogel pores. However, before crosslinking, they were easily able to diffuse throughout the hydrogel resulting in a large degree of mixing. In this way, a segregated distribution of enzymes cannot be realised without encapsulation within some compartment that is bigger than the crosslinked hydrogel pores.

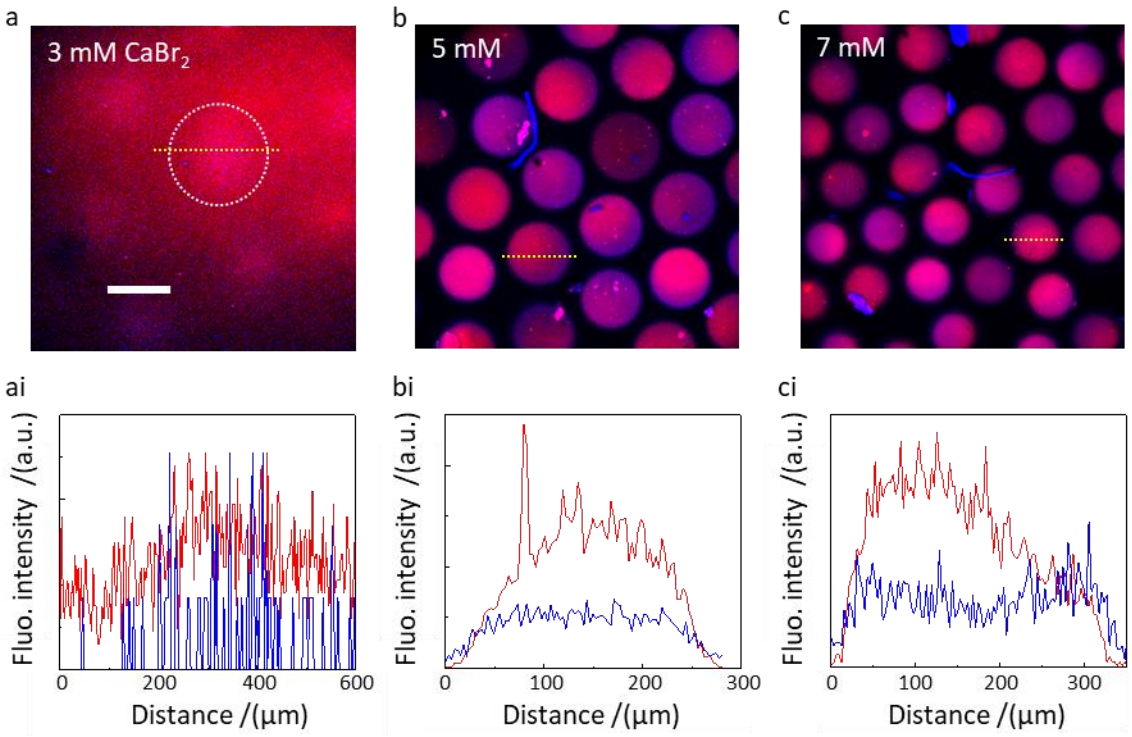

***Figure 3.18**. **Enzyme-encapsulated hydrogel microspheres comprising RITC-GOx and Dy405-HRP. a**, Hydrogel microspheres prepared using RITC-GOx loaded Alg and Dy405-HRP loaded Alg as inner phases respectively. Fluorescence images of the microspheres in water crosslinked with 3 mM (**a**), 5 mM (**b**) and 7 mM (**c**) $CaBr_2$. **Ai-ci**, Fluorescence intensity profile through the cross section of each sphere in **a-c** (yellow dotted line). Scale bar, 400 µm.*

Overall, a binary population of colloidosomes was successfully encapsulated inside alginate hydrogel microspheres and spatially segregated into an internal Janus pattern. Various images and fluorescence analysis techniques were used to confirm that the colloidosome populations remained segregated throughout the microsphere and endured the harsh microfluidic processing.

3.2a.3 Patterning of colloidosome communities within hydrogel platforms

Given the ability of droplet-based microfluidics to afford high levels of sphere size control using velocity and crosslinking parameters, the velocity parameters on colloidosome patterning as a precise control over the structural design (ratios, species, and morphology) was further investigated. First, the Janus ratio of colloidosome communities, within each hydrogel platform, was delicately controlled via the input velocities of each inner phase, as seen in figure 3.19. Each inner phase comprised one colloidosome community, either RITC- GOx or Dy405- HRP/FITC-GOx, dispersed in Alg (3.5 wt.%). Each inner phase was injected at V_{in} = 0.1-0.25 ml h^{-1}, V_{out} = 100 ml h^{-1} and collected in an external solution $CaBr_2$ (3 mM). ~70% volume ratio of colloidosomes containing RITC-GOx was

achieved by a 5 : 2 (0.25 : 0.1 ml h^{-1}) velocity ratio of RITC-GOx : Dy405- HRP/FITC-GOx. ~60% by velocity ratio 5 : 3 (0.2 : 0.12 ml h^{-1}), ~45% by velocity ratio 3 : 5 and ~25% by velocity ratio 2 : 5. Controlling the distribution of colloidosome communities within the hydrogel platform, revealed internal programmability for possible volume-controlled reactions and communication pathways between different sized protocell populations.

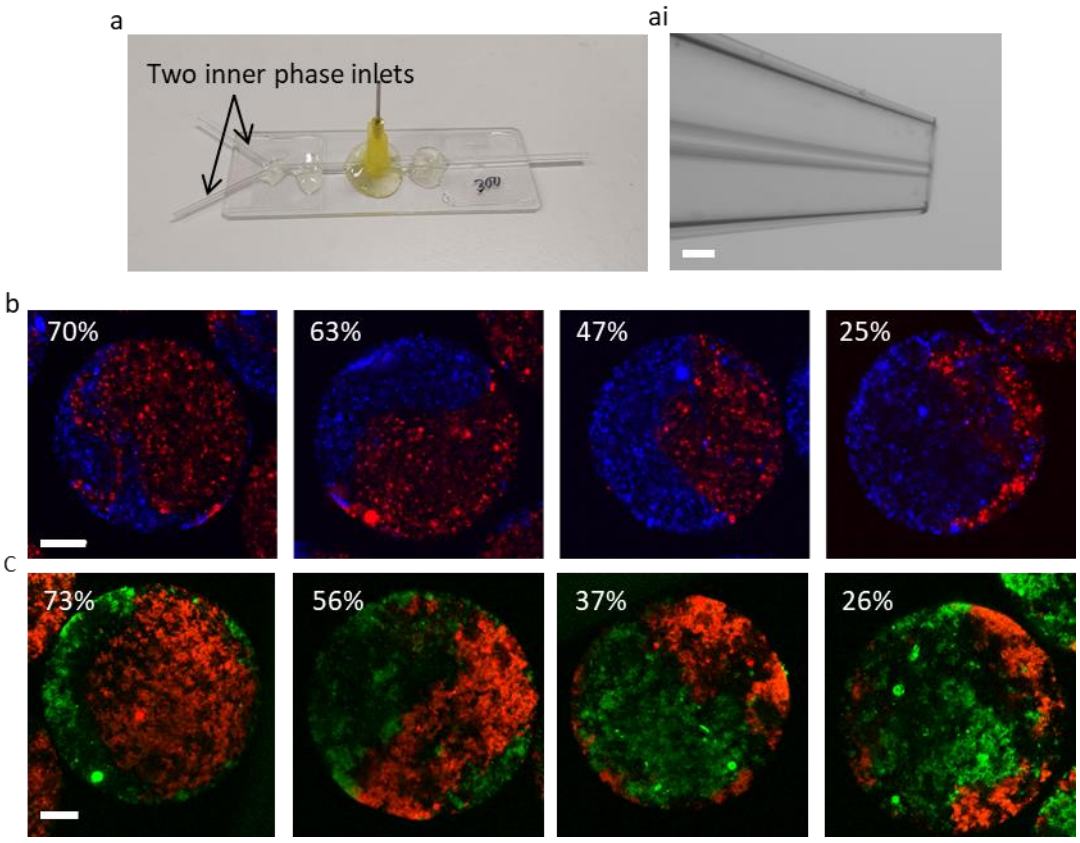

Figure 3.19. Using dual microfluidics to manipulate the volume ratio of spatially segregated colloidosome communities. a*, Camera image of dual capillary microfluidic device with an optical microscope image (**ai**) of the theta inner capillary orifice. Scale bar, 100 µm.* ***b****, CLSM images of hydrogel microsphere with various internal number percentages (7 : 3, 16 : 25, 12 : 25 and 1: 4) of segregated RITC-GOx loaded colloidosome : Dy405-HRP loaded colloidosome populations. Scale bar = 200 µm.* ***c****, CLSM images of hydrogel microsphere with various internal number percentages (7 : 3, 16 : 25, 12 : 25 and 1: 4) of segregated RITC-GOx loaded colloidosome : FITC-GOx loaded colloidosome populations. Scale bar, 100 µm.*

Further complexity in colloidosome population internal patterning was achieved by changing the inner capillary. A three-bore inner capillary was used to replace the theta capillary within the microfluidic device, allowing for three segregated inner phases to be injected (figure 3.20a). RITC-GOx loaded colloidosomes, FITC-GOx loaded colloidosomes and Dy405-HRP loaded colloidosomes were dispersed within three separate alginate solutions (3.5 wt.%) and each was injected separately

into one of the three bores of the inner glass capillary. This resulted in hydrogel microspheres comprising three spatially separated colloidosome communities, wherein each colloidosome population was encapsulated with approximately equal distribution (1 : 1 : 1) . This introduced higher order control over colloidosome community distributions, revealing potential for more complex communication pathways and multiple step reactions within hydrogel microspheres.

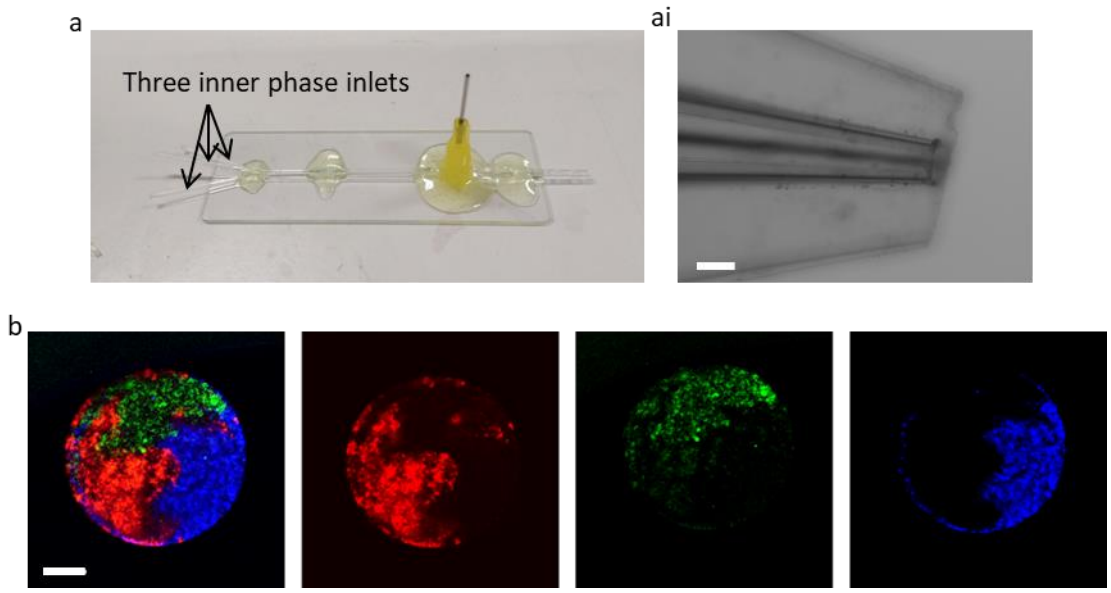

Figure 3.20. *Fabrication of hydrogel microsphere consisting of three spatially segregated colloidosome communities.* ***a****, 3-bore device made using a 3-bore inner capillary and 3 injection capillaries.* ***ai****, Close- up image of the 3-bore orifice. Scale bar, 100 µm.* ***b****, Combined and filtered fluorescence channel images of a hydrogel microspheres with segregated RITC-GOx loaded colloidosomes community (red), FITC-GOx loaded colloidosome community (green) and Dy405-HRP loaded colloidosome community (blue). Scale bar, 200 µm.*

Previous results showed that increasing the concentration of $CaBr_2$ crosslinker changed the morphology of the hydrogel platforms from smooth microspheres to irregular oblong microparticles. Despite morphological changes being potentially interesting, there were several drawbacks to this method of non-spherical hydrogel production, such as not having control over the elongated dimension, extremely high crosslinking density and particles being limited to an oval shape. Alterations to the basic microfluidic capillary device were therefore carried out to enable the controlled production of rod-shaped hydrogel platforms. Specifically, these rod-like shapes were realised by enlarging the orifice, using a smaller collection capillary to spatially confine the droplets, and crosslinking on-device. An additional capillary was also added to the end of the device to extend crosslinking time on-device (figure 3.21a). The fabrication of colloidosome-encapsulated hydrogel microrods was challenging due to frequent blockages by over-crosslinked hydrogels in the device.

The system therefore required a fine balance of parameters so that crosslinking did not block capillaries but was concentrated enough to arrest spheres into a rod-shape so that they did not become spherical (their lowest energy configuration) when released into the decanol collection pool.

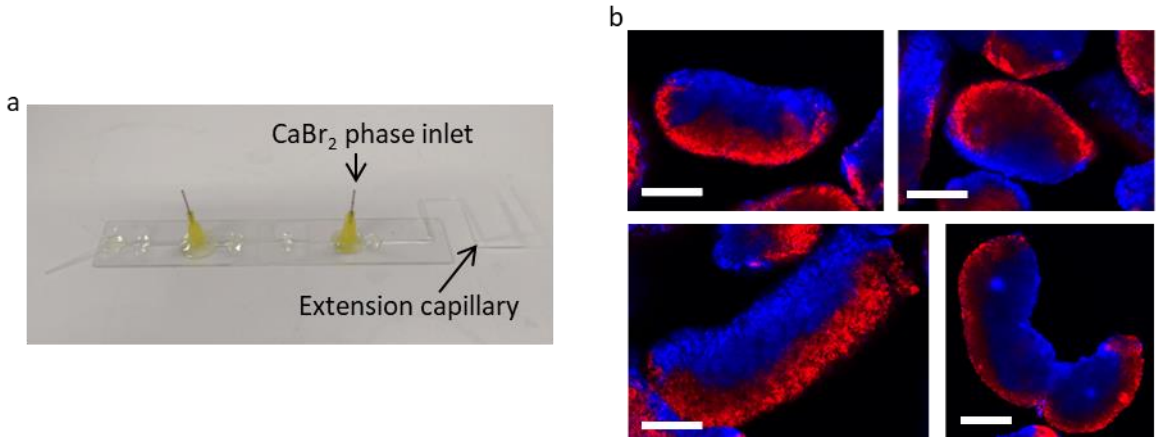

***Figure 3.21. Fabrication of hydrogel rods with spatially segregated colloidosome communities. a**, Microfluidic device for creating rod-shaped hydrogels consisting of an additional outer phase inlet for injecting $CaBr_2$ into the device and an extension capillary for crosslinking to occur within the confines of a capillary. **b**, CLSM images of several rod-shaped hydrogels with a spatially segregated community of RITC-GOx (red) and Dy405-HRP (blue) loaded colloidosome communities. Scale bars, 200 µm.*

Droplet-based co-flow microfluidics has provided an excellent method for controlling the encapsulation of spatially segregated colloidosomes within alginate hydrogel microsphere platforms. The size, shape and internal patterning of each hydrogel platform can be easily regulated by altering device designs and parameters. These hydrogel alginate microparticles are therefore considered excellent physical ECM mimicking scaffolds for colloidosome spatial organisation.

3.2b Prototissue matrix

Despite excellent protocell spatial organisation through microfluidic-aided immobilisation of colloidosomes in an alginate microsphere, the encapsulated colloidosome density was low (1 x10^8 col. ml^{-1}) resulting in significant space between each protocell within a community, and the alginate matrix itself lacked inherent biological properties. It therefore seemed logical to develop a physical scaffold that could simultaneously have a structural and biological impact, whilst comprising a very dense population of protocells. As discussed in the background, a common prototissue engineering technique involves interface bilayer connecting protocells to form a packed protocellular-based matrix. This matrix provides a physical scaffold alongside its own biological functions influenced by each protocell within the matrix. Therefore, if a second population of protocells could be encapsulated by the prototissue, bio-inspired matrix behaviours could be exploited alongside matrix-cell interactions and spatial organisation.

3.2b.1 Colloidosomes encapsulated within coacervate prototissue

Au/PEG-caged coacervates[58] have been applied as suitable building blocks for interconnected prototissue generation wherein a matrix of connected and stable coacervate protocells are fused together within minutes to create a discrete gel-like material. In general, coacervate-based protocells are a good candidate for prototissue design as they are a reasonably good resemblance of early-life cells and rely on simplified self-assembly to compartmentalise a chemically rich interior. Coacervate droplets do not have a membrane however, a membrane can be added (as is the case here) to prevent coacervate coalescence and to help establish an interconnected structure with defined cellular compartments. In this thesis, oppositely charged polydiallyldimethylammonium chloride (PDDA) and carboxymethyl (CM)-dextran macromolecules were self-assembled into coacervate droplets. These coacervates were subsequently coated with Au nanoparticles and TA-PEG-TA polymer. Au has a high tendency to be adsorbed by the coacervate microdroplet due to the strong Au negative charge being attracted to the overall positive coacervate interior. However, the TA-PEG-TA polymer wants to remain outside the coacervate due to its hydrophilic interaction with water. These competing forces result in an Au-PEG membrane being bound at the coacervate interface.

a

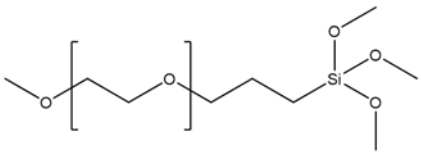

PEG-s

b

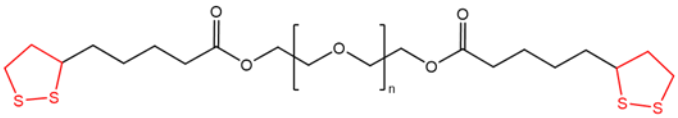

TA-PEG-TA (n≈455)

***Figure 3.22**. **a**, Methpoly(ethylene glycol)propyltrimethoxysilane (PEG-s) molecule which is attached to small colloidosomes to aid dispersion in water. **b**, Thioctic acid (TA)-PEG-TA molecule which is attached to Au-coacervates.*

Small colloidosomes (average diameter, d_A = 4 µm) were made using the method in section 2.3.16, with the addition of methpoly(ethylene glycol)propyltrimethoxysilane (PEG-s) to aid colloidosome dispersion and reduce aggregation by creating a more hydrophilic membrane. RITC-GOx loaded colloidosomes were coated with PEG-s and fluorescence images were recorded to visualise a well-dispersed population of colloidosomes. (figure 3.23a,b). Coacervated microdroplets were fabricated using PDDA and FITC-CM-dextran, coated with Au nanoparticles, and then with TA-PEG-TA molecules, so as to stabilise the microdroplets (figure 3.23c,d).

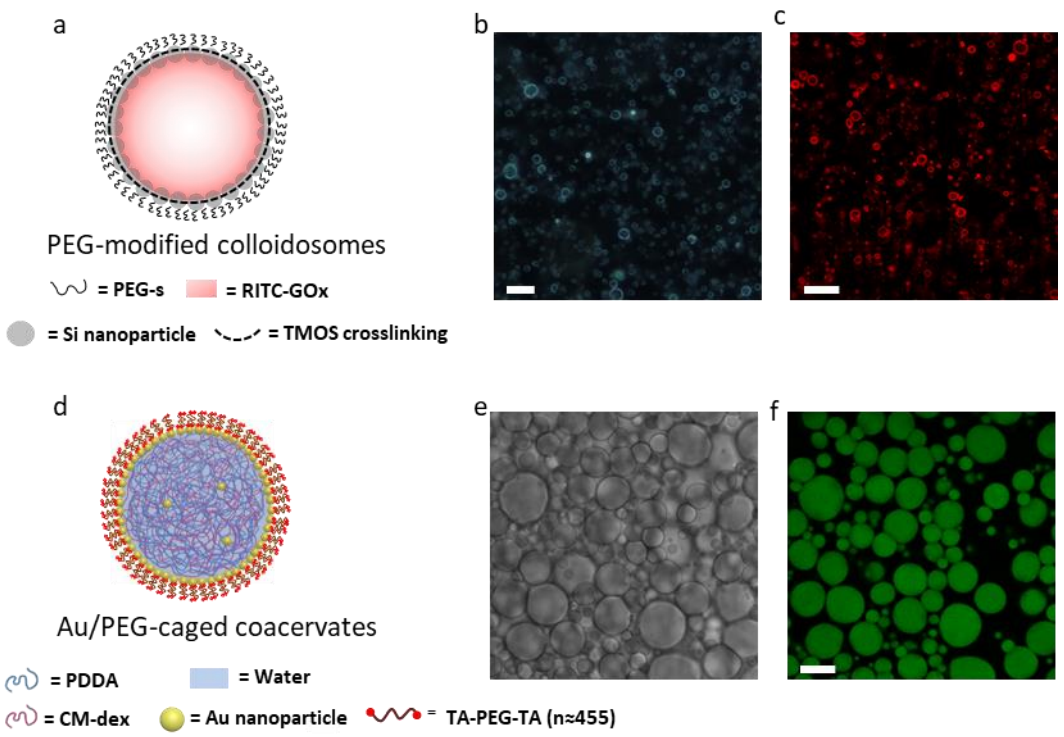

***Figure 3.23**. **Fabrication of PEG-coated colloidosomes and Au-PEG-caged coacervate droplets. a**, Diagram of an RITC-GOx loaded colloidosome with TMOS crosslinking and PEG-s coating. Bright field (**b**) and fluorescence (**c**) images of PEG-s coated colloidosomes dispersed in water. **d**, Diagram of Au-PEG coated coacervates made from PDDA : CM-dextran. Bright field (**e**) and fluorescence (**f**) images of Au-PEG coated coacervates with PDDA : FITC-CM-dextran interior, dispersed in water. Scale bars, 50 µm.*

A colloidosome-rich, free-standing, aqueous, coacervate network was fabricated by the mixing of a colloidosome phase into the Au-PEG-caged coacervates, followed by application of a centrifugal force. The centrifugal force enabled close contact between coacervates so that the TA-PEG-TA could link coacervates together to form a closely packed structure. The small colloidosomes were embedded into interstitial gaps between coacervate droplets within the network, creating small, interspersed focal points (figure 3.24).

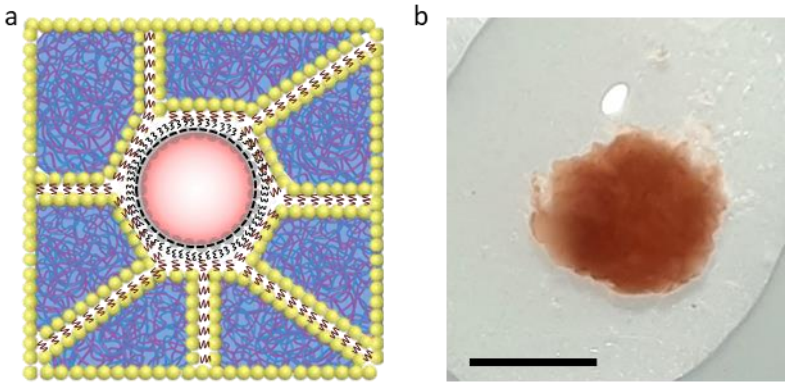

Figure 3.24. Coacervate prototissue with colloidosomes entrapped within the internal network. a, *Diagram of coacervate prototissue fabricated from Au-PEG-coated coacervates and with a PEG-s coated colloidosome trapped within the coacervate network.* ***b****, Optical image of free-standing Au-PEG-coated coacervate tissue with PEG-s coated colloidosome trapped within. Scale bar, 2.5 mm.*

Different concentrations of colloidosomes were immobilised within the coacervate matrix to determine the effect of encapsulation on coacervate network structure. Colloidosomes (10 µl, 5 µl and 2 µl) were added to the Au-PEG caged coacervate suspension (115 µl) before being centrifuged and made into a coacervate tissue. Small colloidosomes were trapped in the interstitial gaps within the coacervate tissue and were well dispersed throughout the network (final number densities; 500 x 10^6 col. ml^{-1}, 300 x 10^6 col. ml^{-1}, 75 x 10^6 col. ml^{-1}). Bright field images show connected coacervates and demonstrate that even with the addition of colloidosomes, the coacervate network is well-maintained (figure 3.25). However, fluorescence images show that the addition of small colloidosomes resulted in interstitial gaps within the tissue as a consequence of disrupted interfacial connection between coacervates. Therefore, at higher number density of colloidosomes the prototissue weakens and a critical number density of small colloidosomes (600 x 10^6 col. ml^{-1}) is observed, above which a coacervate tissue does not form.

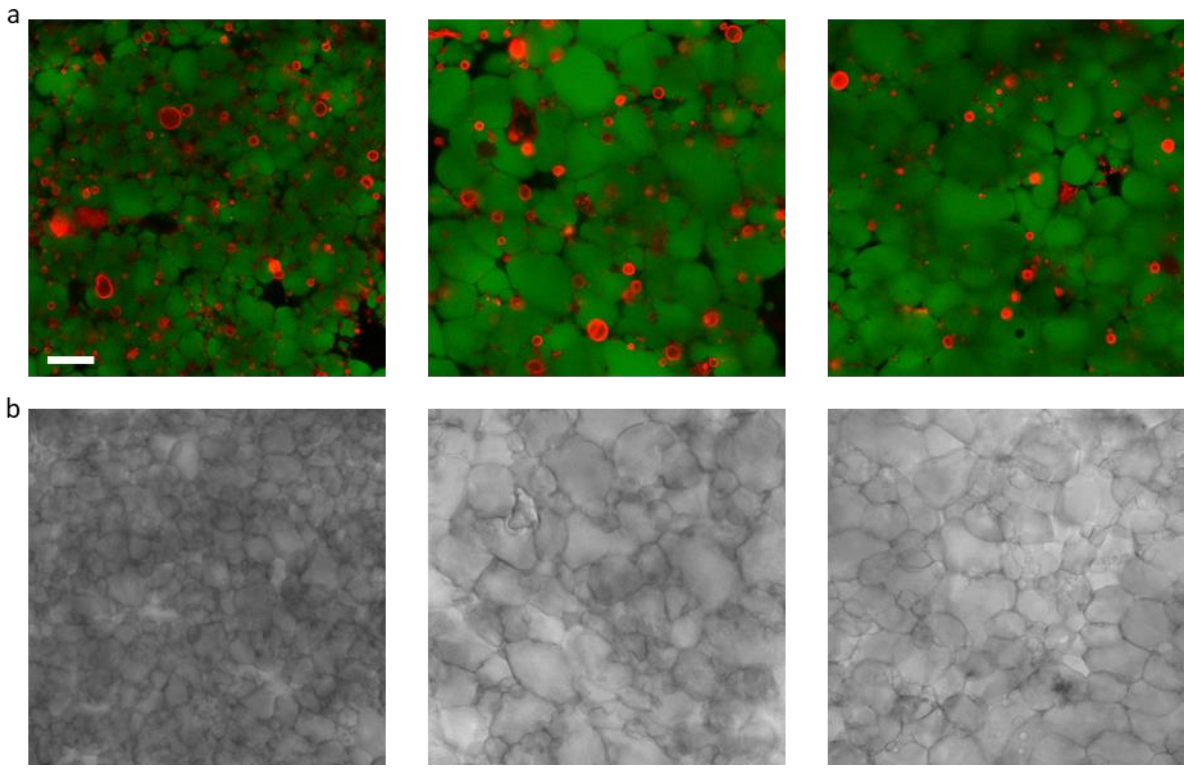

Figure 3.25. Small colloidosomes embedded within Au-PEG-coated coacervate network. *Fluorescence (**a**) and bright field (**b**) images of small RITC-GOx loaded colloidosomes embedded within Au-PEG-coated PDDA : FITC-CM dextran coacervate network. Final colloidosome number densities; 500 x 10^6 col. ml^{-1}, 300 x 10^6 col. ml^{-1}, 75 x10^6 col. ml^{-1} respectively. Scale bar, 50 µm.*

Larger colloidosomes (average diameter, d_A = 50 µm) were made according to the method in section 2.3.17. These colloidosomes were comparable in size to the Au-PEG-caged coacervates (figure 3.23e,f,g) and thus could directly replace a coacervate position within the coacervate-matrix. RITC-β-glucosidase loaded colloidosomes were coated in PEG-s and observed by bright field and fluorescence microscopy. Images showed a well-dispersed population of spherical colloidosomes in water (figure 3.26).

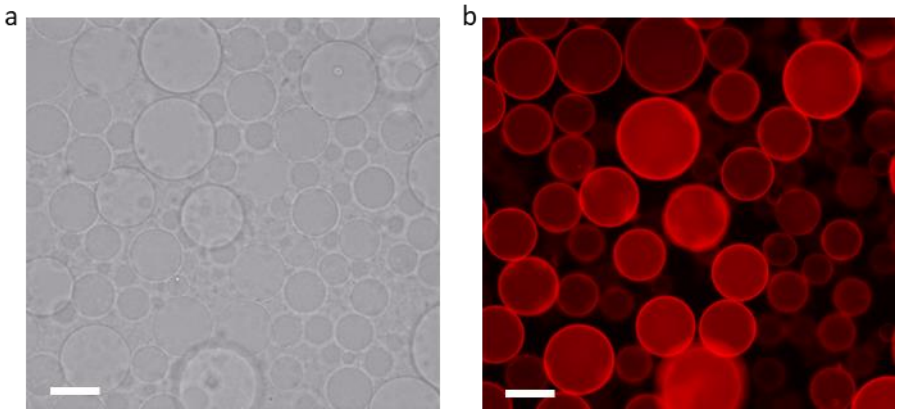

Figure 3.26. *Bright field (**a**) and fluorescence (**b**) images of RITC- β-glucosidase loaded colloidosomes coated with PEG-s. Scale bars, 50 µm.*

A free-standing, aqueous, coacervate network was thus prepared with larger colloidosomes successfully trapped throughout the matrix. Due to the colloidosomes being a comparable size to the coacervate building blocks, the contact points for each coacervate remained high and thus the tissue had minimal 'gaps' or breakages. FITC- β-glucosidase colloidosomes were successfully trapped within the coacervate network, creating a hybrid-like tissue structure combining two different protocell models. This provided a more advanced tissue mimic as often, native tissues comprise a majority cell with minority cell communities interspersed, to supply complementary functions. Colloidosomes (0.5 µl) were added to the Au-PEG coated coacervate suspension (115 µl) before being centrifuged and made into a coacervate tissue. Large colloidosomes were trapped within the coacervate tissue and were well dispersed throughout the network (final number density, 300 $x10^3$ col. ml^{-1}). Again, a critical number density of colloidosomes (2500 x 10^3) was observed.

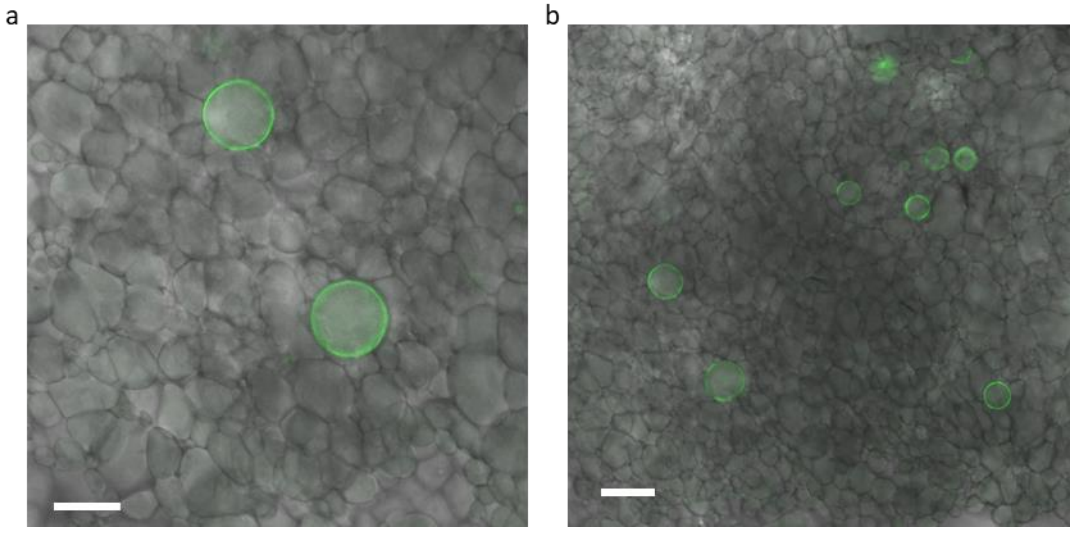

Figure 3.27. Large colloidosomes embedded within Au-PEG-coated coacervate network. *Zoomed in (**a**) and zoomed out (**b**) fluorescence and bright field merged image of FITC-* β *-glucosidase colloidosomes (*300 x10^3 col. ml^{-1}*) trapped within an untagged coacervate matrix. All scale bars, 50 µm.*

The process by which colloidosomes were encapsulated within the coacervate network, was simple and quick. The colloidosomes remained well dispersed throughout the network however, a high number density could not be achieved due to breakdown of the coacervate network as a consequence of reduced coacervate interface contact. The material showed promise as a good tissue mimic which importantly combined two different types of protocells.

3.2b.2 Patterning of colloidosome communities within prototissues

Spatial control was afforded by the modular assembly of tissue layers. Each tissue was sandwiched together by the addition of free-coacervates and an extra centrifugation step. Encapsulating different types of colloidosomes within each tissue and then sandwiching the tissues together could therefore lead to spatial segregation of colloidosome communities and patterning of colloidosomes within the coacervate network. A coacervate tissue harbouring FITC-β-glucosidase loaded colloidosomes was joined together with a coacervate tissue harbouring RITC-β-glucosidase loaded colloidosomes. This resulted in two segregated communities (red and green), separated by a 'no man's land' with no colloidosomes, arisen from the extra glue-purposed coacervates (figure 3.28a). Two coacervate tissues harbouring RITC-β-glucosidase loaded colloidosome communities dispersed throughout were separated by an FITC-labelled coacervate 'no man's land' (figure 3.28b). Finally, three coacervate tissues harbouring Dy405-HRP, RITC-GOx and FITC-GOx loaded colloidosomes respectively were

assembled into one tissue structure (figure 3.28c). These patterns demonstrated that small tissue building blocks could be used to afford more complex patterns and higher order positioning of colloidosomes within a prototissue-based matrix.

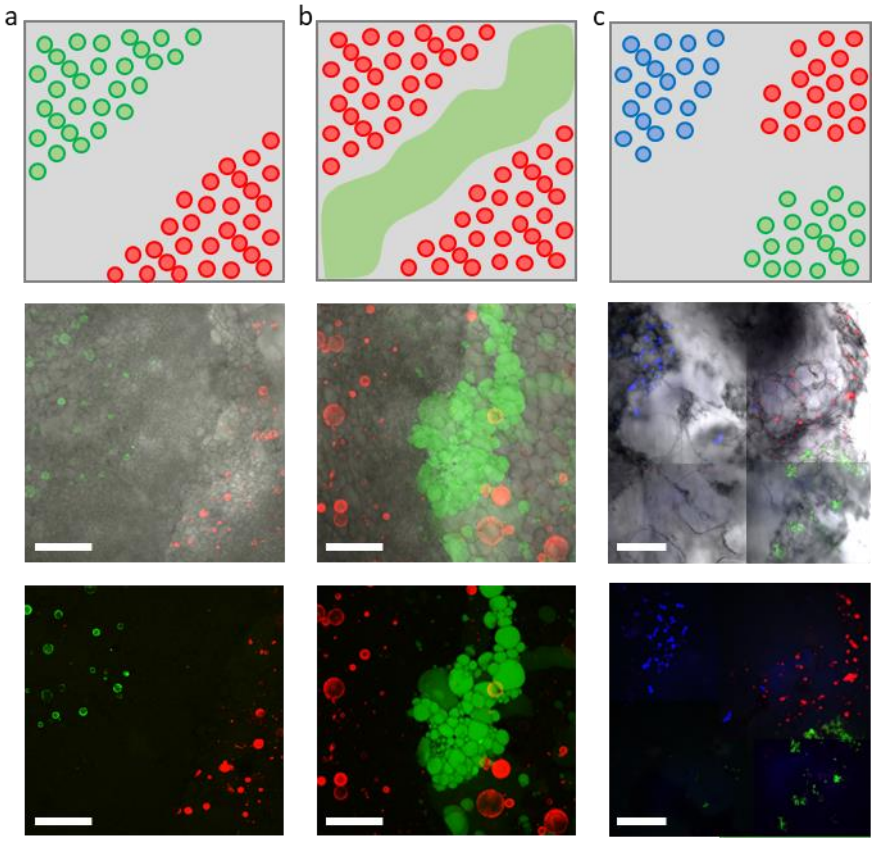

Figure 3.28. Spatial organisation of colloidosomes within a coacervate network. a*, Diagram, bright field merged with fluorescence image and fluorescence image of coacervate tissue made from a coacervate tissue with FITC- β-glucosidase loaded colloidosome, and a coacervate tissue with RITC- β-glucosidase loaded colloidosomes sandwiched together with non-labelled coacervates.* ***b****, Diagram, bright field merged with fluorescence image and fluorescence image of coacervate tissue made from a two coacervate tissues with RITC- β-glucosidase loaded colloidosomes sandwiched together with FITC-labelled coacervates. Scale bars, 300 µm.* ***c****, Diagram, bright field merged with fluorescence image and fluorescence image of coacervate tissue made from a coacervate tissue with FITC-GOx loaded colloidosomes, RITC-GOx loaded colloidosomes and Dy405-HRP loaded colloidosomes. Scale bars, 500 µm.*

In conclusion the coacervate tissue proved a suitable matrix for the trapping and spatial patterning of colloidosome protocell communities. Although micro-patterning was not as easy or well-controlled as in the microfluidic technique, encapsulating colloidosomes within a network that in itself could easily hold biological components was interesting and held huge potential for behavioural studies.

3.3 Conclusions and future works

The above experiments showed how colloidosomes could be successfully immobilised within matrix structures as a facile route to microscale organisation and patterning of protocell communities. Spatial organisation is ubiquitous across all levels of a living system, guiding important interactions between closely related cell communities. Organisation in a living system is often directed by an extracellular scaffold which provides both nutrients and structure to living cells. Both a hydrogel scaffold matrix, mimicking an ECM-like environment, and a protocell interface-connected matrix, mimicking a packed-cell tissue structure, provided excellent candidates for colloidosome trapping and strategic organisation of cell communities, to better mimic the true cellular grouping and anisotropic cell patterning within native tissues. The matrix-trapping of protocells, in comparison to biological molecules such as enzymes, enabled control over biological hotspots.

Capillary-made droplet-based microfluidics offered an excellent technique for the construction of spatially organised colloidosome communities within a spherical hydrogel scaffold. Alginate hydrogel droplets were prepared using a glass capillary co-flow microfluidic device and ionically crosslinked by $CaBr_2$ in an off-device decanol bath. These hydrogel spheres were then transferred to water to produce a monodisperse population of spherical platforms that could be analogous to an extremely basic ECM-scaffold building block.

Utilising a theta inner capillary within the co-flow microfluidic device design, and thus the injection of two alginate phases, led to the fabrication of spatially segregated 'Janus' patterned spheres. Changing the inner and outer phase velocity parameters of the microfluidic system enabled the size of hydrogel spheres to be programmed. When the outer phase velocity was increased, the size of the microspheres decreased and conversely when the inner phase velocities increased the size of the microspheres increased. Changing the outer velocity has a much greater effect (x 1.8) on the size of the microspheres compared to changing the inner velocity, due to fluid dynamics within the device. The effect of both velocities was lessened when microspheres were crosslinked and transferred to water, due to the sensitive swelling properties of the hydrogel. The size of the microfluidic orifice directly correlated to the size of the hydrogel sphere and thus some drawbacks from this microfluidic made-to-measure approach were that spheres made from different devices could not be exactly reproduced (even with the same velocity parameters) and that each device could only be used once due to blockages in the capillaries. Future work would therefore benefit from PDMS microfluidic devices that could be machine-made and capable of repeat experiments.

Small colloidosomes $d_A \sim 5$ µm were loaded with GOx and HRP enzymes. When studying the distribution of enzymes within the colloidosome interior it was observed that GOx aggregated at the membrane of silica nanoparticles, despite showing an overall negative charge. The effect of fluorescent labelling was ruled out by comparing the distribution of fluorescently labelled GOx and HRP enzymes. It was suggested that although having an overall negative charge, one side of GOx has a positive surface charge, which led to its attraction to the negative silica membrane.

Small colloidosomes provided an excellent candidate for immobilisation into alginate hydrogel microspheres to create a basic model of an ECM-scaffold laced with a community of cells. Even when colloidosomes were dispersed within the alginate inner phase, the ionic crosslinking process was successful and the hydrogel microspheres were transferred to water, maintaining a spherical shape and hydrogel properties. Furthermore, spatially segregated internal patterning was maintained, and the colloidosomes were locked in place by the crosslinking process, resulting in a Janus spatially segregated anisotropic patterning of colloidosome communities. Upon further inspection using fluorescence microscopy, colloidosomes were shown to preserve their structure throughout the microfluidic process and maintain a segregated pattern throughout the entire spherical structure.

Variations in the microfluidic device parameters and design led to more detailed and complex internal patterning within the hydrogel spheres, such that different Janus ratios and ternary spatially segregated colloidosome communities could be realised. Changes to the microfluidic device design, including addition of an extra outer phase inlet and collection capillary with a smaller diameter, led to the formation of Janus spatially segregated colloidosome communities within a rod-shaped hydrogel. These anisotropic rods were difficult to make due to crosslinking within the device which resulted in frequent blockages. However, with a PDMS device comprising a longer collection tube, crosslinking within the device could be extended over a longer time meaning that the $CaBr_2$ injection concentration could then be reduced resulting in a lower potential for blockages. Additionally, developing a crosslinking method which utilised internal $CaCl_2$ within the rods could reduce the chance of blockages at critical points within the device. Janus populations of colloidosomes were segregated along the long axis of the rods, however it could be more useful to create a Janus segregated distribution of protocells along the short axis as this would mimic the distribution of cells within early embryos, leading to a north-south pole division of colloidosome populations and potential for chemical gradients between the two. A collection of higher order colloidosome organisations has been achieved however, there is potential for a quaternary segregated community and ring-like patterns.

Despite alginate hydrogels providing a good matrix for micrometre-scaled colloidosome organisation to effectively model living cells within a native tissue ECM, using alginate as a basic building block was perhaps too simple as alginate only satisfies a few key elements within the ECM - the polymer matrix and water content. Thus, to increase the complexity of this alginate scaffold, alter the mechanical strength of the alginate scaffold or improve alginate scaffold-cell interactions, other alginate-binding components could be added. It is well known that hydrogels with bioactive ligands can instruct cell behaviour such as cell adhesion, differentiation, and angiogenesis, and so better mimic an ECM with interactive capabilities. The challenge is to design hydrogels with protoactive ligands that induce similar behaviours in protocells. These interactions between protocells and hydrogel could be physical or chemical. For example, donor and acceptor groups on the hydrogel and protocell membrane could lead to intermolecular adhesion of the two in specific locations. Chemical communication, as explored in chapter 4, could harness enzyme reactions within the protocells, inducing an effect on the hydrogel.

As a different way to improve the inherent biological properties of the matrix, the hydrogel scaffold was replaced with a protocell network. In this way, each protocellular component of the matrix could be engineered with biologically relevant properties. Au-PEG-caged coacervates are a good building block for the fabrication of a protocell network, held together by interacting membranes. Colloidosomes (below a critical concentration) were successfully incorporated into this prototissue to produce a well-dispersed immobilised population within a well-maintained and strongly bound coacervate network. Spatial organisation of protocells within the network was achieved through modular tissue construction, affixed by additional coacervates. This resulted in segregated colloidosome communities linked together via an extended coacervate 'no-man's-land'. The main disadvantage of this model involved the centrifugation tissue-making step, as this resulted in small oval pellets that could only be joined together by centrifuging with additional coacervates. As a result, the modular assembly of tissue pellets was not very precise, segregated communities were not well-controlled and tissue-tissue adhesion was relatively weak (especially when colloidosomes were incorporated). Future work therefore requires a technique whereby these tissues could be formed using a more controlled method and not by centrifuging to offer considerably greater control over colloidosome patterning.

In general, both the alginate scaffold matrix and the Au-PEG-caged coacervate network provide a good platform for the encapsulation, spatial organisation, and segregation of colloidosomes. The hydrogel matrix provides a decent replica of the ECMs physical scaffold and water content, whereas the protocell-based network provides a better mimic of tissues comprising densely packed cells (e.g.

epithelial) with inherent biological properties. In the future, a combination of both these prototissue designs would lead to a more accurate and functional tissue model.

CHAPTER 4

COMMUNICATION AND COLLECTIVE BEHAVIOUR OF COLLOIDOSOMES WITHIN SPATIALLY ORGANISED, MATRIX-BASED PLATFORMS

The aim of this chapter is to mimic ordered cell-cell and cell-environment interactions through immobilised spatial patterning of colloidosomes, encapsulated in both a hydrogel matrix-based and a coacervate network-based platform. Communication pathways are developed firstly within Janus-segregated colloidosome communities trapped in hydrogel microspheres, then within Janus-segregated colloidosome communities encapsulated in rod-shaped hydrogel microparticles and finally within ternary patterned hydrogel microspheres. For the Janus-segregated microsphere system, improved communication compared with the analogous mixed colloidosome population, is explored. Spatial segregation of colloidosomes is exploited, alongside ionic/covalent crosslinking transitions, to obtain enzyme-mediated morphological behaviour through programmed disassembly of a selected hemisphere and expulsion of colloidosomes. Communication pathways are also explored within colloidosome populations immobilised inside of a coacervate network. Communicating colloidosomes are thus utilised as chemical reaction hotspots and employed as signalling beacons within an interconnected prototissue.

4.1 Background

Higher-level living systems rely on a non-linear network of interacting living cells. To mimic these interactions and to study more sophisticated cell-like behaviours, multi protocellular systems and protocell communications are explored. This chapter investigates how colloidosome signalling throughout a matrix can produce emergent and exciting biological functions, mimicking how cell-cell and cell-environment signalling within tissue systems produces morphological, differential, and higher-order responses. Order within closely related cell communities also impacts these living cell interactions. The chapter specifically explores how spatially segregated colloidosome communities can afford localised control over signalling pathways, therein demonstrating how patterned protocell populations can improve communication rates and develop sophisticated collective behaviours and ordered responses, especially connected with their environment.

4.1.1 Enzyme-mediated signalling

This chapter focuses on protocell chemical signalling, which is typically achieved through enzyme cascades between enzyme-loaded protocell (colloidosome) populations. Enzymes are globular proteins made from a 3D folded structure of polypeptide chains. The 3D structure comprises a backbone of folded proteins and an area called the active site. The active site binds a specific substrate allowing it to undergo transformation into a product or products (scheme 4.1), and the folded proteins provide stabilisation for the active site, nurturing the correct environment for substrate interaction. In general, enzymes are biological catalysts used to increase the rate of biochemical reactions. The mechanism for this enzyme catalytic process, wherein a specific substrate fits exactly into an enzyme active site, was hypothesised by Fisher in 1894 and coined the 'lock and key' mechanism.[238] Unfortunately the 'lock and key' analogy is now considered to be too simplistic, with current hypotheses suggesting that enzyme active sites can further mould to accommodate a substrate and thus are not limited to an exact shape. Importantly, enzymes can be used in sequence (enzyme cascade) whereby the product of one enzymatic reaction is used as a substrate in another reaction. The molecule associated with both enzymes is recognised as a signalling molecule.[239]

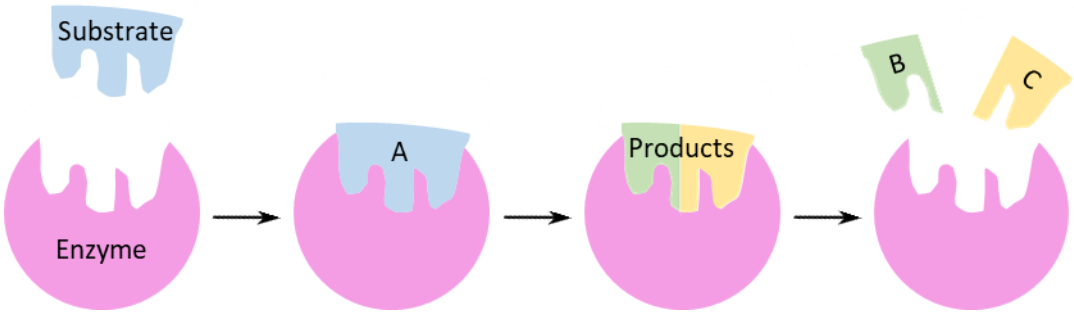

Scheme 4.1. Enzyme lock and key mechanism for substrate A into products B + C. *The substrate (blue) fits into the active site of the enzyme (pink) and becomes an enzyme/substrate complex. The substrate is converted to products (green, yellow) and then released from the active site.*

Within this chapter, predominantly glucose oxidase (GOx), urease (URS) and horseradish peroxidase (HRP) enzymes have been used to catalyse simple chemical transformations. These enzymes have been loaded into colloidosomes to enable them to be localised within matrix-based scaffolds and to mimic biological functions within living cells. Typically, enzyme cascades have been exploited to realise communication between different colloidosome populations and to initiate emergent collective processes.[29] GOx is a glycoprotein consisting of two identical 80 kDa subunits, each with a flavin adenine dinucleotide (FAD) coenzyme which acts as an electron carrier during the catalytic oxidation of d-glucose to d-glucono-1,5-lactone (GDL) and hydrogen peroxide (H_2O_2). D-glucose acts as the electron donating reductant, which requires another molecule (usually oxygen) as the electron accepting oxidant.[240,241] URS is a nickel-containing metalloenzyme that typically catalyses the hydrolysis of urea to ammonia and carbon dioxide. Two nickel ions are thought to be bridged by amino acid residues and a hydroxide group, creating a suitable environment for urea to be hydrolysed.[242] HRP is a globular metalloenzyme comprising three key elements, the heavily glycosylated alpha helixes, the heme group, and the calcium ions positioned in the distil and proximal region of the enzyme. In its resting state, HRP reacts with H_2O_2 to give an intermediate (HRP(I)) consisting of an oxyferryl iron (Fe^{4+}=O) and a porphyrin π-cation radical. This intermediate is subsequently reduced back to the HRP resting state by the two reducing substrate molecules.[243]

$$HRP + H_2O_2 \rightarrow HRP(I) + H_2O \quad \textbf{1}$$

$$HRP(I) + AH_2 \rightarrow HRP(II) + AH^* \quad \textbf{2}$$

$$HRP(II) + AH_2 \rightarrow HRP + AH^* + H_2O \quad \textbf{3}$$

Where HRP is in resting state, HRP (I) is an intermediate which consists of an oxyferryl iron (Fe^{4+}=O) and a porphyrin π-cation radical, HRP (II) is another intermediate, AH_2 and AH^* are the reducing agent and oxidised radical respectively.[244]

As discussed in the general introduction (section 1.2), a plethora of protocell models have been shown to communicate with each other through various biochemical signalling pathways, and especially through enzyme cascade reactions. Such communication networks have been categorised by two common modes: through-space communication (similar to paracrine signalling) and contact-dependent communication (similar to juxtracrine signalling). Within randomly arranged and spatially organised populations of protocells, both through-space and contact-dependent communication pathways have been exploited for cell-mimicking signalling, life-like behaviours, and bio-inspired functions.[145,11] The remainder of this background section will outline the current research concerning protocell communication and collective behaviour in both randomly arranged and spatially organised protocell populations and via through-space and contact-dependent pathways. This research develops protocell chemistries beyond membrane design and internal compartment composition, towards systems interactions and collective processes.

4.1.2 Communication between protocells – randomly arranged

Within randomly arranged populations of protocells, GOx/HRP enzyme cascades are often used to demonstrate chemical communication pathways between binary communities. This enzyme cascade typically involves GOx-mediated conversion of d-glucose to GDL and H_2O_2 in protocell population 1, followed by H_2O_2 signalling which is then used to assist HRP-mediated conversion of a non-fluorescent molecule to a fluorescence output in protocell population 2. This GOx/HRP enzyme cascade has been demonstrated in randomly arranged protocell populations via both through-space and contact-dependent pathways. For example, between randomly arranged biopolymer membrane coated coacervates[78], interconnected proteinosomes[90] and nested GUV protoorganelles[245] (figure 4.1). As discussed in the introduction (section 1.2.3), enzyme cascades with increased complexity (based on the GOx/HRP system) have also been exploited within several randomly arranged through-

space protocell systems. For example, Tang *et al.* exploited gene-expression within liposomes to produce d-glucose, which was released through a lipid membrane gate and received by HRP-containing proteinosomes, initiating the conversion of Amplex red to fluorescent resorufin.[72] Furthermore, Sun *et al.* showed that GOx-mediated H_2O_2 production in a GOx-containing silica colloidosome could be used to induce polymer wall formation in a coexisting population of FeM clay colloidosomes. In turn, this generated self-regulated membrane-gated alkaline phosphatase (ALP) activity.[246] Beyond this, communication pathways in randomly arranged through-space networks have been explored through in vitro gene expression and DNA signalling. Randomly arranged contact-dependent communication has also been developed in systems beyond the GOx/HRP cascade, such as for the killing of cancer cells by melittin-functionalised GOx-containing GUVs[136] and the self-suicide of bacteria by hydrogel-loaded proteinosomes.[247] Randomly arranged protocell communication is relatively simple to design, however these systems are limited to isotropic conditions and are consequently an over-simplified mimic for many higher order living processes.

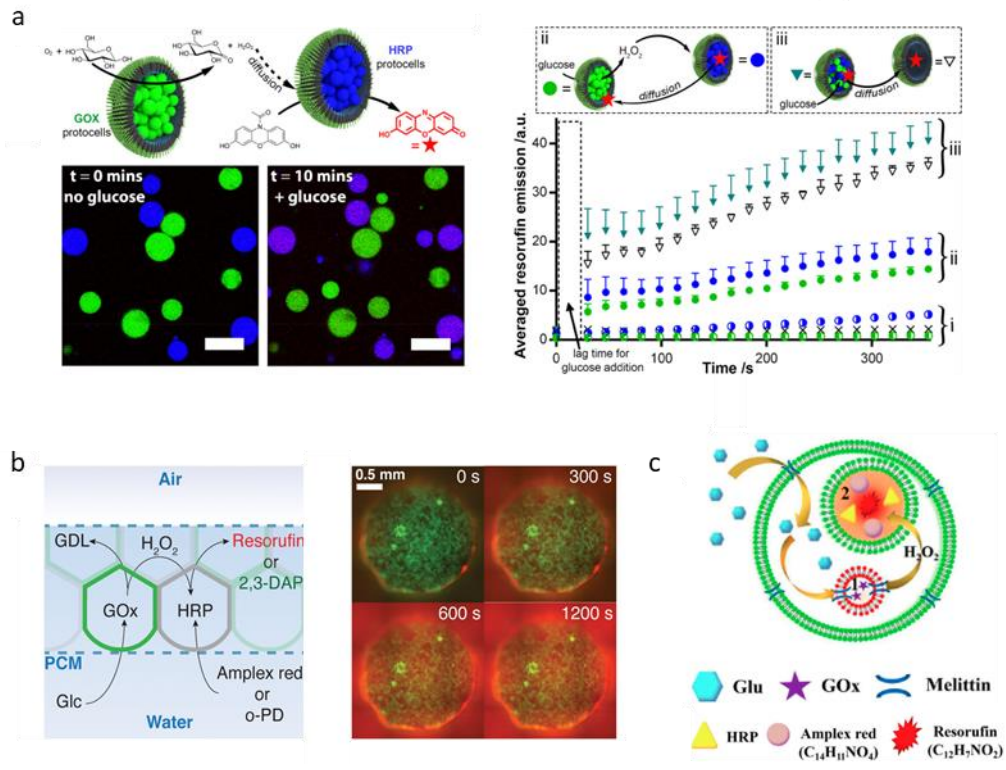

***Figure 4.1. Literature examples of GOx/HRP communication pathways between randomly arranged protocells**. **a**, GOx/HRP cascade between biopolymer membrane-coated coacervates. Taken unchanged from paper by A. Mason et al. under CC-BY-NC-ND.[78] **b**, GOx/HRP cascade between interconnected proteinosomes. Reproduced from paper by A. Galanti et al. under CC BY 4.0.[90] **c**, Communication between two protoorganelles nested within a GUV. Reprinted (adapted) with permission from Li et al. Copyright 2023 American Chemical Society.*[245]

4.1.3 Communication between protocells – spatially organised

Evidence of spatial organisation is observed throughout all levels of a living system.[248] Organisation is often a consequence of, or a route to control, cell-cell and cell-environment interactions. To understand these living interactions, it is therefore important to factor organisation into protocell communication design. Spatially organised protocell communication has been researched to some degree, especially following an advance in protocell organisation techniques through passive construction methods such as magnetophoresis, acoustic trapping and microfluidics. Unfortunately, these methods can be tricky to engineer, thus in recent publications signalling complexity is often lacking, and simplistic through-space enzymatic pathways dominate (figure 4.2). For example, the rudimentary through-space GOx/HRP enzyme cascade has been exploited in binary communities of magnetically arranged GOx- and HRP- loaded GUVs, which were patterned into various spatially segregated arrangements and used to display H_2O_2 signalling to result in an Amplex red to resorufin output.[89] Similarly, acoustically trapped coacervates demonstrated communication through a simple GOx/HRP mediated route.[79] Enzyme cascades with increased complexity (based of the GOx/HRP system) have also been investigated within spatially organised arrangements as shown by the recent work of Han *et al.* who repurposed the magnetic-GUV system to exploit organisational complexity through a ternary communication pathway within a three-component system. GOx-loaded GUVs converted d-glucose to GDL, releasing H_2O_2 into L-arginine-containing GUVs. This released NO into living C6 glioma cells wherein it interacted with the NO fluorescent probe of DAF-FM dye within the cells, to generate a highly fluorescent DAF-T. In acoustic devices, a slightly more advanced GOx/red blood cell (RBC) communication network has been developed in protocell-living cell communities.[137]

Despite through-space communication pathways being more commonly utilised within organised protocell systems, some contact-dependent communication pathways have also been established (figure 4.2d). These methods are particularly challenging due to combining new interconnecting protocell chemistries with information processing. Importantly, contact-dependent protocell communities differ from closely packed communities due to maintained connection in the absence of an external force, often relying on an active chemical change at the protocell interface. For example, Booth *et al.* have designed the 3D printing of lipid droplets to form an interconnected droplet bilayer interface. LA-αHL DNA loaded droplets were printed into a programmed tissue arrangement, patterned by droplets containing no DNA. Upon illumination, αHL protein was expressed, enabling an ionic current through the printed patterned droplets.[249]

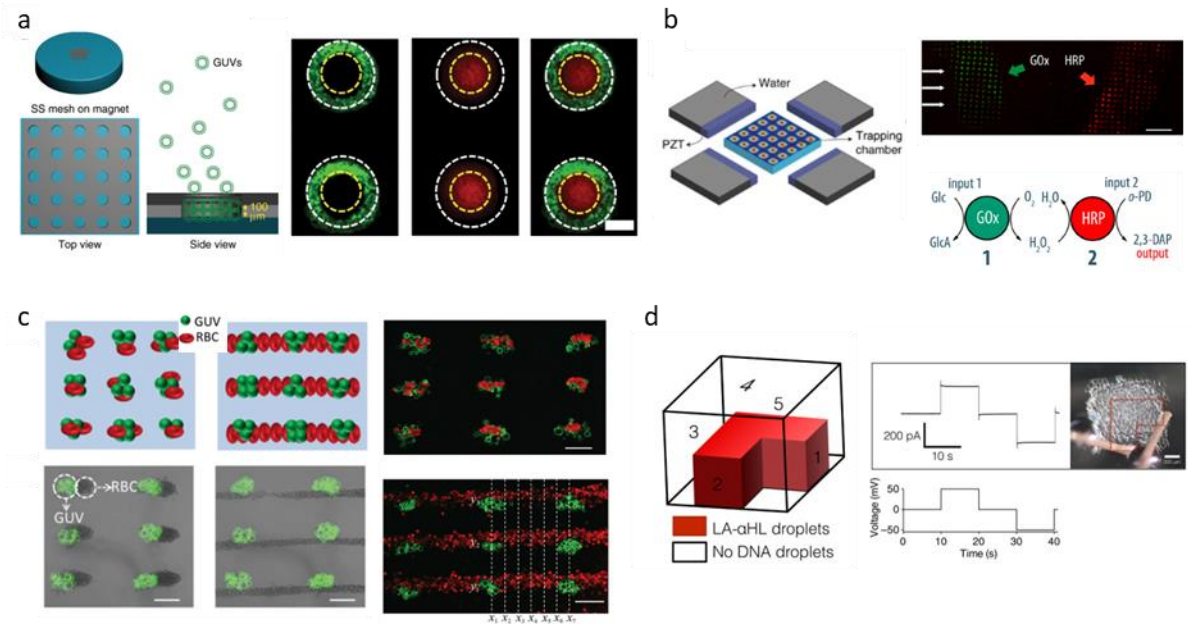

Figure 4.2. Literature examples of communication pathways between spatially organised protocells. ***a****, Use of the magneto-Archimedes effect to organise GUVs in patterned arrays. Demonstration of the GOx/HRP cascade within such patterned communities, observing an Amplex red to resorufin end point. Taken from paper by Q. Li et al. under CC BY 4.0.*[89] ***b****, Acoustic trapping to organise segregated communities of coacervates. The GOx/HRP enzyme cascade with an o-PD to 2,3-DAP output. Reproduced with permission from L. Tian et al.*[79] ***c****, Acoustic trapping to organise GUVs and red blood cells and communication via H_2O_2 with an Amplex red to resorufin output. Reproduced with permission from X. Wang et al.*[137] ***d****, lipid droplets connected via a bilayer, patterned so that an electrical current can flow through the LA-αHL DNA loaded protocells. Taken from paper by M. Booth et al. under CC BY-NC 4.0.*[249]

4.1.4 Collective behaviour within protocell communities – randomly arranged

As discussed, a variety of through-space and contact-dependent signalling pathways within a catalogue of spatially organised and randomly arranged protocell systems have been developed. However, communication is just the baseline as added complexity, through emergent and collective functions, better mimics life-like behaviours and tissue-like properties. Harnessing control over such collective and emergent behaviours, also offers huge potential for biomimetic systems engineering, medical applications, and sensing systems. Collective processes can be categorised by their initiating signal strategy: through-space or contact-dependent.

Through-space communication between enzymatically linked protocell populations has been used to initiate signal amplification, differentiation and adaptive prototissue formation.[250] Despite through-

space communication being adaptable, it is often used in conjunction with a contact-dependent system, to develop more sophisticated collective processes. For example, in the configuration/ reconfiguration of protocell populations based on pH changes, presented by Martin *et al.* This work used URS containing proteinosomes to increase the pH of a solution and drive the assembly of a fatty acid micelle coacervate from HRP-containing fatty acid vesicles around a proteinosome. Upon the addition of d-glucose, along with GOx, a decrease in the pH of the system resulted in disassembly of the coacervate and a reconfiguration of the fatty acid vesicles.[251] Through-space and contact-dependent collective behaviour is also demonstrated by the 'tit-for-tat' system established by Qiao *et al.* (figure 4.3a). This system comprised a GOx-loaded proteinosome (sensitive to protease), a protease-k loaded coacervate (sensitive to pH) and a proteinosome-adhered coacervate (insensitive to pH). When d-glucose was added to the system, the GOx-containing proteinosome released protons to disassemble the protease-k loaded coacervate. The protease-k was subsequently released into the adhered coacervates and then into the proteinosome through a contact dependent route, wherein the protease resulted in the proteinosomes disassembly and 'killing'.[11]

Contact-dependent communications have led to higher order collective processes in systems based on large tissue-like collections of randomly arranged protocells. For example, prototissues fabricated by proteinosome-proteinosome adhesion have displayed thermoresponsive and enzymatically modulated reversible contractions (figure 4.3b). Collective contractive behaviour was mediated by heating/cooling the prototissue and thus, due to the thermoresponsive BSA/PNIPAM nano conjugated membrane, the entire prototissue system contracted and expanded. AGL and GOx containing proteinosomes were exploited to aid hydrogelation within the tissue and thus to enzymatically modulate dampening of the system.[82] Contact-dependent communication within small randomly arranged protocell batches has led to the development of phagocytosis behaviour in colloidosomes and magnetic Pickering emulsion droplets (MPEs) comprising free fatty acid stabilised apertures. Upon the addition of oleic acid, the membrane was destabilised due to increased fluidity of the magnetic membrane such that an aperture appeared. Manipulation of the droplets into direct contact with colloidosomes, along with magnetically induced redistribution of iron oxide particles near the attached colloidosomes, gave rise to colloidosome engulfment.[12]

Nested populations of protocells also communicate via contact-dependent pathways, leading to various collective processes. For example, enzyme-loaded silica colloidosomes have been engulfed within MPE droplets to realise several higher order collective behaviours. Firstly, catalase containing colloidosomes have initiated buoyancy of such MPEs. Secondly, lipase containing colloidosomes have triggered their own artificial phagocytosis by converting triolein to free oleic acid. Thirdly, alkaline phosphatase containing colloidosomes have initiated the nucleation and growth of a supramolecular

hydrogel network inside amino acid containing MPEs.[83] Ru_4PCVs have also been exploited for the collective production of dioxygen to induce buoyancy within a microcapsule. Tens of thousands of Ru_4PCVs were encapsulated within individual semipermeable aminoclay/DNA microcapsules and, in the presence of H_2O_2, these Ru_4PCV protoorganelles produced a single gas bubble causing the capsules to become buoyant and move in a vertical motion.[135] With respect to enzyme powered motility, the buoyancy of catalase-containing organoclay/DNA microcapsules was exploited for the collective floatation of a dialysis bag. About 225 protocells were loaded into a dialysis bag and upon the addition of H_2O_2, the catalase-containing capsules produced oxygen bubbles which grew into a large oxygen bubble within each protocell, resulting in a vertical flotation force on the bag (figure 4.3c).[7] In this case, each individual protocell underwent an enzyme reaction leading to synergistic flotation behaviour.

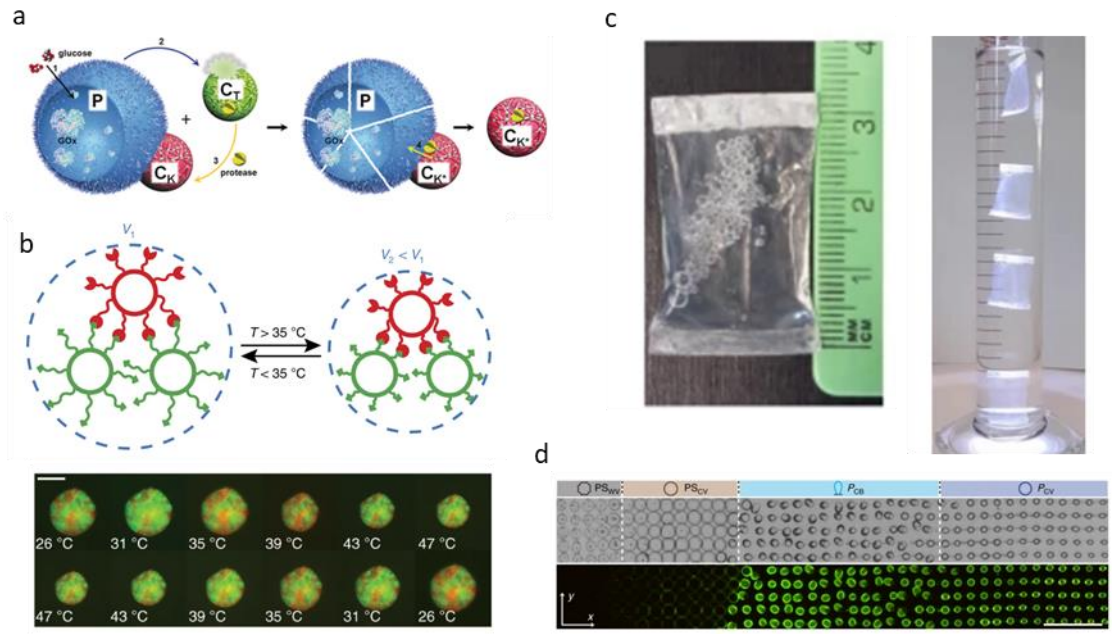

***Figure 4.3. Examples of collective behaviour in randomly arranged and spatially organised protocell communities. a**, 'Tit-for-tat killing mechanism between proteinosome and two types of coacervate.*[11] ***b**, Collective contractile behaviour in alkyne (green) and azide (red) functionalised proteinosome prototissue.*[82] ***c**, Enzyme powered motility of catalase-containing organoclay/DNA microcapsules used to float a dialysis bag.*[7] ***d**, Differentiated protocells viewed after intersection of an opposing reaction-diffusion gradient to give four spatially distinct populations. All images reproduced with permissions from referenced papers.*

4.1.5 Collective behaviour within protocell communities – spatially organised

To date, there is minimal research concerning collective processes within spatially organised protocell systems. However, one key example shows the morphological differentiation of acoustically trapped protocells from a reaction-diffusion gradient of artificial morphogens (figure 4.3d). The positioning of protocells by acoustic trapping means that location-dependent exposure to the artificial morphogen gradient reconfigures droplets into different membrane-bound vesicles, leading to segregated populations with differentiated enzyme activities.[84] Developing communication between spatially organised protocells is challenging due to the integration of patterning techniques with sophisticated signalling pathways. However, developing collective behaviours between spatially organised protocells is substantially more challenging, as signalling pathways need to be cleverly designed in order to exhibit bio-inspired collective functions. Thus, these systems must combine new methods of self-assembly and organisation with innovative collective behaviours, especially at the microscale which better mimics real cell behaviours. Developing ordered collective processes in protocell systems is an important step towards mimicking and understanding tissue-like behaviour and more complexed living processes.

4.1.6 Collective behaviour between protocells and environment

Cell-environment interactions and resulting collective processes are key towards the emergence of living behaviours. However, there are minimal examples in literature due to challenges in combining new materials chemistries and closely linked protocell signalling. One key example is the signal induced movement of helical protocell-embedded hydrogel structures.[13] Particularly in native tissues, the ECM forms an important communicative medium for cell interactions and thus it is important to study the interface between cells and their local environment.

4.1.7 Background conclusion

Enzyme-mediated signalling between protocells is an effective way to mimic juxtacrine and paracrine signalling in living cells. This background has highlighted how enzymes are used to mediate signalling, focusing particularly on GOx, URS and HRP. A GOx/HRP enzyme cascade has been particularly instrumental between randomly arranged protocell networks and has led to more sophisticated signalling in both through-space and contact-dependent systems. This cascade has also been developed in spatially organised protocell systems however, establishing these networks is more challenging due to the integration of patterning techniques with protocell information exchange. Randomly arranged through-space and contact-dependent signalling has led to collective protocell processes that mimic certain biological behaviours. Again, establishing collective behaviours in spatially organised systems remains challenging as new methods of organisation must be combined with innovative collective processes.

This chapter therefore investigates communication and collective processes between organised protocell populations. As a versatile method for organising protocells, matrix-based systems are utilised and for easier engineering, through space communication pathways are employed.

4.2 Results and Discussion

Given the evidence of order within living systems combined with the aforementioned lack of research regarding ordered protocell systems, the aim of this chapter was to explore and develop protocellular communication and collective behaviours within spatially organised, matrix-based colloidosome communities. Firstly, a simplistic GOx/HRP communication pathway was established within a spatially segregated Janus population of colloidosomes, trapped within a hydrogel matrix-based system. Similar GOx/HRP communication pathways were established within more complex spatially organised colloidosome communities, developing communication throughout rod-shaped hydrogel matrices and ternary compartment hydrogel microspheres. Collective behaviour within spatially segregated colloidosome communities was developed to selectively disassemble one hydrogel domain, releasing colloidosome-alginate debris into the environment. Secondly, protocell signalling within a prototissue-based matrix was developed whereby colloidosomes, embedded within a coacervate-tissue matrix, functioned as hotspots for a chemical signal transmission.

4.2.1 Communication within hydrogel-based matrices

The site-specific isolation of two colloidosome communities was exploited to drive a localised catalytic cascade within Janus hydrogel microsphere platforms. RITC-GOx (30 mg ml^{-1}) loaded colloidosomes and Dy405-HRP (30 mg ml^{-1}) loaded colloidosomes were encapsulated within a hydrogel-based micro spherical scaffold. The two colloidosome communities were spatially segregated at a 1 : 1 number ratio within the microsphere using theta-septum co-flow droplet microfluidics, as discussed in section 3.2a.2. Microfluidics was used as an appropriate technique to afford precision over the hydrogel platform size and the distribution of each colloidosome community within the matrix-based network. Hydrogel pore size was controlled by $CaBr_2$ crosslinking concentrations off-device and before hydrogel transferal to water. Typically, a $CaBr_2$ (1 mM) crosslinking solution was used. Applying careful control over such parameters, chemical communication between the two spatially separated colloidosome communities was achieved throughout hydrogel microsphere scaffolds with a $d_A \approx$ 600-800 µm.

The two-step cascade reaction was initiated by the addition of d-glucose (Glu) and o-phenylenediamine (o-PD) into the surrounding environment. Both molecules were able to diffuse into the hydrogel microsphere matrix and further into the semi-permeable colloidosomes. Within the GOx-loaded colloidosome community, GOx catalysed the conversion of d-glucose to GDL and H_2O_2. H_2O_2 subsequently diffused out of the GOx colloidosomes, through the hydrogel sphere and external

medium, into the HRP containing colloidosomes thereby initiating step two of the enzyme cascade and providing a chemical signal between the two localised colloidosome communities. Within the HRP-loaded colloidosomes, o-PD was converted to 2,3-diaminophenazine (2,3-DAP) by the HRP catalyst and using the H_2O_2 signalling molecule. This conversion was confirmed by the emergence of green fluorescence, specifically within the hydrogel core and firstly within the HRP hemisphere of the Janus hydrogel microsphere.

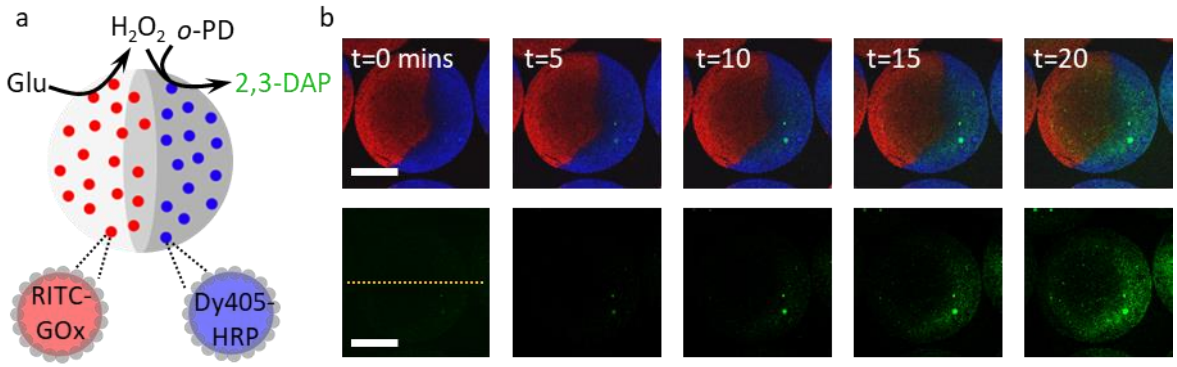

***Figure 4.4. Binary communication between spatially segregated 'Janus' colloidosome communities within an alginate hydrogel microsphere. a**, Diagram showing the GOx/HRP enzyme cascade in each segregated colloidosome hemisphere within an alginate hydrogel microsphere. **b**, Single crosslinked hydrogel microsphere comprising a segregated binary population of colloidosomes containing RITC-labelled GOx (red) and Dy405-labelled HRP (blue). Simultaneous addition of glucose (0.84 M) and o-PD (17 mM) at t = 0 min gives rise to the progressive output of 2,3-DAP (green fluorescence) in the HRP-containing hemisphere over 20 min. Red/blue/green fluorescence overlays (top row); green fluorescence filtered image (bottom row). Samples prepared at a 1 : 1 number ratio; V_{in} = 0.2; V_{out} = 20 ml h^{-1}, [alginate] = 3.5 wt.%, [$CaBr_2$] = 3 mM; scale bar, 400 µm.*

Specifically, 20 spheres were transferred to a microscope slide well, whereby a d-glucose/o-PD mix (total 35 µl, 0.84 M/17 mM) was added to the outside of the hydrogel spheres. CLSM images were taken every 5 min (figure 4.4b). The images revealed spatial segregation between the binary colloidosome communities (red and blue), which were localised by the crosslinked matrix and thus remained stationary throughout the duration of the cascade reaction. Green fluorescence emerged from the hydrogel microsphere indicating the presence of 2,3-DAP, and the successful signalling of H_2O_2 to reach the end point of the cascade reaction. The green fluorescence emerged, initially, from the same location as the blue hemisphere, indicating that the HRP colloidosomes were converting o-PD to 2,3-DAP before the o-PD diffused into the rest of the hydrogel. Chemical communication between two spatially segregated protocell communities, confined within a discrete hydrogel-based matrix microcompartment, was thus demonstrated. The ability to transport chemical signals through

an ECM framework is an important feature of native tissues and thus mimicking such signalling in matrix systems is an important step for developing our understanding of multicellular tissues.

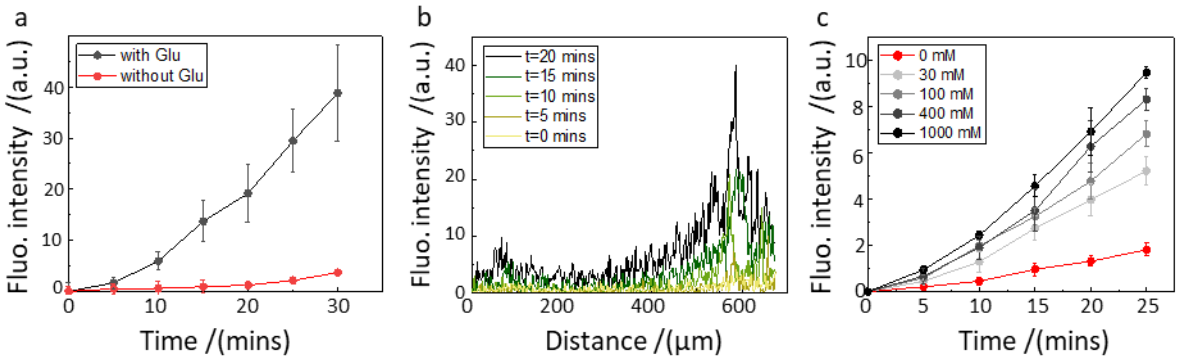

Figure 4.5. Production of 2,3-DAP emerging from the GOx/HRP enzyme cascade. a*, Overall increase in green fluorescence from the whole microsphere.* ***b****, Increase in green fluorescence across the yellow dotted line in figure 4.4, taken at 5 min intervals.* ***c****, Overall increase in green fluorescence from the whole microsphere with increasing concentration of d-glucose. Error bars calculated from the standard deviation over several microsphere samples. Error bars represent standard deviation (n=3).*

As the enzyme cascade proceeded green-fluorescence intensity steadily increased, indicating the production of 2,3-DAP. Figure 4.5a shows that the increase in green fluorescence across the whole hydrogel microsphere is significant compared to the negligible green fluorescence observed in the absence of d-glucose (the initiator for the cascade). The spatially localised output from this cascade was observed by the emergence of green fluorescence specifically in one domain of the sphere as seen in CLSM images and by fluorescence intensity profiles (figure 4.5b). This is expected as HRP (within one colloidosome population) along with H_2O_2, catalyses conversion of o-PD to 2,3-DAP. During the enzyme cascade, fluorescence output increases by a greater extent at 400-700 µm along the x-axis drawn in figure 4.4b (yellow dotted line) than at 0-400 µm. These results demonstrate spatially controlled communication between specified areas within a finite protocell platform, meaning that regions of activity can be cleverly appointed. The concentration of input chemical also affords control over the system. Increasing the concentration of d-glucose, increased the enzyme kinetics within Janus microspheres. Initially, an increase from 0 to 30 mM resulted in a 2.9 x increase in fluorescence output over 25 min. However, an increase from 30 to 1000 mM only resulted in a 1.8 x increase, attributed to the GOx enzyme becoming saturated.

Both GOx and HRP loaded colloidosomes were crucial for the enzyme cascade to occur and thus for colloidosome communication to be achieved. Control experiments using segregated communities of colloidosomes prepared without either GOx or HRP payloads showed minimal 2,3-DAP production in

the presence of d-glucose and o-PD (figure 4.6). Fluorescently labelled BSA was loaded into colloidosomes and used to replace either GOx or HRP enzyme within a population of colloidosomes.

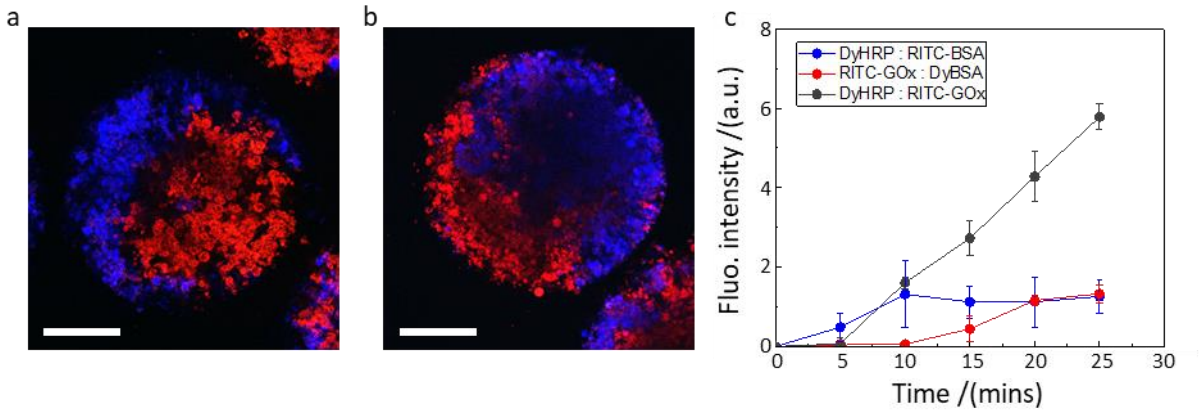

Figure 4.6. Control experiments using segregated colloidosome populations prepared with BSA in place of either GOx or HRP payloads. a*, Segregated population of RITC-labelled BSA-loaded (red) and Dy405-labelled HRP-loaded (blue) colloidosomes in Ca^{2+}-crosslinked hydrogel microsphere.* ***b****, Segregated population of RITC-labelled GOx-loaded (red) and Dy405-labelled BSA-loaded (blue) colloidosomes in crosslinked hydrogel microsphere. Samples (**a**) and (**b**) prepared at a 1 : 1 ratio V_{in} = 0.15 ml h^{-1}, V_{out} = 25 ml h^{-1}, [alginate] = 3.5 wt.%, [$CaBr_2$] = 3 mM; scale bars, 200 µm.* ***c****, Plot showing time-dependent increases in mean green fluorescence (2,3-DAP production) in batches of hydrogel microspheres comprising segregated Janus populations of BSA- and HRP-loaded colloidosomes (**a**, blue line), BSA- and GOx-loaded colloidosomes (**b**, red line) or GOx- and HRP-loaded colloidosomes (black line). Simultaneous addition of glucose (0.84 M) and o-PD (17 mM) at t = 0, followed by continued monitoring of the progressive output of 2,3-DAP (green fluorescence) over 25 min. Error bars represent standard deviation (n=3).*

Changes in the GOx : HRP-colloidosome number densities (*N*) in each hemisphere from 1 : 1 to 3 : 1 had negligible influence on the rate of fluorescence output over 25 min, while an excess of HRP-containing colloidosomes (*N* = 1 : 3) produced a marginal increase in the initial rate of 2,3-DAP production (figure 4.7). This was consistent with a downstream rate-limiting step under the conditions employed.

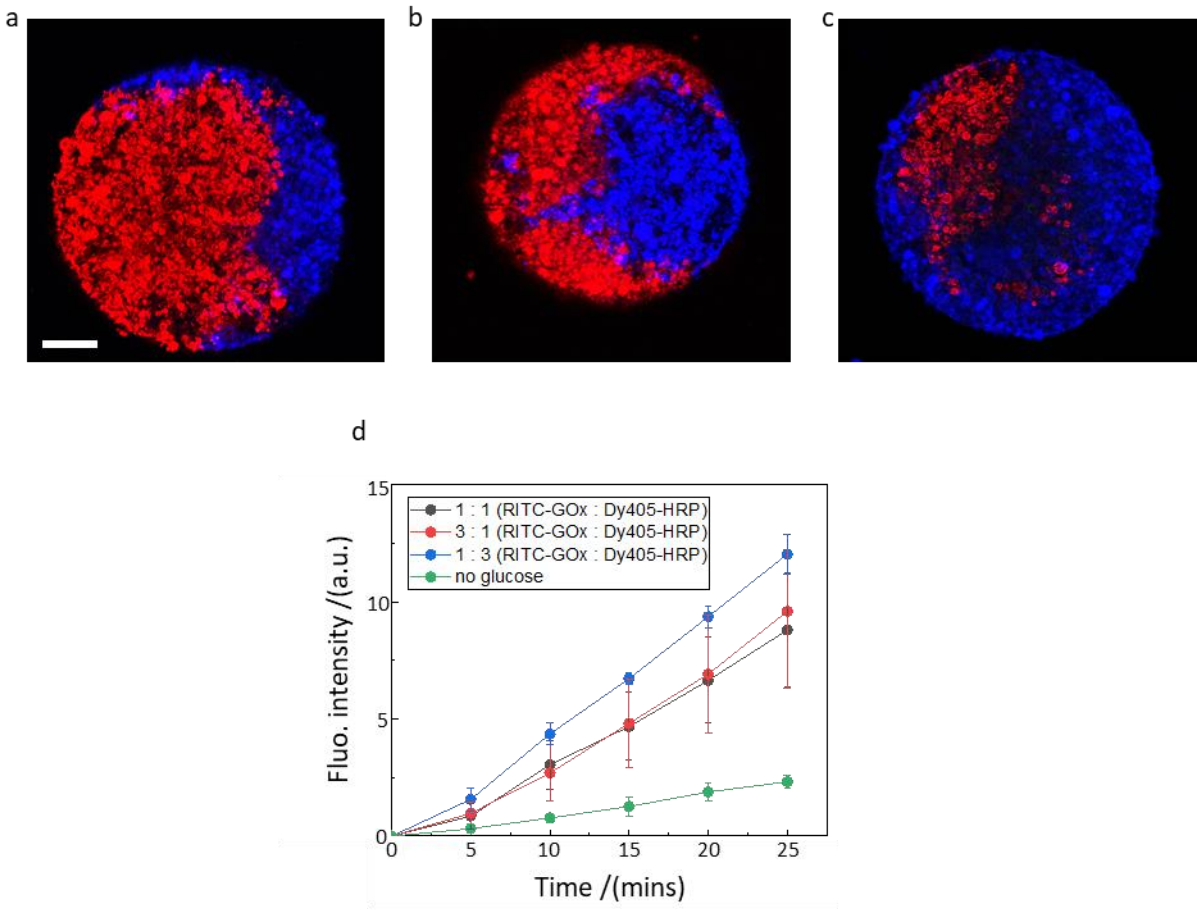

Figure 4.7. GOx/HRP enzyme cascade kinetics in crosslinked hydrogel microspheres containing segregated colloidosome populations with variable population number ratios. *(**a-c**) CLSM images of Ca^{2+}-crosslinked hydrogel microspheres, [alginate] = 3.5 wt%, [$CaBr_2$] = 3 mM, showing segregated populations of immobilised RITC-GOx- (x, red) and Dy405-labelled HRP-loaded (y, blue) colloidosomes prepared with different protocell number ratios (x : y) by changing the inner phase velocities ($V_{in,x}$, $V_{in,y}$) at V_{out} =25 ml h^{-1}; x : y = 3 : 1 (**a**), x : y = 1 : 1 (**b**), and 1 : 3 (**c**) corresponding to $V_{in,x}$: $V_{in,y}$ ratios of 5 : 2 (0.25 and 0.1 ml h^{-1}), 1 : 1 (0.175 and 0.175 ml h^{-1}) and 2 : 5 (0.1 and 0.25 ml h^{-1}). **d**, Plots showing time-dependent increases in mean green fluorescence (2,3-DAP production) in batches of hydrogel microspheres comprising segregated populations of GOx- and HRP-loaded colloidosomes in number ratios x : y = 3 : 1 (**a**, red line), x : y = 1 : 1 (**b**, black line), and 1 : 3 (**c**, blue line). Simultaneous addition of glucose (0.84 M) and o-PD (17 mM) at t = 0 was followed by continued monitoring of the progressive output of 2,3-DAP (green fluorescence) over 25 min. Addition of no glucose (green line). Scale bar, 200 µm. Error bars represent standard deviation, n=3.*

The spatial segregation of colloidosome populations greatly improved the activity of the GOx/HRP cascade. Comparisons between the enzyme kinetics within Janus patterned hydrogel spheres and randomly mixed hydrogel spheres, showed significantly improved activity within the Janus arrangement. This was attributed to a proximity effect related to the presence of discrete domains of chemical activity that are interfaced by a locally produced chemical signal.

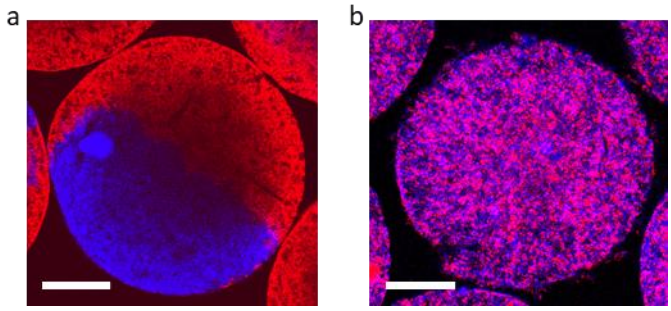

Figure 4.8. Spatially organised vs randomly arranged binary colloidosome population. *Spatially segregated 'Janus' (**a**) and randomly mixed (**b**) populations of RITC-GOx and Dy405-HRP loaded colloidosomes. Scale bars, 200µm.*

Janus hydrogel microspheres were fabricated by microfluidics wherein each microfluidic injection channel comprised RITC-GOx (30 mg ml^{-1}) loaded colloidosomes in Alg 3.5 wt.% and Dy405-HRP (30 mg ml^{-1}) loaded colloidosomes in Alg 3.5 wt.% respectively. Mixed hydrogels were fabricated wherein each microfluidic injection channel comprised a 1 : 1 mix of the RITC-GOx loaded colloidosomes in 3.5 wt.% Alg and Dy405-HRP loaded colloidosomes in 3.5 wt.% Alg that were used in previous Janus hydrogel experiments, keeping the concentration of colloidosomes constant (figure 4.8). After overnight ionic crosslinking, the hydrogel microspheres were transferred to water and a collection (40 spheres) were placed on a microscope well. A d-glucose/o-PD mixture (total 35 µl, 0.84 M/17 mM) was added to the external solution and images were taken at 5 min intervals for a 30 min period. Each experiment was compared to a control experiment whereby o-PD, in the absence of glucose, was added to the external solution. The fluorescence intensity was measured across the entire hydrogel microsphere for each experiment and its glucose-absent control. The final fluorescence intensity was thus calculated as the difference between the fluorescence from the actual experiment and the corresponding control.

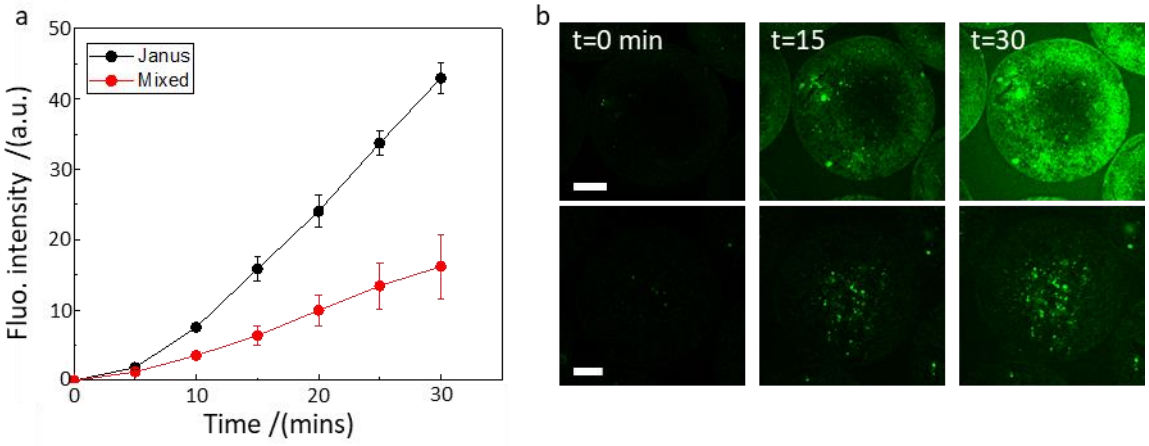

Figure 4.9. Rate of cascade within Janus and mixed hydrogel microspheres. a*, A Graph to show the green-fluorescence output throughout one microsphere in a Janus (black) and mixed (red) population of hydrogel platforms.* ***b****, Images of Janus (top) and mixed (bottom) hydrogel microsphere at time intervals 0, 15 and 30 min after the addition of d-glucose (0.84 M) and o-PD (17 mM). Scale bars, 200 µm. Error bars represent standard deviation (n=3).*

The enzyme kinetics between the Janus population of colloidosomes (black line) were much faster (x 2.6) than the mixed population (red line), as seen by the overall fluorescence intensity increase in the fluorescence profile (figure 4.9a). Interestingly CLSM images showed that in the mixed system (figure 4.9b bottom), fluorescence output appeared from the centre of the microsphere, whereas in the Janus system (figure 4.9b top) fluorescence emerged from the edges of the microsphere. In the case of the mixed system, this is due to the initial fluorescence output appearing from the dispersed population of HRP colloidosomes. The central brightness might be down to the plane in which the microscope took the image. In the Janus system, fluorescence output first appears in the HRP hemisphere and then quickly diffuses into the whole hydrogel. o-PD could also diffuse from the external solution into the edges of the microsphere, causing these areas to have brighter fluorescence.

Overall, a GOx/HRP enzyme cascade was established between a Janus population of colloidosomes encapsulated within a spherical hydrogel platform. The Janus distribution of colloidosomes increased the overall activity of the enzyme cascade compared to a mixed arrangement. The Janus pattern was also significant as the signal output could be localised by the positioning of one colloidosome population. It is interesting that the spatial patterning and organisation of cell communities might improve how they signal to each other.

Communication between spatially immobilised colloidosome populations was next explored in systems with added compositional and organisational complexity. Rod-shaped hydrogel microparticles comprising spatially segregated binary communities of RITC-GOx loaded and Dy-HRP loaded colloidosomes were fabricated. These microparticles were used as a hydrogel-based matrix for anisotropically-involved protocell communication. Specifically, RITC-GOx (30 mg ml^{-1}) loaded colloidosomes and Dy-HRP (30 mg ml^{-1}) loaded colloidosomes were injected into a rod-modified microfluidic device as described in section 3.2a.3. Individual rods were collected in an off-device decanol pool in the absence of $CaBr_2$ crosslinker. Instead, $CaBr_2$ was injected into the device through a second outer injection needle to initiate hydrogel crosslinking within the confined device capillaries. Too much crosslinking resulted in smaller hydrogel pores that restricted the diffusion of chemicals and reduced the rate of communication between protocell populations. A relatively rapid crosslinking process inside the device meant that rod shapes were irregular, and the Janus distribution of protocells was often disrupted. Nevertheless, close inspection of CLSM images (figure 4.10a,b) revealed closely packed colloidosome communities that were spatially segregated (figure 4.10c) within an anisotropic hydrogel platform.

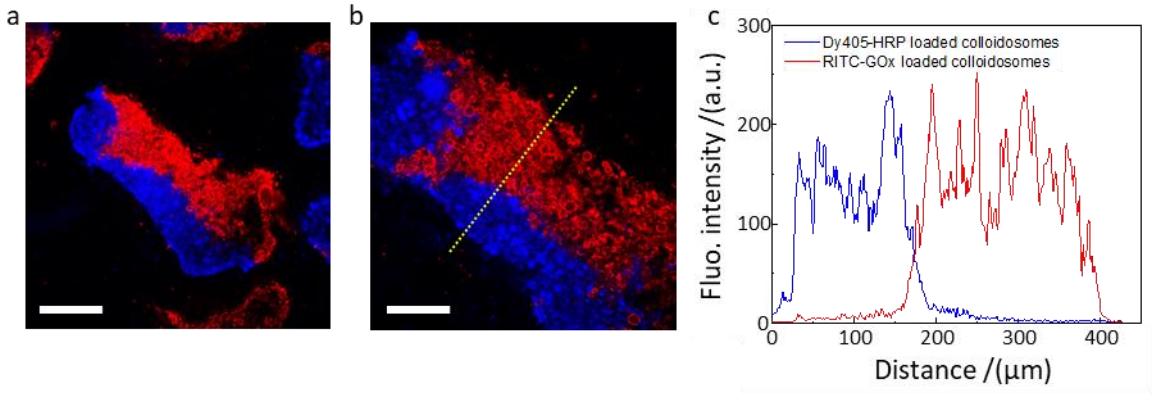

Figure 4.10. Rod-shaped Janus microparticles. *Zoomed out (**a**) and zoomed in (**b**) image of a hydrogel rod containing spatially segregated communities of RITC-GOx loaded colloidosomes (red) and Dy-HRP loaded colloidosomes (blue). Scale bars, 300 and 200 µm respectively. **c**, Fluorescence intensity profile through the cross-section of a single hydrogel rod (yellow dotted line in (**b**)).*

The GOx/HRP enzyme cascade was exploited within rod-shaped hydrogel microparticles to demonstrate colloidosome communication between anisotropically arranged populations and within an anisotropic platform shape. As with the spherical Janus system, d-glucose and o-PD were added to the external solution to initiate and monitor the GOx/HRP enzyme cascade. D-glucose was converted

to H_2O_2 inside the GOx-loaded colloidosomes. The H_2O_2 signalling molecule then diffused into the HRP loaded colloidosomes whereby it catalysed the conversion of o-PD to green-fluorescent 2,3-DAP.

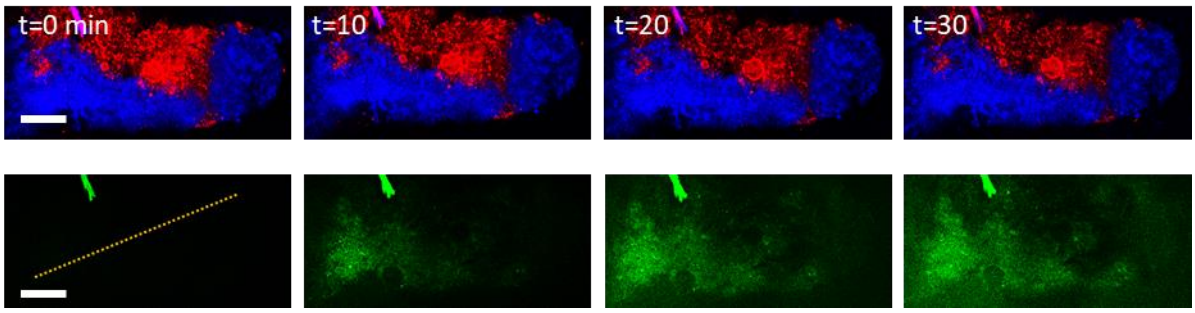

Figure 4.11. Communication between spatially segregated 'Janus' colloidosome communities within an alginate hydrogel microsphere. *CLSM images at 10 min time intervals from t=0 min to t=30 min. Red, blue channels (top row) and filtered green channel (bottom row). Scale bars, 200µm.*

The emergence of green fluorescence within the hydrogel rod, and in the external solution, was captured by CLSM (figure 4.11). Fluorescence intensity measurements across the whole rod were calculated and plotted to observe the increase in green fluorescence intensity over a 30 min time period when d-glucose and o-PD were added into the external solution (figure 4.12a). As with the spherical Janus hydrogel, the fluorescence output was locally released. Initially, there was a greater fluorescence increase within the HRP-loaded colloidosome community however, the fluorescence spread out over the rest of the hydrogel matrix and through the aqueous environment. This can be seen in figure 4.12 by the increase in green fluorescence along the yellow dotted line in figure 4.11.

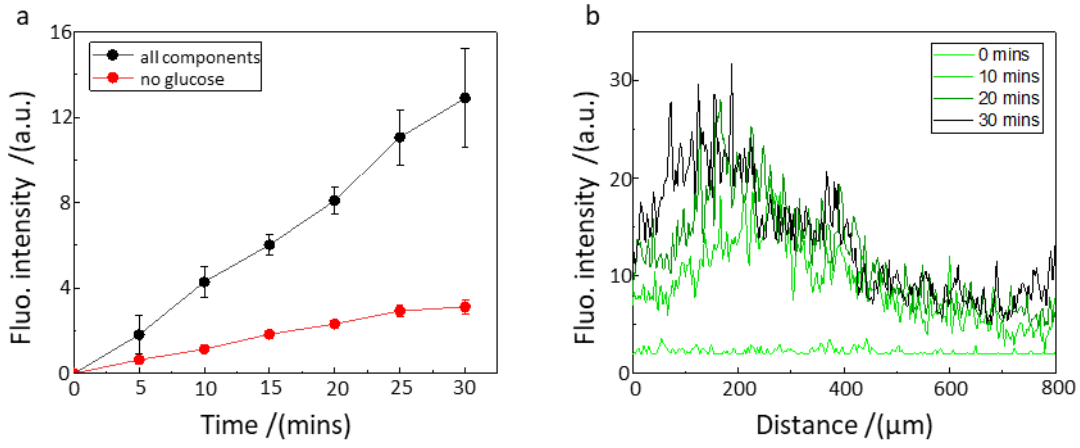

Figure 4.12. Production of 2,3-DAP emerging from the GOx/HRP enzyme cascade within hydrogel rods. a*, Overall increase in green fluorescence from the whole micro rod. Error bars calculated from the standard deviation over several micro rod samples.* ***b****, Increase in green fluorescence across the dotted line in figure 4.9, taken at 10 min intervals. Error bars represent standard deviation (n=3).*

Thus far, communication networks between Janus segregated colloidosome communities have been developed in spherical and rod-shaped hydrogel-based matrix platforms. To achieve added compositional complexity, multicompartmental hydrogel microspheres based on the encapsulation of three segregated colloidosome communities, were generated. This provided opportunity for a more highly ordered and complex matrix-based system, capable of performing a 3-way enzyme cascade. Dy-Invertase (Inv) loaded colloidosomes, RITC-GOx loaded colloidosomes and untagged-HRP loaded colloidosomes were encapsulated into spherical microspheres according to the method in section 2.3.11. Within the Inv containing colloidosomes, sucrose (Suc) was converted to glucose which diffused into the GOx containing colloidosome community. Therein the GOx containing colloidosome community catalysed the conversion of d-glucose to GDL and hydrogen peroxide (H_2O_2). H_2O_2 subsequently diffused out of the GOx colloidosomes and into the HRP containing colloidosomes thereby initiating step three of the enzyme cascade. In the HRP colloidosomes, o-PD was converted to 2,3-diaminophenazine (2,3-DAP) by the HRP catalyst and using the H_2O_2 signalling molecule (figure 4.13).

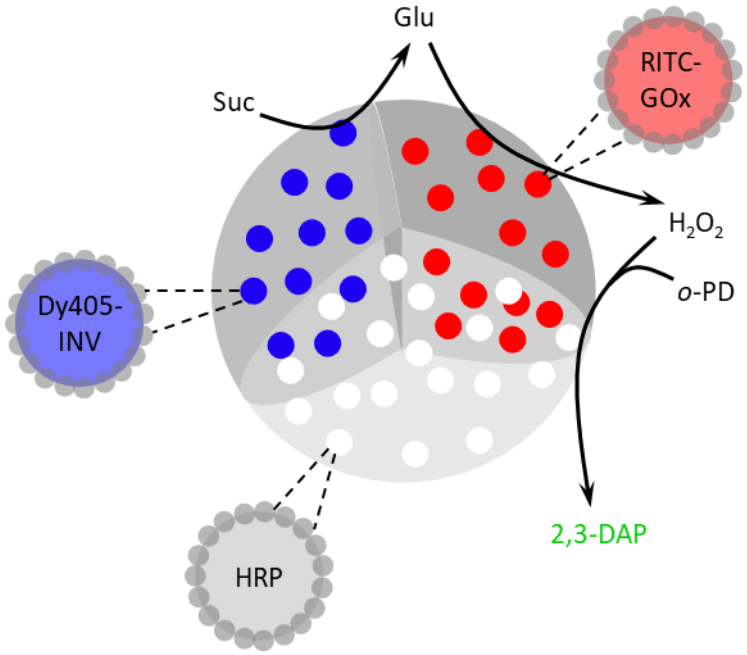

Figure 4.13. Ternary enzyme cascade. *Diagram to show a three-way enzyme cascade between three segregated colloidosome populations within a hydrogel microsphere.*

Specifically, alginate hydrogels were fabricated via microfluidics to encapsulate a ternary spatially segregated community of colloidosomes loaded with Dy-Inv (30 mg ml^{-1}), RITC-GOx (30 mg ml^{-1}) or HRP (30 mg ml^{-1}). Each hydrogel microsphere was made to have a diameter of 600-800 µm and a 1 : 1 : 1 ratio of inner phases. The hydrogel platforms were ionically crosslinked with $CaBr_2$ (1 mM) off-device and then transferred to water. Approximately 15 spheres were transferred to a microscope slide well, whereby a Suc/o-PD mixture (total 35µl, 1.14 M/14.3 mM) was added to the outside of the hydrogel spheres and an image was taken every 5 min. Figure 4.14 highlights the spatial segregation between three colloidosome communities, which are localised by the crosslinked matrix. As seen in the images, each red, blue and non-fluorescent segments remained stationary throughout the experiment, thus showing positional stability of colloidosome communities throughout the duration of the cascade reaction. Green fluorescence emerged within the hydrogel microsphere indicating the presence of 2,3-DAP, the end point of the cascade reaction. For this to be realised, first glucose, then H_2O_2 were released as signal molecules between each of the three communities. The green fluorescence emerged, in general, from the same location as the untagged HRP, indicating that the HRP colloidosomes were converting o-PD to 2,3-DAP. The o-PD then diffused throughout the rest of the hydrogel. The green-fluorescence intensity increase was observed throughout the whole microsphere as an indication that the cascade was occurring (figure 4.14b). In contrast to the sucrose-initiated cascade, in the absence of sucrose green fluorescence did not emerge.

Overall, enzyme cascades between highly ordered colloidosomes populations have been demonstrated. The hydrogel matrix was shown to be a suitable scaffold for organising protocells and allowing communication between localised populations.

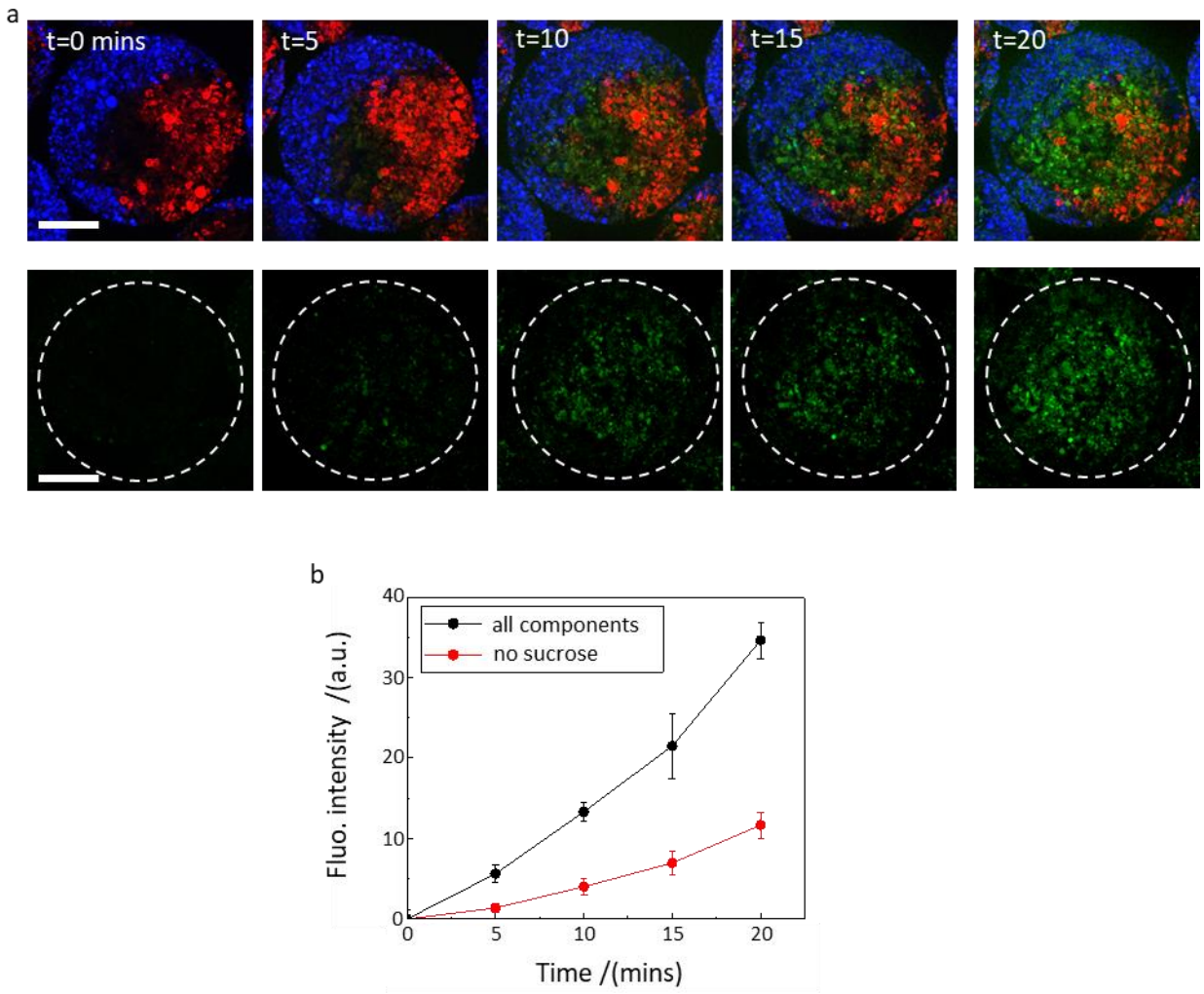

Figure 4.14. Enzyme cascade within ternary populated hydrogel matrix. a*, Single crosslinked hydrogel microsphere comprising a segregated tertiary population of colloidosomes containing Dy405-labelled Inv (blue), RITC-labelled GOx (red) and non-labelled HRP. Simultaneous addition of sucrose (0.84 M) and o-PD (17 mM) at t = 0 min gives rise to the progressive output of 2,3-DAP (green fluorescence) over 20 min. Red/blue/green fluorescence overlays (top row); green fluorescence filtered image (bottom row). Samples prepared at a 1 : 1 : 1 number ratio;* V_{in} *= 0.15;* V_{out} *= 100 ml* h^{-1}*, [alginate] = 3.5 wt%,* $[CaBr_2]$ *= 3 mM; scale bar, 200 µm.* ***b****, Overall increase in green fluorescence from 2,3-DAP across the whole microsphere. Error bars represent standard deviation (n=3).*

4.2.2 Collective behaviour within hydrogel-based matrices

Since communication has been well-established between spatially organised colloidosome populations within various hydrogel systems, the next challenge was to utilise this communication to result in an emergent behaviour. Alongside this, its seemed important to focus on the link between inter-colloidosome communication with colloidosome-environment communication, as both cell-cell and cell-environment interactions are important within living systems. A key aim was thus to mimic how living cells interact with their ECM to result in biologically advanced functions.

As the first step to achieving colloidosome-environment communication and collective colloidosome behaviours, the activity of URS (within colloidosomes) was exploited to disassemble the surrounding hydrogel scaffold, releasing colloidosomes and debris into the environment. Ionically crosslinked alginate hydrogel microspheres embedded with URS-loaded colloidosomes were fabricated via droplet-based microfluidics. Upon addition of urea (1 M) to the external aqueous environment, URS within the colloidosomes catalysed urea's conversion to ammonia, water and a carbonate ion, which subsequently lead to the disassembly of the hydrogel matrix structure. This disassembly was attributed to the combination of carbonate ions (produced by the enzyme reaction) with the Ca^{2+} crosslinking ions, removing them and consequently withdrawing ionic crosslinking capability (figure 4.15a).

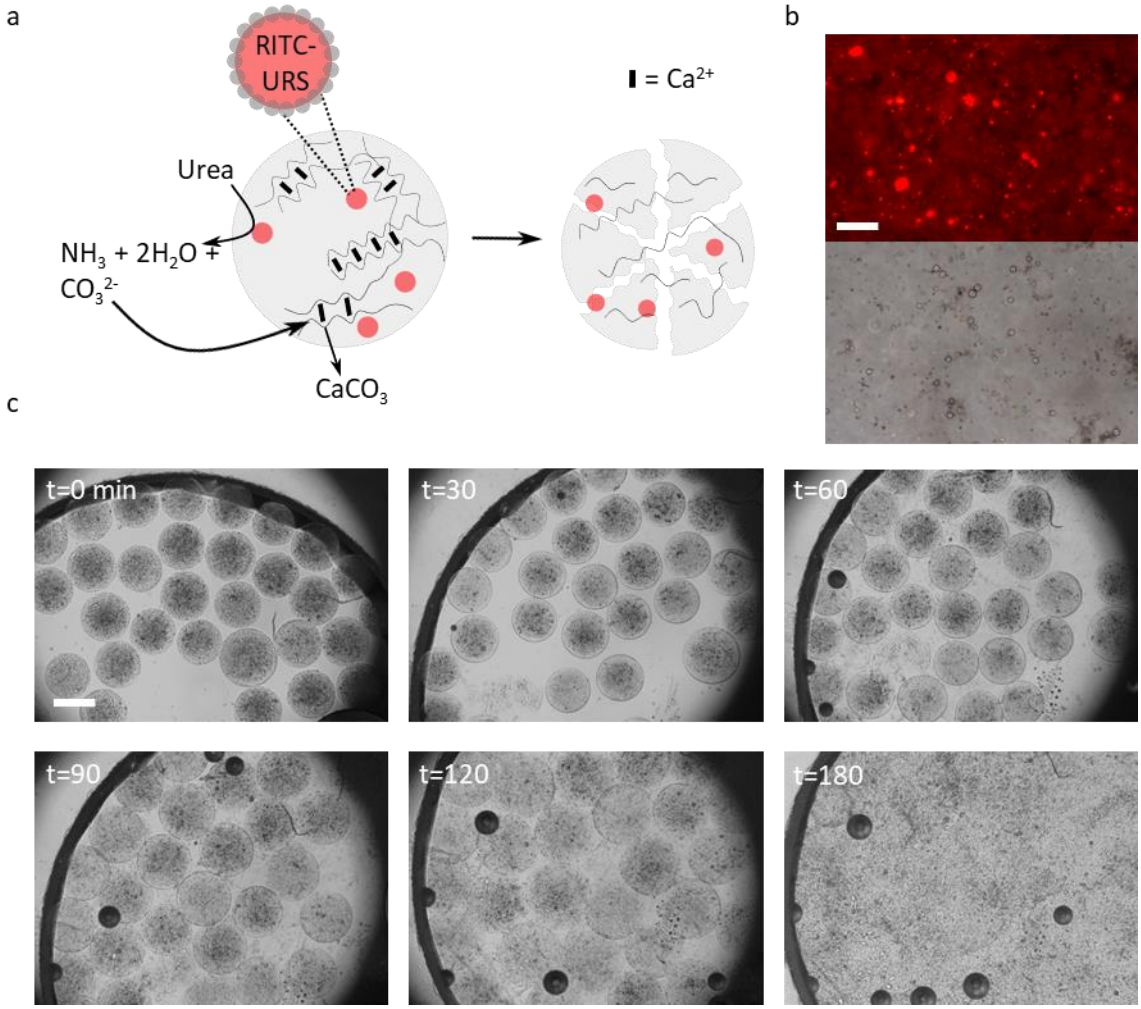

***Figure 4.15**. **URS-mediated disassembly of hydrogel microspheres.** **a**, Diagram to show the disassembly of alginate matrix based upon the urease-mediated conversion of urea to ammonia, water and a carbonate ion. **b**, Fluorescence and bright field images of RITC-Urease loaded colloidosomes dispersed within sodium alginate (3.5 wt.%) 3 hrs after the addition of urea to the environment surrounding microspheres with encapsulated urease colloidosomes. Scale bar, 400 µm. **c**, Bright field images taken at 30 min time intervals of a selection of hydrogel microspheres embedded with urease-loaded colloidosomes. Scale bar, 40 µm.*

Figure 4.15b shows that over a period of 180 min after urea exposure, hydrogel microspheres were gradually disassembled by the carbonate-producing URS-loaded colloidosomes trapped within the hydrogel matrix structure. Disassembly was minimal within the first hour, suggesting that a threshold concentration of carbonate was required for notable disassembly to occur. However, once the disassembly process began, alginate chains became weaker and thus calcium crosslinking ions were less strongly bonded and more easily taken up by the carbonate ions, meaning that complete disassembly was achieved relatively quickly. In these images we also observe hydrogel microsphere swelling before they disassemble. As the alginate crosslinks are weakened, more water enters the gel causing it to swell. This also pushes the chains further apart, and thus helps towards the dissociation

process. There is an increase in pH from the urea conversion to ammonia which increases the negative charge of alginate chains and potentially helps them repel and weaken, however this is largely counteracted by a stronger affinity to the Ca^{2+} crosslinking ions. In these experiments RITC-labelled URS was used to help visualise the dispersion of colloidosomes upon disassembly. Figure 4.15c shows a fluorescence (top) and bright field (bottom) image of the alginate hydrogels, 3 h after addition of urea. Colloidosomes remain intact thus demonstrating a passive release from microspheres into the environment. The system could therefore be considered as a potential delivery method for selectively releasing colloidosomes from a biocompatible entity. Alternatively, the hydrogel scaffold could represent a protective packaging that is easily removed when it is no longer needed. Control experiments showed that in the absence of urea, decrosslinking did not occur (figure 4.16). Although it was demonstrated that colloidosomes could collectively afford a macroscopic effect on the matrix environment, the next step was to increase complexity in both the colloidosome behaviour and the hydrogel environment.

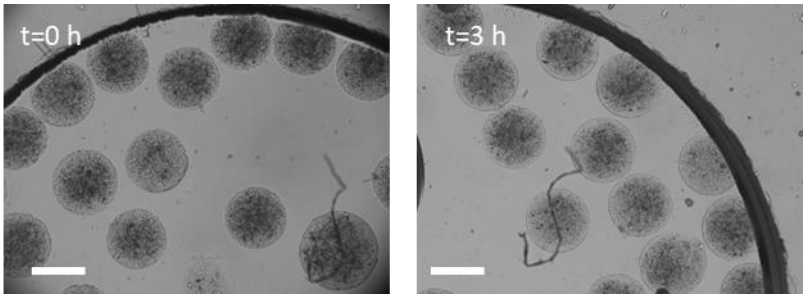

Figure 4.16. URS disassembly control experiment. *Bright field microscopy images of Ca^{2+}-crosslinked alginate hydrogel microspheres containing a homogeneous population of urease-loaded colloidosomes in the absence of urea. Images were taken before (left, t=0) and 3 h after (right) addition of water (no urea) and show no changes in microsphere stability in the absence of urease activity and tyramine crosslinking. Scale bar, 400 µm.*

As a second step to achieving colloidosome-environment communication and collective behaviour, sodium alginate was covalently tagged with tyramine (ty) via NHSS/EDC chemistry. The UV-Vis spectra in figure 4.17a shows the successful addition of tyramine groups to the alginate backbone chain. The percentage substitution of tyramine functional groups was approximated as 3% using a calibration curve of tyramine at different percentages in distilled water and the absorbance measured at 275 nm (section 2.4.3). The modified ty-Alg was subsequently crosslinked via HRP/H_2O_2 oxidative coupling as seen in figure 4.17b.

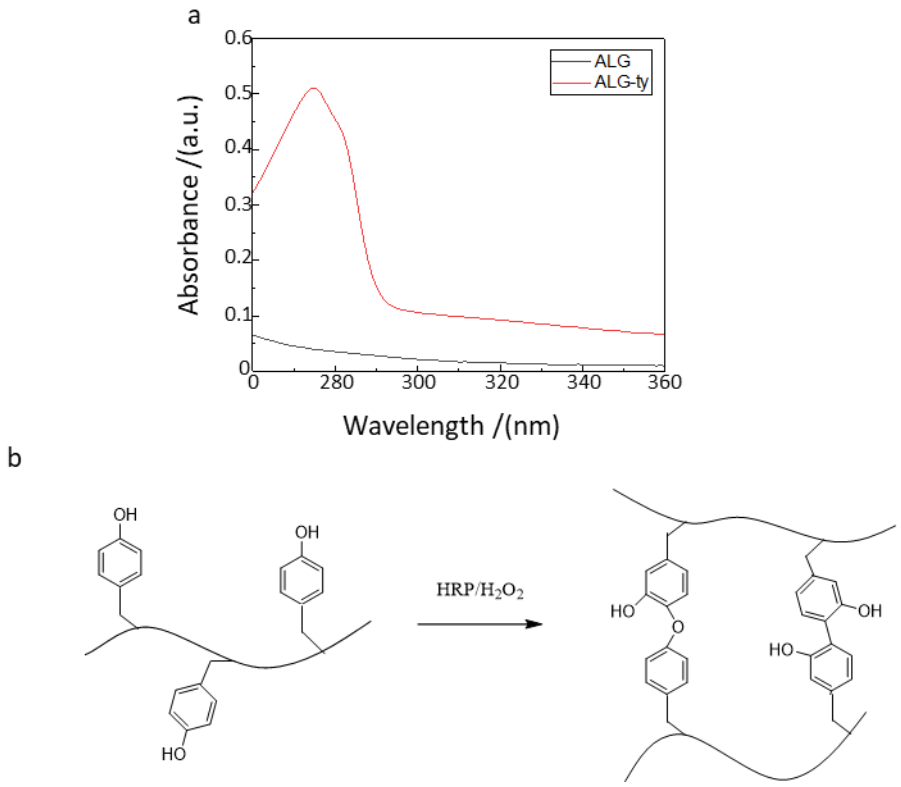

Figure 4.17. Tyramine functionalisation of alginate. a*, UV-vis spectrum of alginate and alginate-tyramine. Peak at 275 nm derived from the benzene moieties from the tyramine functional groups.* ***b****, Schematic of HRP/H_2O_2 oxidative coupling between ty-Alg chains.*

Hydrogel droplets comprising an inner phase of ty-Alg were fabricated using droplet microfluidics and ionically crosslinked using $CaBr_2$. After being transferred to water, the ty-Alg hydrogel droplets were immersed in an aqueous solution of H_2O_2 and HRP, which led to the covalent gelation of chains due to the coupling of the phenol moieties. Calcium ions involved in the ionic crosslinking of the hydrogel spheres were subsequently removed by the addition of sodium citrate (figure 4.18a). Hydrogel platforms held their spherical structure due to sufficient covalent crosslinking, induced by H_2O_2 and HRP. In comparison, hydrogels that had not undergone covalent crosslinking (absence of HRP or H_2O_2) dissolved upon sodium citrate addition due to the removal of the Ca^{2+} ions (figure 4.18b,c). It was thus shown that microspheres made with ty-Alg could be covalently crosslinked via the addition of H_2O_2 and HRP.

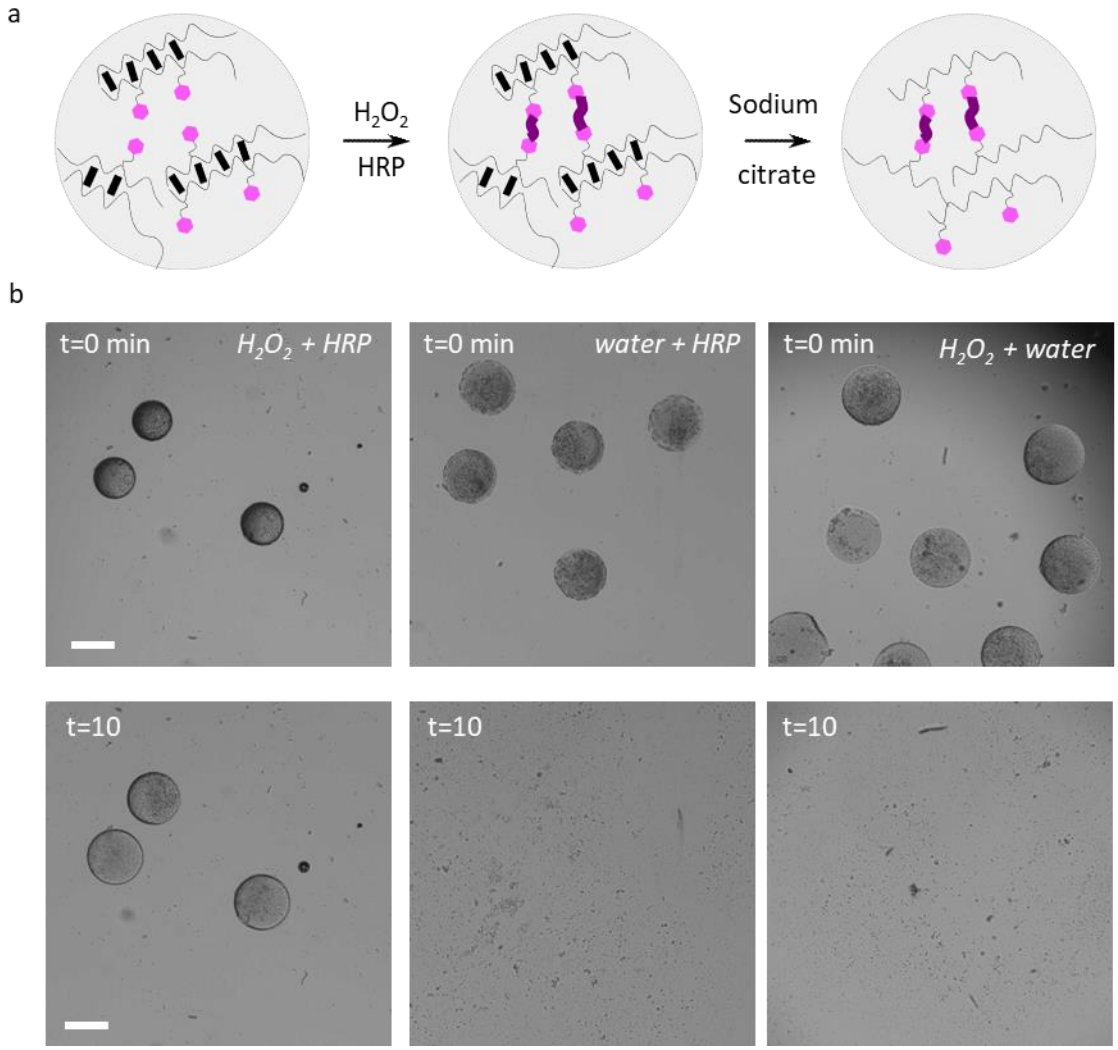

***Figure 4.18. Covalent crosslinking of ty-Alg hydrogel spheres via H_2O_2 and HRP. a**, Schematic diagram showing ty-Alg hydrogel spheres ionically crosslinked with Ca^{2+}, the addition of H_2O_2 and HRP to covalently crosslinking the ty-Alg chains and the removal of Ca^{2+} by sodium citrate. **b**, Bright field microscope images of ty-Alg hydrogel spheres at t=0 mins incubated in H_2O_2 + HRP (0.8 mM, 18 U), water + HRP (18 U) and H_2O_2 (0.8 mM) + water respectively for 17 h. Scale bar, 400 µm. c, Bright field microscope images of ty-ALG hydrogel spheres at t=10 min after the addition of sodium citrate (1 wt.%). Scale bar, 400 µm.*

To develop protocell-environment communication, the enzymatic activity of GOx (to produce H_2O_2)-loaded colloidosomes was exploited for the covalent crosslinking of ty-Alg hydrogel microspheres. Droplet microfluidics was used to fabricate ty-Alg hydrogel microspheres consisting of FITC-GOx loaded colloidosomes encapsulated within the ty-Alg hydrogel that has been crosslinked ionically using $CaBr_2$. Upon addition of d-glucose and HRP into the environment, GOx catalysed d-glucose conversion to GDL and H_2O_2, as previously discussed (section 4.2.1). In this case, H_2O_2 produced as a by-product from the d-glucose to GDL conversion, was used to covalently crosslink the ty-Alg

hydrogel spheres in the presence of HRP. The GOx-loaded colloidosomes embedded inside the hydrogel matrix, were thus integral to the crosslinking of the external environment, introducing a key protocell-environment interaction. HRP could not be loaded into colloidosomes as the ty-Alg chains needed direct contact with HRP for the catalytic process. Figure 4.19 demonstrates the successful covalent crosslinking of hydrogel microspheres via this colloidosome entrapped enzyme-initiated process. Upon addition of sodium citrate to the external solution, the hydrogel microspheres that had been previously exposed to d-glucose and HRP maintained their spherical condition (due to covalent crosslinking), whilst those that had not been exposed to glucose or HRP (no covalent crosslinking) quickly disassembled.

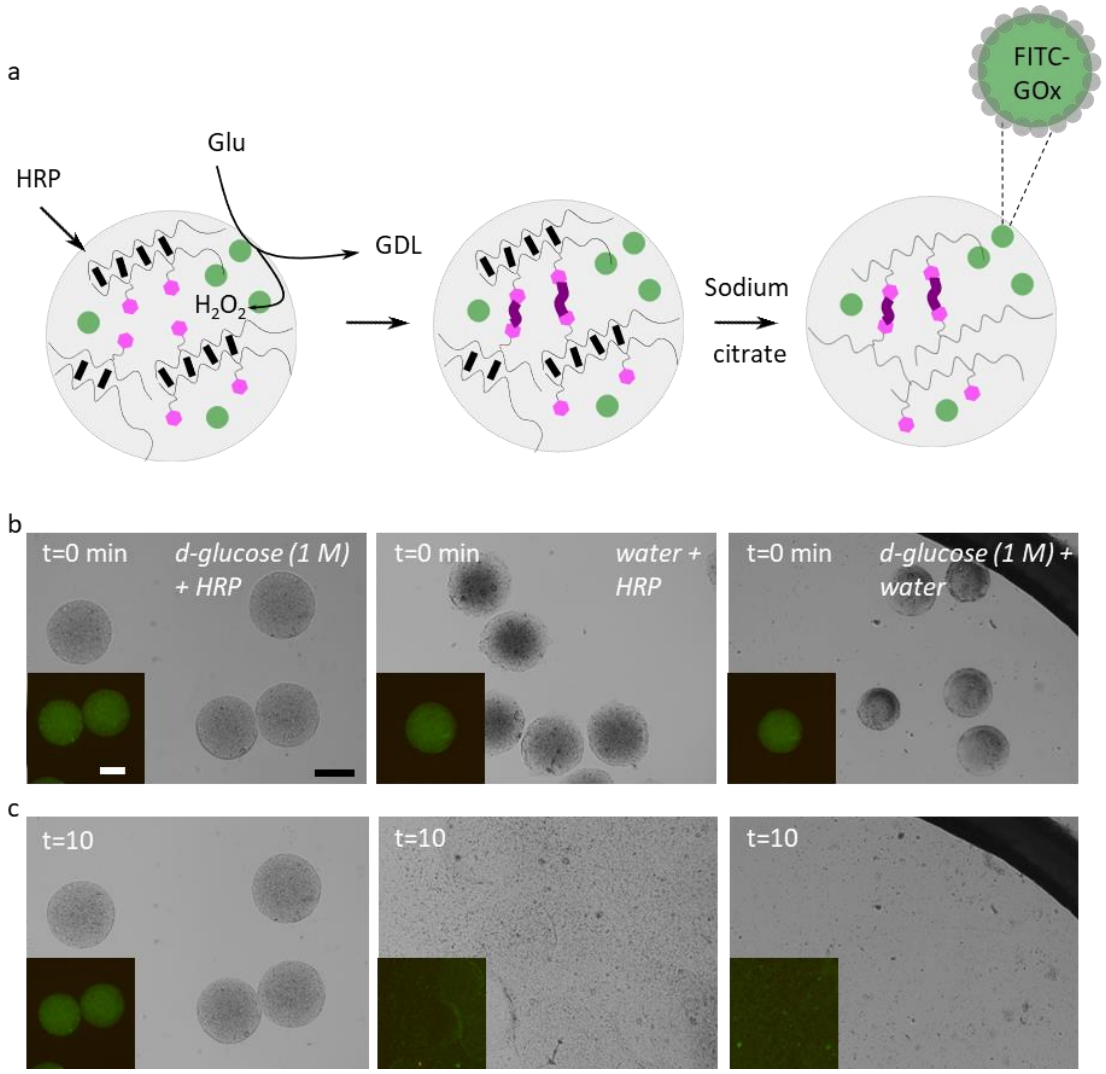

***Figure 4.19. Covalent crosslinking of ty-Alg hydrogel spheres via HRP and GOx-mediated production of H_2O_2. a**, schematic diagram showing ty-Alg hydrogel spheres loaded with FITC-GOx and ionically crosslinked with Ca^{2+}, the addition of glucose and HRP to covalently crosslinking the ty-Alg chains and the removal of Ca^{2+} by sodium citrate. **b**, Bright field microscope images with CLSM inset of ALG-ty hydrogel spheres at t=0 mins incubated in d-glucose + HRP (0.96 M, 9 U), water + HRP (9 U) and d-glucose (0.96 M) + water respectively for 3 hr. **c**, Bright field microscope images with CLSM inset of ty-Alg hydrogel spheres at t = 10 min after the addition of sodium citrate (1 wt.%). Scale bars, 400 µm.*

The ability to control internal patterning within hydrogel microspheres using microfluidics was herein utilised. Segregated patterning of the alginate hydrogel spheres was exploited for spatially controlled covalent crosslinking and hydrogel disassembly by combining the disassembly of unmodified Alg hydrogels with the GOx-aided covalent crosslinking (assembly) of modified ty-Alg hydrogels. Microspheres were thus prepared with one domain comprising unmodified alginate and URS-loaded colloidosomes and the other domain comprising ty-Alg and FITC-GOx loaded colloidosomes. The hydrogels were ionically crosslinked off-device using $CaBr_2$ akin to the previously mentioned microspheres. Firstly, the effectiveness of GOx colloidosomes to covalently crosslink one half of a hydrogel was tested. A collection of microspheres ($n \sim 20$) were added to a well-plate and a HRP and d-glucose mixture was added to the external solution to initiate the covalent crosslinking process. Within the ty-Alg (green) hemisphere, FITC-GOx mediated the conversion of d-glucose to gluconolactone and H_2O_2, which was used alongside HRP to covalently crosslink the ty-Alg. The crosslinking process was left to occur over a 3 h period. Then, sodium citrate (0.5 wt. %) was added into the well to remove any ions involved in the ionic crosslinking of the hydrogel. As a result, the hemisphere made from unmodified alginate disassembled by the removal of Ca^{2+} ions from the matrix, whilst the hemisphere containing ty-Alg, that was covalently crosslinked, remained intact, even with the removal of Ca^{2+} ions (figure 4.20a). Control experiments in the absence of both d-glucose and HRP, showed that without the opportunity for covalent crosslinking, the whole hydrogel disassembled upon addition of sodium citrate (figure 4.20b). On the other hand, without sodium citrate, disassembly did not occur (figure 4.20c).

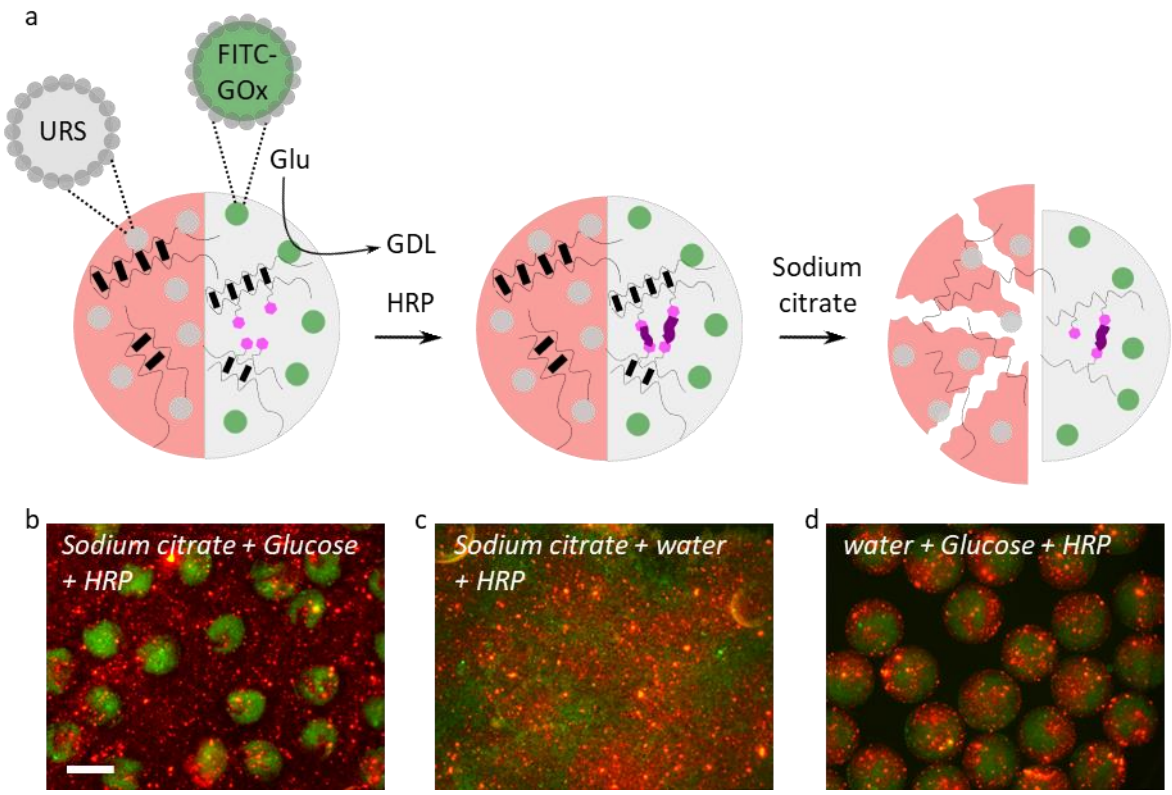

Figure 4.20. Spatially controlled disassembly of selected hydrogel sphere domain. a*, Diagram showing the hydrogel composition and covalent crosslinking of ty-Alg hemisphere in the presence of HRP followed by the ionic crosslinking removal and thus disassembly of URS-loaded colloidosome containing hemisphere in the presence of sodium citrate.* ***b****, Fluorescence image of hydrogel spheres after covalent crosslinking of ty-Alg hemisphere and addition of sodium citrate.* ***c****, Fluorescence image of hydrogel after the addition of sodium citrate and unsuccessful covalent crosslinking due to exposure of only HRP and not H_2O_2.* ***d****, Fluorescence image of hydrogel spheres without the addition of sodium citrate. Scale bar, 600 µm.*

To introduce function in 'opposing' protocell populations, the URS-mediated disassembly of unmodified Alg hydrogels was combined with the GOx-aided covalent crosslinking (assembly) of modified ty-Alg hydrogels, within a single Janus hydrogel microsphere. Dual microfluidics was used to carefully fabricate hydrogel microspheres with one domain comprising RITC-unmodified Alg and URS loaded colloidosomes (100 KU ml^{-1}) and the other domain comprising modified ty-Alg and FITC-GOx loaded colloidosomes (4.5 KU ml^{-1}) at a URS : GOx number ratio 6 : 1 and Alg : ty-Alg volume ratio 3 : 1. The hydrogels were ionically crosslinked off-device using $CaBr_2$ akin to previously mentioned microspheres. These hydrogels were transferred to water and subsequently to a microscope slide well, whereby the addition d-glucose, HRP and urea initiated the crosslinking/resilience behaviour. Within the ty-Alg (green) hemisphere FITC-GOx mediated the conversion of d-glucose to GDL and H_2O_2 which was used alongside HRP to covalently crosslink the ty-Alg. Within the unmodified Alg

(red) hemisphere, URS initiated the conversion of urea to ammonia + carbonate which released the ionic crosslinking.

Onset of the enzyme reactions resulted in disassembly of domain **1**, and subsequent release of the URS-containing protocells over 20 h, while the GOx-colloidosome population in segment **2** remained immobilised under the diffusive flux of carbonate across the interface (figure 4.21b). The results indicated that formation of covalent crosslinks in domain **2** by resident GOx/HRP activity was sufficiently competitive under the conditions employed to offset the flux-mediated depletion of Ca^{2+} ions in domain **2**. The disassembly of unmodified alginate part-released URS colloidosomes into the external solution alongside alginate debris. This waste material could be collected manually using a pipette, leaving the remaining covalently crosslinked ty-Alg and FITC-GOx colloidosome hydrogel, thus demonstrating the distinction between the two domains (figure 4.21c). Control experiments showed that in the absence of d-glucose (when ty-Alg is not covalently crosslinked), both hemispheres disassembled upon addition of urea (figure 4.21d). On the other hand, in the absence of urea, disassembly in either hemisphere did not occur (figure 4.21e).

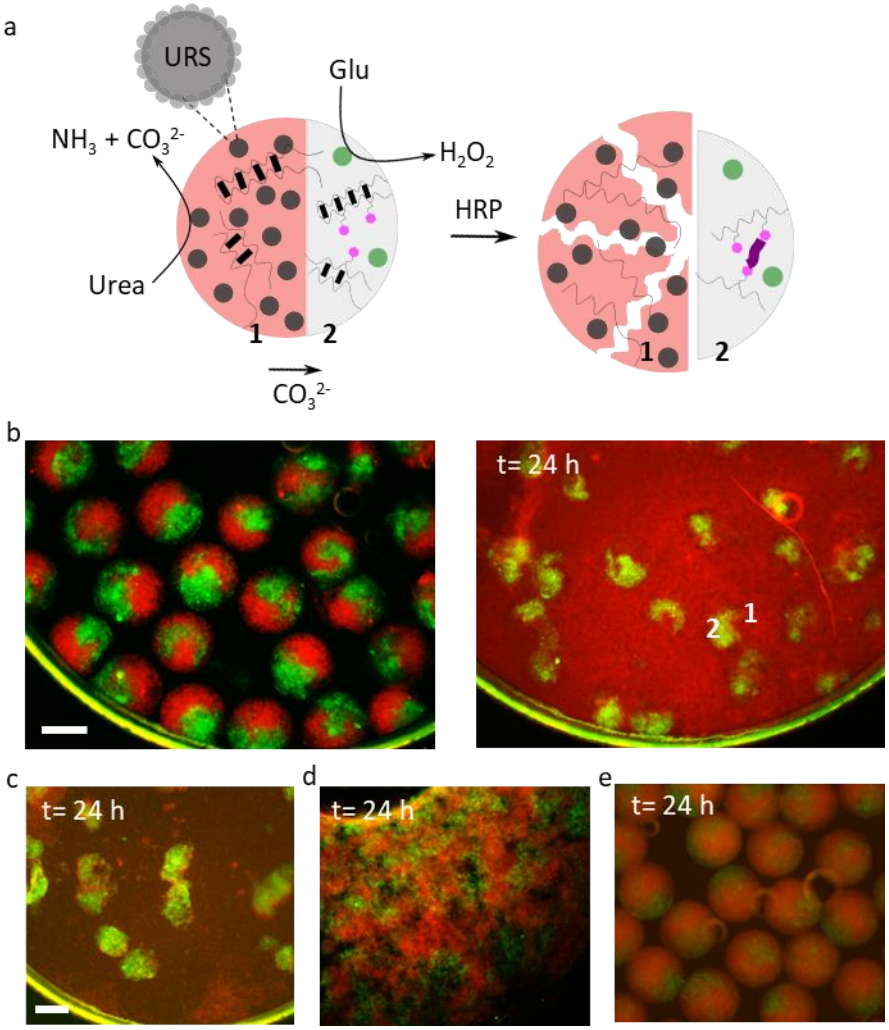

Figure 4.21. Spatially controlled disassembly of hydrogel sphere using URS/GOx enzymatic reactions. ***a****, Diagram showing the two-domain hydrogel composition and covalent crosslinking of ty-Alg domain in the presence of glucose and HRP, alongside the ionic crosslinking removal and thus disassembly of URS-loaded colloidosome containing domain in the presence of urea.* ***b****, Fluorescence image at t=0 and t=24 hrs after the addition of urea, HRP and glucose into the external aqueous medium.* ***c****, Removal of the uncrosslinked hydrogel and URS-containing colloidosomes leaving behind covalently crosslinked ALG-ty hemispheres containing FITC-GOx loaded colloidosomes.* ***d****, Fluorescence image at t=24 hrs after the addition of urea but no glucose.* ***e****, Fluorescence image taken at t=24 hrs after the addition of glucose but not urea. Scale bars, 600 µm.*

It was observed by CLSM images (figure 4.22) that the disassembly of the unmodified hydrogel domain via URS activity was a non-linear process which started slowly, then proceeded relatively quickly upon reaching a certain threshold. Minimal disassembly of the unmodified domain occurred before 9 h however, full disassembly was achieved by 10 h. Once again, swelling is attributed to removal of some Ca^{2+} ions, resulting in the weakening of alginate chains and increased water uptake into the network, further weakening the network, until rapid decrosslinking can occur.

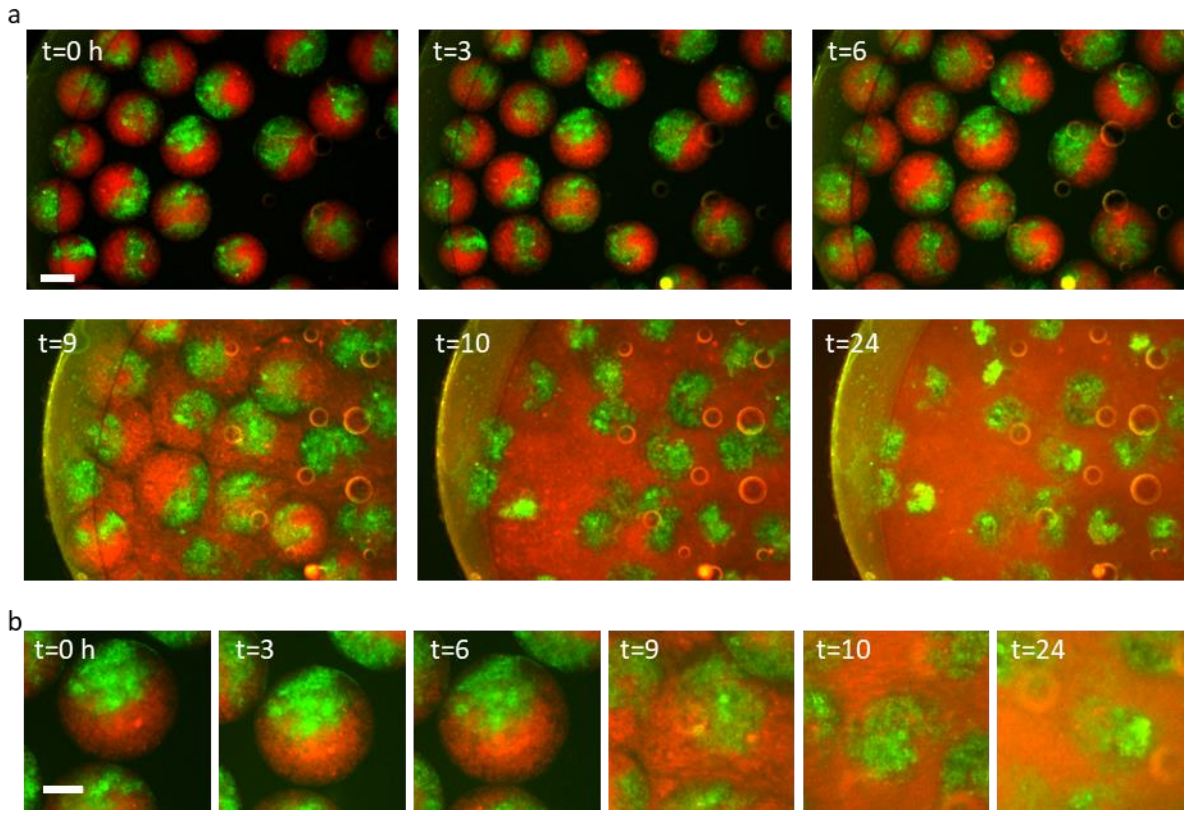

***Figure 4.22. Step by step analysis of the hydrogel disassembly method**. **a**, Fluorescence images taken over a 24 hr period showing the gradual disassembly of URS loaded colloidosome containing hemispheres. Scale bar, 600 µm. **b**, Zoomed in images of a single hydrogel sphere. Scale bar, 300 µm.*

The localised degradation or resilience of domains was further programmed by changing the concentration of URS within a fixed number density colloidosome population, resulting in three distinct regimes. At a constant GOx concentration of 4.5 KU ml^{-1} and fixed 6 : 1 colloidosome number ratio, both hydrogel domains remained intact when the urease concentration was decreased to $\leq$50 KU ml^{-1} due to an insufficient flux of carbonate ions (figure 4.23). Conversely, complete microsphere degradation occurred within 9 h when the encapsulated urease concentration was increased to 150 KU ml^{-1}, implying that urease-mediated degradation of the Ca^{2+}-crosslinks was considerably faster in both hydrogel segments than GOx-mediated covalent crosslinking specifically in domain **2.** Programming collective protocell behaviours provides a step towards well-regulated biological processes and shows potential for controlling the delivery of biological substances.

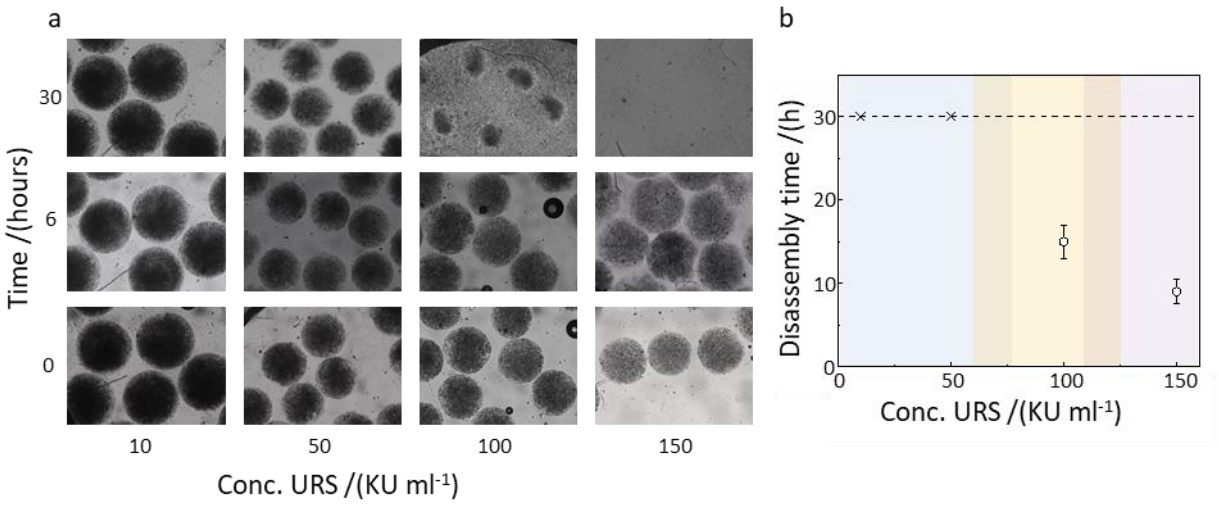

Figure 4.23. Programmed hydrogel disassembly. a*, Bright field image grid showing hydrogels over a 30 hr period with different concentrations of URS within URS-loaded colloidosomes.* ***b****, A graph to show the rate of disassembly of all or part of the hydrogel sphere.*

Further experiments were conducted to show the relevance and importance of spatial organisation within these systems. Experiments showed that a Janus pattern was imperative to the disassembly and resilience process described, as the expulsion of a single protocell population is dependent on the competition between the rates of hydrogel disassembly and stabilisation, which in turn are determined by the opposing fluxes of enzyme products and their proximity to their cognate reaction sites within the different domains of the chemically differentiated hydrogel matrix. Analogous experiments undertaken with partitioned calcium alginate and calcium alginate/tyramine-alginate microspheres comprising a homogeneous mixture of URS- and GOx-containing colloidosomes showed minimal degradation over 20 h (figure 4.24b). Minimal levels of disassembly were also observed for microspheres prepared with a homogenous matrix of calcium alginate/tyramine-alginate and non-segregated community of urease- and GOx-containing colloidosomes (figure 4.24 c). In both cases, the observations were attributed to the absence of discrete reaction domains, which in the segregated colonies facilitate the accumulation of higher carbonate concentrations and corresponding increased levels of ionic decrosslinking.

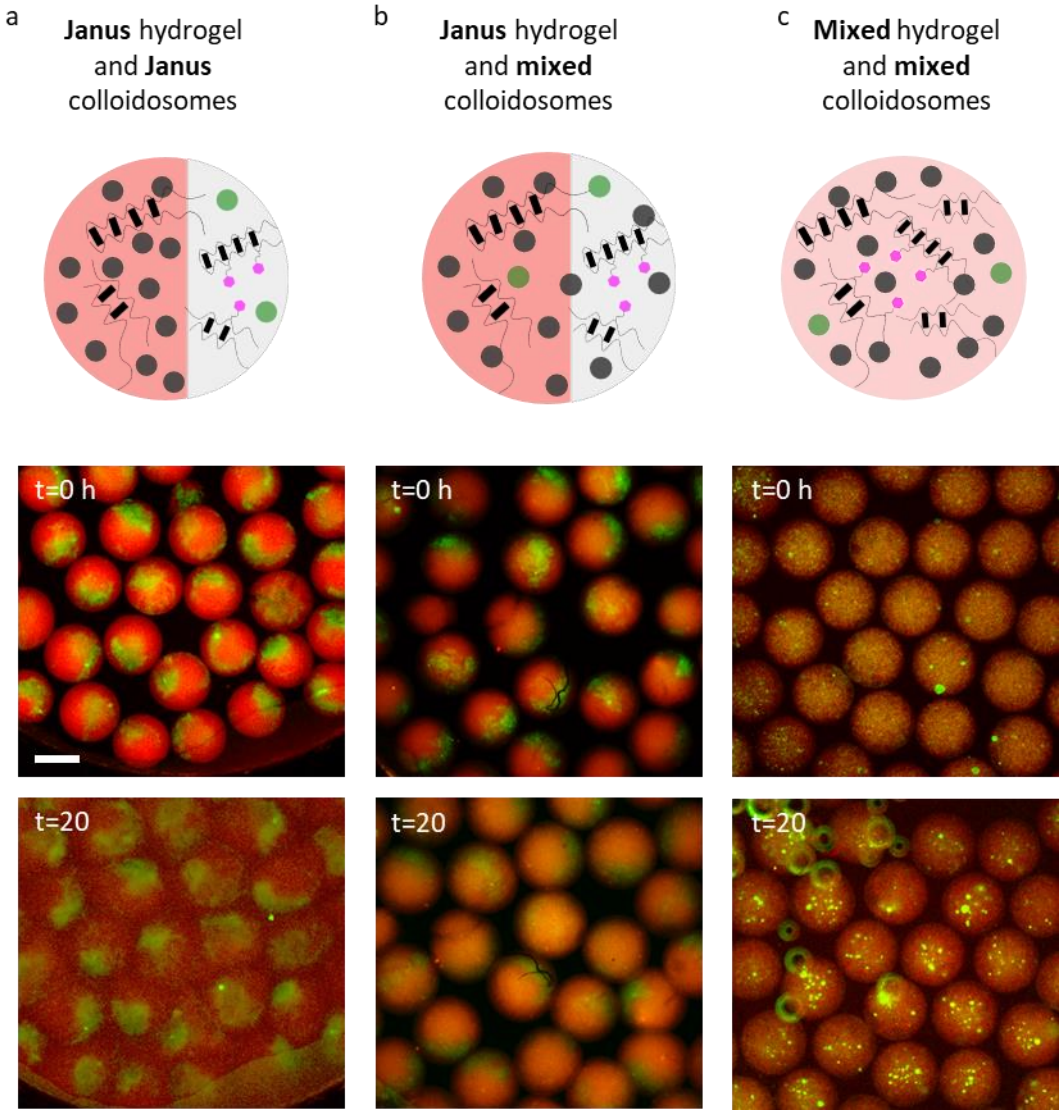

Figure 4.24. Comparison between Janus and mixed populations of colloidosome and hydrogels. a, *Janus distribution of URS and GOx containing colloidosomes encapsulated within the hydrogel sphere. Janus distribution of unmodified alginate and ty-Alg. Fluorescence images of these hydrogels at t=o and t=20 hrs after the addition of HRP, glucose and urea.* ***b,*** *Mixed distribution of URS and GOx containing colloidosomes encapsulated within the hydrogel sphere. Janus distribution of unmodified alginate and ty-Alg. Fluorescence images of these hydrogels at t=0 and t=20 hrs after the addition of HRP, glucose and urea.* ***c,*** *Mixed distribution of URS and GOx containing colloidosomes encapsulated within the hydrogel sphere. Mixed distribution of unmodified alginate and ty-Alg. Fluorescence images of these hydrogels at t=o and t=20 hrs after the addition of HRP, d-glucose and Urea.*

As a final step to improve the potential usefulness of this disassembly/resilience system, cross-hydrogel communication between colloidosomes and the hydrogel environment in opposite domains was explored. Dual microfluidics was used to carefully fabricate hydrogel microspheres with one domain comprising unmodified Alg and FITC-GOx loaded colloidosomes (4.5 KU ml^{-1}) and the other domain comprising modified ty-Alg (28%), RITC unmodified Alg (72%) and URS loaded colloidosomes (100 KU ml^{-1}) at a GOx : URS number ratio 3 : 2 and Alg : ty-Alg volume ratio 3 : 1. Onset of the enzyme reactions resulted in disassembly of domain **1**, and subsequent release of the GOx-containing protocells over 20 h, while the URS-colloidosome population in segment **2** remained immobilised under the diffusive flux of carbonate across the interface (figure 4.21b). In this final case, H_2O_2 that was produced in domain **1** by GOx-loaded colloidosomes had to travel through the hydrogel into the opposite domain whereby it caused the covalent crosslinking of the ty-Alg. Simultaneously, carbonate ions were produced by the URS catalysed breakdown of urea in domain **2** which then travelled through the hydrogel to the opposite domain therein causing the disassembly of unmodified Alg in domain **1**. This process mimicked jettisoning behaviour whereby the GOx colloidosomes were used to crosslink the opposite hemisphere, then when they had completed this task and were no longer needed, they were jettisoned out of the microsphere system along with alginate debris. This demonstrated a sophisticated communication pathway between protocells and their environment whilst also displaying a complex method for biological material release.

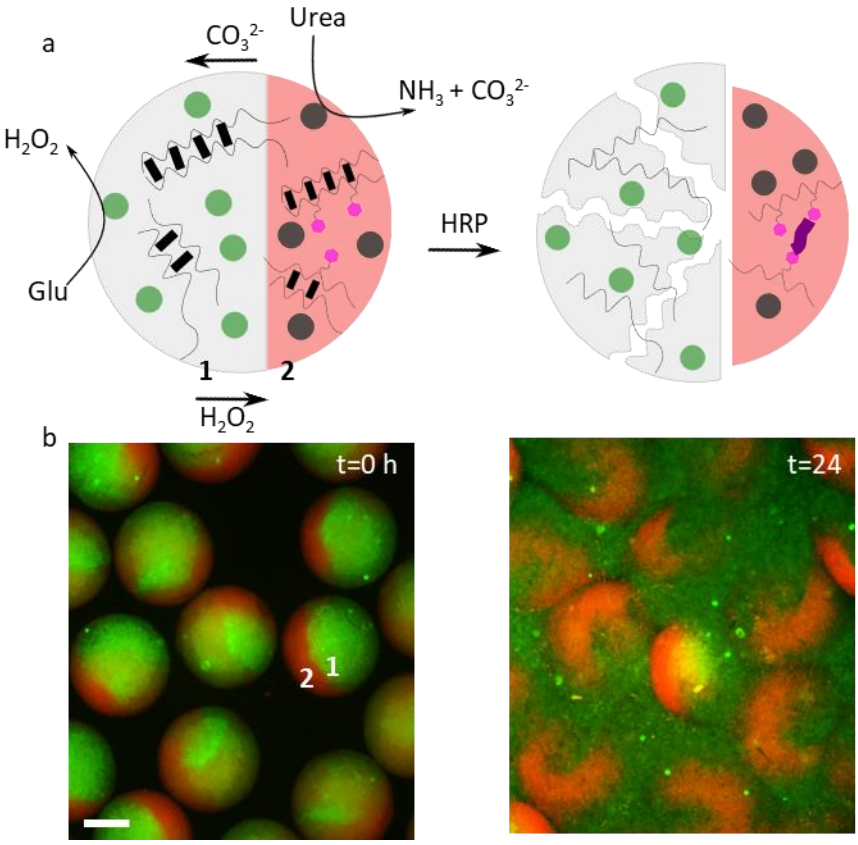

Figure 4.25. Jettisoning hydrogels with communication between opposite hydrogel domains. a, *schematic showing hydrogels with one hemisphere consisting unmodified Alg and FITC-Gox loaded colloidosomes and the other hemisphere consisting modified ty-Alg and URS loaded colloidosomes.* ***b,*** *Fluorescence images showing that upon addition of urea and d-glucose, the ty-Alg hydrogel hemisphere is crosslinked, and the unmodified hydrogel is disassembled releasing Gox loaded colloidosomes. Scale bar, 400 µm.*

4.2.3 Communication within coacervate-based matrices

Despite successful signalling and collective behaviour between spatially segregated colloidosome populations immobilised throughout alginate hydrogel networks, the signalling rates were relatively slow, high concentrations of enzymes were required and the colloidosome population density was relatively low. Embedding colloidosomes within a coacervate tissue was therefore utilised as an alternative matrix-based system with the potential to deliver higher rates of communication (as signals travelled through coacervate phase) and for a more densely packed tissue structure.

Signalling from colloidosome hotspots was achieved using a simple d-glucose/GOx reaction (figure 26a). Tissues were made according to section 3.2b.1 with GOx loaded colloidosomes encapsulated within a coacervate tissue network. These tissues were transferred to a microscope well-plate and d-

glucose, HRP and o-PD substrates were added to the external solution, through which they diffused into the coacervate network and further into the colloidosomes. H_2O_2 produced in the colloidosome as a side product of the GOx mediated d-glucose transformation into GDL, quickly diffused out of the colloidosome and aided the transformation, alongside HRP, of o-PD into fluorescent 2,3-DAP. Figure 4.26b shows that minimal fluorescence is observed inside the colloidosome hotspots, with most the fluorescence appearing in the coacervate tissue surrounding the colloidosomes. This is attributed to the fact that GOx tends to be situated on the inner edge of the colloidosomes and thus the signal favourably diffuses outward into the coacervate network. 2,3-DAP is also hydrophobic and so has greater affinity to the coacervate phase.

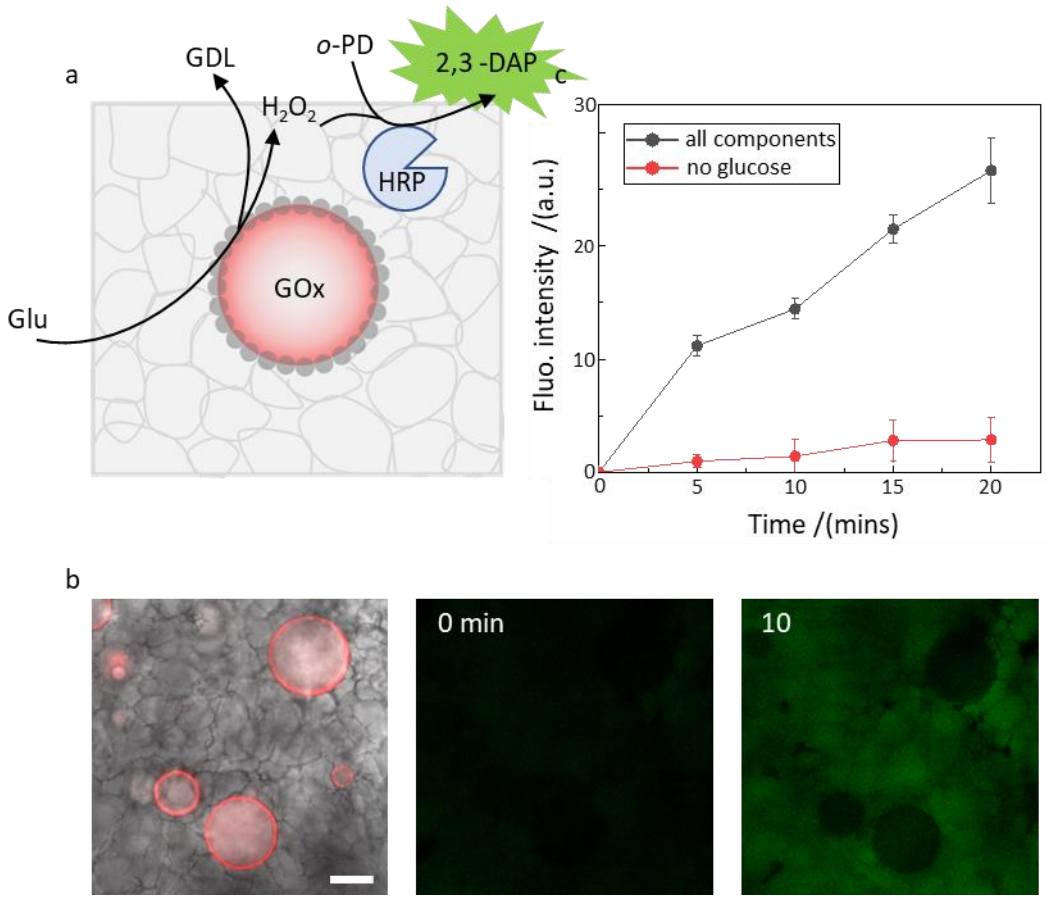

***Figure 4.26. GOx catalysis by GOx-loaded colloidosomes within a coacervate network. a**, Schematic showing GOx/glucose signal from large GOx-loaded colloidosomes encapsulated within a coacervate network. **b**, Grey and red merged CLSM image and green fluorescence filtered image of colloidosomes embedded into coacervate matrix at t=0 and t=10 min after the addition of final conc. d-glucose (0.15 M), o-PD (0.015 M) and HRP (0.2 mg ml^{-1}) at t=0 min. Scale bar, 50 µm. Error bars represent standard deviation (n=3).*

Similarly, signalling was shown by a *β*-glucosidase/*fluorescein* di-*β*-D-glucopyranoside hydrolysis reaction within the prototissue-like networks (figure 4.27a). *β*-glucosidase within the colloidosome hotspot initiated the cleavage of glucose from fluorescein di-*β*-D-glucopyranoside (FDGlu), leaving a fluorescent green fluorescein. In this case, green fluorescence dispersed quickly throughout the tissue and CLSM images are only collected in one plane, thus we cannot see fluorescence emerging directly from the colloidosome hotspot but rather throughout the coacervate network itself.

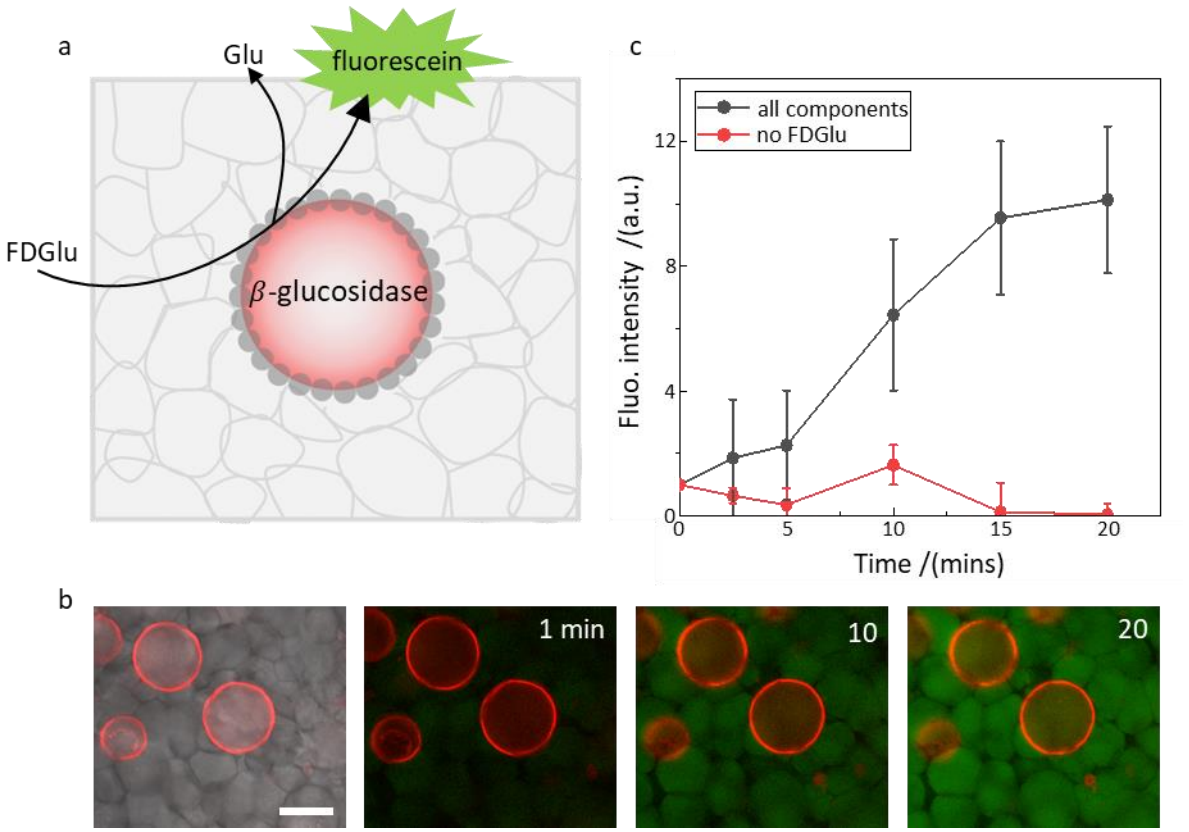

Figure 4.27. β-glucosidase catalysis by colloidosome within a coacervate network. a, *Schematic showing β -glucosidase/*fluorescein *di-*β*-D-glucopyranoside (FDGlu) hydrolysis signal from β -glucosidase-loaded colloidosome within a coacervate network.* ***b****, Grey and red merged CLSM image at t=0 and green-fluorescence filtered image of colloidosomes embedded into coacervate matrix at t=1, 10 and 20 min after the addition of* fluorescein *di-*β*-D-glucopyranoside final conc. = 0.025 mg ml^{-1}, at t=0 min. Scale bar, 50 µm. Error bars represent standard deviation (n=3).*

Furthermore, a GOx/HRP enzyme cascade was established between two segregated populations of colloidosomes immobilised within the coacervate tissue, as a comparative system to the hydrogel microspheres. As with previous systems, a communication pathway could be established between the two communities to produce a fluorescence output. However, this system gave a less localised fluorescence output, perhaps due to easier diffusion throughout the coacervate network compared to the crosslinked hydrogel or more macroscopic colloidosome segregation.

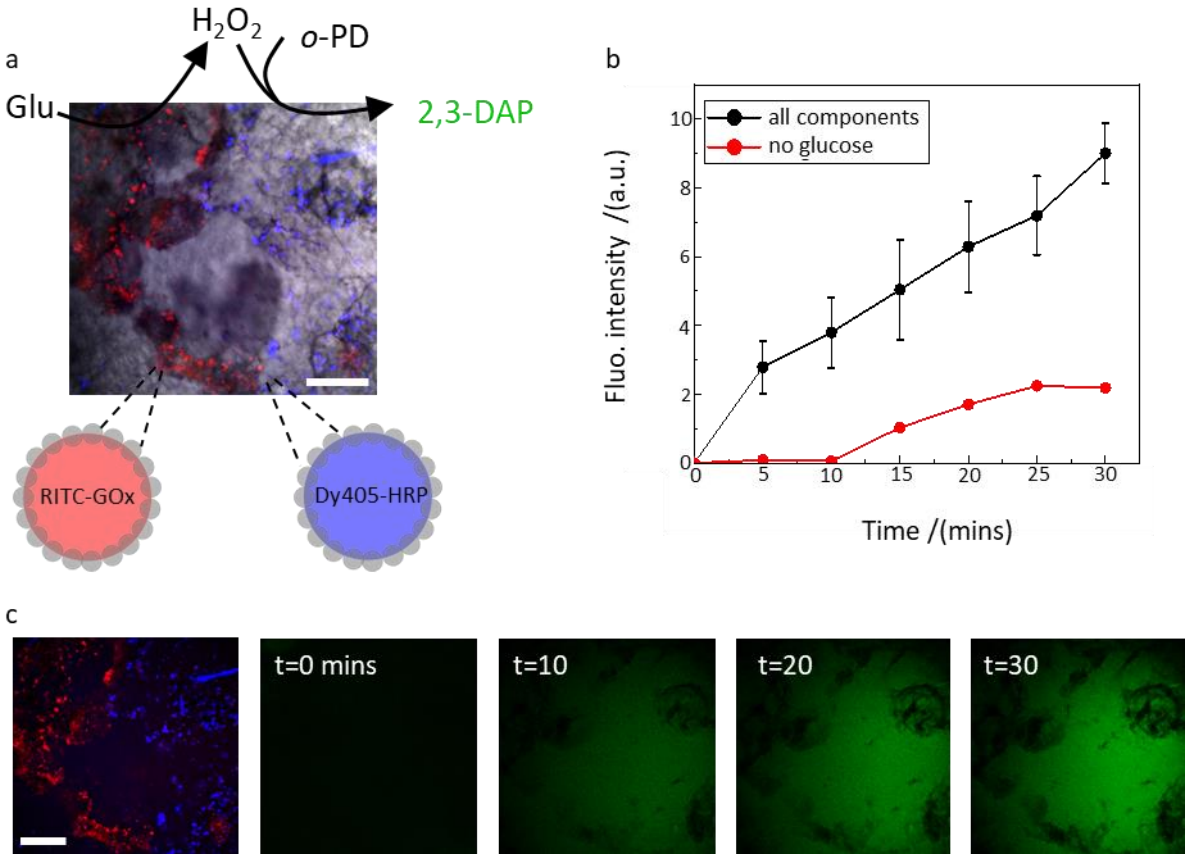

Figure 4.28. Communication between spatially segregated colloidosome populations within a coacervate network. a*, Bright field, and fluorescence overlay image of RITC-GOx loaded colloidosome community and Dy405-HRP loaded colloidosome community immobilised within a coacervate tissue. GOx/HRP enzyme cascade schematic shown over the image.* ***b****, Graph showing the overall increase in green-fluorescence intensity from the o-PD conversion to 2,3-DAP.* ***c****, Fluorescence images showing the appearance of green fluorescence within the coacervate network over a 30 min time period. Scale bars, 300 µm. Error bars represent standard deviation (n=3).*

Coacervate prototissues are capable of encapsulating colloidosomes that retain enzyme function and can therefore be used as a structural medium to support protocell signalling. Interestingly, reaction products can diffuse away from the colloidosomes and thus these colloidosomes can be used as signalling beacons housed within a coacervate prototissue-like network. One main advantage of a coacervate matrix could be combined bio-inspired activity between coacervates and colloidosomes.

4.3 Conclusions and future works

Enzyme-mediated signalling of colloidosomes can lead to communication between spatially segregated populations immobilised within an external matrix, whilst also nurturing an interactive protocell-environment relationship. Although through-space GOx/HRP enzyme networks have been established between many randomly arranged protocell systems, spatially organised GOx/HRP signalling has appeared more challenging due to the integration of patterning techniques with signalling pathways. Current spatially organised networks require an active external force to maintain order throughout a communication process, however in this chapter GOx/HRP signalling is achieved in a passive micropatterned system. Interestingly spatial organisation is observed to improve communication kinetics compared to randomly arranged populations. Cell-environment interactions underpin many living processes, yet to-date most protocell-based systems have focused on cell-cell interactions. In this chapter colloidosomes were therefore shown to interact with their external hydrogel matrix, specifically to change the hydrogel crosslinking properties and to realise a collective process.

Spatially segregated populations of GOx and HRP colloidosomes were shown to communicate with each other via enzyme mediated signalling of H_2O_2. The fluorescence output of 2,3-DAP from o-PD was initially localised to the HRP-loaded colloidosome population and thus a chemically rich hemisphere within the microsphere was achieved. The rate of 2,3-DAP production was higher in spatially segregated populations of GOx and HRP-loaded colloidosomes compared to a randomly mixed community of both GOx and HRP-loaded colloidosomes. This was attributed to a highly localised concentration of signalling molecule and thus large concentration gradient, increasing the rate of diffusion between each hemisphere.

Enzyme cascade reactions were also demonstrated between binary segregated colloidosome populations within a micro rod and segregated ternary internal arrangements in a microsphere. Both these experiments showed that increased complexity in the shape and internal patterning of hydrogel platforms, could be translated into higher order and more complex chemical communication pathways. Within the rod microsphere, the GOx/HRP cascade produced a fluorescence output, localised within the HRP colloidosomes section, akin to observations in the Janus system. In the ternary microsphere, the Suc/GOx/HRP cascade produced an output that was less obviously confined to the HRP section. This was attributed to the section being less well defined due to non-labelled HRP.

Collective behaviour between a binary segregated population of colloidosomes within a hydrogel microsphere was demonstrated. Firstly, URS colloidosomes were shown to disassemble a hydrogel platform due to the removal of Ca^{2+} crosslinking ions. Secondly, tyramine-alginate hydrogel microspheres were shown to covalently crosslink via exposure to HRP and H_2O_2. GOx-loaded colloidosomes were subsequently added into the microspheres to initiate the production of H_2O_2 through the oxidation of d-glucose, which aided their covalent crosslinking. Importantly, this illustrated localised colloidosome-environment interactions for the purpose of disassembling or assembling matrix platforms. URS-mediated and GOx-mediated colloidosome activities were combined into one micro spherical system, enabling the simultaneous covalent crosslinking of one hemisphere with the disassembly of the other hemisphere. This behaviour was controlled through collective enzyme-mediated communication between colloidosomes and their hydrogel environment. In the first instance, URS-mediated flux of carbonate resulted in disassembly of its corresponding domain, and subsequent release of the URS-containing colloidosomes over 20 h, while GOx-mediated production of H_2O_2 immobilised the GOx-colloidosome population in a second domain through covalent crosslinking. In the second instance, URS-mediated flux of carbonate resulted in disassembly of the opposite GOx-containing domain, and subsequent release of the GOx-containing colloidosomes over 20 h, while GOx-mediated production of H_2O_2 immobilised the URS-colloidosome population in an opposite domain through covalent crosslinking. This second instance illustrated a jettisoning system wherein unwanted material was ejected after its use and was proposed as a potential cell or drug delivery mechanism. In such experiments, URS-mediated disassembly was slow, and a high concentration of enzyme was required.

It was also shown that segregated populations of colloidosomes improved the rate of enzyme activities. This meant that a segregated population of colloidosomes was critical for the spatially controlled disassembly/resilience behaviour. Microspheres with segregated hemispheres of Alg and ty-Alg were prepared with a segregated population of colloidosomes and with a mixed population of colloidosomes. Over a 24 h period, the microspheres with a segregated colloidosome population showed collective disassembly of one hemisphere whereas the mixed colloidosome population failed to disassemble. It was also shown that the concentration of URS greatly affected the assembly/resilience process and thus by changing the concentration of URS, this collective behaviour could be programmed. Under a fixed GOx concentration, at high concentration of URS the hydrogel was completely disassembled due to insufficient flux of carbonate ions, at a concentration of URS 75-100 KU the collective process disassembled one domain, and at low concentration of URS the microsphere was not disassembled, implying that urease-mediated degradation of the Ca^{2+}-crosslinks was considerably faster in both hydrogel segments than GOx-mediated covalent crosslinking.

Programmed disassembly of a selected hydrogel domain to release colloidosomes into the environment demonstrates an advanced delivery system of cells upon a cue. However, the activity of colloidosomes once released into the environment has not yet been tested or developed. The released colloidosomes could be programmed to interact with a protocell population in the environment. In this way, the colloidosomes would be protected (from prey) within the hydrogel microsphere and then when they were released, they would interact with protocells in the environment to initiate a useful function. The colloidosome-protocell interaction would require contact-dependency so that communication was blocked by the hydrogel microsphere. Another piece of work could exploit potential communication between colloidosomes in one microsphere and colloidosomes in another microsphere. In this way a system could be developed combining Janus microspheres and homogeneous microspheres so that a segregated population might signal through the hydrogel matrix (replicating signalling through a tissue ECM) and then signal across an aqueous gap into another microsphere (replicating more distant signalling throughout the body).

Finally in this chapter, colloidosomes were used as signalling hotspots within a coacervate network. Colloidosomes received a chemical signal from the environment and then produced a fluorescence output that diffused away from the colloidosomes and into the surrounding coacervate tissue. In comparison to a hydrogel scaffold, these coacervate scaffold systems lacked microscale spatial control over the signalling output and did not improve the rate of communication. A rudimentary through-space GOx/HRP cascade was demonstrated between two spatially segregated colloidosome populations, however more sophisticated signalling might be developed to understand how colloidosome hotspots within a coacervate network might better mimic specialised cells within closely packed tissue structures. Furthermore, localised enzymes or genetic material loaded into the coacervate network might be interlinked with the colloidosome hotspots through signalling networks.

Chapter 3 showed that ECM-mimicking matrix-based networks can provide a good scaffold for the immobilisation of colloidosomes. Due to excellent levels of spatial control, especially by microfluidic preparation, these systems can be programmed for communication and collective behaviours exploiting close relationships between protocell populations and the matrix environment as shown in chapter 4.

CHAPTER 5

COMMUNICATION BETWEEN MATRIX-FREE SPATIALLY ORGANISED COLLOIDOSOMES

This chapter seeks to develop adaptive communication within matrix-free spatially organised colloidosome communities. This is attempted through the pH-responsive, self-assembly of colloidosomes, triggered by electrostatic and/or hydrogen-bonded interactions in an aqueous solution. As a technique for colloidosome self-assembly, alginate and chitosan polymers are grafted onto colloidosome silica nanoparticle membranes. At pH 4.5, salt-bridge interactions between oppositely charged polymer-coated colloidosomes lead to the formation of large aggregates comprising a binary colloidosome population. Different pH environments lead to changes in polymer charges and consequently the colloidosome surface charges. This in turn results in a corresponding change in protocell community organisation. Dynamic self-assembly reorganisation is therefore explored using endogenous GOx-mediated pH reduction, enabling the binary colloidosome population to cycle from a self-sorted arrangement, through a transient co-assembled state to a contrasting self-sorted system. This pH-responsive organisation is also used to develop a temporally controlled rate of communication between protocell communities, in the presence of a hostile environment.

5.1 Background

As discussed, living systems rely on cell-cell and cell-environment interactions to perform living processes. There is a close relationship between these interactions and cell order,[252] thus understanding spatially regulated interactions within living systems is foundational but complicated. Protocells can be used as simplified living cell mimics to understand how organised patterning is created through cellular interactions and how cellular communication may change because of organised patterning.

Cell organisation within living systems can be either fixed or dynamic.[253] Previous chapters have focused on fixed protocell organisation, specifically the matrix-based organisation of colloidosomes as suitable mimics of tissue-like living systems. Despite these matrix models providing an easy way to intricately pattern colloidosome populations within discrete structures, the immobilisation of protocells means that patterns are pre-determined, show minimal response to environmental changes, and tend to communicate through a potentially interruptive external medium. In nature, cells dynamically adjust to their environment and sensory inputs to change spatial states, proximity, and communicative behaviours.[254] For example, the immune system flexibly adapts in response to various pathogen doses for controlled responses[255], and bacterial competition influences the structural organisation of bacterial communities according to their metabolic and physiological needs.[256] Cells also undergo migration for living processes such as tissue development and maintenance.[257] These natural processes all depend on dynamic capability within cell communities, thus it is important to understand and mimic dynamic organisation using protocell chemistries.

Dynamic protocell organisation is commonly achieved by membrane-driven interactions. For example, proteinosomes have been self-sorted through photo switchable polymers[258] and predator-prey coupling has been realised through electrostatic interactions.[145] Although these examples show interesting dynamic interactions, their organisation is not directly related or influenced by the surrounding environment. The challenge is therefore to create a protocell system with organised complexity that dynamically responds to its environment. Consequently, this chapter adopts intermolecular/interprotocellular electrostatic and hydrogen bonding interactions between surface-modified colloidosomes as a strategy to create self-organised communities that respond to environmental pH fluctuations.

5.1.1 Non-covalent interactions

Intermolecular forces between molecules within a polymer chain are intrinsic to how polymers interact with each other and potentially self-organise. Intermolecular interactions tend to be much weaker than typical intramolecular interactions. In general, the strength of covalent and ionic bonding varies from 150 - 650 kJ mol^{-1} whereas the strength of intermolecular interactions remain typically <100 kJ mol^{-1}.[259] This weaker bond property enables transitions between structures, which often leads to materials that are responsive to external stimuli. Intermolecular forces play a critical role within living systems. In protein structures the interaction between oppositely charged residues < 5 Å apart is usually called a salt-bridge interaction and has a strength of 12 kJ mol^{-1}.[260] Charged and polar groups on proteins can form salt-bridges and other less specific electrostatic interactions to enable various functions such as maintaining secondary/tertiary structures and controlling paired interactions/complexes (figure 5.1a).[261] Electrostatic interactions are also important on the macroscale, such as when bacteria assemble into biofilms (figure 5.1b).[262]

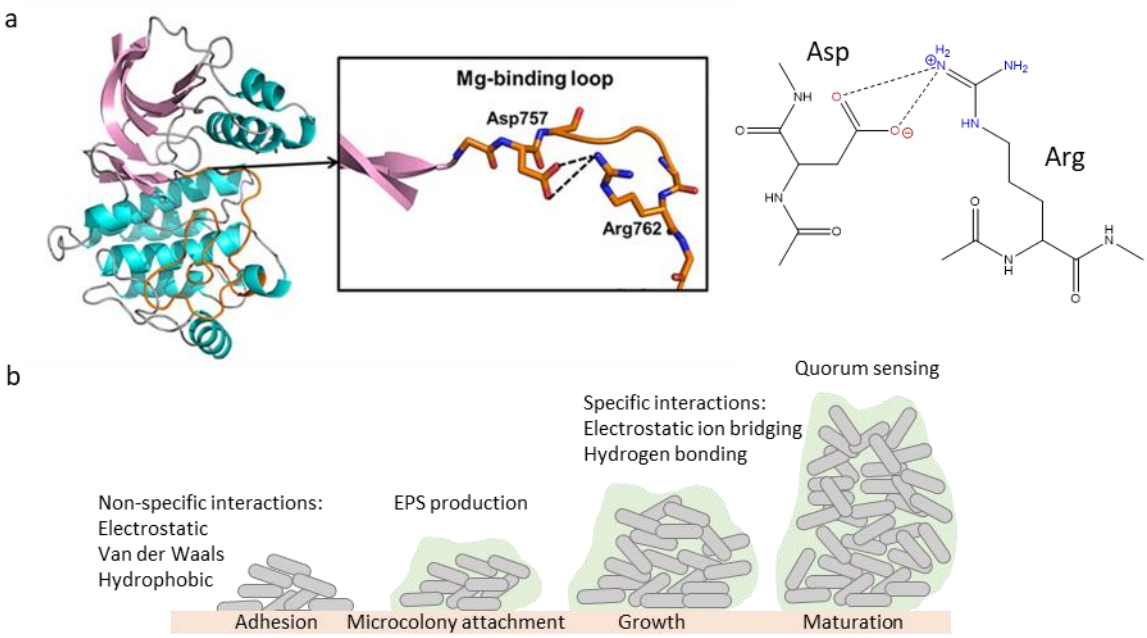

***Figure 5.1. Electrostatic interactions in living systems. a**, Salt-bridge interactions between arginine (Arg) and aspartic (Asp) amino residues in the structure of autoinhibited EphA2 tyrosine kinase. Reproduced and adapted from papers by Q. Wei et al. and S. Pylaeva et al. under CC BY 4.0.*[261] ***b**, The development of a biofilm comprising bacteria (grey) and extracellular polymeric substance (EPS, green. Key interactions and processes noted.*[262,263]

5.1.2 Hydrogen bonding

Hydrogen bonding is a particularly strong type of intermolecular force, with literature strength values typically range from 2 - 20 kJ mol^{-1}.[264] In a hydrogen bond, a small hydrogen atom is bonded to particularly electronegative atoms such as oxygen, nitrogen, or fluorine. The partial positive charge on the hydrogen atom is attracted to the opposite partial negative charge on the other molecule, resulting in a strong interaction between the two molecules.[265]

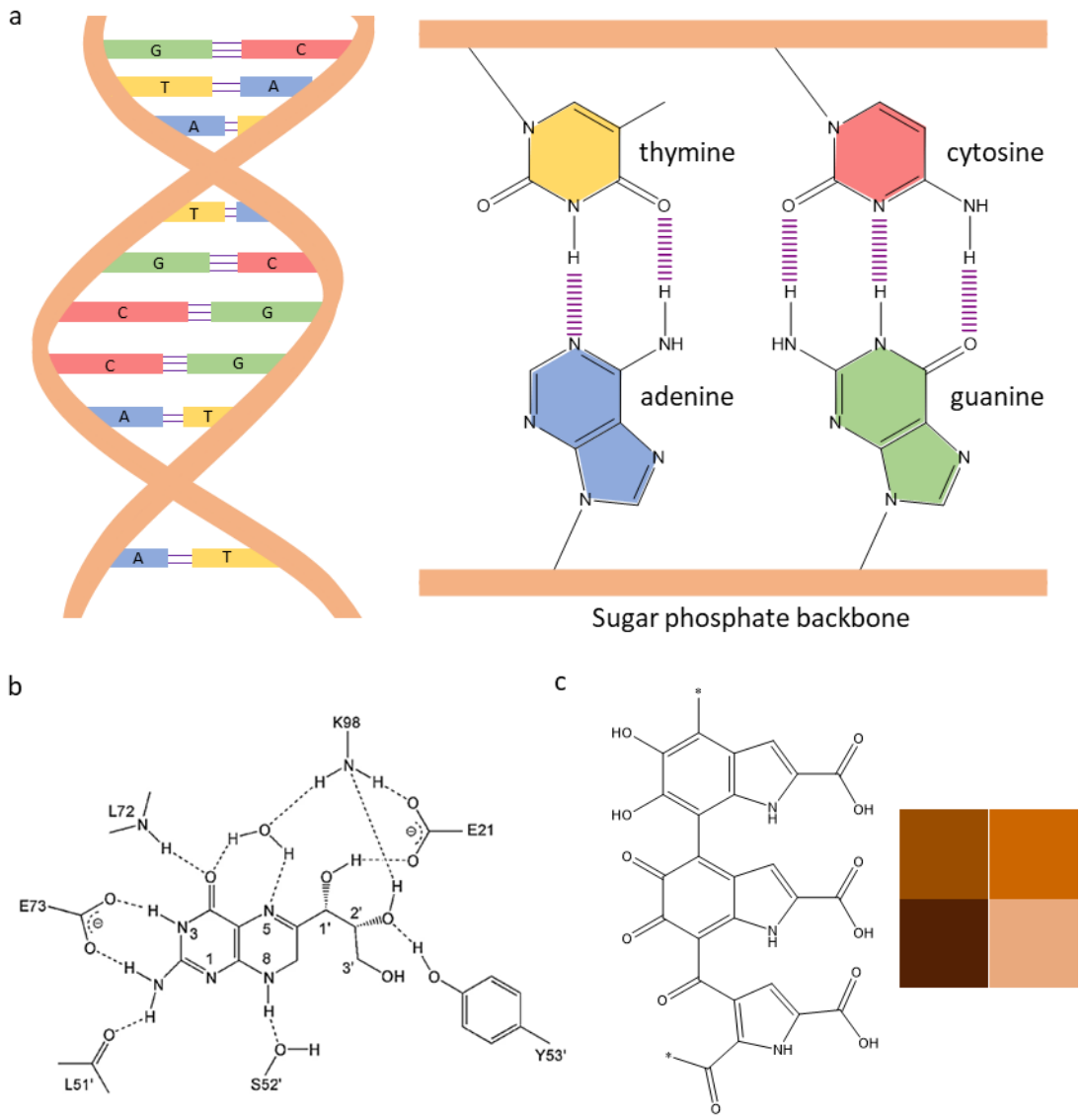

Figure 5.2. Hydrogen bonding in living systems. ***a****, Hydrogen bonding between base pairs in Watson-Crick DNA model.*[266] ***b****, Hydrogen bonding in enzyme:substrate complex, specifically to anchor DHNP substrate in EcDHNA complex. Reproduced from paper by J. Blaszczyk et al. CC BY 4.0.*[267] ***c****, An example of the polymerised heterocycles that comprise melanin and could lead to possible hydrogen bonding. Skin tone images as an example of the physical appearance when a body produces different levels of melanin.*[268]

Within living systems hydrogen bonding is crucial for DNA double helix formation, as described by Watson and Crick[269] (figure 5.2a) and is often central to secondary and tertiary protein folding. Hydrogen bonding is also important in many paired interactions between biomolecules, for example in enzyme-substrate binding (figure 5.2b). Despite the fact that biological systems are vastly complex, hydrogen bonding is often deemed critical for many processes, such as the interactions between eumelanin which is responsible for hair and skin colour (figure 5.2c).[268]

Intermolecular interactions are fundamental to the relationship between polymers and are ubiquitous within living systmes. In this chapter, polymer intermolecular forces are exploited to control protocell interactions. Importantly, in a similar way to nature, modulation of charges causes significant effects on protocell organisation and behaviour.

5.1.3 Signalling and spatial proximity

Exploiting intermolecular interactions between polymer-coated protocells provides a route towards spatially controlled protocell communication and interactivity. Spatial control is important in living systems, as sender-receiver cell signalling depends on cell proximities. As mentioned in this thesis introduction, signalling proximities can be characterised by terms autocrine, juxtracrine, paracrine and endocrine (figure 1.4). Autocrine signalling occurs in many living systems for functions such as embryo development and proliferation of T-cells. Within synthetic cells, autocrine communication has been shown by simple enzyme cascades within and related to a single protocell.[270] In living systems juxtracrine communication (inter cell distance (L) and size (d), L = d) is observed between killer immune cells and target cells to release a killing signal. This process has been somewhat mimicked in a synthetic system.[145] Paracrine cell communication (L > d) in living systems is observed by synaptic signalling and in synthetic cases by enzyme cascades between spatially distributed protocells.[79] Finally, endocrine communication (L >> d), is often seen in multicellular organisms through the transportation of hormones through the circulatory system.[65] In synthetic systems, giant vesicles have demonstrated signal amplification over longer length scales. [69]

Importantly, a change in proximity can modulate receiver signal intensities which can result in a change of communication rate. Communication often relies on the exchange of a chemical signal through molecular diffusion from one cell to another, following normal diffusion dynamics. This means that receiver cells at a greater distance away from the sender take longer to receive a signal and that the signal is often weaker due to diffusion effects (figure 5.3a,b). In addition, a longer diffusion path exposes the communication sequence to potential issues. For example, the signal

could be interrupted by other molecules (figure 5.3c) or by broken pathways (figure 5.3d). Diseases often occur when communication breaks down in this way, such as in multiple sclerosis which occurs when the synaptic pathway is interrupted.[271] Living cells dynamically adjust their spatial organisation and number density, to control intercell distances, for monitoring signalling networks. Although spatial proximity in artificial cells can be controlled by microfluidics, acoustic trapping and optical tweezers, dynamic and adaptive proximity control has thus far received minimal attention. Therefore, the aim of this chapter is to explore dynamic self-sorting and proximity control through polymer interactions, and to monitor the influence on communication pathways.

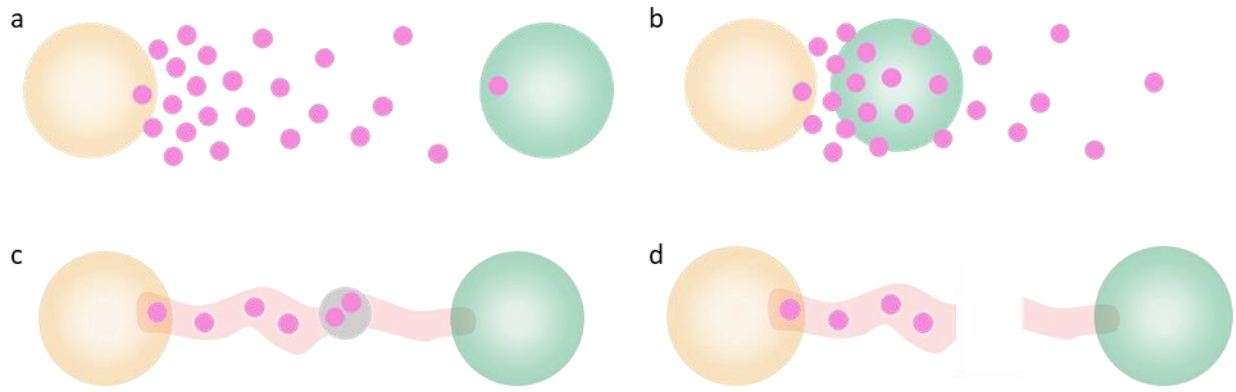

***Figure 5.3. The effect of distance on signalling. a**, Weak signal due to diffusion effects and distance of receiver cell (green). **b**, Stronger signal due to close proximity of receiver cell. **c**, Hostile molecule consuming signal from sender cell before it reaches the receiver cell. **d**, Broken or damaged signalling pathway between sender (yellow and receiver cell.*

5.1.4 Living cell dynamic aggregation

There are many examples highlighting how living systems adapt to their environment in order to change their spatial organisation, spatial proximity and ultimately the communication and interaction between cell communities. Notably, the immune system must have organisational flexibility so that it can respond to various doses of pathogen. Signalling over shorter length scales (less than an organ) can result in localised signal concentration domains that lead to these variable cell responses and in turn, diverging paths of differentiation.[255] Moreover, bacterial cell communities are organised and patterned by interactions and competition between neighbouring cells and the external environment, according to their metabolic and physical needs. As a result, the organisation of these communities dynamically changes when such environments change, for example bacteria in the gastrointestinal tract.[256] Furthermore, sorting and organisation of biological components is ubiquitous within cell

structures. Examples include the feedback loop between biochemical and mechanical properties of actin organisation[272] and the mitotic spindle.[273]

5.1.5 Colloidal aggregation

As discussed, cell-cell proximity has a significant effect on the interactions and communications within living systems. Dynamic and adaptable cell organisation is used to control cell proximity and thus tune cellular interactions. Mimicking dynamic cell proximity/organisation using protocells could therefore provide insight into how and why cells organise. As a synthetic guide for the self-assembly and self-sorting between protocell compartments, colloid self-assembly and self-sorting has been studied. There are many ways in which colloids have attained reversible co-assembled structures from external triggers such as temperature, light and pH. For example, thermo-responsive peptides[274] and polymers[275] have been attached to gold nanoparticles for temperature controlled self-assembly. Complementary DNA strands attached to the surface of micrometre sized colloids have also been carefully assembled and optically manipulated into more organised patterns and annealed upon heating.[276] Temperature-dependent self-assembly is well researched in these systems, however high temperatures are not practical for cell-mimicking systems due to denaturing effects. Light-induced self-assembly has been developed in systems involving spiropyrans[277], nitrobenzene cleavage, and host-guest interactions[278], which could offer more biologically promising self-assembly mechanisms.

Beyond self-assembled structures, colloidal particles can be self-sorted into categorised communities. This has been demonstrated through selective αCD/azobenzene[278,279] and βCD/ferrocene[280] polymer host-guest interactions, and by blue/red light protein interactions. In the first instance, a community of four different colloids, coated in polymers with either αCD, βCD, azobenzene or ferrocene functionality has been separated into two different clusters with variable ratios.[279] In the latter example, colloid particles with either blue or red light-sensitive proteins have been self-assembled under specific light condition and thus under light of one colour, one community can narcissistically self-sort.[281] Furthermore, colloid systems can show self-regulatory properties by accelerating their own destruction through the co-assembly of enzyme-loaded microgels. In this system close proximity enhances an acid-producing enzyme cascade that accelerates the microgel disassembly.[282]

5.1.6 Protocell self-sorting

Implementing colloidal self-sorting techniques into protocell systems can afford self-assembled and sorted arrangements that mimic dynamic living cell networks. However, to-date there are limited examples. Despite being on a small scale and relying on several types of interactions, a predator-prey system exploits selective attraction between two protocells through electrostatic interactions. In a recent example, three populations of proteinosomes have been self-sorted via complementary protein adhesion to communicate through DNA signalling. Red and blue light responsive protein-protein interactions act as membrane adhesion mediators so that self-sorted and self-assembled multiprotocellular structures can be realised.[258] In this way, protocells have been used to mimic the spatial organisation of sender receiver cells for short range paracrine biological communication. Dynamic spatial and structural organisation can also be displayed within the internal structuring of protocells. As an example, protein structural organisation within a GUV, in response to external pH, can initiate the activation of enzyme signalling.[283]

5.1.7 Background conclusions

In conclusion, spatial organisation in living systems is intrinsic to living interactions/behaviours. There are four types of signalling in living systems, categorised by cell proximities: autocrine, juxtracrine, paracrine and endocrine. Cell-cell proximity affects signalling strength such that cells further away experience weaker signalling due to diffusion and are exposed to potential threats. In nature, signalling systems are flexible so that dynamic adaptability in organisations can change cell-cell proximity and thus change communication pathways in response to external stimuli. Although there are several examples of dynamic organisation in colloidal systems, there are few examples in protocell communities. This chapter develops dynamic self-sorting in colloidosome communities and reviews the effect of proximity on communication, especially in the presence of a hostile guest.

5.2 Results and Discussion

5.2.1 Polymer attachment to colloidosomes

In the following work, co-assembled and self-sorted protocell systems were fabricated through intermolecular interactions between a binary population of polymer-functionalised silica-membrane colloidosomes. This was achieved by grafting alginate and chitosan polymers onto the silica membrane of colloidosomes using a (3-Glycidyloxypropyl) trimethyoxysilane (GLYMO) strategy. GLYMO was added shortly after the tetramethyl orthosilicate (TMOS) crosslinking step, to introduce an active epoxide into the crosslinked membrane of the colloidosomes. After being transferred to water, either alginate or chitosan polymer (aq. 0.09 wt.%) was mixed with the colloidosomes (24 h), therein initiating epoxide ring opening and appendage binding of the polymers via hydroxyl groups on the polymer chains (method 2.5.1.). Alginate and chitosan polymers were chosen due to their oppositely charged functional groups and thus the potential for aggregation. In addition, both polymers are biocompatible, possess relatively long and simple chains, and chitosan has already been attached to colloidosomes in previous literature.[13]

A dispersed population of FITC-GOx-loaded colloidosomes coated in RITC-Alg, was confirmed using CLSM imaging (figure 5.4). Close analysis of a single alginate-coated colloidosome, confirmed the appearance of an FITC-GOx (green) inner ring and an RITC-Alg (red) outer ring. As with observations in the previous chapter, FITC-GOx showed a high affinity to the silica membrane and thus congregated in a ring formation around the interior edge of the colloidosome. This was attributed to one side of the GOx surface being positively charged and thus being attracted to the negative silica nanoparticle colloidosome membrane. A fluorescence intensity profile (figure 5.4f) through the diameter of a single colloidosome (yellow dotted line) further confirmed RITC-Alg (red line) surrounding the outside of the FITC-GOx loaded colloidosome (green line) wherein the GOx was attracted to the colloidosome circumference. 3D reconstructed images showed that alginate was unevenly distributed around the colloidosome, which could be due to uneven interaction of the colloidosome walls with dissolved polymer chains (figure 5.4g,h).

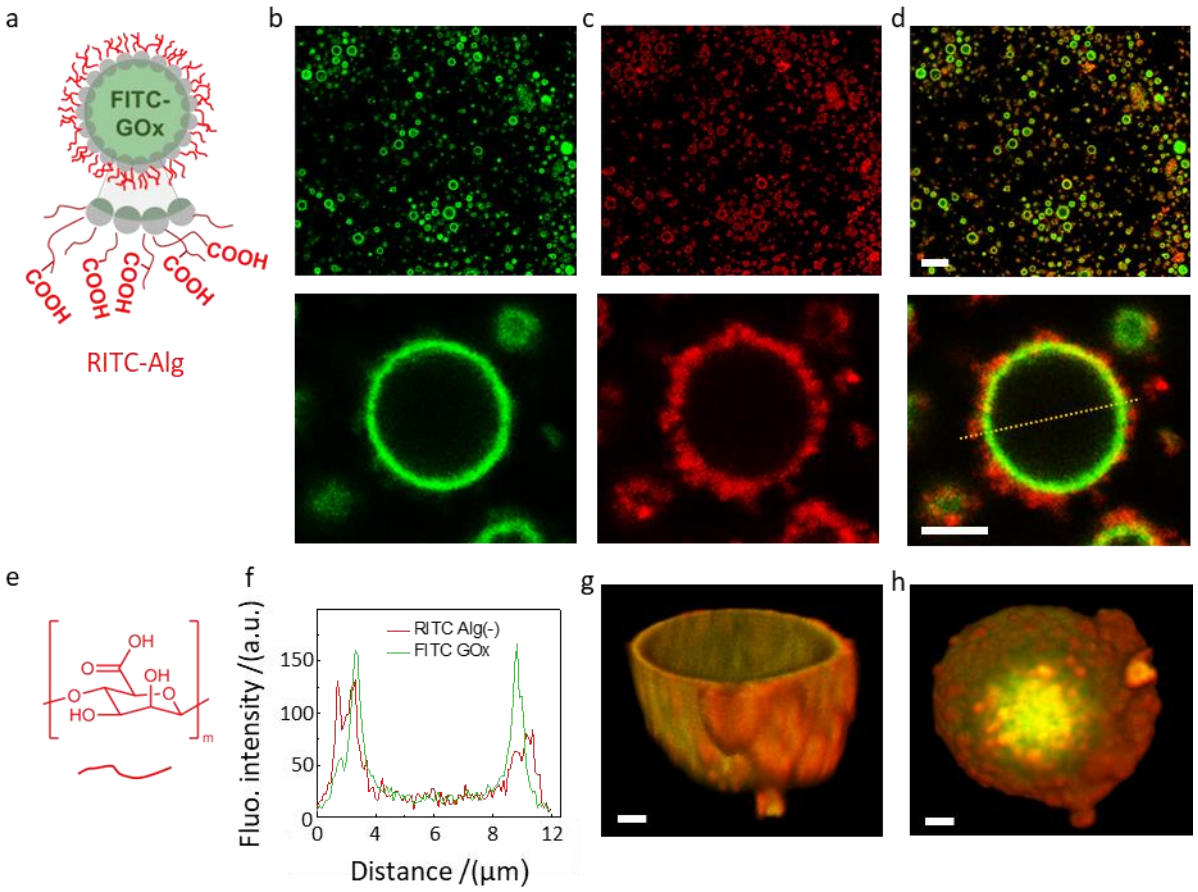

Figure 5.4. Alginate-coated GOx-loaded colloidosomes. ***a****, Diagram showing FITC-GOx-loaded colloidosome with RITC-Alg polymer attached to the silica nanoparticle membrane.* ***b****,* ***c****,* ***d****, Green fluorescence filtered image (**b**), red fluorescence filtered image (**c**) and red/green overlay image (**d**) of colloidosomes described in (**a**) with zoomed image displaying one colloidosome. Scale bars, 10 (zoomed-out) and 4 (zoomed-in) µm.* ***e****, Chemical structure of alginate polymer.* ***f****, Fluorescence intensity profile across the diameter (yellow line) of single colloidosome in (**d**) depicting green and red fluorescence channels.* ***g****,**h****, Side view (**g**) and bottom view (**h**) of 3D reconstructed colloidosome as described in (**a**). Scale bars, 2 µm.*

The attachment of alginate to colloidosome membranes was further analysed using zeta potential and size distribution measurments (figure 5.5). Uncoated colloidosomes had an average dimater of 4.23 µm, in comparison to alginate-coated colloidosomes which had an average diameter of 4.94 µm. This showed a diameter increase upon addition of alginate to the silica membrane. However, the distribution width in coated colloidosomes was slightly greater than in uncoated colloidosomes and thus the small change in size could be attributed to a wider spread in the data. Uncoated colloidosomes had a negative surface charge due to the silica nanoparticle membrane. Upon addition of alginate at pH 5, the surface charge decreased (figure 5.5d). This was atttributed to the negative charge of carboxylate groups on the alginate polymer.

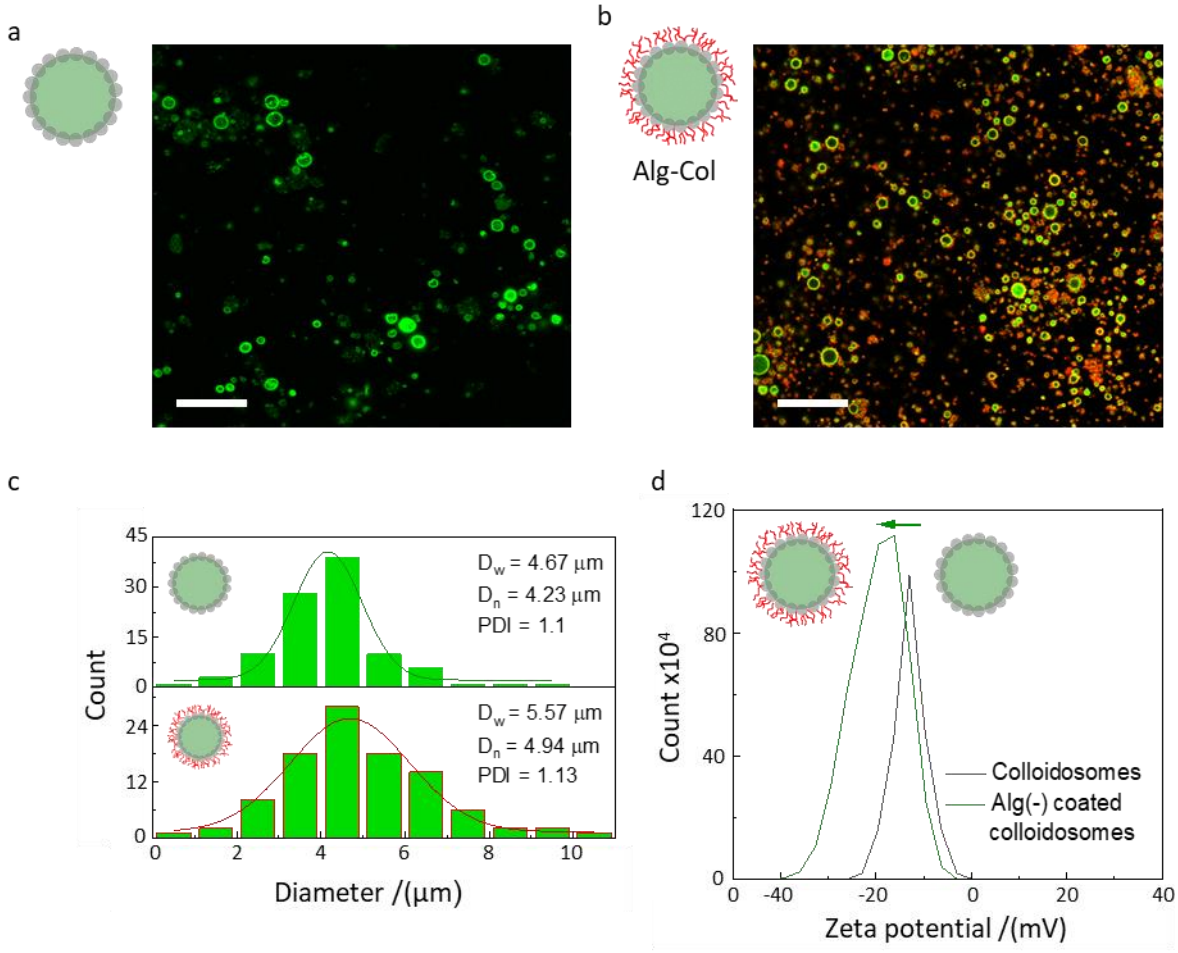

Figure 5.5. Comparative size and zeta potential of uncoated and alginate-coated colloidosomes. a, b*, Schematic and CLSM image of uncoated (**a**) and RITC-alginate-coated (**b**) FITC-GOx loaded colloidosomes. **c**, Size distribution of uncoated (top) and alginate-coated (bottom) FITC-GOx loaded colloidosomes showing an average diameter (D_n) = 4.23 and 4.94 respectively. **d**, Zeta potential of uncoated (grey line) and alginate-coated (green line) FITC-GOx loaded colloidosomes showing a shift to more negative charge upon alginate coating.*

Chitosan attachment to colloidosome membranes was analysed in the same way as the alginate-coated colloidosomes. A dispersed population of RITC-GOx-loaded colloidosomes coated in FITC-chitosan (FITC-Ch), was confirmed using CLSM imaging (figure 5.6). Close analysis of a single chitosan-coated colloidosome confirmed the appearance of an RITC-GOx inner ring (red) and an FITC-Ch outer ring (green). Again, RITC-GOx showed affinity to the silica membrane and thus congregated in a ring around the edge of the colloidosome interior. A fluorescence intensity profile through the diameter of a single colloidosome (yellow dotted line) further confirmed FITC-Ch (green line) surrounding the outside of the RITC-GOx loaded colloidosome (red line) wherein the GOx was attracted to the colloidosome circumference. Again, 3D reconstructed images showed that chitosan was unevenly distributed around the colloidosome.

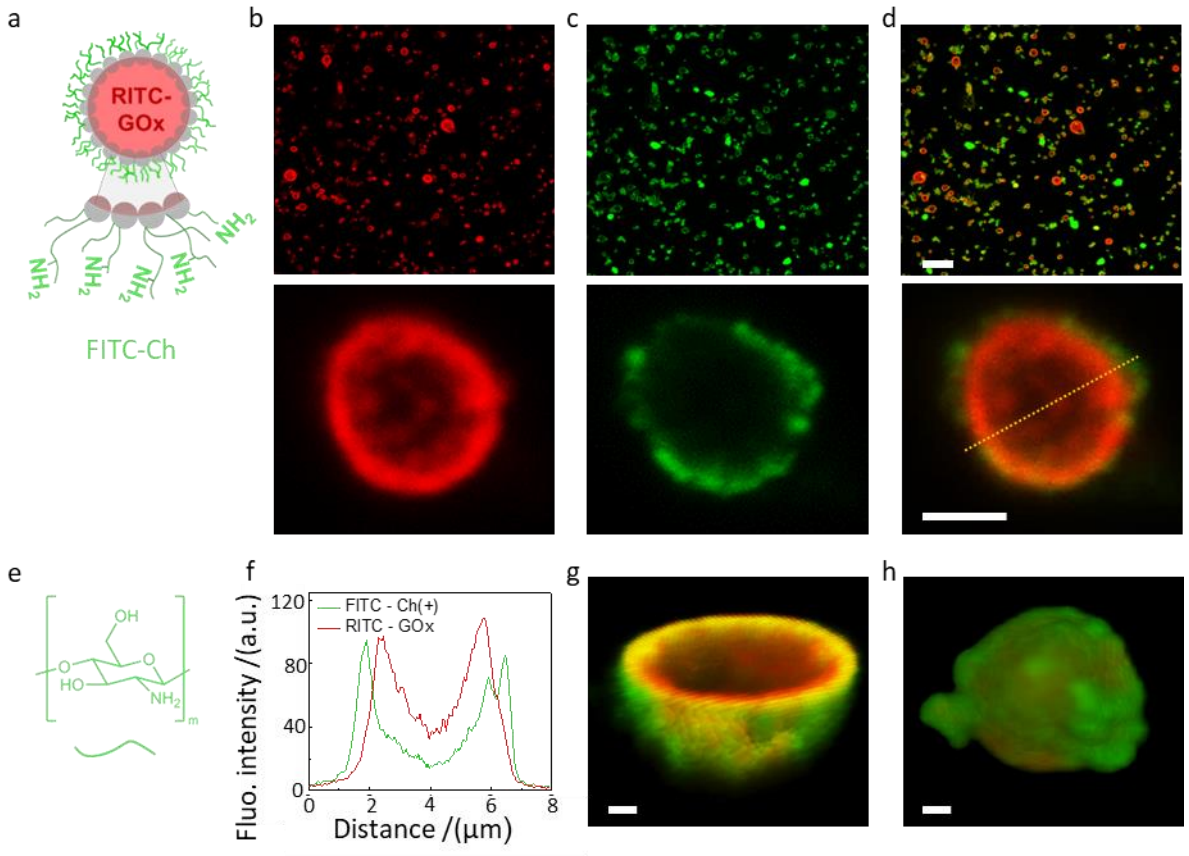

Figure 5.6. Chitosan-coated GOx-loaded colloidosomes. ***a****, Diagram showing RITC-GOx-loaded colloidosome with FITC-chitosan polymer attached to the silica nanoparticle membrane.* ***b****,* ***c****,* ***d****, Red fluorescence filtered image (**b**), green fluorescence filtered image (**c**) and red/green overlay image (**d**) of colloidosomes described in (**a**) with zoomed-in image of one colloidosome. Scale bars, 10 (zoomed-out) and 4 (zoomed-in) µm.* ***e****, Chemical structure of chitosan polymer.* ***f****, Fluorescence intensity profile across the diameter (yellow line) of single colloidosome in (**d**) depicting green and red fluorescence channels.* ***g****,**h****, Side view (**g**) and bottom view (**h**) of 3D reconstructed colloidosome as described in (**a**). Scale bars, 2 µm.*

The attachment of chitosan to colloidosomes was further analysed using zeta potential and size distribution measurments (figure 5.7). Uncoated colloidosomes had an average diamater of 4.23 µm, in comparison to chitosan-coated colloidosomes with an average diameter of 4.72 µm. This showed a negligible diameter increase upon addition of chitosan to the silica membrane. Uncoated colloidosomes had a negative surface charge of -19.3 mV, however at pH 5 upon addition of chitosan, the surface charge increased to a positive surface charge of +22 mV, due to positively charged amine groups on the chitosan polymer (figure 5.7d).

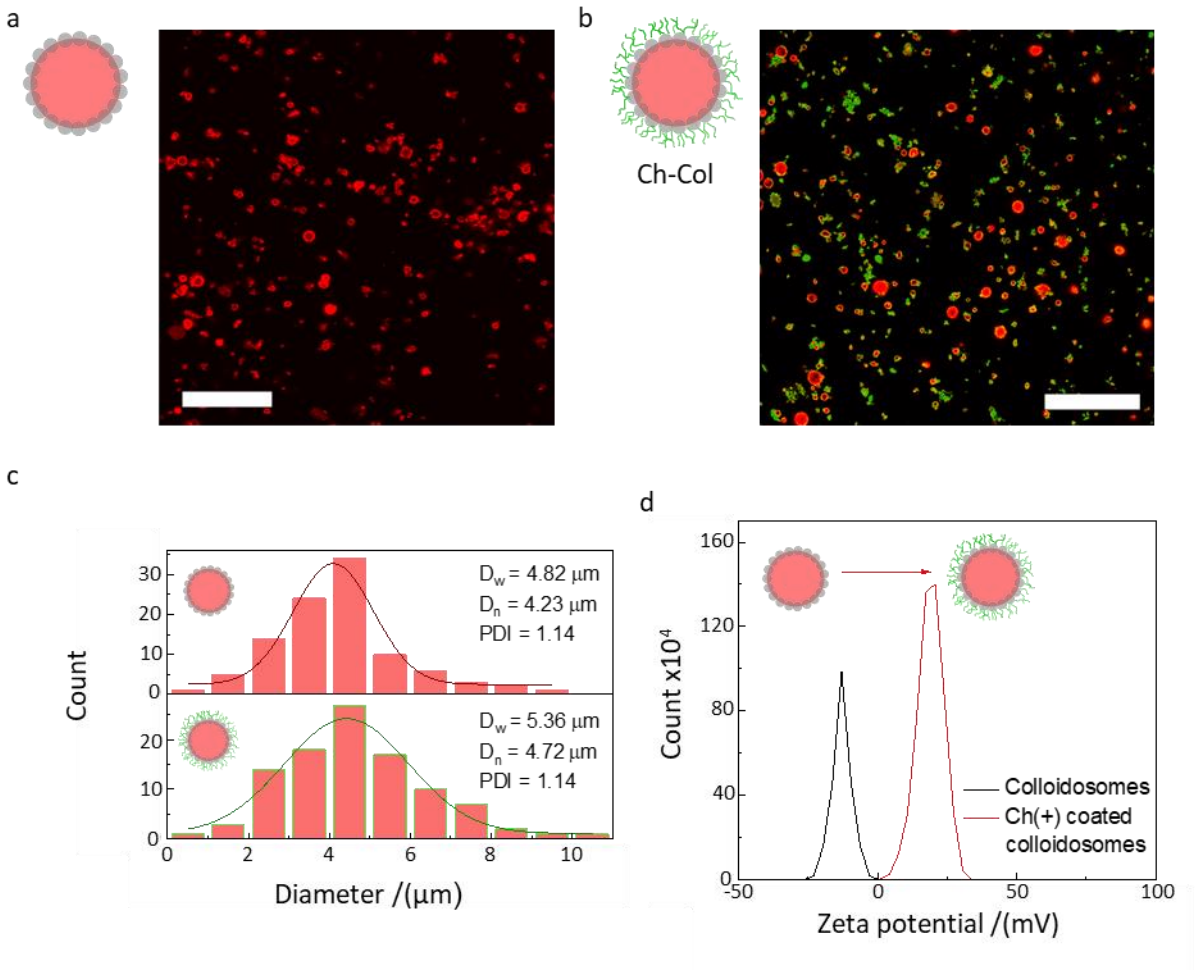

***Figure 5.7. Comparative size and zeta potential of uncoated and chitosan-coated colloidosomes. a**, **b**, Schematic and CLSM image of uncoated (**a**) and FITC-chitosan-coated (**b**) RITC-GOx loaded colloidosomes. **c**, Size distribution of uncoated (top) and chitosan-coated (bottom) RITC-GOx loaded colloidosomes showing an average diameter (D_n) = 4.23 and 4.72 respectively. **d**, Zeta potential of uncoated (grey line) and chitosan-coated (red line) RITC-GOx loaded colloidosomes showing a shift to more positive charge upon chitosan coating.*

Alginate-coated colloidosomes were also analysed at higher resolution using scanning electron microscopy (SEM) techniques (Figure 5.8). Upon alginate binding at the silica nanoparticle membrane the colloidosome exterior appeared rougher and more textured, attributed to the polymer hairs and clusters. Scanning transmission electron microscopy–dark field (STEM-DF) was used in conjunction with energy dispersive x-ray spectroscopy (EDX) to further confirm the presence of alginate hairs on the colloidosome membrane. STEM-DF images of alginate-coated colloidosomes showed an uneven, cloud-like halo structure. This was compared to the sharper, more defined edge that surrounded the uncoated colloidosome. A minimal amount of Ca^{2+} was added to uncoated and alginate-coated colloidosome samples, as a method to crosslink the alginate polymer coating bound to the colloidosome membranes, without crosslinking colloidosomes together. In the uncoated

colloidosome sample, Ca^{2+} could not be retained in the washing step and was therefore washed clean, resulting in no Ca signal from EDX analysis. Conversely, in the alginate-coated colloidosomes, Ca^{2+} remained in the sample due to being involved in alginate crosslinking. This resulted in a strong Ca signal observed in EDX analysis (figure 5.8e). High-definition analysis therefore confirms that alginate was successfully grafted to the colloidosome exterior.

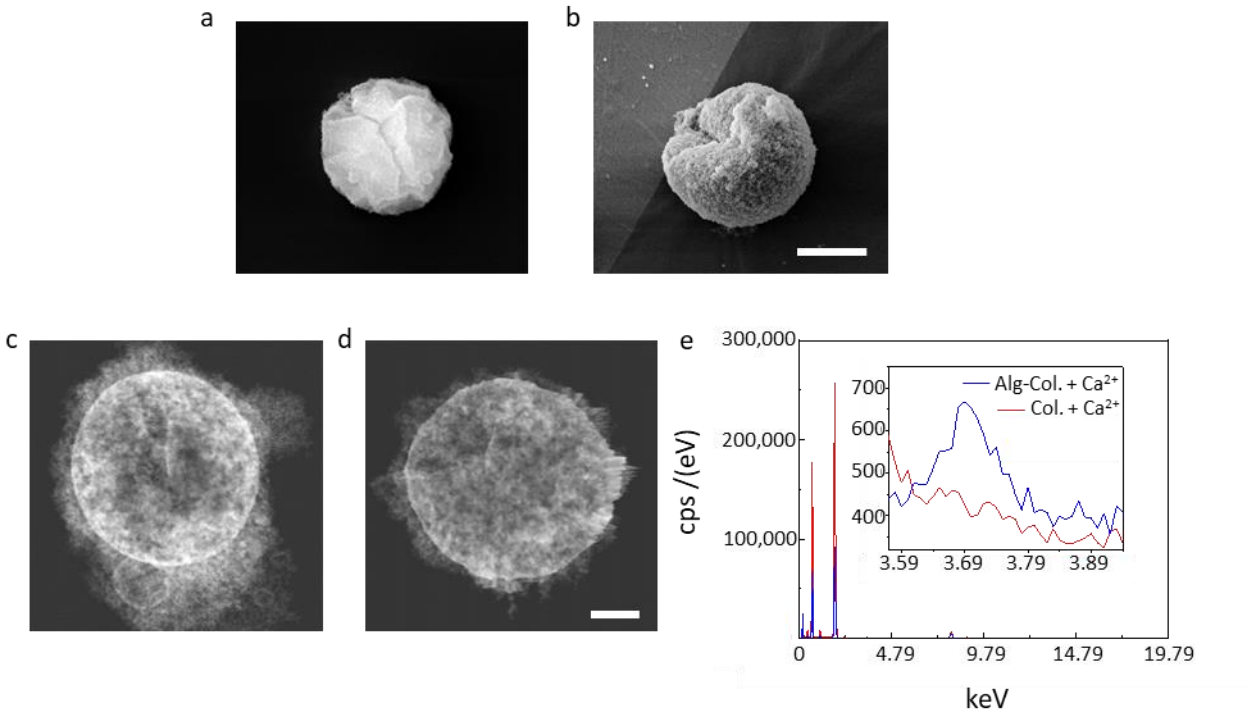

Figure 5.8. Structural characterisation of alginate coated and uncoated colloidosomes. a, b*, SEM images of uncoated (**a**) and alginate-coated (**b**) colloidosome. Scale bar, 4 µm.* ***c, d****, STEM-DF image of uncoated (**c**) and alginate-coated (**b**) colloidosome. Scale bar, 500 nm.* ***e****, EDX analysis of Ca^{2+} loaded uncoated and alginate-coated colloidosome with inset showing Ca^{2+} peak in alginate-coated colloidosome.*

The function of GLYMO in the polymer binding process was analysed by Fourier-Transformation Infrared Spectroscopy (FT-IR). FT-IR confirmed the appearance of epoxide ring modes at 849 (symmetric C-O-C stretch) and 912 (asymmetric C-O-C stretch) cm^{-1} in a dry sample of GLYMO coated colloidosomes isolated at an intermediate step. These epoxide modes subsequently disappeared when polymer was added, demonstrating the opening of the GLYMO epoxide ring and binding of polymers (Figure 5.9).

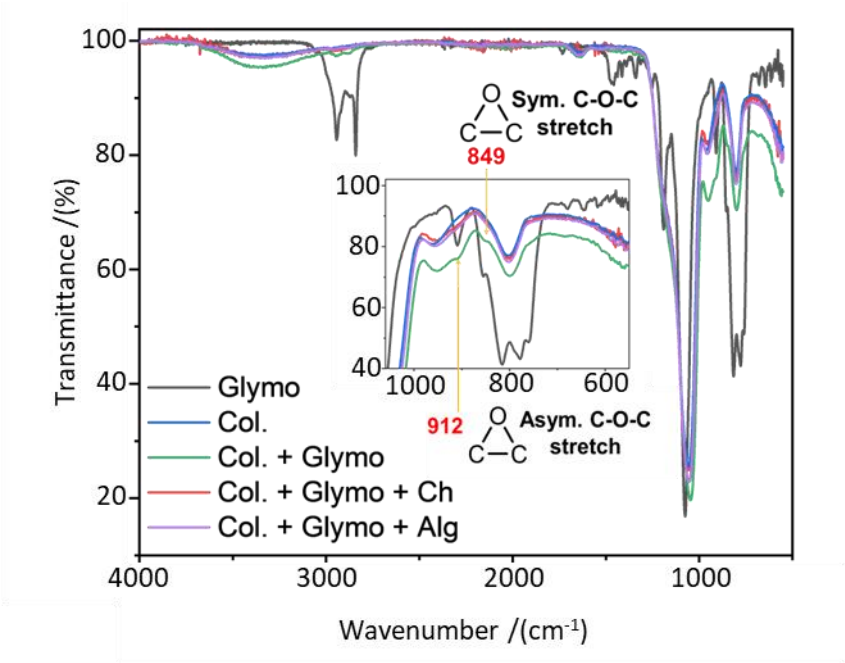

Figure 5.9. Mechanistic characterisation of GLYMO ring opening polymer binding to colloidosome surface. *FITR spectra for GLYMO (black), uncoated colloidosomes (blue), GLYMO-coated colloidosomes, an intermediate for the polymer coating of colloidosomes (green), chitosan-coated colloidosomes (red) and alginate-coated colloidosomes (purple). Inset shows zoomed in FTIR region of interest indicating epoxide ring stretches. All colloidosome samples were transferred to water and air-dried before the spectra was recorded.*

The significance of a GLYMO step was also confirmed by comparing CLSM images of polymer-coated colloidosomes made via the original GLYMO-inclusive technique and in the absence of a GLYMO step. FITC-GOx colloidosomes were fabricated using TMOS crosslinking, followed by the addition of RITC-Alg, in the absence of GLYMO. Similarly, RITC-GOx colloidosomes were fabricated with TMOS, followed by the addition of FITC-Ch in the absence of GLYMO. After washing steps, both samples showed minimal fluorescence from the added polymers (figure 5.10). This suggested that alginate and chitosan had been unable to attach to the silica membrane in the absence of GLYMO. Fluorescence line profiles across individual colloidosomes only showed fluorescence from the interior GOx enzyme.

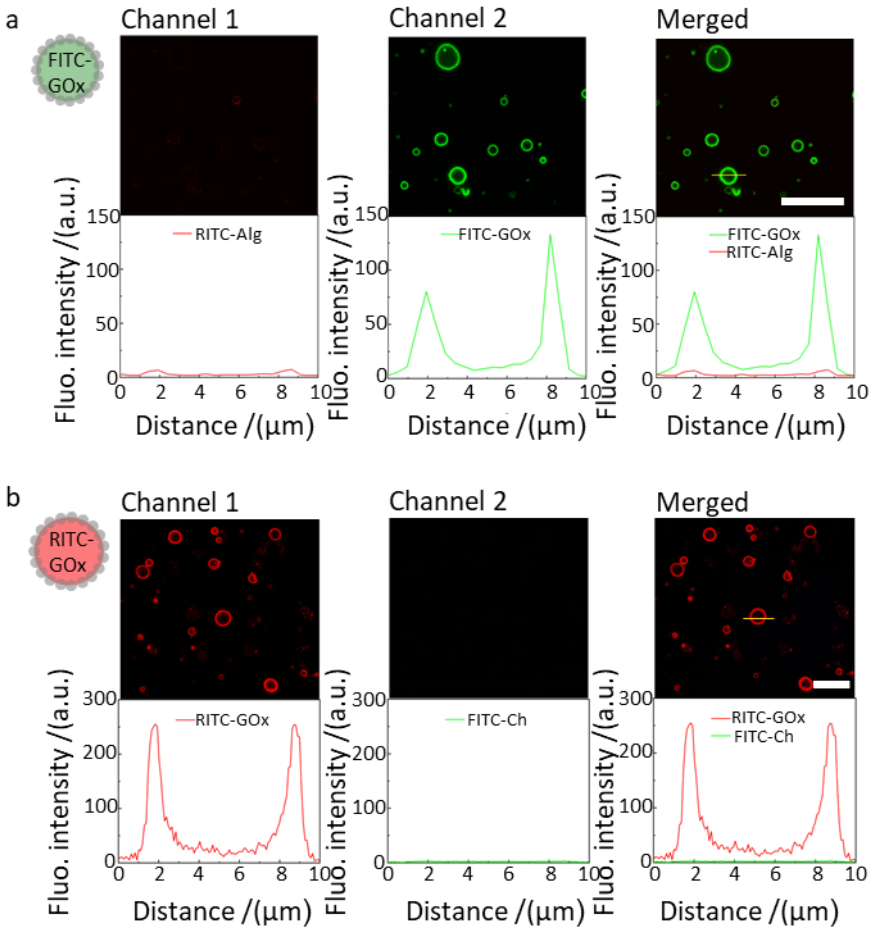

Figure 5.10. Unsuccessful polymer coating of GOx-loaded colloidosomes in the absence of GLYMO. ***a****, Filtered red (channel 1), green (channel 2) and merged CLSM images with corresponding fluorescence intensity profiles across single FITC-GOx-loaded colloidosomes fabricated in the absence of GLYMO and after the addition of RITC-alginate (yellow line)* ***b****, Filtered red (channel 1), green (channel 2) and merged CLSM images with corresponding fluorescence intensity profiles across single RITC-GOx-loaded colloidosomes fabricated in the absence of GLYMO after the addition of FITC-chitosan and washing steps (yellow line). Scale bars, 10 μm.*

5.2.2 Aggregation and spatial sorting of colloidosomes

At pH 5, the zeta potential measurements of alginate-coated and chitosan-coated colloidosomes suggested a strongly negative and positive surface charge respectively. Co-assembly of alginate-coated and chitosan-coated colloidosomes was thus achieved by exploiting the electrostatic attraction between positively and negatively charged membrane-bound polymers. Aggregation was observed upon 1 : 1 (v : v) mixing and 5 min stirring of a binary population of polymer-coated colloidosomes in a pH 5 PBS solution (0.01 M). The resulting colloidosome assembly comprised a

randomly mixed population of clusters ca. 100 µm in diameter and suspended in water. Before mixing, individual solutions of chitosan-coated (red) and alginate-coated (green) colloidosomes showed defined and dispersed populations, which were measured by a fluorescence intensity profile through a selected area across a sample CLSM image (figure 5.11a,b). High areas of fluorescence correspond to individual polymer-coated colloidosomes. After co-assembly the red and green - fluorescence intensity profile through the selected CLSM image, showed a continuous region wherein all colloidosomes were closely packed with overlapping regions (figure 5.11c). 3D reconstructed images of FITC-Ch or RITC-Alg coated untagged-GOx-loaded colloidosomes showed clear interdigitation between the surface polymers, owing to the electrostatic interaction (figure 5.11d). Aggregation was also observed between colloidosome communities that comprised different sizes. Smaller colloidosomes (Alg-coated FITC-GOx loaded) were concentrated and assembled around larger colloidosomes (Ch-coated RITC-GOx loaded) to establish a mother-daughter -like community.

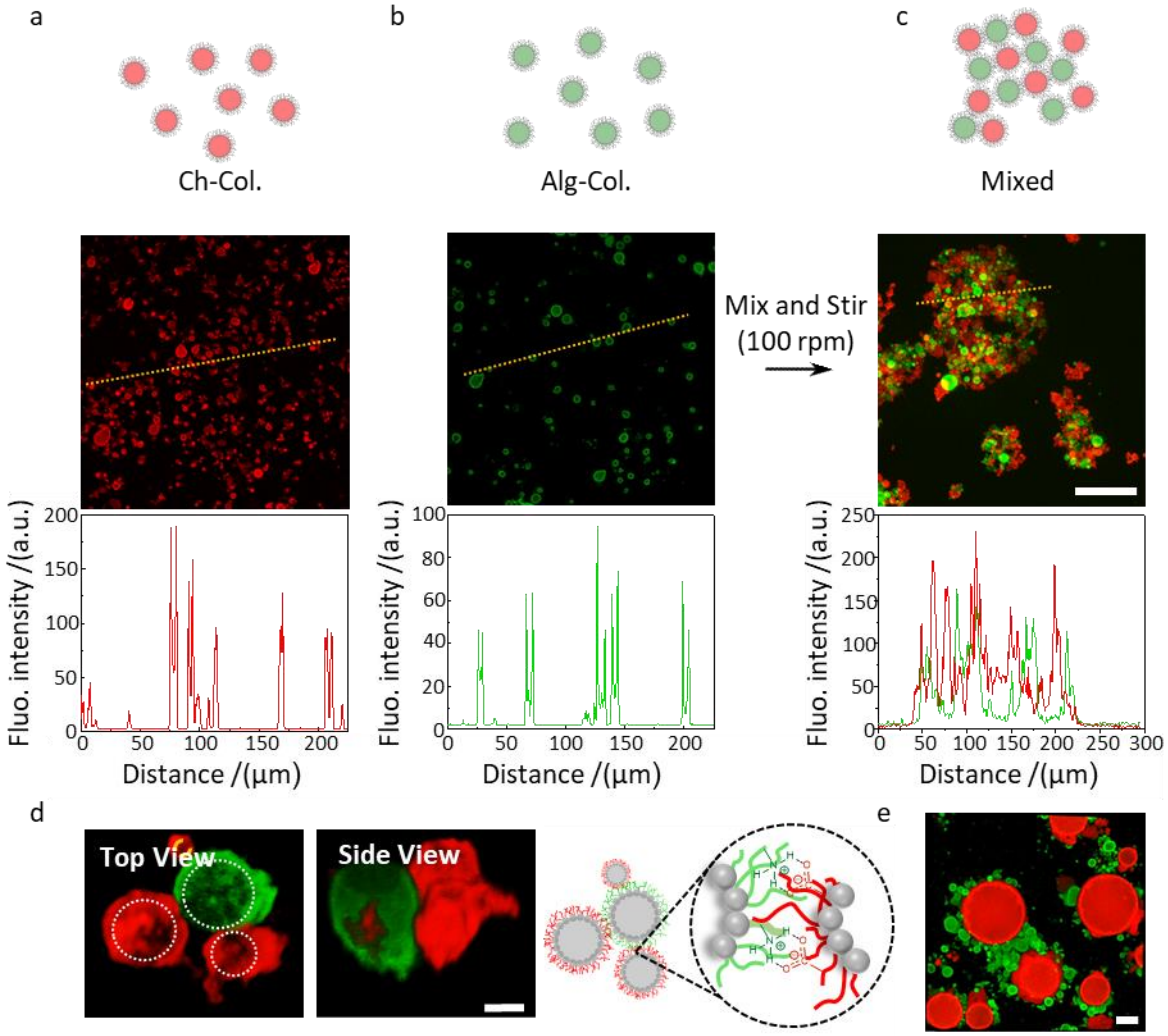

Figure 5.11. Aggregation of alginate-coated and chitosan-coated colloidosomes upon mixing. a, b, c, *Diagram, CLSM image and fluorescence intensity profile across selected region (yellow line) of chitosan-coated RITC-GOx loaded colloidosomes pre mixing (**a**), alginate-coated FITC-GOx colloidosomes pre mixing (**b**) and colloidosomes in (**a**) and (**b**) after 1 : 1 (v : v) mixing (**c**). Scale bar, 100 μm. **d**, Top and side view of 3D constructed CLSM images and schematic showing interdigitation between RITC-labelled-alginate-coated buffer-filled colloidosomes and FITC-labelled-chitosan-coated buffer-filled colloidosome. Scale bar, 2 μm. **e**, Top view 3D reconstructed CLSM image of large chitosan-coated RITC-GOx loaded colloidosomes (red) surrounded by small alginate-coated FITC-GOx loaded colloidosomes (green) after 1 : 1 (v : v) mixing. Scale bar, 10 μm.*

As a control system, uncoated colloidosomes were mixed at a 1 : 1 (v : v) ratio and stirred for 5 min (figure 5.12). Uncoated colloidosomes remained dispersed throughout solution, as seen by CLSM images and by the fluorescence profile (along yellow line). Camera videos were also taken to visualise that in bulk, aggregation did not occur. The solution remained transparent over a 5 min period.

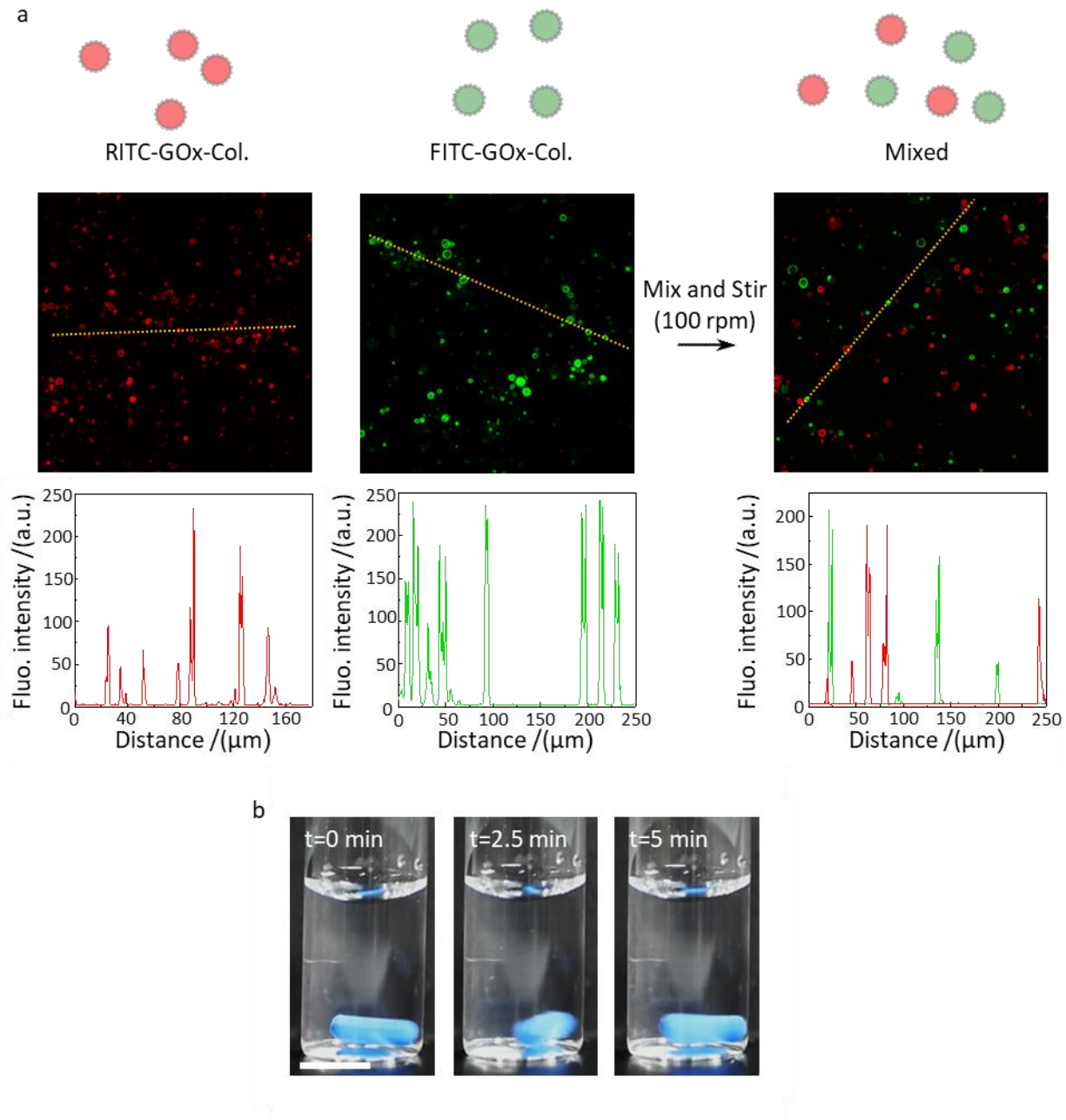

Figure 5.12. Absence of aggregation in uncoated colloidosome populations. a, *Diagram, CLSM image and fluorescence intensity profile across selected region (yellow line) of uncoated RITC-GOx loaded colloidosomes (red) and FITC-GOx loaded colloidosomes (green) before and after 1 : 1 (v : v) mixing.* ***b****, Consecutive camera images taken of colloidosomes described in (**a**) at t = 0, 2.5 and 5 min after mixing. Scale bar, 500 μm.*

Fluorescence activated cell sorting (FACS) analysis was carried out to observe a quantitative measurement for binary colloidosome mixing and co-assembly aggregation (figure 5.13). For FACS analysis, colloidosome populations were mixed at a 1 : 1 (v : v) ratio in PBS solution and then passed through the FACS machine wherein the side-scattered (SSC) and forward-scattered (FSC) light was measured from each individual entity. Data showed that when uncoated colloidosomes were mixed,

their scattering values were relatively low, corresponding to smaller entities (most likely individual colloidosomes). When alginate and chitosan coated polymers were mixed, both the side and forward scattering values were higher, corresponding to larger entities (most likely aggregates of colloidosomes). TRITC (red) and FITC (green) fluorescence intensity was also measured from each entity. When uncoated colloidosomes were mixed, either red or green fluorescence was detected from each individual signal. Only 0.003 % of entities displayed high levels of both red and green fluorescence (Q2). In comparison, when polymer coated colloidosomes were mixed, high florescence in both red and green was displayed by each entity as seen by an 11.9% signal in Q2. This suggested that within the mixed polymer coated sample, each entity comprised an aggregate of both Ch-RITC-GOx and Alg-FITC-GOx colloidosomes.

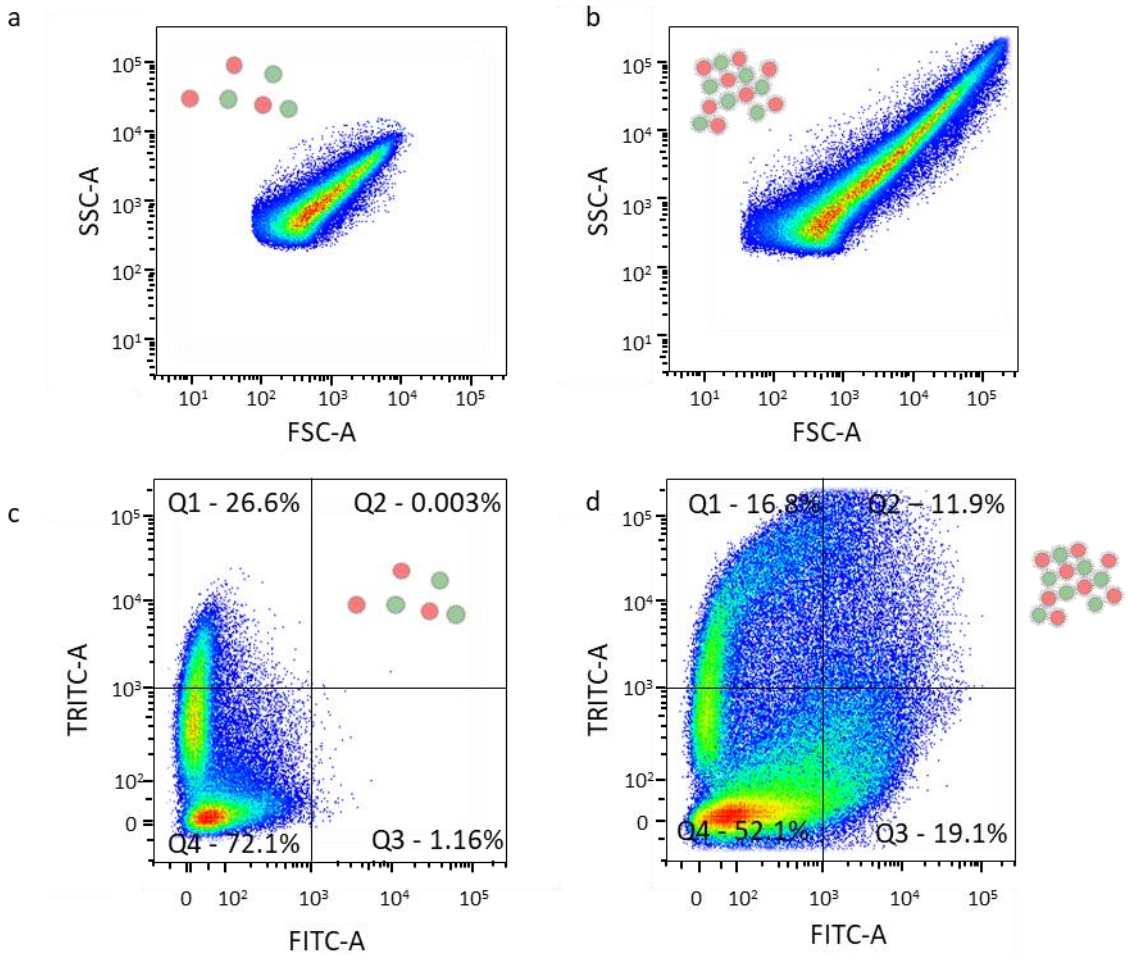

Figure 5.13. FACS data to show aggregation of polymer-coated colloidosomes. a*, Plot showing the side scattered (SSC) verses forward scattered (FSC) light for a 1 : 1 (v : v) mix of uncoated FITC-GOx loaded and RITC-GOx loaded colloidosomes, stirred for 5 min.* ***b****, Plot showing the SSC vs FSC light for a 1 : 1 (v : v) mix of Alg-coated FITC-GOx loaded and Ch-coated RITC-GOx loaded colloidosomes.* ***c****, TRITC vs FITC fluorescence intensity detected from the mixed uncoated sample in (**a**).* ***d****, TRITC vs FITC fluorescence absorbance detected from the mixed polymer coated sample in (**b**). Insets show the percentage of total particles in each quadrant.*

Despite convincing electrostatic induced co-assembly between polymer-coated colloidosomes, this aggregation process lacked control and high-level organisation. The challenge was thus to create a spatially arranged organisation of polymer-coated colloidosome aggregates to render order in the system. In bulk solution this was difficult to visualise. Aggregation in bulk relied on a balance between electrostatic forces of attraction when colloidosomes came into close proximity, and the shear force of the stirring. When the ratio of colloidosomes was changed in an attempt to pattern aggregates, the electrostatic forces of attraction were not strong enough to overcome the shearing forces. Therefore, an external force was required to help arrange colloidosomes into a desired pattern and in close proximity so that electrostatic interactions could then be established. Acoustic trapping was used to assist the ratio manipulation of colloidosome populations, to create programmable aggregates within interesting organisation. The colloidosomes were trapped within a 2D sample chamber under acoustic field (7.00/7.01 MHz and amplitude of 10 V) to create segregated collections of binary-populated colloidosome communities. At a 1 : 1 (v : v) mix of colloidosomes, the aggregated communities were completely random. The acoustic device was switched off to observe the small aggregates as the arrangement was retained owing to interprotocellular interactions. At extreme ratios 10 : 1 and 1 : 10 (Alg-coated : Ch-coated), colloidosome communities comprised one community surrounded by the other in a satellite-like pattern. As the ratios tended towards equal 1 : 1 ratio, communities became less ordered. These experiments showed that an external force, such as acoustic wave formation, could be coupled with electrostatic interactive forces to help create spatial organisation and patterning within colloidosomes communities. In each case, after an arrangement had been achieved, the acoustic force was removed and colloidosomes remained in satellite positions due to their electrostatic attraction.

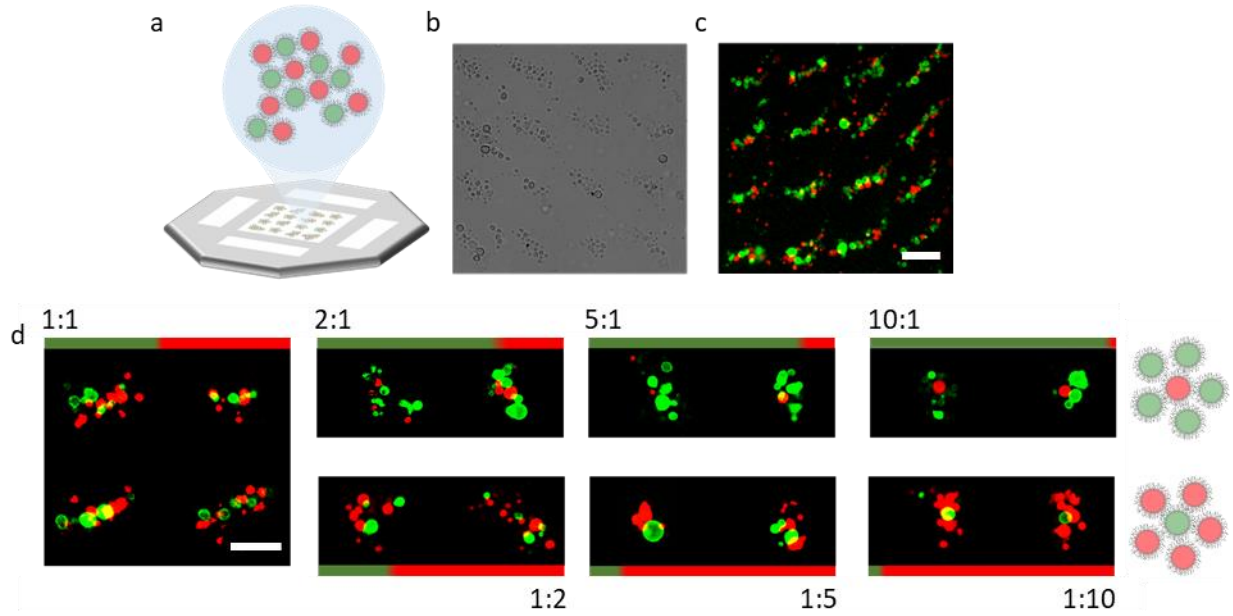

Figure 5.14. Spatial organisation via acoustic trapping-aided electrostatic interaction of polymer-coated colloidosomes. ***a****, Diagram of mixed alginate-coated FITC-GOx loaded colloidosome and chitosan-coated RITC-GOx loaded colloidosome populations aggregated at the nodes of a custom-built acoustic trapping device with transducers having frequencies of 7.00/7.01 MHz and amplitude of 10 V.* ***b****,* ***c****, Bright field (****b****) and fluorescence (****c****) microscope images of an in situ 2D array of self-assembled chitosan-coated RITC-GOx loaded and alginate-coated FITC-GOx loaded colloidosomes after acoustic device switch-off. [PBS] = 1 mM, pH 4.5, total volume = 0.5 ml.* ***d****, Self-assembled populations of alginate-coated colloidosomes (x, green) : chitosan-coated colloidosomes (y, red) at ratios x : y (v : v) from 10 : 1 to 1 : 10. Scale bar,. For ratios 10 : 1 to 2 : 1 alginate-coated colloidosomes were added, followed by chitosan-coated colloidosomes. For ratios 1: 2 to 1 : 10 chitosan colloidosomes were added, followed by alginate-coated colloidosomes. At ratio 1 : 1, polymer-coated colloidosomes were added simultaneously. All solutions were added into the acoustic device, then kept standing for 30 min to ensure formation of homogeneous colloidosome assembly at a separation of 50 µm.*

Binary protocell populations comprising alginate and chitosan coated colloidosomes could be co-assembled at pH 5. Under external pH fluctuations, these colloidosomes could be further modulated between different spatial arrangements. This occurred due to the strong pH dependent charges associated with alginate and chitosan coated colloidosomes. At low pH, amine groups (on Ch polymer) become protonated, thus expressing a positive charge (NH_3^+), whilst carboxylic groups (on Alg polymer) favour -COOH, meaning that the overall colloidosome charge reduces in negative charge and approaches a neutral charge. As pH is increased, the colloidosomes become deprotonated, carboxylic groups become negatively charged ($-COO^-$) and amine groups tend towards neutrality ($-NH_2$). Alg and Ch have pKa's 1.5-3.5[284] and 6.5[285] respectively, as reported in the literature. Thus, at pH 2 all Alg-coated colloidosomes are neutral with an expected tendency to aggregate due to hydrogen bonding, whist Ch-coated colloidosomes are protonated (NH_3^+), with an

expected tendency to electrostatically repel from each other. At pH 6.5 all Ch-coated colloidosomes are expected to display a neutral charge and thus hydrogen bond together, whilst Alg-coated colloidosomes are deprotonated (-COO^-) and thus expected to repel from each other. The expected interactions between polymer coated colloidosomes are presented in a tabulated figure below (figure 5.15).

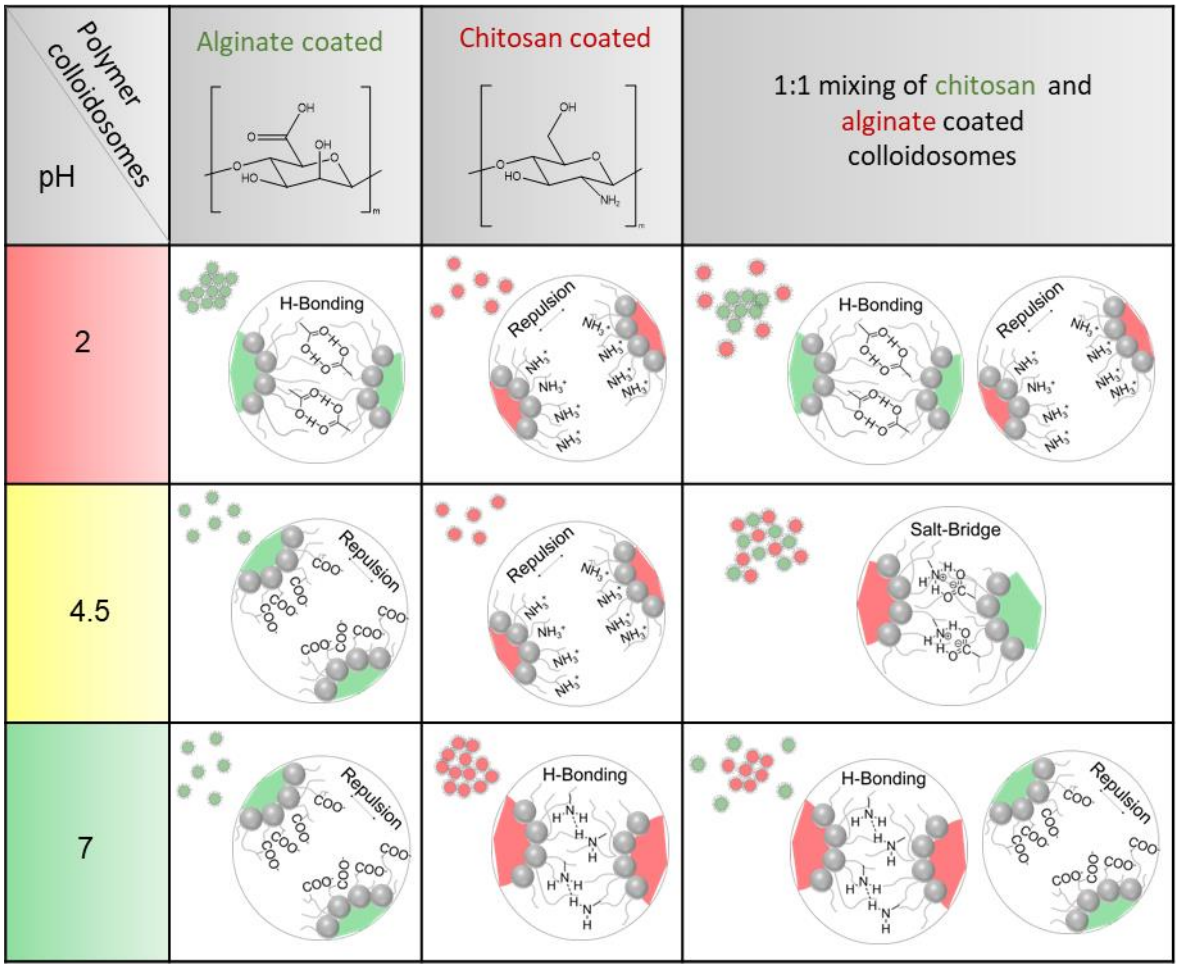

Figure 5.15. Schematic representation of various colloidosome interactions in different pH environments.

Figure 5.16a,b shows the zeta potential measurements for each alginate-coated and chitosan-coated colloidosomes, tracking the change in charges across various pH environments. As predicted, at pH 2 alginate-coated colloidosomes were neutral whereas chitosan-coated colloidosomes were positively charged. At pH 4.5 both polymer-coated colloidosomes had opposite charges and at pH 7 alginate-coated colloidosomes were negatively charged and chitosan-coated colloidosomes were neutral. At each pH 2, 4.5 and 7, three distinct colloidosome binary arrangements could thus be regulated by decreasing or increasing pH. CLSM images were taken to visually observe each sorted arrangement at the microscale and as predicted a neutral population of colloidosomes aggregated via hydrogen bonding whereas strongly charged populations of like-charged colloidosomes repelled each other (figure 5.16c). To quantify this observation, each region of fluorescence in the images was delineated and counted as a region of interest (ROI). Aggregated arrangements thus gave a low ROI count whereas dispersed colloidosome arrangements gave a high ROI count. The images were also processed into heat maps, wherein each pixel was equated to a value of fluorescence intensity. Values of fluorescence intensity above a threshold were coloured in red or green, whereas values below that threshold were coloured in black to represent minimal fluorescence. These heat maps displayed a clearer image of aggregated and dispersed distributions of colloidosomes.

In living systems, bacterial communities often bind to themselves through surface structures to form autoaggregated clumps of individual populations. This widely observed phenomenon is poorly understood however it is thought to help protect bacteria from environmental stresses, is important for colonisation and is seen in the early stages of biofilm formation.[286] The colloidosome systems described in this chapter importantly provide a step towards mimicking autoagreggated bacterial systems.

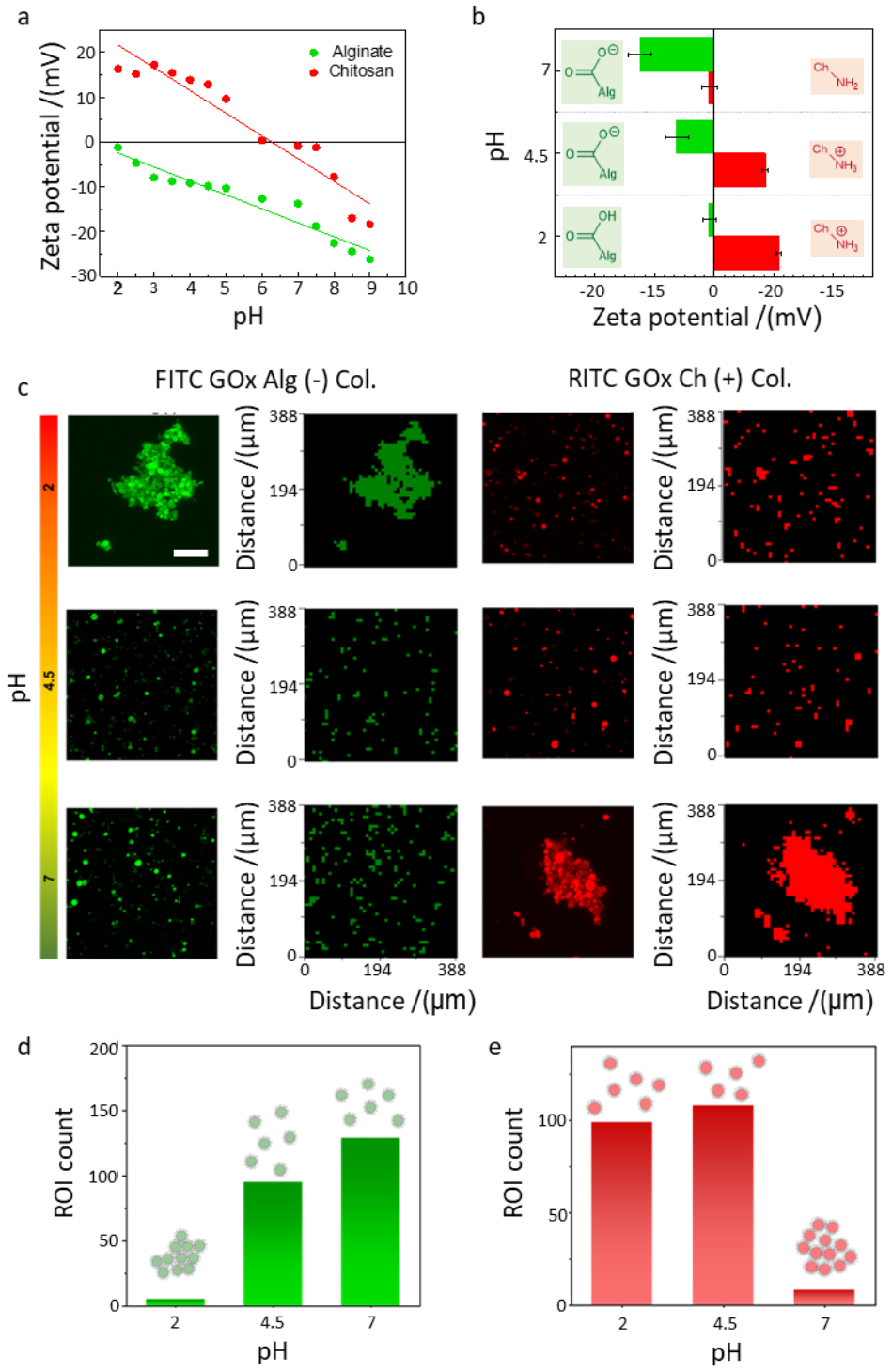

Figure 5.16. The effect of pH on the aggregation of single populations of polymer-coated colloidosomes. ***a****, Zeta potential of alginate- (green) and chitosan- (red) coated colloidosomes from pH 2-9.* ***b****, Graph to show the zeta potential of alginate- and chitosan- coated colloidosomes at pH 2, 4.5 and 7 with corresponding polymer structures.* ***c****, CLSM images and analogous fluorescence intensity heat map of alginate- (green) and chitosan- (red) coated colloidosomes at pH 2, 4.5 and 7 after stirring for 5 mins (100 rpm), showing aggregated or separated organisation of colloidosomes.* ***d****,* ***e****, Graphs showing the ROI count calculated from images in (****c****) at pH 2, 4.5 and 7 for alginate-coated colloidosomes (****d****) and chitosan-coated colloidosomes (****e****). Scale bar, 90 µm.*

Due to contrasting aggregation in individual Alg and Ch-coated colloidosome populations at specific pHs, self-sorting arrangements in a binary 1 : 1 mixed population of colloidosomes could be realised. At pH 2, the aggregation of Alg-coated colloidosomes was coupled with the dispersion of Ch-coated colloidosomes and at pH 7, the autoaggregation of Ch-coated colloidosomes was coupled with the dispersion of Alg-coated colloidosomes. Thus, in each pH solution, a self-sorted arrangement of colloidosomes (aggregated/dispersed) was established. The sorted organisation was clearly observed by filtered fluorescence and merged channels in CLSM images (figure 5.17a). ROI analysis quantified Alg-coated colloidosome aggregation and Ch-coated colloidosome dispersion through low and high counts respectively (figure 17c). The opposite ROI count was observed at pH 7, and at pH 4.5 there was a very low colloidosome ROI count for both polymer-coated colloidosomes, due to large co-assembled conglomerates. Self-sorting processes are responsible for many regulatory and controlled functions within all levels of a living system. Being able to a socially separate colloidosome populations by their spatial segregation, as a mimic of these living systems, thus provides a step towards understanding and utilising biologically valuable behaviours (figure 17b).

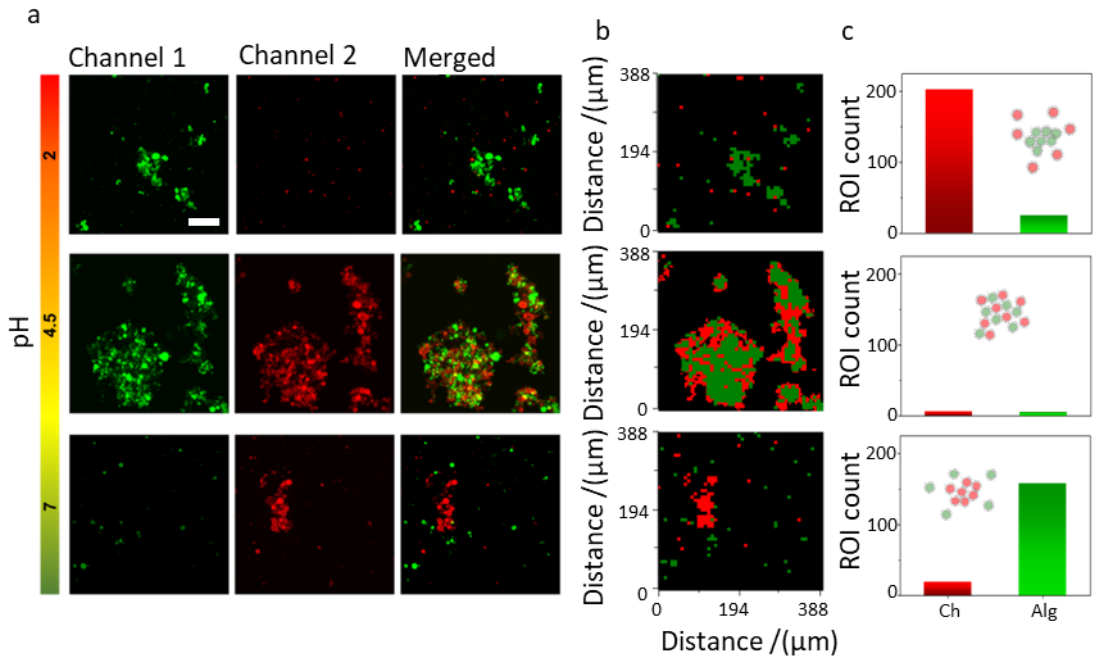

Figure 5.17. The effect of pH on the aggregation of mixed populations of polymer-coated colloidosomes. a*, Filtered green (channel 1), red (channel 2) and merged CLSM images of a mixed population of alginate- (green) and chitosan- (red) coated colloidosomes at pH 2, 4.5 and 7.* ***b****, Corresponding fluorescence intensity maps extrapolated from merged CLSM images in (**a**).* ***c****, Graphs showing the ROI count of chitosan- (red) coated and alginate- (green) coated colloidosomes, calculated from images in (**a**). 500 µl of each colloidosome population mixed and stirred for 5 mins (100 rpm). Scale bar, 90 µm.*

The electrostatic interactions within and between each colloidosome population was observed on a macroscopic scale through video capture and analysis. Figure 5.18 shows schematic depictions and videos screenshots at t = 0 and 5 min for each separated or mixed colloidosome arrangement in various pH environments. This macroscopic video evidence confirmed previous observations of bulk aggregation in pH 2 between Ch-coated colloidosomes, in pH 4.5 between mixed polymer-coated colloidosomes and in pH 7 between Alg-coated colloidosomes.

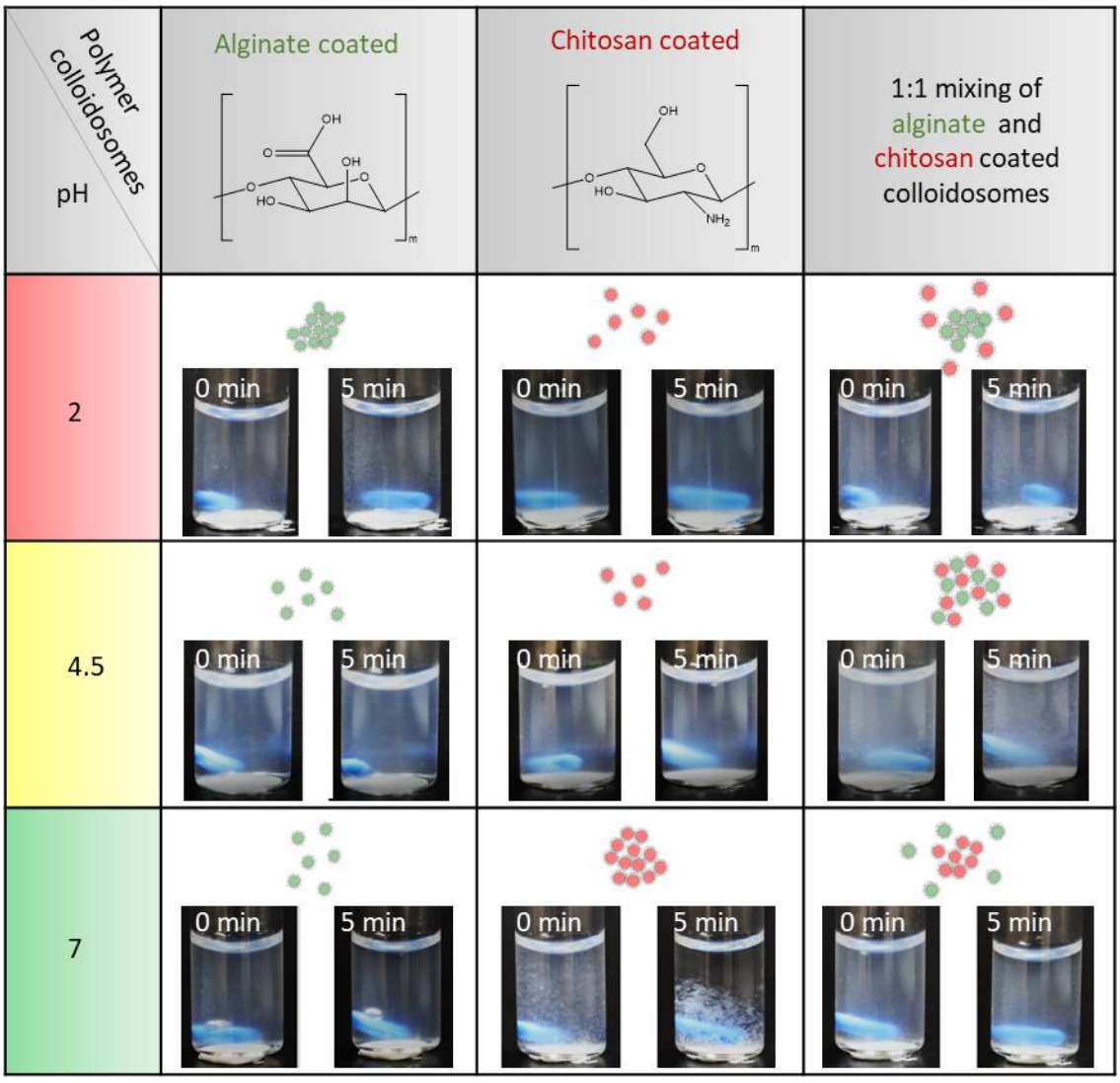

Figure 5.18. Further analysis of pH effect on the aggregation and separation of mixed populations of polymer-coated colloidosomes. ***a****, Diagrams representing the primary electrostatic interactions between alginate-coated and chitosan-coated colloidosomes at pH 2, 4.5 and 7, within individual solutions and in a mixed 1 : 1 (v : v) ratio.* ***b****, Schematic representation and consecutive camera images taken at t=0 and t=5 mins of alginate-coated and chitosan-coated colloidosomes at pH 2, 4.5 and 7, within individual solutions and after the 1 : 1 (v : v) mixing with constant stirring.*

As additional evidence for aggregation/dispersion within polymer-coated colloidosome populations, the turbidity of each colloidosome solution was measured in various pH environment (figure 5.19). Aggregated colloidosomes increased turbidity due to increased scattering of light from a hazier solution. Conversely, lesser-aggregated solutions appeared clearer and thus had a lower turbidity value. Mixed 1: 1 (v : v) populations of uncoated colloidosomes did not aggregate at any pH, as demonstrated by consistently low turbidity values (figure 5.19a). Ch-coated colloidosomes measured a higher turbidity value (46) for colloidosomes at pH 7, in comparison to at pH 2 (21), whereas Alg-coated colloidosomes measured a higher turbidity value (60) at pH 2, in comparison to at pH 7 (14). In the 1 : 1 (v : v) mixed sample, turbidity values at pH 2 and 7 measured 40, which lay between the dispersed and aggregated turbidity measurements from previous experiments. At pH 4.5, turbidity measurements were slightly higher (53), consistent with complete aggregation.

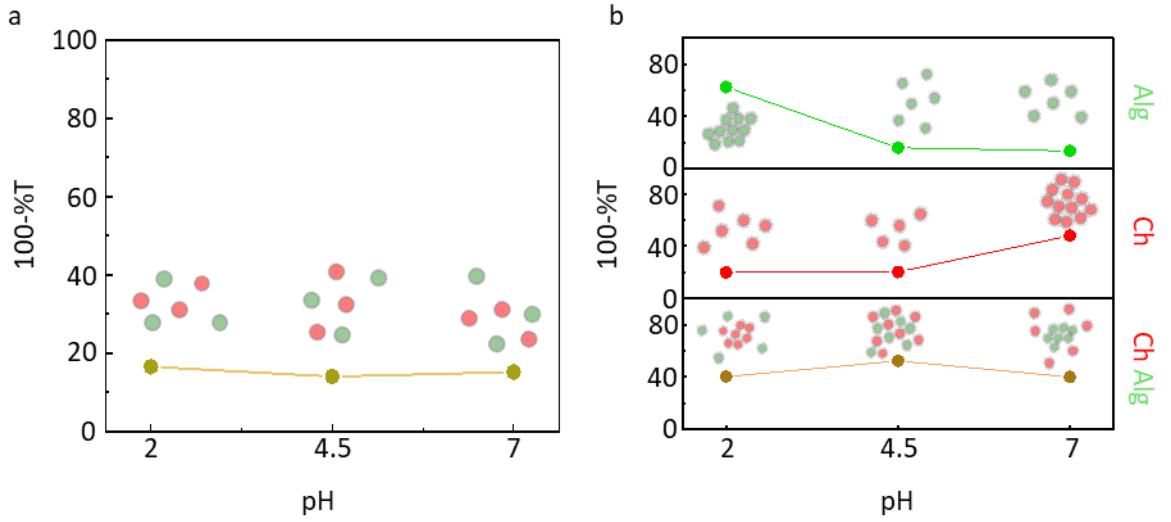

Figure 5.19. Turbidity measurements to support colloidosomes aggregation at different pH levels. ***a****, Graph to show turbidity measurements for solutions of mixed un-coated colloidosomes at pH 2, 4.5 and 7.* ***b****, Graph to show turbidity measurements of colloidosomes at pH 2, 4.5 and 7 for alginate-coated colloidosomes (top, green), chitosan-coated colloidosomes (middle, red) and a mixed 1 : 1 (v : v) ratio of chitosan-coated and alginate-coated colloidosomes (bottom, orange). Inset schematics depicting the aggregation or dispersion of colloidosomes. [colloidosomes] = 6 x 10^5 col ml^{-1}, [PBS] = 1 mM, total volume = 0.5 ml.*

The aggregation of cells within a living system is often a prerequisite to tissue formation. Therefore, the aggregation and interaction between polymer-coated colloidosomes was exploited to create interconnected tissue-like networks. Alg-coated colloidosomes were aggregated by stirring in a $CaCl_2$, pH 2 solution and then left to rest. At a high enough concentration, Ca^{2+} ionically crosslinked alginate-coated colloidosomes aggregates, to achieve an interconnected network of protocells within a connective polymer medium for extra stability and scaffolding (figure 5.20a-c). Here, a super-

packed colloidosome-hydrogel platform was constructed within minutes, as a tissue mimic (prototissue). This prototissue fabrication process was also executed using a moulded technique to produce a prototissue that could be suspended in air by a glass slide (figure 5.20e) and had potential for shape tunability. A concentrated solution of Alg-coated colloidosomes was added into a PDMS mould and left to settle, followed by the removal of supernatant. $CaCl_2$ was then added to the mould and left overnight to crosslink colloidosomes together. To better mimic the variation of cells within a tissue, a population of Alg (green) and Ch (red) -coated colloidosomes were mixed (1 : 1, v : v) at pH 5 and glued together through $CaCl_2$ crosslinking of Alg-coated colloidosomes (figure 5.20f-h). This tissue was slightly weaker than the alginate-only tissue due to Ch-coated colloidosomes not being involved in the scaffolding matrix.

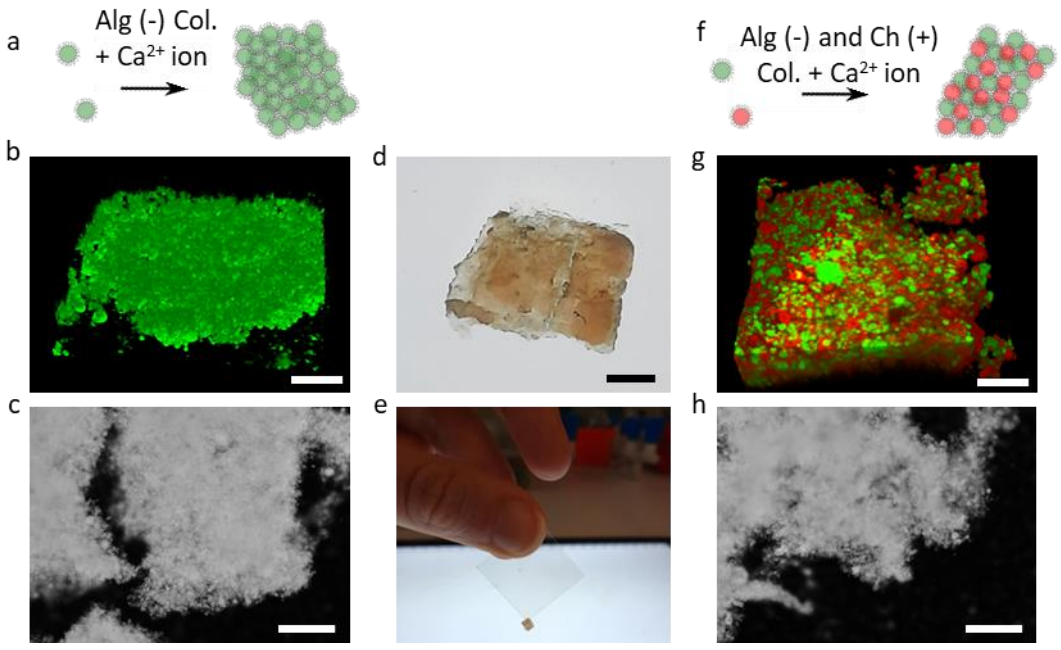

Figure 5.20. Tissue formation via hydrogelation of alginate-coated colloidosomes. ***a****, schematic representing tissue formation upon the addition of* Ca^{2+} *into a solution of alginate-coated FITC-GOx containing colloidosomes (green).* ***b****, 3D reconstructed CLSM image of colloidosome tissue described in (****a****) Scale bar, 20 µm.* ***c****, 3D reconstructed CLSM image of colloidosome tissue described in (****a****). (****b****) and (****c****) prepared by the addition of* $CaCl_2$ *(50 mM) to a colloidosome -PBS (1 mM, pH 5) solution (0.5 ml) and stirring for 5 min (100 rpm) and left to crosslink for 30 min before washing and analysis.* ***d****,* ***e****, Camera images of tissue in (****b****) on surface (****d****) and suspended from a cover slip (****e****). Scale bar, 1.5 mm.* ***f****, schematic representing tissue formation upon the addition of* Ca^{2+} *into a solution of alginate-coated FITC-GOx containing colloidosomes (green) and chitosan-coated RITC-GOx containing colloidosomes (red).* ***g****,* ***h****, 3D reconstructed CLSM image (****g****) and optical microscope images (****h****) of tissue described in (****f****) respectively. Scale bars, 20 and 100 µm.*

Cells within a living system are often dynamically arranged for processes such as repairs, delivery, or growth. The remainder of this chapter aims to exploit the dynamics of a polymer-coated colloidosome system, as a step towards these living processes. Firstly, a binary community of small and large colloidosomes were assembled and disassembled through manual changes in external pH conditions, as a mimic of how smaller cell communities could deliver mass or information to larger cells. A solution of large Ch-coated colloidosomes (red) was mixed at a 1 : 1 (v : v) ratio with a solution of small Alg-coated colloidosomes (green) at pH 4.5. A sample was taken from the bulk solution and a z stack of CLSM images was captured and reconstructed into a 3D representation. The pH of the solution was then reduced to pH 2 by the addition of HCl (1 M) with constant stirring. After 10 min stirring at pH 2, another sample was removed and imaged via CLSM. It was clear that small colloidosomes had disassociated from the large colloidosomes and were released therefore back into the environment. The large colloidosomes did not aggregate within 10 min as due to their size, the effect of the polymer coating was not as strong.

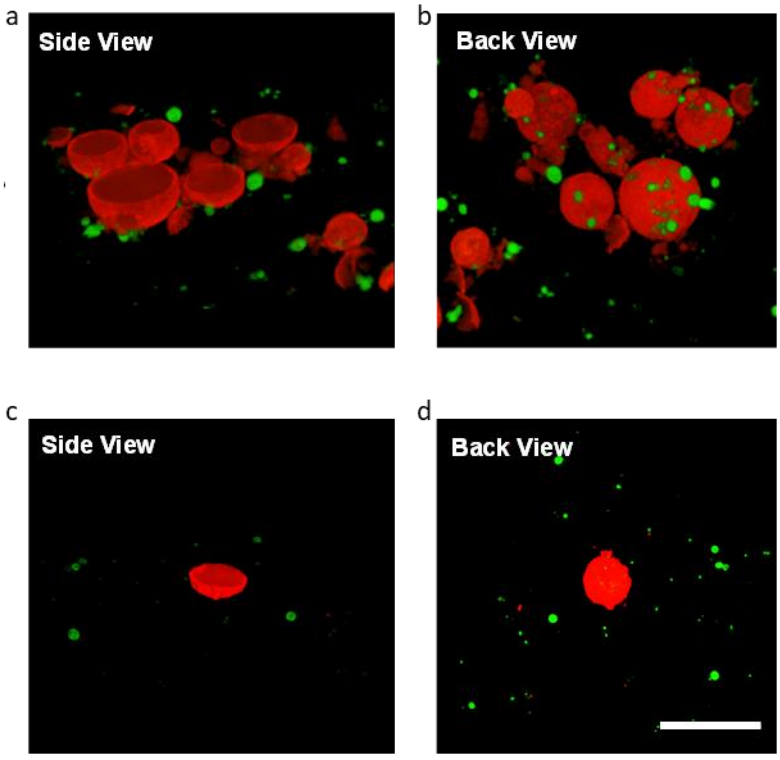

Figure 5.21. Detachment of small colloidosome population from larger colloidosomes via external pH increase. a, b, *Side view (**a**) and bottom view (**b**) 3D reconstructed CLSM images showing aggregated population of large chitosan-coated RITC-GOx loaded colloidosomes (red) and alginate-coated FITC-GOx loaded colloidosomes (green) at pH 4.5 (PBS, 0.1 mM).* ***c, d,*** *Side view (**c**) and bottom view (**d**) 3D reconstructed CLSM image of polymer coated colloidosomes in (**a** and **b**) after pH increase to pH 7 (NaOH, stirring for 10 min) to show detachment of small colloidosomes from the large colloidosome surface. Scale bar, 100 µm.*

Based on this ability to assemble and then disassemble at various external pHs, a sorting cycle was established wherein the arrangement of a binary polymer-coated colloidosome population cycled from self-sorted to co-assembled to self-sorted in response to pH modulations. These cyclic arrangements could be autonomously controlled through endogenous enzyme reactions within each colloidosome community as a method to alter the external pH environment. D-glucose was added to the external solution at t=0, to initiate a d-glucose GOx-catalysed reaction in both colloidosome populations. Through the conversion of d-glucose to GDL and H_2O_2, the pH decreased from pH 7 to pH 3 over several hours. Colloidosomes were kept under continuous stirring conditions at pH 7, in an organisation where Alg-coated -colloidosomes were dispersed and Ch-coated colloidosomes were aggregated together. As the pH dropped (due to the endogenous GOx cascade), both populations aggregated together to form a mixed colloidosome agglomerate and then further separated back out into alginate-coated colloidosome aggregates and chitosan-coated colloidosome dispersion. This dynamic change in colloidosome organisation, from self-sorted to co-assembled to self-sorted, demonstrated a step towards temporally controlled localised reactions.

The zeta potential and turbidity of Ch-coated, Alg-coated and 1 : 1 mixed polymer-coated colloidosome samples were measured at pHs from 7 to 2.75, to monitor the sorting process (figure 5.22). In the Ch-coated system, turbidity decreased with decreasing pH due to the colloidosomes becoming more dispersed. The zeta potential increased from neutral charge to positive charge (+18 mV) due to protonation of the NH_3 to NH_4^+ causing colloidosomes to repel from each other into a dispersed arrangement. Conversely, in the Alg-coated system, turbidity increased with decreasing pH due to the colloidosomes becoming more aggregated. The zeta potential increased from a negative charge (-19 mV) to neutral charge due to protonation of COO^- to OH, causing colloidosomes to attract each other through hydrogen bonding. In the mixed sample, both Ch-coated and Alg-coated colloidosomes behaved in opposing ways and thus the overall turbidity remained consistently high with a small peak around pH 4.5 due to co-assembly. The overall zeta potential of the mixed polymer-coated colloidosome solution increased from pH 7 to 2.75 due to the system transforming from negatively charged COO- and neutral NH_3 at pH 7 to neutral OH and positive NH_4^+ at pH 2.75.

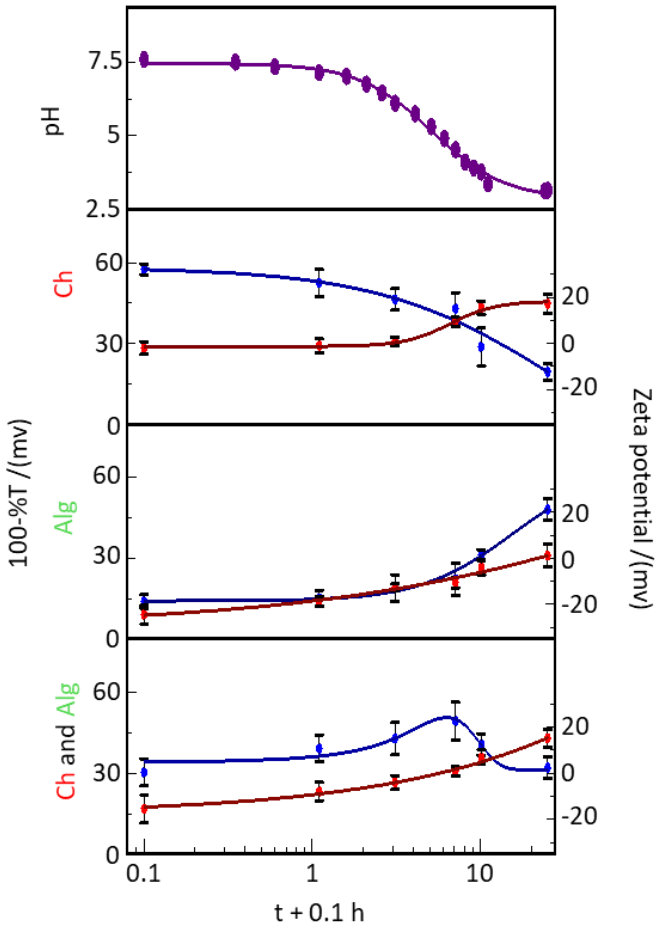

Figure 5.22. Turbidity and zeta potential measurements of dynamic colloidosome arrangements. *Zeta potential (red) and turbidity (blue) measurements of Ch-coated population of GOx-loaded colloidosomes, Alg-coated population of GOx-loaded colloidosomes and mixed population of GOx-loaded colloidosomes, taken over a 24 h period.*

This autonomous cyclic organisation was evidenced by CLSM images, taken at specific pH intervals (figure 5.23). Firstly, the pH was modulated by GOx within a single population of Ch-coated RITC-GOx loaded colloidosomes. Samples were acquired from the continuously stirred bulk solution, and CLSM images taken at pH 7, pH 4.5 and pH 2.75. Large aggregates at pH 7 were disbanded as the pH dropped. Secondly, the pH was modulated by GOx within a single population of Alg-coated FITC-GOx loaded colloidosomes which showed aggregation upon pH decrease over 24 h. Thirdly, the pH was modulated by GOx within a mixed binary community of alginate and chitosan GOx-loaded colloidosomes. CLSM images showed self-sorted arrangements of Ch-coated and Alg-coated colloidosomes at pH 7 cycling through a co-assembled state at pH 4.5, and then back into a self-sorted state at pH 2.75. The spatial organisation and proximity of colloidosome populations was thus temporally controlled through an endogenous colloidosome signal. However, the next key challenge was to exploit these colloidosome proximity changes for temporal control over protocell communication.

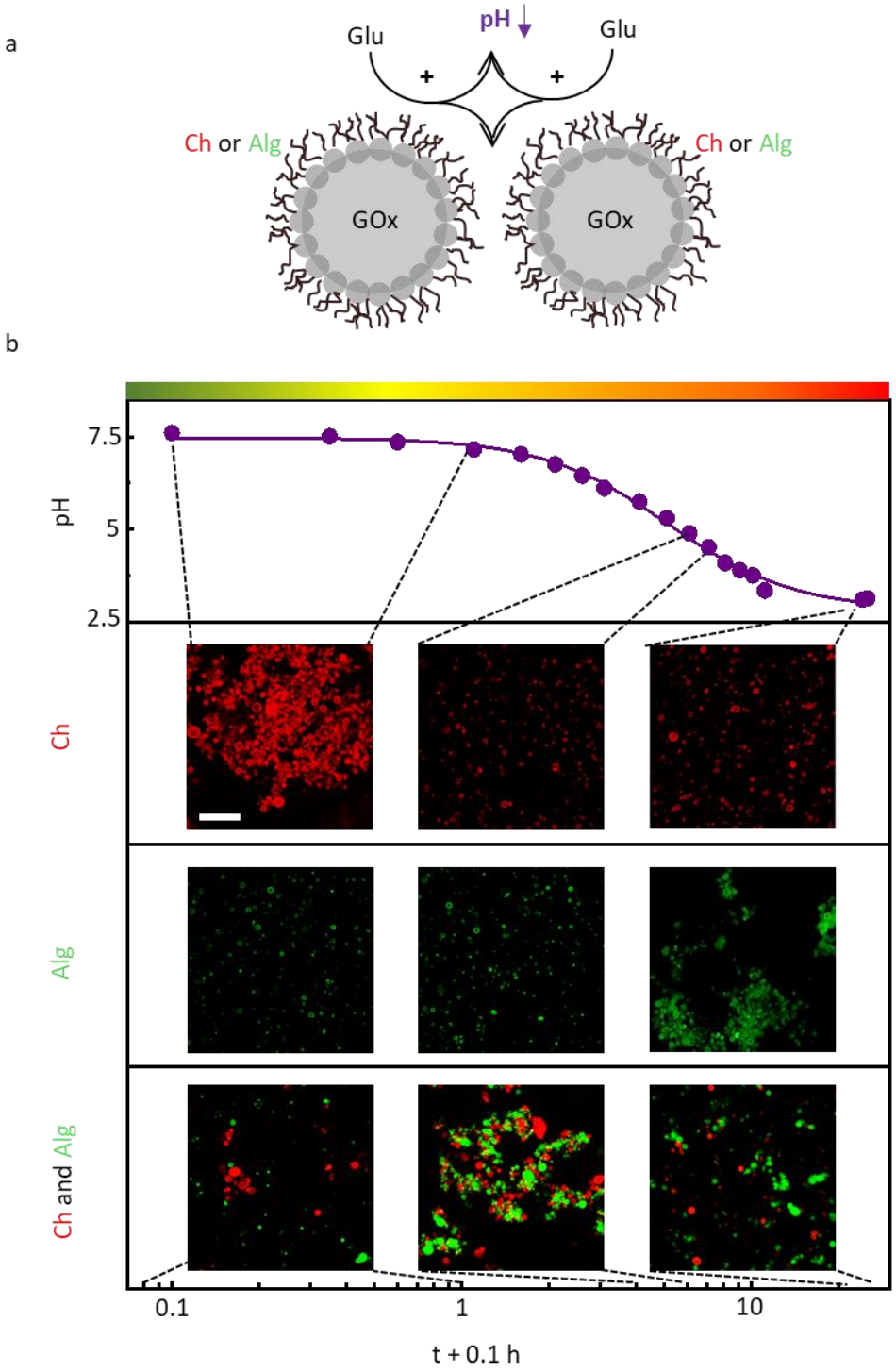

Figure 5.23. Enzyme-induced colloidosome re-organisation. a*, Diagram showing polymer-coated colloidosomes undergoing a glucose-initiated GOx enzyme reaction to decrease external pH****. b,*** *Graph showing pH reduction from 7.5 to 2.75 due to GOx enzyme reaction within polymer-coated GOx loaded colloidosomes upon addition of glucose* (0.5 M). *Three samples taken from a chitosan-coated population of GOx-loaded colloidosomes (red), alginate-coated population of GOx-loaded colloidosomes (green) and mixed population of GOX-loaded colloidosomes (red and green) at t = 0-2 h, 7-9 h and 24-26 h with CLSM images of samples taken at exactly t = 0.5, 7.5 and 24 h and corresponding ROI calculations with schematic depiction of colloidosome aggregation or dispersion. Scale bar, 50 µm.*

5.2.3 Communication between polymer-coated colloidosomes

Often, communication between cells varies according to cell-cell proximity. In this last piece of work, polymer-coated colloidosome communities have been used to monitor communication changes as a consequence of temporally controlled, pH modulated spatial patterning, to mimic living cell communication proximity effects. A community of Alg-coated FITC-AOx loaded colloidosomes and Ch-coated Dy405-HRP loaded colloidosomes were mixed together at a 1 : 1 (v : v) ratio. GDL was added into the external solution to decrease the pH through ring-opening hydrolysis to gluconic acid. The original idea was to initiate pH reduction using an endogenous GOx enzyme reaction however, the reaction happened over a timeline that was too long, and GOx would have interrupted the communication pathway. An AOx/HRP mediated cascade between colloidosomes was achieved upon addition of ethanol to the external solution. AOx converted ethanol to ethanal and H_2O_2 which was subsequently used in the HRP conversion of o-PD to 2,3-DAP which had a green fluorescence associated with it (figure 5.24a). In these experiments, a UV-Vis technique was used to monitor the fluorescence output of the solution, rather than analysing microscope images. This was due to the requirement for continuous stirring. Light was absorbed at 420 nm (corresponding to the fluorescent 2,3-DAP), with increasing absorbance over 6 h as the cascade progressed (figure 5.24b).

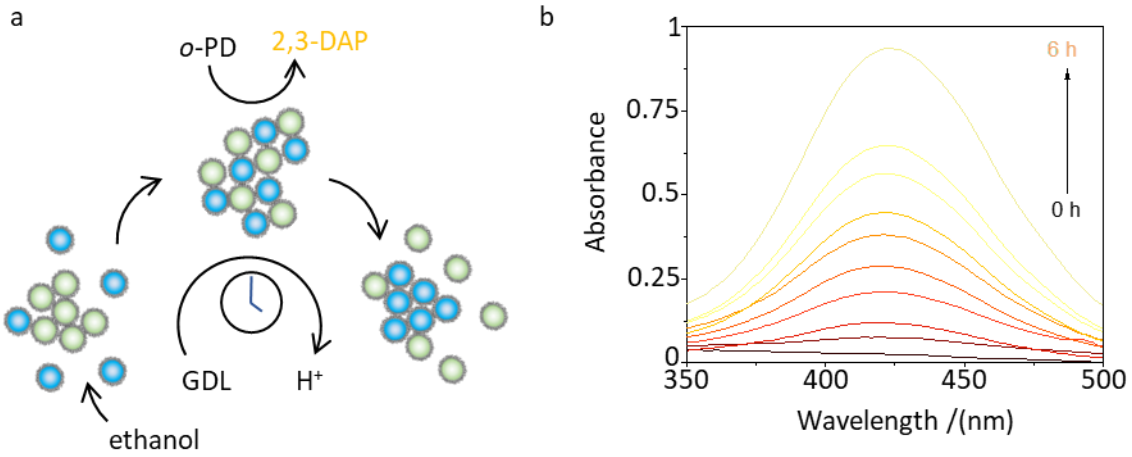

***Figure 5.24. AOx/HRP enzyme cascade in polymer-coated colloidosomes. a**, Schematic of alginate-coated AOx (30 mg ml^{-1})-loaded colloidosomes (green) and chitosan-coated HRP (30 mg ml^{-1})-loaded colloidosomes (blue) in arrangements from ~pH 7 to ~pH 2.5 (clockwise). GDL was added to the external solution to decrease the pH, therein changing the arrangement of polymer-coated colloidosomes. Ethanol and o-PD were added to the external solution, inducing the AOx/HRP cascade reaction between binary populations of polymer-coated colloidosomes resulting in conversion of o-PD to fluorescent 2,3-DAP output. **b**, Fluorescence absorbance from 2,3-DAP produced in polymer-coated colloidosome solution described in (**a**) after addition of ethanol (10 µl, [20 mM]), GDL (20 µl, [50 mM]) and o-PD (5 µl, [25 mM] PBS = 1 ml) simultaneously at t=0 h. Spectra taken at time intervals from t = 0 to t = 6 h (dark red to yellow).*

The pH was decreased from pH 7.75 to 2.75, over a 2 h period by the hydrolysis of GDL in the aqueous environment. At t=0 (pH 7.75) a 1 : 1 (v : v) mix of Alg-coated AOx-loaded and Ch-coated HRP-loaded colloidosomes were stirred into the solution. As previous observations showed, this resulted in the alginate-coated AOx-loaded colloidosomes being dispersed (green) and the chitosan-coated HRP colloidosomes being aggregated (blue). As the pH decreased through pH 4.5, both populations of colloidosomes aggregated together, and then a further decrease in pH to pH 2.75 resulted in the dispersion of chitosan colloidosomes and the aggregation of alginate colloidosomes. When both populations of colloidosomes were aggregated and in contact, the transfer of H_2O_2 signalling molecule was hypothesised to be quicker than when one population was dispersed due to distance-dependent diffusive signalling. Thus, the rate of communication should have been faster around pH 4.5, in the aggregated phase, and slower at pH 2 and 7. This was only observed to a minimal degree as distances between each colloidosome population were very small and thus the effect of proximity on chemical communication rate was negligible. A rate difference between juxtracrine and paracrine communication was thus undetectable. Experiments were also undertaken at constant pH in the absence of GDL. These results showed the highest rate of communication at pH 7, attributed to the intrinsic activity of GOx. To show a convincing increase of communication rate upon aggregation at 5, the rate of reaction has to surpass the rate at pH 7.

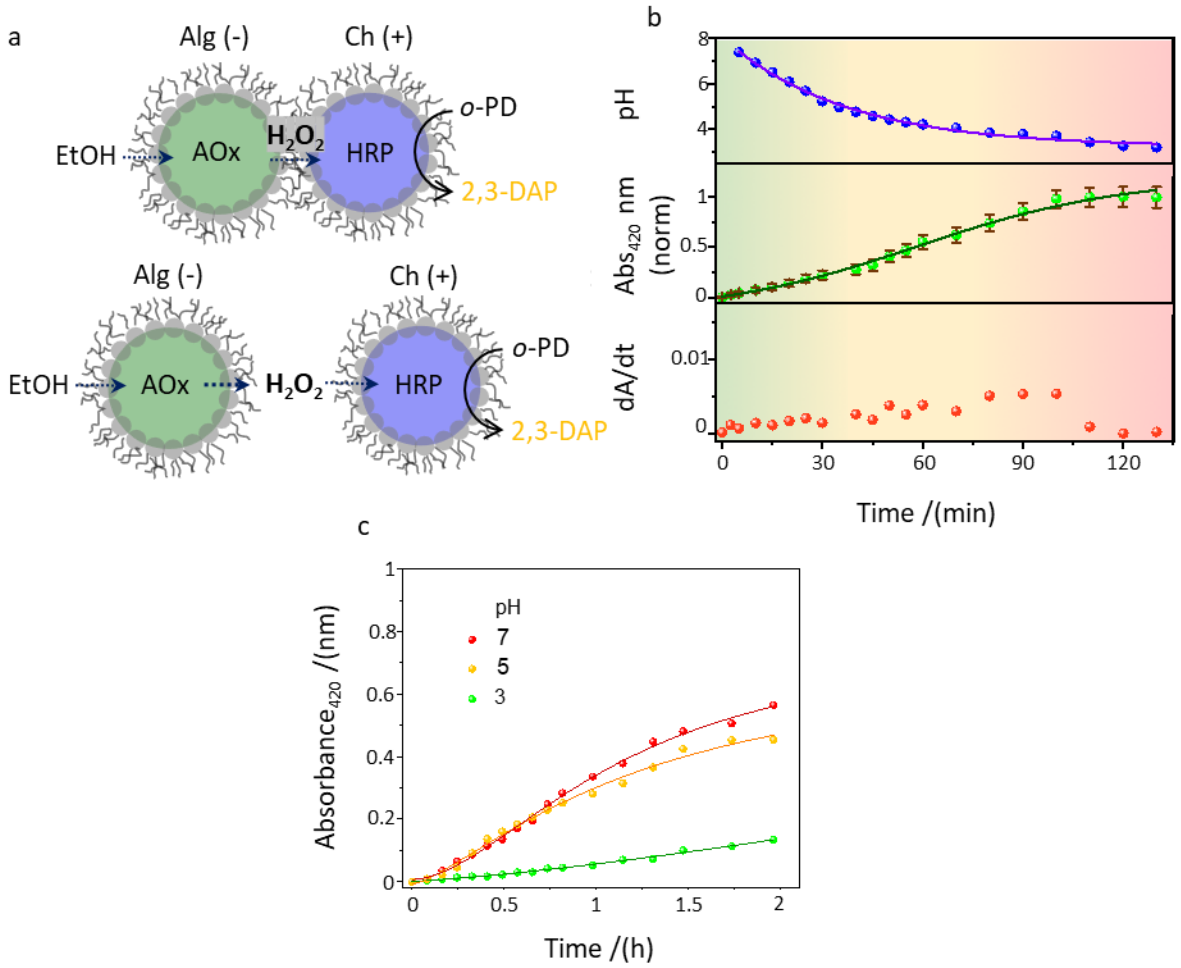

Figure 5.25. Effect of dynamic colloidosome arrangements on the rate of cascade reaction without catalase. a, *Schematic to show juxtracrine and paracrine-like communication between alginate-coated FITC-AOx loaded colloidosomes (green) and chitosan-coated Dy405-HRP loaded colloidosomes.* ***b****, Graph to show the decrease in pH with corresponding fluorescence output (from 2,3-DAP) and the rate of reaction between AOx/HRP loaded polymer-coated colloidosomes with GDL to temporally decrease the external pH.* **c**, *Graph to show AOx/HRP enzyme cascade between binary population colloidosomes at pH 3, 5 and 7.*

However, upon addition of Cat to the external solution a more obvious change in communication in response to spatial rearrangement was observed (figure 5.26). Cat acted as a hydrogen peroxidase scavenger from the system, thus when there was space between the communities, Cat had increased opportunity to act as a signalling blocker. When the colloidosomes were aggregated and thus interconnected, H_2O_2 could transfer directly between populations thus not being exposed or removed by the Cat. As such, at pH 7 a slow rate of reaction was observed, where most of the H_2O_2 signalling molecule was being consumed by the catalase in solution. As the pH decreased to pH 4.5, the rate of reaction increased due to direct signalling between colloidosomes and avoidance of Cat. At even lower pH, the populations were once again separated, and the rate of reaction decreased. Overall, this system showed a temporal effect on the rate of reaction through dynamic spatial co-assembly or self-sorting of colloidosomes through a Cat scavenger, competing for the H_2O_2 signalling molecule. Often in living systems, communication breaks down when scavenger molecules disrupt the communication pathway. This system mimics such a phenomenon, as a step towards creating sophisticated cell interaction networks. Experiments were also undertaken at constant pHs (3, 5 and 7) in the absence of GDL. These results showed the highest rate of communication at pH 5, attributed to the assembly and contact-dependent transfer of H_2O_2 with less exposure to Cat scavenger. Importantly, the rate at pH 5 was convincing higher than at pH 7, which is the naturally faster environment due to optimum GOx activity.

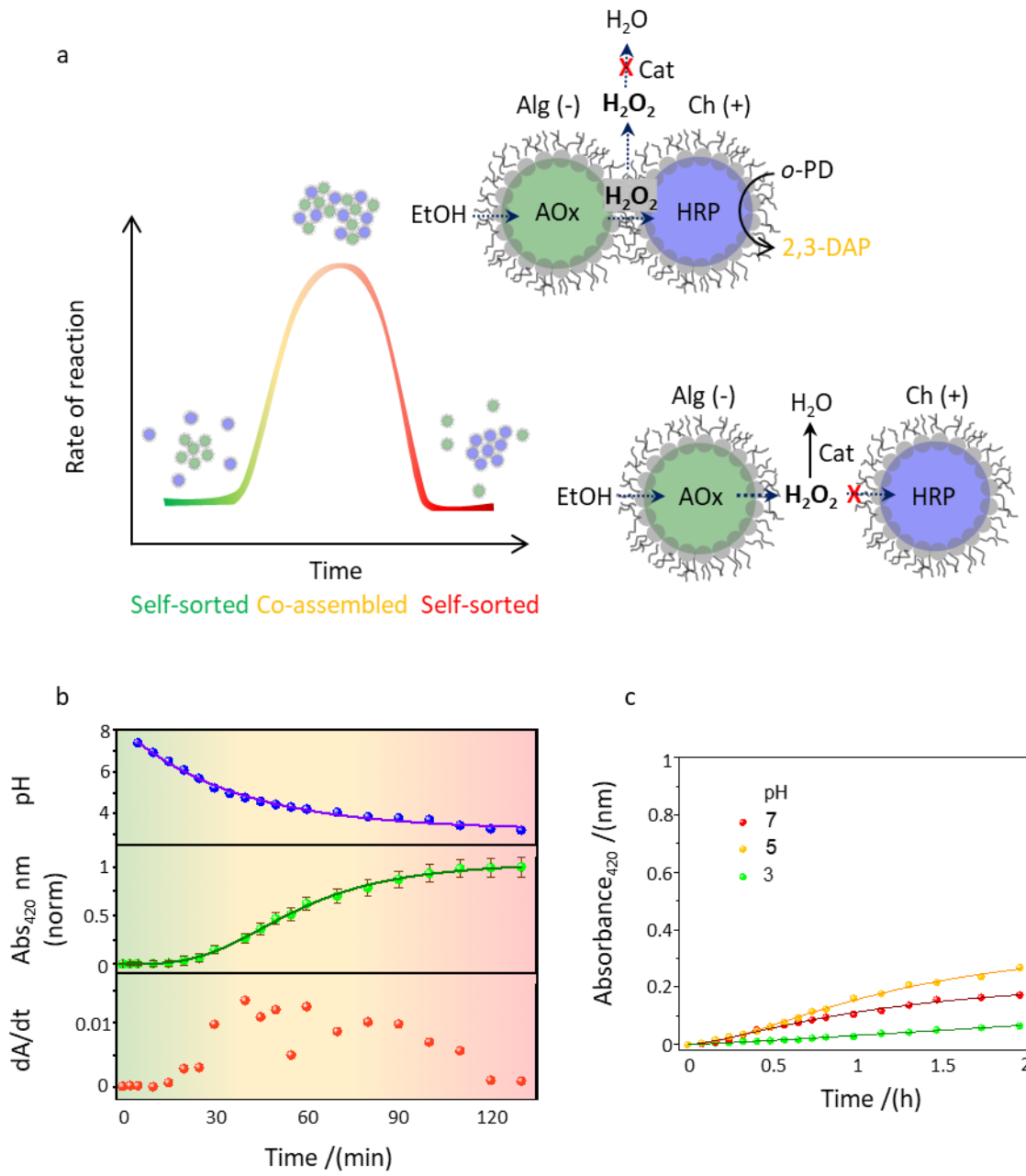

Figure 5.26. Effect of dynamic colloidosome arrangements on the rate of cascade reaction with catalase a*, Schematic of AOx/HRP enzyme cascade between aggregated (top) and dispersed (bottom) populations of polymer-coated colloidosomes. H_2O_2 signalling molecule shown to travel further in dispersed (bottom) population, compared to aggregated (top) population. Catalase scavenger molecule trying to remove H_2O_2 signalling molecule. Graph shows the spatial distribution of colloidosomes as the pH decreases over time.* ***b****, Graph showing pH change (blue), absorbance at 420 nm (green) and rate of change of absorbance (dA/dt, red) of colloidosome solution over 130 min.* ***c****, Graph to show AOx/HRP enzyme cascade between binary population colloidosomes at pH 3, 5 and 7. All the experiments were carried out in a cuvette with colloidosome solution mixed and stirred at 100 rpm. (alginate AOx colloidosome and chitosan HRP colloidosome = 6 µl each, PBS = 1 ml, 20 µL of 50 mM GLA, 5 µl of 25 mM o-PD, 10 µl of 20 mM EtOH, 0.01 mg ml^{-1} Cat).*

Attaching a polymer coating to the colloidosome membrane significantly affected the overall kinetics of colloidosome communication attributed to slowed down diffusion across the colloidosome membrane. At pH 3, 5 and 7 the AOx/HRP enzyme cascade between uncoated colloidosomes proceed relatively quickly. Notably, the reaction rate decreased from pH 7 to 3 according to the optimum enzyme environments (figure 5.27a). When catalase was added to the external environment, the same pattern was observed at proportionally lower rates, due to catalase removing some of the signalling H_2O_2 molecules (figure 5.27c). In all cases the colloidosomes remained spatially dispersed in solution.

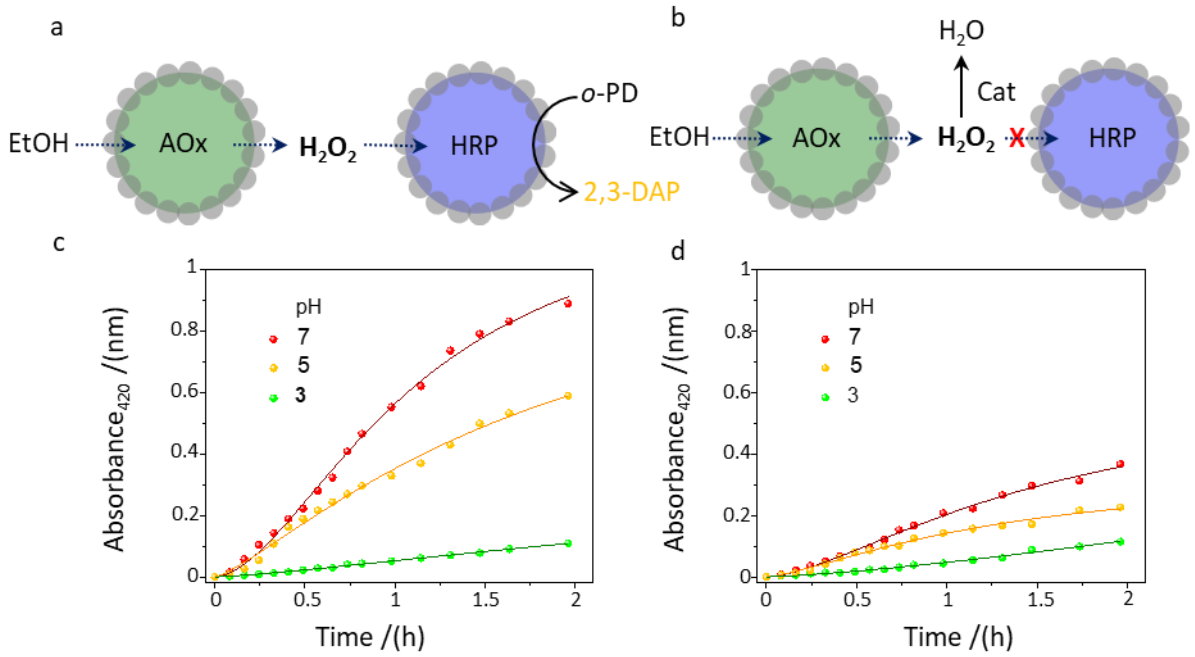

***Figure 5.27. AOx/HRP enzyme cascade in uncoated colloidosomes. a, b**, Schematic diagram (**a**) and graph (**b**) to show AOx/HRP enzyme cascade between binary population of uncoated AOx (30 mg m^{-1})-loaded (green) and HRP (30 mg ml^{-1})-loaded (blue) colloidosomes in the absence of Cat. **c, d**, Schematic diagram (**c**) and graph (**d**) to show AOx/HRP enzyme cascade between binary population of uncoated AOx (30 mg m^{-1})-loaded (green) and HRP (30 mg ml^{-1})-loaded (blue) colloidosomes in the presence of Cat (0.001 mg ml^{-1}). Absorbance at 420 nm monitored over a 2 h period at pH 3 (green), pH 5 (yellow) and pH 7 (red) to map production of 2,3-DAP as the cascade output. Simultaneous addition of ethanol (10 µl, 20 mM) and o-PD (5 µl, 25 mM) at t=0 h into 1 ml colloidosome solution (PBS, 1 mM).*

The effect of catalase (Cat) concentration on the system was also investigated. The catalase was varied from 0.01-0.1 at each pH environment. Increasing the concentration of Cat decreased the rate of cascade due to more H_2O_2 signalling molecules being consumed by the hostile guest and not being available for the complete cascade. A threshold concentration of Cat was needed in order to see a switch in rate between pH 5 and pH 7.

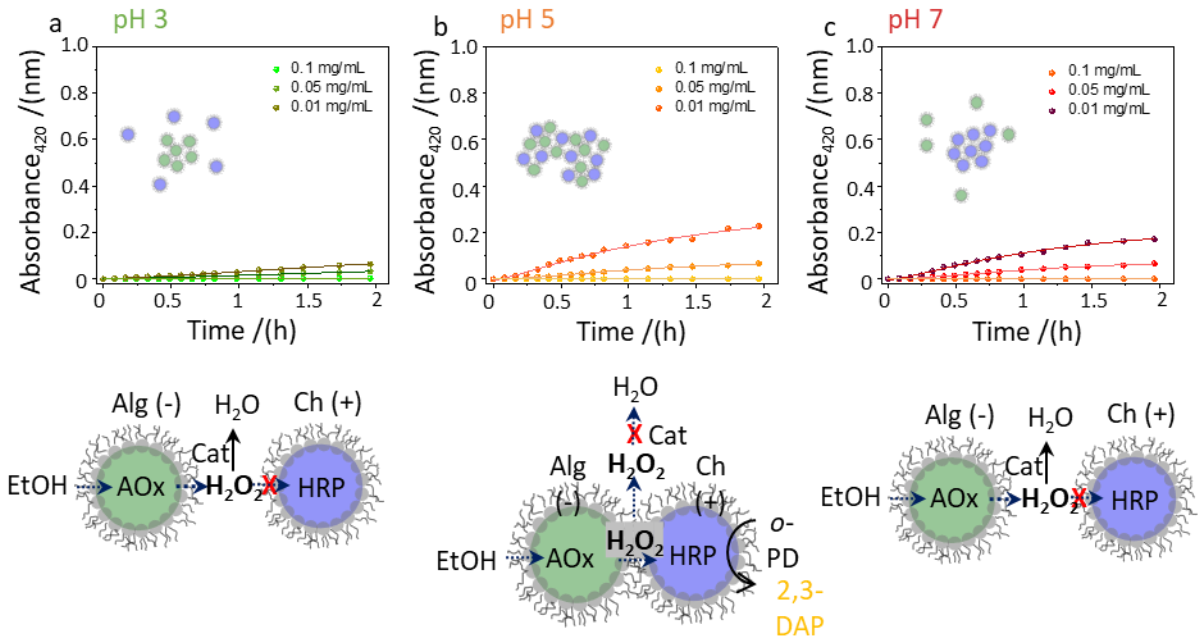

Figure 5.28. The effect of catalase concentration on the AOx/HRP enzyme cascade in different colloidosome arrangements. a, b, c, *Graph and schematic to show AOx/HRP enzyme cascade at pH 3 wherein chitosan-coated HRP-loaded (30 mg ml^{-1}) colloidosomes are aggregated and alginate-coated AOx-loaded (30 mg ml^{-1}) colloidosomes are dispersed (**a**), pH 5 wherein, chitosan-coated HRP-loaded colloidosomes and alginate-coated AOx-loaded (30 mg ml^{-1}) colloidosomes are aggregated (**b**) and pH 7 wherein chitosan-coated HRP-loaded colloidosomes are dispersed and alginate-coated AOx-loaded colloidosomes are aggregated (**c**). Catalase 0.1, 0.05, 0.01 mg ml^{-1} (dark to light) was added to the colloidosome external solution (1 ml, PBS 1 mM) alongside addition of ethanol (10 µl, 20 mM) and o-PD (5 µl, 25 mM) at t=0 h. The absorbance at 420 nm was monitored over 2 h, mapping fluorescence output from the production of 2,3-DAP.*

5.3 Conclusions

In a living system, cell-cell and cell-environment interactions are closely related to cell proximities and spatial order within a cell community. Interactions are delicately controlled through dynamic changes in spatial order according to environmental cues, for example in bacteria competition, immune system response and biofilm formation. Dynamic protocell organisation can be used to mimic complex cellular interaction/organisation behaviours however, these systems need to be environment-responsive, automated and show the relationship between spatial proximities and cell-cell interactions. In this chapter, the dynamic organisation of colloidosomes has been achieved in response to environmental pH cues. Through endogenous enzyme-mediated reduction in external pH, colloidosome communities regulated their own cycle from self-sorted to co-assembled to self-sorted organisations and finally, the rate of communication between colloidosomes was shown to modulate in response to pH-driven colloidosome organisation in the presence of a signalling scavenger.

As a strategy for dynamic protocell organisation, alginate and chitosan polymers were covalently attached to the silica membrane of colloidosomes via a GLYMO ring opening process. The attachment of polymers resulted in a rough 'hairy' surface texture, wherein uneven distributions of polymer could be observed via CLSM, SEM and TEM. Polymer coating altered the surface charge of colloidosomes, such that alginate-coating reduced the surface charge from -19 mV to -25 mV, whereas chitosan-coating increased surface charge from -19.3 mV to +22 mV, at pH 5. This was attributed to negative carboxylate groups on alginate and positive amine groups on chitosan.

The surface charge difference between alginate-coated and chitosan-coated colloidosomes was exploited to achieve binary-populated self-assembled structures. Interdigitation between alginate and chitosan polymer chains, due to electrostatic interactions, resulted in strong co-assembly of colloidosomes when agitated by stirring at pH 4.5. Co-assembly was also achieved in colloidosome populations of different sizes, such that small colloidosomes (d_A = 5 µm) could be aggregated around the circumference of larger colloidosomes (d_A = 70 µm).

The electrostatically driven co-assembly was developed for the formation of connected tissue-like structures, as a novel way of forming an extremely closely packed prototissue comprising protocells within a minimal hydrogel matrix. Alginate (attached to the colloidosome membrane) was ionically crosslinked using Ca^{2+} ions to affix colloidosomes together to form the tissue-like scaffold. Alginate crosslinking could form a stable network for chitosan colloidosomes to be trapped inside, forming a binary populated prototissue.

Further spatial patterning between co-assembled polymer-coated colloidosome populations was achieved by altering the ratio of each community. Acoustic trapping was used to afford control over the positioning of colloidosomes so that specific ratios could be maintained. Ratios of alginate-coated : chitosan-coated colloidosomes (1 : 10 to 10 : 1) were achieved so that one community encompassed another community, demonstrating a satellite-like arrangement. At ratios close to 1 : 1, a random co-assembled structure was observed.

A 1 : 1 co-assembled arrangement was spatially self-sorted through manual environmental pH changes. Due to the charged polymers becoming neutralised in specific pH environments, a single population could be assembled or dispersed according to high or low pH. Co-assembly occurred in a single colloidosome population when polymers (and thus colloidosome surface charges) were neutral, due to hydrogen-bonding. Dispersed arrangements occurred when polymers (and thus colloidosome surface charges) were charged, due to like-charges repelling. Self-sorted arrangements were realised when a colloidosome population comprised a charged community and a neutral community so that the neutral colloidosomes aggregated through hydrogen-bonding and the charged colloidosomes dispersed due to like-charges repelling. These arrangements were monitored with CLSM and turbidity measurements.

A population of small alginate-coated colloidosomes was released from a population of large chitosan-coated colloidosomes by exploiting this electrostatic-pH dependency and so reducing the external pH using sodium hydroxide. This revealed a facile route to the delivery of cargo from one protocell community to another.

Based on this ability to assemble and then disassemble colloidosome populations at various external pHs, a sorting cycle was established wherein the arrangement of a binary polymer-coated colloidosome population cycled from self-sorted to co-assembled to self-sorted in response to pH modulations. GOx-loaded colloidosomes were used to endogenously decrease the external pH in a temporally controlled process, as a self-regulated way of change the spatial arrangements of colloidosome populations.

Finally, the dynamic organisation of colloidosomes was exploited for regulating the rate of communication between a binary population of AOx-containing and HRP-containing colloidosomes. In the presence of a catalase hostile guest, the rate of reaction was interchanged according to either a self-assembled or co-assembled arrangement. As the external pH was decreased from 7 to 2.75 through a GDL ring-opening mechanism, the colloidosomes dynamically arranged from a self-sorted pattern, to co-assembled and back to self-sorted. As a response to these spatial organisations, the rate of enzyme cascade varied from slow to fast to slow, wherein the fast reaction occurred through

contact communication so that the signalling molecule was not subjected to catalase (signal-removing) guest. Although the work was unable to convincingly show a change in communication rate due to diffusion related proximity effects, the system was able to mimic how separated cells can succumb to slower signalling due to the presence of unwanted guest molecules that might scavenge signals.

5.4 Future works

This final chapter presents an exciting step towards understanding the relationship between protocell communication and the dynamic spatial organisation of protocell communities. Although electrostatic interactions are sensitive to environmental cues thus making them easily adaptable and dynamic, they do not form very specific interactions between populations. Living system are highly complex meaning that interactions are often targeted and specific. Developing dynamic organisation based on specific protocell interactions is therefore an important step in understanding the complexity of a living system.

GLYMO-based polymer coating of colloidosomes is a relatively general process and as such, alginate and chitosan could be substituted for polymers with different interactive properties. As briefly mentioned in the introduction, the host-guest interaction has been used to self-assemble colloids and is therefore a plausible strategy for colloidosome self-assembly. With this in mind, α-cyclodextrin and azobenzene were attached to PAH polymers for surface addition to colloidosomes. FITC-α-CD-PAH coated RITC-GOx loaded colloidosomes were prepared according to the GLYMO method as previously discussed. CLSM images and fluorescence intensity profiles suggested successful coating of the polymer on the colloidosome surface.

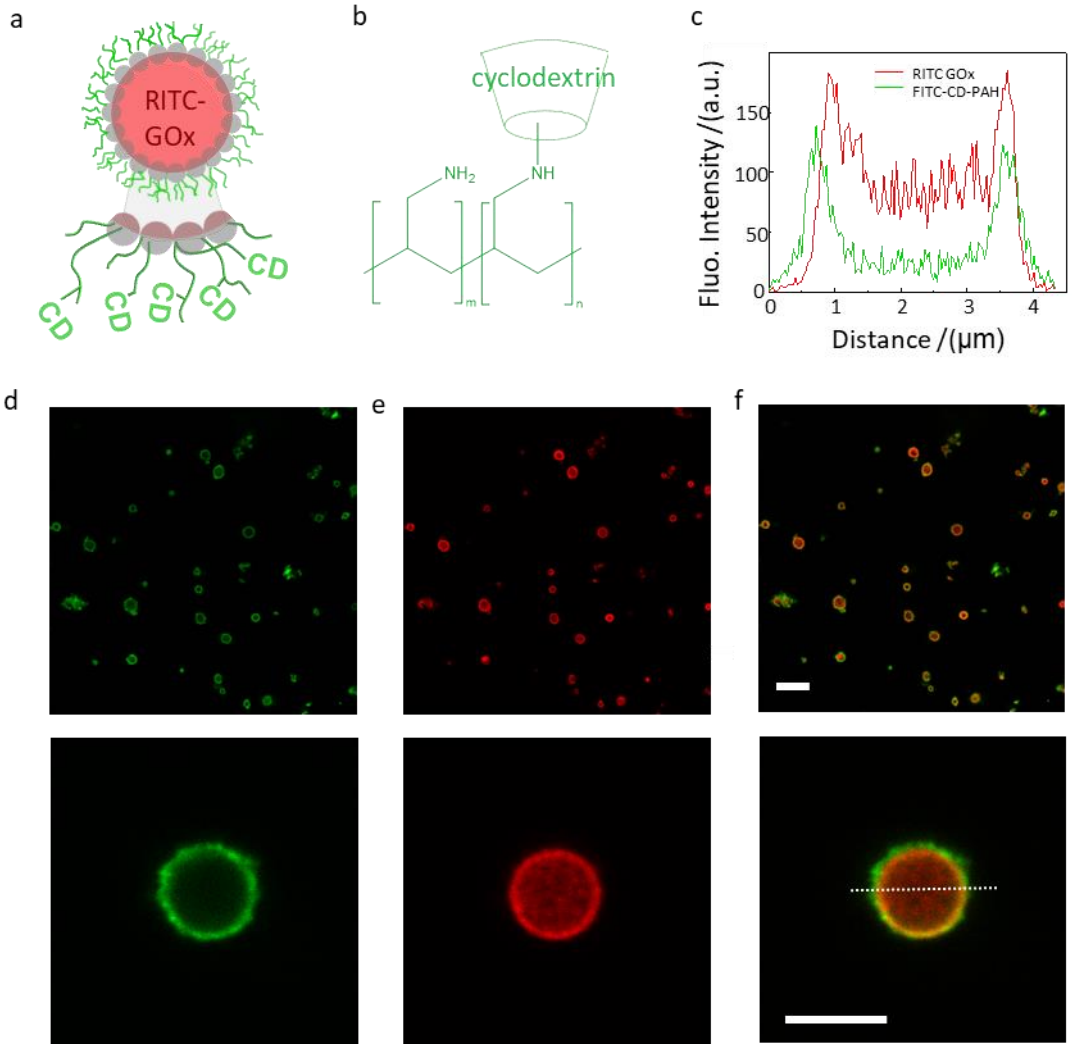

Figure 5.29. *α-**cyclodextrin-poly(allylamine hydrochloride)-coated GOx-loaded colloidosomes.** **a**, Diagram showing RITC-labelled GOx-loaded colloidosome with FITC-labelled α-CD-PAH polymer attached to the silica nanoparticle membrane.* ***b,*** *Chemical structure of α-CD-PAH polymer* ***c**, Fluorescence intensity profile across the diameter (white line) of single colloidosome in (**f**).* ***d**, **e**, **f**, Green fluoresence filtered image (**d**), red fluorescence filtered image (**e**) and red/green overlay image (**f**) of colloidosomes described in (**a**) with zoomed image displaying one colloidosome. Scale bars, 10 and 4 μm (zoomed).*

Similarly, RITC-azobenzene-PAH coated FITC-GOx loaded colloidosomes were prepared and analysed. Azobenzene attachement to colloidosomes resulted in some aggregation due to low solubility in aquoeus solution. Despite this, CLSM images showed sucessful polymer attachemet to the surface of colloidosomes.

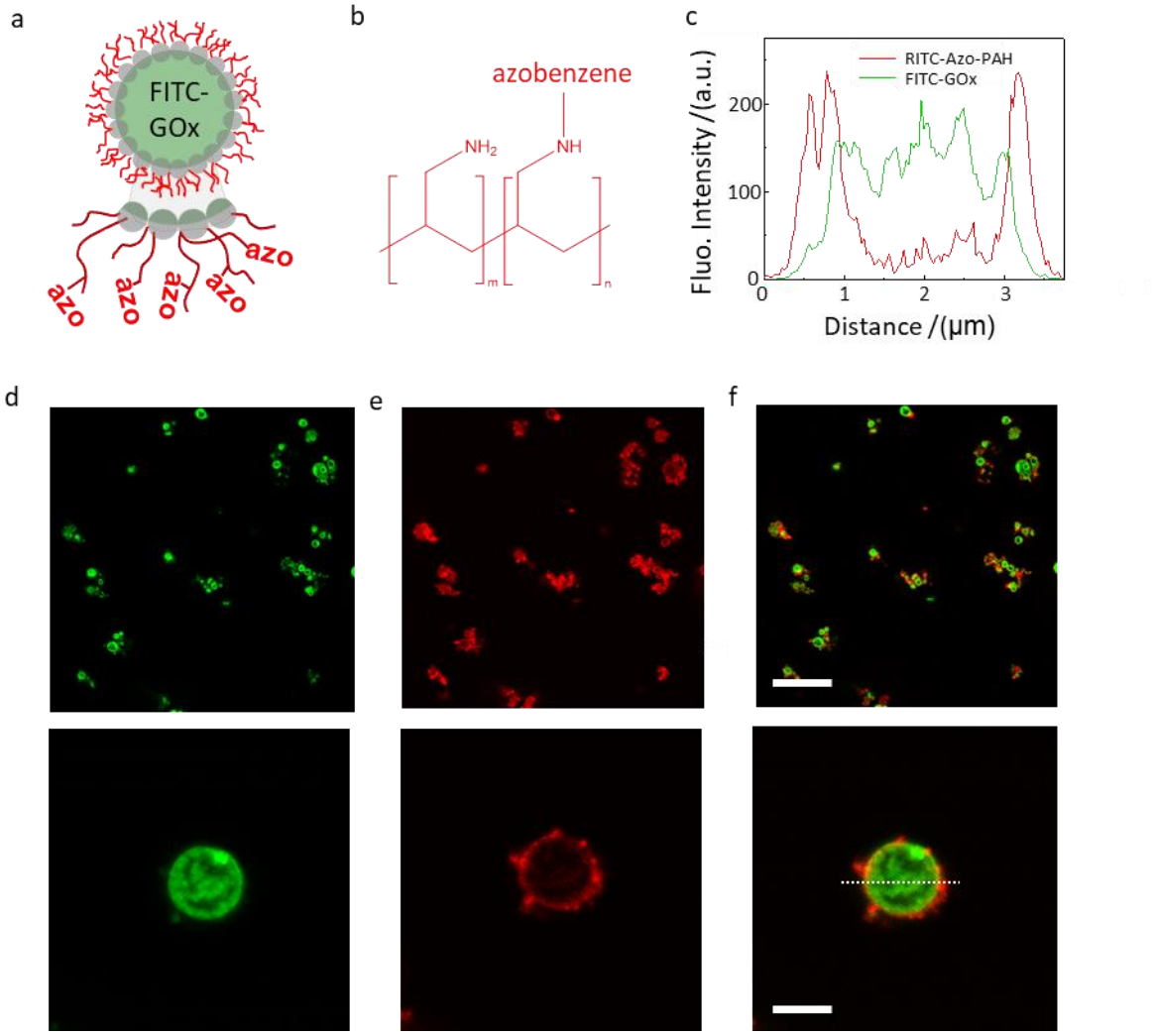

Figure 5.30. azobenzene-poly(allylamine hydrochloride)-coated GOx-loaded colloidosomes. ***a****, Diagram showing FITC-labelled GOx-loaded colloidosome with RITC-labelled azo-PAH polymer attached to the silica nanoparticle membrane.* ***b,*** *Chemical structure of azo-PAH polymer* ***c****, Fluorescence intensity profile across the diameter (white line) of single colloidosome in (****f****).* ***d****,* ***e****,* ***f****, Green fluoresence filtered image (****d****), red fluorescence filtered image (****e****) and red/green overlay image (****f****) of colloidosomes described in (****a****) with zoomed image displaying one colloidosome. Scale bars, 10 and 2 μm (zoomed).*

An azo-PAH-coated colloidosome community (red) and α-CD-PAH-coated colloidosome community were mixed together in a pH 7 environment at 1 : 1 (v : v) ratio which resulted in aggregation attributed to host-guest interaction. The pKa of PAH is 8.5 thus, in the absence of host-guest interactions, PAH-coated colloidosomes were expected to aggregate at pH > 8.5 due to hydrogen bonding and disperse at pH < 8.5 due to positively charged repulsion. In the case where α-CD and azobenzene are attached to PAH aggregation was observed at pH 7 attributed to host-guest interactions. Interestingly at pH 10, clumps of aggregated colloidosomes co-assembled to create population domains. The key challenge was to separate these aggregates at pH 7 through shining UV

light and thus changing the confirmation of azo benzene from linear to bent so that it no longer interacted with α-CD. The experiment was conducted by stirring samples for 10 min and then shining UV light (100-400 nm) emitted from a Xenon lamp into the sample (duration 30 min), before immediately viewing through an optical microscope. Unfortunately, this experiment did not work which was most likely due to polymer chains becoming intertwined and thus other intermolecular interactions having significant influence. In the future, this work could be improved so that host-guest chemistry might be used to reversibly aggregate colloidosome communities. This could be achieved by attaching the host or guest molecule to the surface of colloidosome without polymer (or with very short polymers) so that polymer interactions do not interfere with the host-guest chemistry. Eventually a system with four protocell communities could be dynamically self-sorted via αCD/azobenzene and βCD/ferrocene interactions and sophisticated communication networks within such system could be designed. As an interesting thought, a system could be designed to try competing reactions between self-sorted populations to observe how one population affects the other.

There is increasing interest relating to protocellular materials for bio-inspired applications and cytomimetic functions. With this in mind, the alginate-coated colloidosome prototissue could be developed into a more advanced material capable of organised communication or healing.

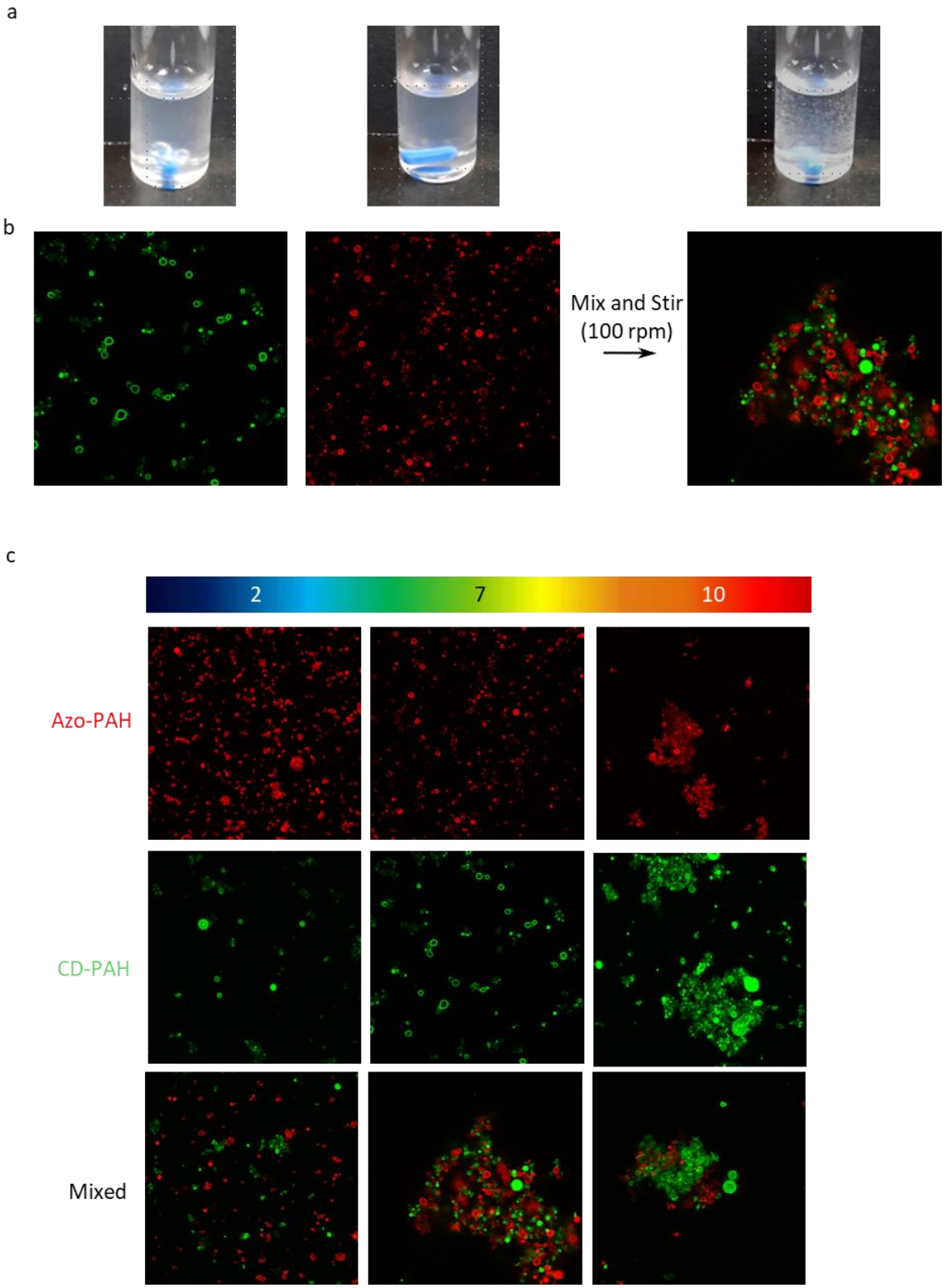

Figure 5.31. Host-guest interactions between α-CD-PAH and azo-PAH coated colloidosomes. a, *Screenshots at t=5 min from videos of CD-PAH coated colloidosomes mixed together, azo-PAH coated colloidosomes mixed together and 1 : 1 ratio of CD-PAH coated colloidosomes and azo-PAH coated colloidosomes.* ***b****, CLSM images of CD-PAH coated (green) and azo-PAH coated (red) colloidosomes before and after 1 : 1 mixing for 5 min.* ***c****, CLSM images of colloidosomes described in (**b**) in different external pH conditions 2, 7, 10. Images taken after stirring for 5 min.*

CHAPTER 6

THESIS CONCLUSIONS

Living systems are formed and cultivated through mass, information, and energy interactions.[1] Such interactions rely on cell-cell and cell-environment chemical networks, that can be modelled through the bottom-up construction and integration of artificial cell (protocell) communities. Despite an emerging catalogue of protocell systems capable of communication and collective behaviours, we recognise that micro-organised structures, cell-environment communication, and protocell dynamics have received minimal attention. Throughout this thesis I was able to address such challenges through matrix-based and matrix-free inorganic protocell (colloidosome) systems.

Firstly, a hydrogel matrix-based strategy for the construction of highly micro-organised colloidosome communities was developed. To date, hydrogel-immobilised protocells have been used for prototissue construction,[202] flow microreactors[144] and chemically mediated micro-actuators.[13] However, in these systems protocells are homogenously arranged in macroscopic hydrogel configurations. Microfluidic techniques offer an easy way to manipulate protocells at the microscale, yet despite the use of droplet-based microfluidics for fabricating hydrogel droplets, immobilising living cells,[216] higher order micro- patterning[232] and proteinosome-encapsulation,[13] utilising microfluidics for the spatially segregated patterning of micro-scale protocell colonies has received minimal attention. The first experimental chapter concludes that microfluidic-prepared hydrogel microspheres are ideal scaffolds for tuneable microscopic colloidosome patterning. An interconnected coacervate matrix was also prepared for colloidosome scaffolding and spatial organisation. Interconnected prototissues have been used for thermoresponsive motions,[82] self-

folding[88] and electrical pathways.[249] However, these systems rely on the connection of a single type of protocell model and spatial organisation through pattering of protocell building blocks. The first experimental chapter concludes that interconnected coacervate-networks can be fabricated quickly as suitable scaffolds for a different type of protocell and for the spatial organisation of guest colloidosomes immobilised within homogeneously arranged coacervate building blocks.

A droplet-based coaxial microfluidic device was used as a novel technique for creating colloidosome-embedded hydrogel micro platforms with customisable parameters via tuneable velocity and device geometry variables. Hydrogel microspheres could be made larger by decreasing the outer phase velocity or increasing the inner velocity injection into the device. Microsphere diameters also depended upon crosslinking concentration in an off-device collection pool, which had secondary effects on monodispersity and shape. It was noted that the orifice diameter proportionally affected the microsphere size, meaning that experiments using different devices could not be directly comparable. Janus-like arrangements of spatially segregated colloidosome colonies were encapsulated within the hydrogel microspheres and colloidosome colony number ratios were programmed through changing the inner velocity ratios. Further organisational complexity could be afforded by changing the device geometry, resulting in ternary segregated colloidosome colonies and rod-shaped platforms albeit with Janus internal patterning. Finally, a coacervate matrix was used to entrap spatially organised colloidosome communities through a modular assembly technique. Significantly this generated a protocell-only matrix, combining two distinct protocell communities: one being the scaffold and one being the guests. In conclusion, matrix-based immobilisation of colloidosomes was a suitable strategy for spatially organising protocells within tissue-like materials as a mimic of organised living cells within an ECM.

Since highly micro-organised colloidosome colonies could be readily established, the next chapter explored the influence of spatial organisation on protocell-protocell and protocell-environment interactions. To date, protocells have exploited interprotocellular signalling interactions in both disordered[10-12] and ordered populations,[13-20] via through-space and contact-dependent routes. Consequently, collective behaviours such as predator-prey relationships,[21] activation of protocell membranes,[12,30,] protocell differentiation,[14,31] signal amplification,[10] programmable motility,[32] morphological adaptation[33] and DNA computing[13,34] have been achieved. However, collective behaviours in spatially organised protocell systems and protocell-environment interactions have received minimal attention. The second experimental chapter concludes that matrix-based spatially organised protocell systems are suitable platforms for interprotocellular enzyme cascades and for protocell-matrix interactions, which can both lead to interesting collective behaviours.

A GOx/HRP cascade between segregated colonies trapped within a hydrogel platform showed proximity-mediated communication that was improved in comparison to a homogenous distribution of colloidosomes. Communication was developed in rod-shaped microparticles and in ternary segregated microspheres through a Suc/GOx/HRP enzyme cascade. Within the Janus system, segregated URS-loaded colloidosomes were shown to disassemble an alginate-matrix domain through a diffusive flux of carbonate, whereas segregated GOx-loaded colloidosomes were shown to covalently crosslink a tyramine-labelled alginate-matrix domain to offset flux-mediated depletion of Ca^{2+} ions. As a result, simultaneous disassembly/resilience of domains within the two-domain microsphere was achieved. The two-domain system was programmed by URS concentration to establish three different regimes under conditions that led to either an insufficient, balanced, or excess flux of carbonate. Jettisoning behaviour was observed when colloidosome-hydrogel interactions were established between opposite domains. Interprotocellular communication was also developed between colloidosome-immobilised hotspots within the coacervate-matrix, as a step towards extended communication networks through interconnected prototissue materials. In conclusion, developing communication networks in spatially organised communities of protocells can lead to interesting collective behaviours, but can be challenging due to the combination of new organisation techniques and sophisticated interaction designs.

Whilst matrix-immobilised colloidosomes facilitate highly ordered spatial organisations, organisation within living systems is often dynamic. A matrix-free strategy for the dynamic organisation of colloidosomes was therefore developed. Dynamic organisation allows cells to be influenced by environmental cues for behaviours such as bacteria competition[256], immune system response[255] and biofilm formation.[262] Protocell dynamic organisation has been explored for predator-prey relationships[145] and proteinosome self-sorting.[258] However, these systems lack endogenous re-organisation and temporally controlled communication pathways. Dynamic protocell systems that can endogenously self-assemble and self-sort for temporally controlled protocell-protocell interactions have received minimal attention. The third experimental chapter concludes that matrix-free electrostatically organised colloidosomes can dynamically self-assemble via environmental pH cues, to increase the rate of interprotocellular communication in the presence of a signal scavenger.

Chitosan and alginate polymers were affixed to colloidosome appendages to achieve colloidosome self-assembly or self-sorting under certain pH conditions. In a mixed 1 : 1 (v : v) population of polymer-coated colloidosomes, various spatial arrangements were achieved through hydrogen bonding, electrostatic attraction and charged repulsion. GOx-loaded colloidosomes were used to endogenously decrease the external pH in a temporally controlled process, as a self-regulated

method for their own spatial arrangement. Finally, signalling between AOx-loaded and HRP-loaded polymer-coated colloidosomes was controlled through dynamic colloidosome re-organisation. In the presence of a catalase scavenger, aggregation of colloidosomes was shown to increase the rate of communication, whereas self-sorted arrangements of colloidosomes were shown to decrease the rate of communication. The increased rate was attributed to a proximity-mediated interference of the signal by scavenging catalase. In conclusion, dynamically changing the spatial organisation of protocell communities was shown to directly affect their interprotocellular interactions, as a step towards understanding competition and pathogen responses in living systems.

Overall, the importance of spatial organisation for developing cell-cell and cell-environment interactions within inorganic protocell communities, as a mimic of interactive living systems, has been highlighted. A study into model living system interactions has been achieved by developing fixed and dynamic spatial organisation through matrix-based and matrix-free colloidosome populations. Exploring living system interactions in this way could lead to novel opportunities for the design of spatially organised cytomimetic materials, deepens current understanding of living systems and provides insight into spatially significant interactions at the Origin of Life.

CHAPTER 7

THESIS FUTURE WORKS

Spatially organised inorganic protocell communities have a bright future in living system mimics, cytomimetic material design and bioinspired engineering. Improved protocell-protocell chemical communication, as a result of enzyme-loaded colloidosome spatial segregation, might be especially useful in enzyme therapies and prototissue engineering. When faster transferral of signalling molecules may be required for a life-like process, spatial segregation of senders and receivers could be exploited.

The matrix-based and matrix-free systems discussed, offer core strategies for addressing three key challenges a) developing protocellular models with high levels of organisational tunability, b) achieving cell-environment bilateral communication, and c) realising autonomous self-assembly and regulation of protocell systems. Future work could continue to address these challenges in evermore complexed ways. Colloidosomes embedded within matrix-based materials could display more sophisticated cell-environment interactions through improved matrix designs. For example, enzymatic activity within a coacervate matrix could be coupled to activity within the embedded colloidosomes or, hydrogels with protoactive ligands could be used to explore phenomena such as protocell migration and matrix repair or growth. Matrix-free organisation of colloidosomes could be developed for more sophisticated and autonomous signalling networks, for example by more specific protocell sorting or programmed feedback loops.

As a direct extension of the work discussed, microfluidic-produced colloidosome-embedded hydrogel microspheres could be developed into a multi-tier system wherein communication would be developed between different microspheres or initiated by protocell release from the microspheres. Due to mechanical weakness in the coacervate matrix, spatial patterning of colloidosomes is challenging and could be improved by a new assembly technique such as 3D printing or a sophisticated microfluidic set-up. Supramolecular chemistries could be used within dynamic protocell systems to create opportunities for advanced cell sorting, biofilm production mimicries or more in-depth communication studies.

Overall, the spatial organisation of colloidosomes (and perhaps other protocell models) via matrix-based and matrix-free strategies remains a promising area of research, closely linked to current fields involving protocellular materials and protocellular collective behaviours.

BIBLIOGRAPHY

CHAPTER 1: INTRODUCTION NEW CITATIONS

[1] J. Miller, J. Miller.
Greater than the sum of its parts.
Behavioral Science, 37(1): 1-9, 1992.

[2] J. Miller, J. Miller.
The reproducer.
Behavioral Science, 37(1): 10-23, 1992.

[3] J. Miller, J. Miller.
The boundary.
Behavioral Science, 37(1): 23-39, 1992.

[4] I. Gözen, E. Köksal, I. Põldsalu, L. Xue, K. Spustova, E. Pedrueza-Villalmanzo, R. Ryskulov, F. Meng, A. Jesorka.
Protocells: Milestones and Recent Advances.
Small, 18(5): 2106624, 2022.

[5] A. Dzieciol, S. Mann.
Designs for life: Protocell models in the laboratory.
Chemical Society Reviews, 41(1): 79-85, 2012.

[6] M. Li, R. Harbron, J. Weaver, B. Binks, S. Mann.
Electrostatically gated membrane permeability in inorganic protocells.
Nature Chemistry, 5(6): 529-536, 2013.

[7] P. Kumar, A. Patil, S. Mann.
Enzyme-powered motility in buoyant organoclay/ DNA protocells.
Nature Chemistry, 10: 1154-1163, 2018.

[8] K. Kumar, R. Harniman, A. Patil, S. Mann.
Self-transformation and structural reconfiguration in coacervate-based protocells.
Chemical Science, 7(9): 5879-5887, 2016.

[9] N. Martin, M. Li, S. Mann.
Selective uptake and refolding of globular proteins in coacervate microdroplets.
Langmuir, 32(23): 5881-5889, 2016.

[10] S. Wang, M. Li, A. Patil, S. Sun, L. Tian, D. Zhang, M. Cao, S. Mann.
Design and construction of artificial photoresponsive protocells capable of converting day light to chemical energy.
Journal of Materials Chemistry A, 5(47): 24612-24616, 2017.

[11] Y. Qiao, M. Li, D. Qiu, S. Mann.
Response-retaliation behavior in synthetic protocell communities.
Angewandte Chemie - International Edition, 58: 17758-17763, 2019.

[12] L. Rodríguez-Arco, M. Li, S. Mann.
Phagocytosis-inspired behaviour in synthetic protocell communities of compartmentalized colloidal objects.
Nature Materials, 16: 857-863, 2017.

[13] N. Gao, M. Li, L. Tian, A. Patil, P. Kumar, S. Mann.
Chemical-mediated translocation in protocell-based microactuators.
Nature Chemistry, 13(9): 868-879, 2021.

[14] G. Murtas.
Early self-reproduction, the emergence of division mechanisms in protocells.
Molecular BioSystems, 9(2): 195-204, 2013.

[15] D. Balleza.
Toward understanding protocell mechanosensation.
Origins of Life and Evolution of Biospheres, 41(3): 281-304, 2010.

[16] N. Pirie.
The origins of lfe: Moscow symposium.
Nature, 180: 886-888, 1957.

[17] J. Bernal.
The origins of life.
Nature, 180: 1220, 1957.

[18] M. Bitbol, P. Luisi.
Autopoiesis with or without cognition: defining life at its edge.
Journal of the Royal Society Interface, 1(1): 99-107, 2004.

[19] S. Mann.
Systems of creation: The emergence of life from nonliving matter.
Accounts of Chemical Research, 45(12): 2131-2141, 2012.

[20] R. Solé, A. Munteanu, C. Rodríguez-Caso, J. Macía.
Synthetic protocell biology: From reproduction to computation.
Philosophical Transactions of the Royal Society B: Biological Sciences, 362(1486): 1727-1739, 2007.

[21] C. Xu, N. Martin, M. Li, S. Mann.
Living material assembly of bacteriogenic protocells.
Nature, 609(7929): 1029-1037, 2022.

[22] A. Oparin.
The origin of life on the earth.
Oliver and Boyd, 3rd Edition, 1957.

[23] K. Kurihara, Y. Okura, M. Matsuo, T. Toyota, K. Suzuki, T. Sugawara.
A recursive vesicle-based model protocell with a primitive model cell cycle.
Nature Communications, 6(1): 1-7, 2015.

[24] Y. Elani, R. Law, O. Ces.
Vesicle-based artificial cells as chemical microreactors with spatially segregated reaction pathways.
Nature Communications, 5(1): 1-5, 2014.

[25] I. Chen, P. Walde.
From self-assembled vesicles to protocells.
Cold Spring Harbor Perspectives in Biology, 2(7): 1-5, 2010.

[26] S. Mansy.
Model protocells from single-chain lipids.
International Journal of Molecular Sciences, 10(3): 835, 2009.

[27] X. Huang, M. Li, D. Green, D. Williams, A. Patil, S. Mann.
Interfacial assembly of protein-polymer nano-conjugates into stimulus-responsive biomimetic protocells.
Nature Communications, 4(1): 1-9, 2013.

[28] X. Huang, A. Patil, M. Li, S. Mann.
Design and construction of higher-order structure and function in proteinosome-based protocells.
Journal of the American Chemical Society, 136(25): 9225-9234, 2014.

[29] J. Park, A. Galanti, I. Ayling, S. Rochat, M. Workentin, P. Gobbo.
Colloidosomes as a protocell model: Engineering life-like behaviour through organic chemistry.
European Journal of Organic Chemistry, 43: 2022.

[30] J. Lefley, C. Waldron, C. Becer.
Macromolecular design and preparation of polymersomes.
Polymer Chemistry, 11(45): 7124-7136, 2020.

[31] S. Koga, D. Williams, A. Perriman, S. Mann.
Peptide-nucleotide microdroplets as a step towards a membrane-free protocell model.
Nature Chemistry, 3(9): 720-724, 2011.

[32] R. Poudyal, R. Guth-Metzler, A. Veenis. E. Frankel, C. Keating, P. Bevilacqua.
Template-directed RNA polymerization and enhanced ribozyme catalysis inside membraneless compartments formed by coacervates.
Nature Communications, 10(1): 1-13, 2019.

[33] M. Li, X. Huang, T. Tang, S. Mann.
Synthetic cellularity based on non-lipid micro-compartments and protocell models.
Current Opinion in Chemical Biology, 22: 1-11, 2014.

[34] A. Brizard, J. Van Esch.
Self-assembly approaches for the construction of cell architecture mimics.
Soft Matter, 5(7): 1320-1327, 2009.

[35] Y. Xia, B. Gates, Y. Tin, Y. Lu.
Monodispersed colloidal spheres: Old materials with new applications.
Advanced Materials, 12(10): 693-713, 2000.

[36] H. Yow, A. Routh.
Formation of liquid core-polymer shell microcapsules.
Soft Matter, 2(11): 940-949, 2006.

[37] D. Ortiz, C. Pochat-Bohatier, J. Cambedouzou, M. Bechelany, P. Miele.
Current trends in Pickering emulsions: morphology and applications.
Engineering, 6(4): 468-482, 2020.

[38] B. Binks, J. Clint.
Solid Wettability from Surface Energy Components: Relevance to Pickering Emulsions.
American Chemical Society, 18(4): 1270-1273, 2002.

[39] S. Saraf, R. Rathi, C. Kaur, S. Saraf.
Colloidosomes an advanced vesicular system in drug delivery.
Asian Journal of Scientific Research, 4(1): 1-15, 2011.

[40] C. Albert, M. Beladjine, N. Tsapis, E. Fattal, F. Agnely, N. Huang.
Pickering emulsions: Preparation processes, key parameters governing their properties and potential for pharmaceutical applications.
Journal of Controlled Release, 309: 302-332, 2019.

[41] K. Thompson, M. Williams, S. Armes.
Colloidosomes: Synthesis, properties and applications.
Journal of Colloid and Interface Science, 447: 217-228, 2014.

[42] M. Li, D. Green, J. Anderson, B. Binks, S. Mann.
In vitro gene expression and enzyme catalysis in bio-inorganic protocells.
Chemical Science, 2(9): 1739-1745, 2011.

[43] S. Sun, M. Li, F. Dong, S. Wang, L. Tian, S. Mann.
Chemical signalling and functional activation in colloidosome-based protocells.
Small, 12(14): 1920-1927, 2016.

[44] P. Keen, N. Slater, A. Routh.
Encapsulation of amylase in colloidosomes.
Langmuir, 30(8): 1939-1948, 2014.

[45] J. López-de-Luzuriaga, M. Monge, J. Quintana, M. Rodríguez-Castillo.
Single-step assembly of gold nanoparticles into plasmonic colloidosomes at the interface of oleic acid nanodroplets.
Nanoscale Advances, 3(1): 198-205, 2021.

[46] B. Binks, R. Murakami.
Phase inversion of particle-stabilized materials from foams to dry water.
Nature Materials, 5: 865-869, 2006.

[47] T. Kostakis, R. Ettelaie, B. Murray.
Effect of high salt concentrations on the stabilization of bubbles by silica particles.
Langmuir, 22(3): 1273-1280, 2006.

[48] M. Li, X. Huang, S. Mann.
Spontaneous growth and division in self-reproducing inorganic colloidosomes.
Small, 10(16): 3291-3298, 2014.

[49] E. Gomes, J. Shorter.
The molecular language of membraneless organelles.
The Journal of Biological Chemistry, 294(18): 7115, 2019.

[50] D. Williams, S. Koga, C. Hak, A. Majrekar, A. Patil, A. Perriman, S. Mann.
Polymer/nucleotide droplets as bio-inspired functional micro-compartments.
Soft Matter, 8(22): 6004-6014, 2012.

[51] D. Tang, D. Van Swaay, A. DeMello, J. Ross Anderson, S. Mann.
In vitro gene expression within membrane-free coacervate protocells.
Chemical Communications, 51(57): 11429-11432, 2015.

[52] N. Martin, K. Sharma, R. Harniman, R. Richardson, R. Hutchings, D. Alibhai, M. Li, S. Mann.
Light-induced dynamic shaping and self-division of multipodal polyelectrolyte-surfactant microarchitectures via azobenzene photomechanics.
Scientific Reports, 7: 41327, 2017.

[53] P. Kumar, J. Fothergill, J. Bretherton, L. Tian, A. Patil, S. Davis, S. Mann.
Chloroplast-containing coacervate micro-droplets as a step towards photosynthetically active membrane-free protocells.
Chemical Communications, 54(29): 3594-35597, 2018.

[54] R. Poudyal, R. Guth-Metzler, A. Veenis, E. Frankel, C. Keating, P. Bevilacqua.
Template-directed RNA polymerization and enhanced ribozyme catalysis inside membraneless compartments formed by coacervates.
Nature Communications, 10(1): 1-13, 2019.

[55] J. Crosby, T. Treadwell, M. Hammerton, K. Vasilakis, M. Crump, D. Williams, S. Mann.
Stabilization and enhanced reactivity of actinorhodin polyketide synthase minimal complex in polymer–nucleotide coacervate droplets.
Chemical Communications, 48(97): 11832-11834, 2012.

[56] D. Tang, C. Hak, A. Thompson, M. Kuimova, D. Williams, A. Perriman, S. Mann.
Fatty acid membrane assembly on coacervate microdroplets as a step towards a hybrid protocell model.
Nature Chemistry, 6: 527-533, 2014.

[57] S. Liu, Y. Zhang, M. Li, L. Xiong, Z. Zzhang, X. Yang, X. He, K. Wang, J. Liu, S. Mann.
Enzyme-mediated nitric oxide production in vasoactive erythrocyte membrane-enclosed coacervate protocells.
Nature Chemistry, 12: 1165-1173, 2020.

[58] N. Gao, C. Xu, Z. Yin, M. Li, S. Mann.
Triggerable protocell capture in nanoparticle-caged coacervate microdroplets.
Journal of the American Chemical Society, 144(9): 3855-3862, 2022.

[59] J. Li, X. Liu, L. Abdelmohsen, D. Williams, X. Huang.
Spatial organization in proteinaceous membrane-stabilized coacervate protocells.
Small, 15(36): 1902893, 2019.

[60] H. Chang, H. Jing, Y. Yin, Q. Zhang, D. Liang.
Membrane-mediated transport in a non-equilibrium hybrid protocell based on coacervate droplets and a surfactant.
Chemical Communications, 54(98): 13849-13852, 2018.

[61] D. Williams, A. Patil, S. Mann.
Spontaneous structuration in coacervate-based protocells by polyoxometalate-mediated Membrane Assembly.
Small, 10(9): 1830-1840, 2014.

[62] R. Booth, Y. Qiao, M. Li, S. Mann.
Spatial positioning and chemical coupling in coacervate-in-proteinosome protocells.
Angewandte Chemie - International Edition, 58(27): 9120-9124, 2019.

[63] Z. Yin, L. Tian, A. Patil, M. Li, S. Mann.
Spontaneous membranization in a silk-based coacervate protocell model.
Angewandte Chemie - International Edition, 134(17): e202202302, 2022.

[64] V. Mukwaya, S. Mann, H. Dou.
Chemical communication at the synthetic cell/living cell interface.
Communications Chemistry, 4(1): 1-12, 2021.

[65] H. Karoui, P. Patwal, P. Kumar, N. Martin.
Chemical communication in artificial cells: basic concepts, design and challenges.
Frontiers in Molecular Biosciences, 9(5): 1-16, 2022.

[66] L. Wang, S. Song, J. van Hest, A. Loai, X. Huang, S. Sanchez.
Biomimicry of Cellular Motility and Communication Based on Synthetic Soft-Architectures.
Small, 16(27): 1907680, 2020.

[67] S. Yang, P. Pieters, A. Joesaar, B. Bögels, R. Brouwers, I. Myrgorodska, S. Mann, T. se Greef.
Light-activated signaling in dna-encoded sender-receiver architectures.
ACS Nano, 14(11): 15992-16002, 2020.

[68] Q. Yang, Z. Guo, H. Liu, R. Peng, L. Xu, C. Bi, Y. He, Q. Liu, W. Tan.
A cascade signaling network between artificial cells switching activity of synthetic transmembrane channels.
Journal of the American Chemical Society, 143(1): 232-240, 2021.

[69] A. Joesaar, S. Yang, B. Bögels, A. van der Linden, P. Pieters, B. Kumar, N. Dalchau, A. Phillips, S. Mann, T. de Greef.
DNA-based communication in populations of synthetic protocells.
Nature Nanotechnology, 14(4): 369-378, 2019.

[70] H. Niederholtmeyer, C. Chaggan, N. Devaraj.
Communication and quorum sensing in non-living mimics of eukaryotic cells.
Nature communications, 9: 5027, 2018.

[71] K. Adamala, D. Martin-Alarcon, K. Guthrie-Honea, E. boyden.
Engineering genetic circuit interactions within and between synthetic minimal cells.
Nature Chemistry, 9(5): 431-439, 2017.

[72] T. Tang, D. Cecchi, G. Fracasso, D. Accardi, A. Coutable-Pennarun, A. Perriman, J. Anderson, S. Mann.
Gene-mediated chemical communication in synthetic protocell communities.
ACS synthetic biology, 7(2): 339-346, 2018.

[73] Y. Combarnous, T. Nguyen.
Cell communications among microorganisms, plants, and animals: origin, evolution, and interplays.
International Journal of Molecular Sciences, 21: 8052, 2020.

[74] B. Alberts, A. Johnson, J. Lewis, M. Raff, K. Roberts, P. Walter.
General principles of cell communication.
Molecular Biology of the cell.
Garland Science, 4th edition, 2002.

[75] C. Cotman, J. McGaugh.
Synaptic transmission.
Behavioral Neuroscience, 151-208, 1980.

[76] S. Hennig, G. Rödel, K. Ostermann.
Artificial cell-cell communication as an emerging tool in synthetic biology applications.
Journal of Biological Engineering, 9(1): 1-12, 2015.

[77] P. Grimes, A. Galanti, P. Gobbo.
Bioinspired networks of communicating synthetic protocells.
Frontiers in Molecular Biosciences, 8: 2021.

[78] A. Mason, B. Buddingh, D. Williams, J. Van Hest.
Hierarchical self-assembly of a copolymer-stabilized coacervate protocell.
Journal of the American Chemical Society, 139(48): 17309-17312, 2017.

[79] L. Tian, M. Li, L. Juntai, A. Patil, B. Drinkwater, S. Mann.
Nonequilibrium spatiotemporal sensing within acoustically patterned two-dimensional protocell arrays.
American Chemical Society Central Science, 4(11): 1551-1558, 2018.

[80] P. Gardner, K. Winzer, B. Davis.
Sugar synthesis in a protocellular model leads to a cell signalling response in bacteria.
Nature Chemistry, 1: 377-383, 2009.

[81] Y. Elani, T. Trantidou, D. Wylie, L. Dekker, K. Polizzi, R. Law, O. Ces.
Constructing vesicle-based artificial cells with embedded living cells as organelle-like modules.
Scientific Reports, 8: 4564, 2018.

[82] P. Gobbo, A. Patil, M. Li, R. Harniman, W. Briscoe, S. Mann.
Programmed assembly of synthetic protocells into thermoresponsive prototissues.
Nature Materials, 17: 1145-1153, 2018.

[83] L. Rodríguez-Arco, P. Kumar, M. Li, A. Patil, S. Mann.
Modulation of higher-order behaviour in model protocell communities by artificial phagocytosis.
Angewandte Chemie - International Edition, 58(19): 6333-6337, 2019.

[84] L. Tian, M. Li, A. Patil, B. Drinkwater, S. Mann.
Artificial morphogen-mediated differentiation in synthetic protocells.
Nature Communications, 10: 3321, 2019.

[85] H. Bayley, I. Cazimoglu, C. Hoskin.
Synthetic tissues.
Emerging Topics in Life Sciences, 3(5): 615-622, 2019.

[86] P. Gobbo.
From protocells to prototissues: A materials chemistry approach.
Biochemical Society transactions, 48(6): 2579-2589, 2020.

[87] M. Booth, H. Bayley.
3D-printed synthetic tissues.
The Biochemist, 38(4): 16-19, 2016.

[88] G. Villar, A. Graham, H. Bayley.
A tissue-like printed material.
Science, 340: 48-52, 2013.

[89] Q. Li, S. Li, X. Zhang, W. Xu, X. Han.
Programmed magnetic manipulation of vesicles into spatially coded prototissue architectures arrays.
Nature Communications, 11: 232, 2020.

[90] A. Galanti, R. Moreno-Tortolero, R. Azad, S. Cross, S. Davis, P. Gobbo.
A Floating Mold Technique for the Programmed Assembly of Protocells into Protocellular Materials Capable of Non-Equilibrium Biochemical Sensing.
Advanced Materials, 33(24): 2100340, 2021.

[91] A. Stroock.
Microfluidics
Optical Biosensors: Today and tomorrow.
Elsevier, 2nd edition: 659-681, 2008

[92] M. Tarn, N. Pamme.
Microfluidics
Reference Module in Chemistry, Molecular Sciences and Engineering.
Elsevier, 2013

[93] B. Rapp.
Introduction
Microfluidics: Modelling, Mechanics and Mathematics.
Elsevier, 2017

[94] G. Whitesides.
The origins and future of microfluidics.
Nature, 442: 368-373, 2006.

[95] A. Abou-Hassan, O. Sandre, V. Cabuil.
Microfluidics in inorganic chemistry.
Angewandte Chemie - International Edition, 49(36): 6268-6286, 2010.

[96] X. Mu, W. Zheng, J. Sun, W. Zhang, X. Jiang.
Microfluidics for manipulating cells.
Small, 9(1): 9-21, 2013.

[97] Y. Huang, A. Streets.
Chip in a lab: Microfluidics for next generation life science research.
Biomicrofluidics, 7(1): 11302, 2013.

[98] D. Beebe, G. Mensing, G. Walker.
Physics and applications of microfluidics in biology.
Annual Review of Biomedical Engineering, 4: 261-286, 2002.

[99] R. Sweet.
High frequency recording with electrostatically deflected ink jets.
Review of Scientific Instruments, 36(2): 131-136, 1965.

[100] N. Convery, N. Gadegaard.
30 years of microfluidics.
Micro and Nano Engineering, 2: 76-91, 2019.

[101] S. Terry, J. Herman, J. Angell.
A gas chromatographic air analyzer fabricated on a silicon wafer.
IEEE Transactions on Electron Devices, 26(12): 1880-1886, 1979.

[102] C. Hull.
US4575330A: Apparatus for production of three-dimensional objects by stereolithography.
Filed 1984, granted 1986.

[103] J. McDonald, D. Duffy, J. Anderson, D. Chiu, H. Wu, O. Schueller, G. Whitesides.
Fabrication of microfluidic systems in poly(dimethylsiloxane).
Electrophoresis, 21(1): 27-40, 2000.

[104] K. Viravaidya, M. Shuler.
Incorporation of 3T3-L1 cells to mimic bioaccumulation in a microscale cell culture analog device for toxicity studies.
Biotechnology Progress, 20(2): 590-597, 2004.

[105] A. Martinez, S. Phillips, M. Butte, G. Whitesides.
Patterned paper as a platform for Inexpensive, low-volume, portable bioassays.
Angewandte Chemie, 119(8): 1340-1342, 2007.

[106] X. Solvas, A. de Mello.
Droplet microfluidics: recent developments and future applications.
Chemical Communications, 47(7): 1936-1942, 2010.

[107] J. Wang, J. Wang, J. Han.
Fabrication of advanced particles and particle-based materials assisted by droplet-based microfluidics.
Small, 7(13): 1728-1754, 2011.

[108] Y. Schaerli, R. Wootton, T. Robinson, V. Stein, C. Dunsby, M. Neil, P. French, A. de Mello, C. Abell, F. Hollfelder.
Continuous-flow polymerase chain reaction of single-copy DNA in microfluidic microdroplets.
Analytical Chemistry, 81(1): 302-306, 2009.

[109] H. Feng, T. Zheng, M. Li, J. Wu, H. ji, J. Zhang, W. Zhao, J. Guo.
Droplet-based microfluidics systems in biomedical applications.
Electrophoresis, 40(11): 1580-1590, 2019.

[110] C. Baroud, F. Gallaire, R. Dangla.
Dynamics of microfluidic droplets.
Lab on a Chip, 10(16): 2032-2045, 2010.

[111] C. Martino, A. de Mello.
Droplet-based microfluidics for artificial cell generation: A brief review.
Interface Focus, 6(4): 2016.

[112] J. Atencia, D. Beebe.
Controlled microfluidic interfaces.
Nature, 437: 648-655, 2005.

[113] G. Christopher, S. Anna.
Microfluidic methods for generating continuous droplet streams.
Journal of Physics D: Applied Physics, 40(19): 319-336, 2007.

[114] L. Shang, T. Cheng, Y. Zhao.
Emerging droplet microfluidics.
Chemical Reviews, 117(12): 7964-8040, 2017.

[115] H. Gu, M. Duits, F. Mugele.
Droplets formation and merging in two-phase flow microfluidics.
International Journal of Molecular Sciences, 12(4): 2572-2597, 2011.

[116] N. Kovalchuk, M. Sagisaka, K. Steponavicius, D. Vigolo, M. Simmons.
Drop formation in microfluidic cross-junction: jetting to dripping to jetting transition.
Microfluidics and Nanofluidics, 23(8): 103, 2019.

[117] Z. Hayat, A. El Abed.
High-throughput optofluidic acquisition of microdroplets in microfluidic systems.
Micromachines, 9(4): 183, 2018.

[118] Y. Tan, J. Fisher, A. Lee, V. Cristini, A. Lee.
Design of microfluidic channel geometries for the control of droplet volume, chemical concentration, and sorting.
Lab on a Chip, 4(4): 292-298, 2004.

[119] M. Cordero, F. Gallaire, C. Baroud.
Quantitative analysis of the dripping and jetting regimes in co-flowing capillary jets.
Physics of Fluids, 23(9): 94111, 2011.

[120] J. Xu, S. Li, J. Tan, G. Luo.
Drnodispersed calcium alginate microbeads in a novel microfluidic system.
Chemical Engineering and Technology, 31(8): 1223-1226, 2008.

[121] M. Seo, C. Paquet, Z. Nie, S. Xu, E. Kumacheva.
Microfluidic consecutive flow-focusing droplet generators.
Soft Matter, 3(8): 986-992, 2007.

[122] Y. Ding, X. Solvas, A. de Mello.
"V-junction": A novel structure for high-speed generation of bespoke droplet flows.
Analyst, 140(2): 414-421, 2015.

[123] S. Doonan, R. Bailey.
K-channel: A multifunctional architecture for dynamically reconfigurable sample processing in droplet microfluidics.
Analytical Chemistry, 89(7): 4091-4099, 2017.

[124] M. Leshansky, M. Pismen.
Breakup of drops in a microfluidic T junction.
Physics of Fluids, 21(2): 23303, 2009.

[125] C. Yeh, Q. Zhao, S. Less, Y. Lin.
Using a T-junction microfluidic chip for monodisperse calcium alginate microparticles and encapsulation of nanoparticles.
Sensors and Actuators A: Physical, 151(2): 231-236, 2009.

[226] H. Shum, Y. Zhao, S. Kim, D. Weitz.
Multicompartment polymersomes from double emulsions.
Angewandte Chemie - International Edition, 50(7): 1648-1651, 2011.

[227] N. Deng, M. Yelleswarapu, W. Huck.
Monodisperse uni- and multicompartment liposomes.
Journal of the American Chemical Society, 138(24): 7584-7591, 2016.

[228] N. Deng, W. Huck.
Microfluidic formation of monodisperse coacervate organelles in liposomes.
Angewandte Chemie - International Edition, 56(33): 9736-9740.

[129] M. Faraday.
XVII. On a peculiar class of acoustical figures; and on certain forms assumed by groups of particles upon vibrating elastic surfaces.
Philosophical Transactions of the Royal Society of London, 121: 299-340, 1831.

[130] A. Kundt.
Acoustic experiments.
The London, Edinburgh, and Dublin Philosophical Magazine and Journal of Science, 35(234): 41-48, 1868.

[131] M. Dyson, B. Woodward, J. Pond.
Flow of red blood cells stopped by ultrasound.
Nature, 232: 572-573, 1971.

[132] M. Evander, J. Nilsson.
Acoustofluidics 20: Applications in acoustic trapping.
Lab on a Chip, 12(22): 4667-4676, 2012.

[133] H. Bruus.
Acoustofluidics 7: The acoustic radiation force on small particles.
Lab on a Chip, 12(6): 1014-1021, 2012.

[134] M. Hill.
A one-sided view of acoustic traps.
Physics, 9(3): 2016.

[135] P. Gobbo, L. Tian, P. Kumar, S. Turvey, M. Cattelan, A. Patil, M. Carraro, M. Bonchio, S. Mann.
Catalytic processing in ruthenium-based polyoxometalate coacervate protocells.
Nature Communications, 11: 41, 2020.

[136] X. Wang, L. Tian, H. Du. M. Li, W. Mu, B. Drinkwater, X. Han, S. Mann.
Chemical communication in spatially organized protocell colonies and protocell/living cell micro-arrays.
Chemical Science, 10(41): 9446-9453, 2019.

[137] X. Wang, L. Tian, Y. Ren, Z. Zhao, H. Du, Z. Zhang, B. Drinkwater, S. Mann.
Chemical information exchange in organized protocells and natural cell assemblies with controllable spatial positions.
Small, 16(27): 1906394, 2020.

[138] M. Nichols, R. Kumar, P. Bassindale, L. Tian, A. Barnes, B. Drinkwater, A. Patil, S. Mann.
Fabrication of micropatterned dipeptide hydrogels by acoustic trapping of stimulus-responsive coacervate droplets.
Small, 14(26): 1800739, 2018.

[139] A. Su, S. Al Aref.
History of 3D printing.
3D Printing Applications in Cardiovascular Medicine.
Elsevier, 1-10, 2018.

[140] M. Booth, V. Schild, S. Box, H. Bayley.
Light-patterning of synthetic tissues with single droplet resolution.
Scientific Reports, 7(1): 2017.

[141] A. Mundaz, M. Shiddiky, N. Nguyen.
Recent advances and current challenges in magnetophoresis based micro magnetofluidics.
Biomicrofluidics, 12(3): 031501, 2018.

[142] N. Hirota, M. Kurashige, M. Iwasaka, M. Ikehata, H. Uetake, T. Takayama, H. Nakamura, Y. Ikezoe, S. Ueno, K. Kitazawa.
Magneto-Archimedes separation and its application to the separation of biological materials.
Physica B: Condensed Matter, 346(1-4): 267-271, 2004.

[143] D. Rawtani, Y. Agrawal.
Emerging strategies and applications of layer-by-layer self-assembly.
Nanobiomedicine, 1: 2014.

[144] J. Liu, L. Tian, Y. Qiao, S. Zhou, A. Patil, K. Wang, M. Li, S. Mann.
Hydrogel-immobilized coacervate droplets as modular microreactor assemblies.
Angewandte Chemie - International Edition, 59(17): 6853-6859, 2020.

[145] Y. Qiao, M. Li, R. Booth, S. Mann.
Predatory behaviour in synthetic protocell communities.
Nature Chemistry, 9: 110-119, 2017.

[146] Q. Chai, Y. Jiao, X. Yu.
Hydrogels for biomedical applications: Their characteristics and the mechanisms behind them.
Gels, 3(1): 6, 2017.

[147] K. Wang, Y. Hao, Y. Wang, J. Chen, L. Mao, Y. Deng, J. Chen, S. Yuan, T. Zhang, J. Ren, W. Liao.
Functional hydrogels and their application in drug delivery, biosensors, and tissue engineering.
International Journal of Polymer Science, 2019.

[148] O. Wichterle, D. Lím.
Hydrophillic gels for biological use.
Nature, 185: 117-118, 1960.

[149] C. Echeverria, S. Fernandes, M. Godinho, J. Borges, P. Soares.
Functional stimuli-responsive gels: Hydrogels and microgels.
Gels, 4(2): 54, 2018.

[150] H. Tekin, J. Sanchez, T. Tsinman, R. Langer, A. Khademhosseini.
Thermoresponsive platforms for tissue engineering and regenerative medicine.
AIChE Journal, 57(12): 3249-3258, 2011.

[151] A. Hoffman.
Hydrogels for biomedical applications.
Advanced Drug Delivery Reviews, 64: 188-23, 2012.

[152] L. Yahai. N. Chirani, L. Gritsch, F. Motta, S. Chirani, S. Fare.
History and applications of hydrogels.
Journal of Biomedical Sciences, 4: 2015.

[153] D. Gyles, L. Castro, J. Silva, R. Ribeiro-Costa.
A review of the designs and prominent biomedical advances of natural and synthetic hydrogel formulations.
European Polymer Journal, 88: 373-392, 2017.

[154] K. Lee, D. Mooney.
Alginate: Properties and biomedical applications.
Progress in Polymer Science, 37(1): 106-126, 2012.

[155] N. Sachan, S. Pushkar, A. Jha, A. Bhattcharya
Sodium alginate: the wonder polymer for controlled drug delivery.
Journal of Pharmacy Research, 2(8): 1191-1199, 2009.

[156] D. Sánchez-Machado, J. López-Cervantes, M. Correa-Murrieta, G. Sánchez-Duarte, P. Cruz-Flores, S. la Mora-López.
Chitosan.
Nonvitamin and Nonmineral Nutritional Supplements, 485-493, 2019.

[157] I. Aranaz, A. Alcántara , M. Civera, C. Arias, B. Elorza, A. Caballero, N. Acosta.
Chitosan: An overview of its properties and applications.
Polymers, 13(19), 2021.

[158] B. Rehm.
Alginates: Biology and Applications.
Springer Berlin, Heidelberg, 2010.

[159] H. El-Rehim.
Characterization and possible agricultural application of polyacrylamide/sodium alginate crosslinked hydrogels prepared by ionizing radiation.
Journal of Applied Polymer Science, 101(6): 3572-3580, 2006.

[160] S. Saghazadeh, C. Rinoldi, M. Schot, S. Kashaf, F. Sharifi, E. Jalilian, K. Nuutila, G. Gaiatsidis. P. Mostafalu, H. Derakhshandeh, K. Yue, W. Swieszkowski, A. Memic, A. Tamayol, A. Khademhosseini.
Drug delivery systems and materials for wound healing applications.
Advanced Drug Delivery Reviews, 127: 138-166, 2018.

[161] Z. Mohamadnia, M. Zohuriaan-Mehr, K. Kabiri, A. Jamshidi, H. Mobedi.
pH-sensitive IPN hydrogel beads of carrageenan-alginate for controlled drug delivery.
Journal of Bioactive and Compatible Polymers, 22(3): 342-356, 2007.

[162] J. Douliez, N. Martin, T. Beneyton, J. Eloi, J. Chapel, L. Navailles, J. Baret, S. Mann, L. Béven.
Preparation of swellable hydrogel-containing colloidosomes from aqueous two-phase pickering emulsion droplets.
Angewandte Chemie - International Edition, 57(26): 7780-7784, 2018.

CHAPTER 2: NEW CITATIONS

[163] M. Spencer.
Fundamentals of Light Microscopy.
Cambridge University Press, 1982

[164] M. Sanderson, I. Smith, I. Parker, M. Bootman.
Fluorescence microscopy.
Cold Spring Harbor protocols, 10: 2014.

[165] J. Pawley.
Handbook of Biological Confocal Microscopy.
Springer, 3rd edition, 1-16, 1989.

[166] E. Stelzer, F. Strobl, B. Chang, F. Preusser, S. McDole, R. Fiolka.
Light sheet fluorescence microscopy
Nature Reviews Methods Primers, 1(1): 1-25, 2021.

[167] M. Henini.
Scanning electron microscopy: an introduction.
III-Vs Review, 13(4): 40-44, 2000.

[168] W. Zhou, R. Apkarian, Z. Wang, D. Joy.
Fundamentals of scanning electron microscopy (SEM).
Scanning Microscopy for Nanotechnology: Techniques and Applications.
Springer, 1-40, 2006.

[169] M. Winey, J. Meehl, E. O'Toole, T. Giddings.
Conventional transmission electron microscopy.
Molecular Biology of the Cell, 25(3): 319-323, 2014.

[170] H. Perkampus.
UV-VIS Spectroscopy and Its Applications
Springer-Verlag, 3-9, 1992.

[171] K. Dyamenahalli, A. Familli, R. Shandas.
Characterization of shape-memory polymers for biomedical applications.
Shape Memory Polymers for Biomedical Applications, 35-63, 2015

[172] B. Stuart.
Infrared spectroscopy: Fundamentals and applications.
John Wiley & Sons, 1-13, 2004.

[173] W. Veeman.
Nuclear magnetic resonance, a simple introduction to the principles and applications.
Geoderma, 80(3-4): 225-242, 1997.

[174] J. Stetefeld, S. McKenna, T. Patel.
Dynamic light scattering: a practical guide and applications in biomedical sciences.
Biophysical Reviews, 8(4): 409, 2016.

[175] S. Falke. C. Betzel.
Dynamic light scattering (DLS).
Radiation in Bioanalysis, 8: 173-193, 2019.

[176] V. Selvamani.
Stability Studies on Nanomaterials Used in Drugs.
Nanoscience and Nanotechnology in Drug Delivery, 425-444, 2019.

[177] K. Makino, H. Ohshima.
Electrophoretic mobility of a colloidal particle with constant surface charge density.
Langmuir, 26(23): 18016-18019, 2010.

[178] X. Ning, C. Yao, L. Guan, T. Bai.
Fluorescent sodium alginate applied to papermaking furnish with polyamideamine epichlorohydrin.
BioResources, 13(4), 7519-7533, 2018.

[179] H. Zhu, R. Srivastava, J. Brown, M. Mcshane.
Combined physical and chemical immobilization of glucose oxidase in alginate microspheres improves stability of encapsulation and activity.
Bioconjugate Chemistry, 16(6): 1451-1458, 2005.

[180] H. Taylor.
Using microfluidics to create and utilise anisotropy within protocell communities encapsulated inside hydrogel platforms.
MSci Thesis, 2019.

[181] D. Vllasalie, R. Exposito-Harris, A. Heras, L. Casettari, M. Garnett, L. Illum, S. Stolnik.
Tight junction modulation by chitosan nanoparticles: Comparison with chitosan solution.
Pharmaceutical Nanotechnology, 10(1-2): 183-193, 2010.

[182] S. Sakai, K. Kawakami.
Synthesis and characterization of both ionically and enzymatically cross-linkable alginate.
Acta Biomaterialia, 3(4): 495-501, 2007.

CHAPTER 3: NEW CITATIONS

[183] A. Theocharis, S. Skandalis, C. Gialeli, N. Karamanos.
Extracellular matrix structure.
Advanced Drug Delivery Reviews, 97: 4-27, 2016.

[184] B. Yue.
Biology of the extracellular matrix: An overview.
Journal of glaucoma, 23(8): S20, 2014.

[185] C. Frantz, K. Stewart, V. Weaver.
The extracellular matrix at a glance.
Journal of cell Science, 123(24): 4195-4200, 2010.

[186] J. Nicolas, S. Magli, L. Rabbachin, S. Sampaolesi, F. Nicotra, L. Russo.
3D extracellular matrix mimics: Fundamental concepts and role of materials chemistry to influence stem cell fate.
Biomacromolecules, 21(6), 1968-1994, 2020.

[187] H. Geckil, F. Xu, X. Zhang, S. Moon, U. Demirci.
Engineering hydrogels as extracellular matrix mimics.
Nanomedicine, 5(3): 469, 2010.

[188] K. Kyburz, K. Anseth.
Synthetic mimics of the extracellular matrix: How simple is complex enough?
Annals of Biomedical Engineering, 43(3): 489-500, 2015.

[189] S. Amorim, C. Reis, R. Reis, R. Pires.
Extracellular matrix mimics using hyaluronan-based biomaterials.
Trends in Biotechnology, 39(1): 90-104, 2021.

[190] O. Smidsrød, G. Skjåk-Bræk.
Alginate as immobilization matrix for cells.
Trends in Biotechnology, 8: 71-78, 1990.

[191] S. Dutta, D. Patel, K. Lim.
Functional cellulose-based hydrogels as extracellular matrices for tissue engineering.
Journal of Biological Engineering, 13(1): 1-19, 2019.

[192] M. Tibbitt, K. Anseth.
Hydrogels as extracellular matrix mimics for 3D cell culture.
Biotechnology and Bioengineering, 103(4): 655-663, 2009.

[193] P. Guan, C. Liu, D. Xie, S. Mao, Y. Ji, Z. Chen, Q. Wang, L. Fan, Y. Sun.
Exosome-loaded extracellular matrix-mimic hydrogel with anti-inflammatory property Facilitates/promotes growth plate injury repair.
Bioactive Materials, 10: 145-158, 2022.

[194] B. Schmidt.
Multicompartment hydrogels.
Macromolecular Rapid Communications, 43(7): 2100895, 2022.

[195] Z. Yu, J. Liu, C. Tan, O. Scherman, C. Abell.
Supramolecular nested microbeads as building blocks for macroscopic self-healing scaffolds.
Angewandte Chemie - International Edition, 57(12): 3079-3083, 2018.

[196] S. Yue, X. Sun, N. Wang, Y. Wang, Y. Wang, Z. Xu, M. Chen, J. Wang.
SERS-Fluorescence Dual-Mode pH-Sensing Method Based on Janus Microparticles.
ACS Applied Materials and Interfaces, 9(45): 39699-39707, 2017.

[197] J. Meyer, L. Meyer, S. Kara.
Enzyme immobilization in hydrogels: A perfect liaison for efficient and sustainable biocatalysis.
Engineering in Life Sciences, 22(3-4): 165, 2022.

[198] N. Gao, T. Tian, J. Cui, W. Zhang, X. Yin, S. Wang, J. Ji, G. Li.
Efficient construction of well-defined multicompartment porous systems in a modular and chemically orthogonal fashion.
Angewandte Chemie - International Edition, 56(14): 3880-3885, 2017.

[199] D. Baxani, A. Morgan, W. Jamieson, C. Allender, D. Barrow, O. Castell.
Bilayer networks within a hydrogel shell: A robust chassis for artificial cells and a platform for membrane studies.
Angewandte Chemie - International Edition, 55(46): 14240-14245, 2016.

[200] A. Billard, L. Pourchet, S. Malaise, P. Alcouffe, A. Montembault, C. Ladavière.
Liposome-loaded chitosan physical hydrogel: Toward a promising delayed-release biosystem.
Carbohydrate Polymers, 115: 651-657, 2015.

[201] M. Dowling, J. Lee, S. Raghavan.
pH-responsive jello: Gelatin gels containing fatty acid vesicles.
Langmuir, 25(15): 8519-8525, 2009.

[202] S. Liu, Y. Zhang, X. He, M. Li, J. Huang, X. Yang, K. Wang, S. Mann, J. Lui.
Signal processing and generation of bioactive nitric oxide in a model prototissue.
Nature Communications, 13(1): 1-12, 2022.

[203] B. Chung, K. Lee, A. Khademhosseini, S. Lee.
Microfluidic fabrication of microengineered hydrogels and their application in tissue engineering.
Lab on a Chip, 12(1): 45-59, 2011.

[204] A. Sattari, S. Janfaza, M. Mashhadi, N. Tasnim, P. Hanafizadeh, M. Hoorfar.
Microfluidic on-chip production of alginate hydrogels using double coflow geometry.
ACS Omega, 6(4): 25964-25971, 2021.

[205] H. Ahmed, B. Stokke.
Fabrication of monodisperse alginate microgel beads by microfluidic picoinjection: a chelate free approach.
Lab on a Chip, 21(11): 2232-2243, 2021.

[206] C. Zhang, R. Grossier, N. Candoni, S. Veesler.
Preparation of alginate hydrogel microparticles using droplet-based microfluidics: a review of methods.
Biomaterials Research, 25(41): 2021.

[207] R. Puscaselu, A. Lobiuc, M. Dimian, M. Covasa.
Alginate: From food industry to biomedical applications and management of metabolic disorders.
Polymers, 12(10): 1-30, 2020.

[208] Y. Hu, G. Azadi, A. Ardekani.
Microfluidic fabrication of shape-tunable alginate microgels: Effect of size and impact velocity.
Carbohydrate Polymers, 120: 38-45, 2015.

[209] W. Tan, S. Takeuchi.
Monodisperse alginate hydrogel microbeads for cell encapsulation.
Advanced Materials, 19(18): 2696-2701, 2007.

[210] C. Choi, J. Jung, Y. Rhee, D. Kim, S. Shim, C. Lee.
Generation of monodisperse alginate microbeads and in situ encapsulation of cell in microfluidic device.
Biomedical Microdevices, 9(6): 855-862, 2007.

[211] S. Anna, N. Bontoux, H. Stone.
Formation of dispersions using “flow focusing” in microchannels.
Applied Physics Letters, 82: 364, 2003.

[212] L. Mazutis, R. Vasiliauskas, D. Weitz.
Microfluidic production of alginate hydrogel particles for antibody encapsulation and release.
Macromolecular Bioscience, 15(12): 1641-1646, 2015.

[213] C. Shen, F. Liu, L. Wu, C. Yu, W. Yu.
Dripping, jetting and regime transition of droplet formation in a buoyancy-assisted microfluidic device.
Micromachines, 11(11): 2020.

[214] J. Guerrero, Y. Chang, A. Fragkopoulos, A. Fernandez-Nieves.
Capillary-based microfluidics—coflow, flow-focusing, electro-coflow, drops, jets, and instabilities.
Small, 16(9): 2020.

[215] A. Utada, L. Chu, A. Fernandez-Nieves, D. Link, C. Holtze, D. Weitz.
Dripping, Jetting, Drops, and Wetting: The Magic of Microfluidics.
MRS Bulletin, 32: 702-708, 2007.

[216] S. Akbari, T. Pirbodaghi.
Microfluidic encapsulation of cells in alginate particles via an improved internal gelation approach.
Microfluidics and Nanofluidics, 16(4): 773-777, 2014.

[217] T. Le, J. Zhai, W. Chiu, P. Tran, N. Tran.
Janus particles: recent advances in the biomedical applications.
International Journal of Nanomedicine, 14: 6749-6777, 2019.

[218] J. Ostberg, R. Barth, J. Frelinger.
The Roman god Janus: A paradigm for the function of CD43.
Immunology Today, 19(12): 546-550.

[219] A. Walther, A. Müller.
Janus particles.
Soft Matter, 4(4): 6630668, 2008.

[220] A. Perro, S. Reculusa, S. Ravaine, E. Bourgeat-Lami, E. Duguet.
Design and synthesis of Janus micro- and nanoparticles.
Journal of Materials Chemistry, 15(35-36): 3745-3760, 2005.

[221] J. Guzowski, P. Korczyk, S. Jakiela, P. Garstecki.
The structure and stability of multiple micro-droplets.
Soft Matter, 8(27): 7269-7278, 2012.

[222] T. Nisisako, T. Torii, T. Takahashi, Y. Takizawa.
Synthesis of monodisperse bicolored janus particles with electrical anisotropy using a microfluidic co-flow system.
Advanced Materials, 18(9): 1152-1156, 2006.

[223] M. Marquis, D. Renard, B. Cathala.
Microfluidic generation and selective degradation of biopolymer-based Janus microbeads.
Biomacromolecules, 13(4): 1197-1203, 2012.

[224] Y. Komazaki, H. Hirama, T. Torii.
Electrically and magnetically dual-driven Janus particles for handwriting-enabled electronic paper.
Journal of Applied Physics, 117(15): 154506, 2015.

[225] S. Lone, I. Cheong.
Fabrication of polymeric Janus particles by droplet microfluidics.
Royal Society of Chemistry Advances, 4(26): 13322013333, 2014.

[226] S. Seiffert, M. Romanowsky, D. Weitz.
Janus microgels produced from functional precursor polymers.
Langmuir, 26(18): 14842-14847, 2010.

[227] S. Yang, F. Guo, B. Kiraly, X. Mao, M. Lu, K. Leong, T. Huang.
Microfluidic synthesis of multifunctional Janus particles for biomedical applications.
Lab on a Chip, 12(12): 2097-2102, 2012.

[228] R. Shepherd, J. Conrad, S. Rhodes, D. Link, M. Marquez, D. Weitz, J. Lewis.
Microfluidic assembly of homogeneous and Janus colloid-filled hydrogel granules.
Langmuir, 22(21): 8618-8622, 2006.

[229] S. Kim, S. Jeon, W. Jeong, H. Park, S. Yang.
Optofluidic synthesis of electroresponsive photonic J.
anus balls with isotropic structural colors.
Advanced Materials, 20(21): 4129-4134, 2008.

[230] S. Xu, Z. Nie, M. Seo, P. Lewis, E. Kumacheva, H. Stone, P. Garstecki, D. Weibel, I. Geitlin, G. Whitesides.
Generation of monodisperse particles by using microfluidics: Control over size, shape, and composition.
Angewandte Chemie - International Edition, 44(5): 724-728, 2005.

[231] Y. Lin, C. Yang, Y. Hsu, C. Hsieh.
Microfluidic synthesis of tail-shaped alginate microparticles using slow sedimentation.
Electrophoresis, 34(3): 425-431, 2013.

[232] K. Maeda, H. Onoe, M. Takinoue, S. Takeuchi.
Controlled synthesis of 3D multi-compartmental particles with centrifuge-based microdroplet formation from a multi-barrelled capillary.
Advanced Materials, 24(10): 1340-1346, 2012.

[233] A. Alcinesio, O. Meacock, R. Allan, C. Monica, V. Restrepo, I. Cazimoglu, M. Cornall, R. Krishna, H. Bayley.
Controlled packing and single-droplet resolution of 3D-printed functional synthetic tissues.
Nature Communications, 11: 1-13, 2020.

[234] M. Booth, V. Schild, F. Downs, H. Bayley.
Functional aqueous droplet networks.
Molecular BioSystems, 13: 1658, 2017.

[235] G. Bolognesi, M. Friddin, A. Salehi-Reyhani, N. Barlow, N. Brooks, O. Ces, Y. Elani.
Sculpting and fusing biomimetic vesicle networks using optical tweezers.
Nature Communications, 9: 1-11, 2018.

[236] N. Stuhr-Hansen, C. Vagianou, O. Blixt.
Clustering of giant unilamellar vesicles promoted by covalent and noncovalent bonding of functional groups at membrane-embedded peptides.
Bioconjugate Chemistry, 30(8): 2156-2164, 2019.

[237] Y. Xie, Z. Li, J. Zhou.
Hamiltonian replica exchange simulations of glucose oxidase adsorption on charged surfaces.
Physical Chemistry Chemical Physics, 20(21): 14587-14596, 2018.

CHAPTER 4: NEW CITATIONS

[238] R. Lemieux, U. Spohr.
How Emil Fischer was led to the lock and key concept for enzyme specificity.
Advances in Carbohydrate Chemistry and Biochemistry, 50(C): 1-20, 1994.

[239] S. Hornig, M. Michael, A. Grinyer, J. Turner.
Introduction to enzymes and their applications.
Introduction to Pharmaceutical Biotechnology, 2: 9, 2018.

[240] J. Bauer, M. Zámocká, J. Majtán, V. Bauerová-Hlinková.
Glucose oxidase, an enzyme “Ferrari”: Its structure, function, production and properties in the light of various industrial and biotechnological applications.
Biomolecules, 12(3): 2012

[241] C. Wong, K. Wong, X. Chen.
Glucose oxidase: Natural occurrence, function, properties and industrial applications.
Applied Microbiology and Biotechnology, 78(6): 927-938, 2008.

[242] L. Mazzei, F. Musiani, S. Ciurli.
The structure-based reaction mechanism of urease, a nickel dependent enzyme: tale of a long debate.
Journal of Biological Inorganic Chemistry, 25(6): 829-845, 2020.

[243] G. Berglund, G. Carlsson, A. Smith, H. Szöke, A. Henriksen, J. Hajdu.
The catalytic pathway of horseradish peroxidase at high resolution.
Nature, 417: 463-468, 2002.

[244] J. Rodríguez-López, D. Lowe, J. Hernández-Ruiz, A. Jiner, F. Carcía-Cánovas, R. Thorneley.
Mechanism of reaction of hydrogen peroxide with horseradish peroxidase: identification of intermediates in the catalytic cycle.
Journal of the American Chemical Society, 123(48): 11838-11847, 2001.

[245] S. Li, X. Wang, W. Mu, X. Han.
Chemical signal communication between two protoorganelles in a lipid-based artificial cell.
Analytical Chemistry, 91(10): 6859-6864, 2019.

[246] S. Sun, M. Li, F. Dong, S. Wang, L. Tian, S. Mann.
Chemical signal communication between two protoorganelles in a lipid-based artificial cell.
Small, 12(14): 1920-1927, 2016.

[247] C. Zhao, M. Zhu, Y. Fang, X. Liu, D. Chen, X. Huang.
Engineering proteinosomes with renewable predatory behaviour towards living organisms.
Materials Horizons, 7: 157-163, 2020.

[248] N. Yewdall, A. Mason, J. Van Hest.
The hallmarks of living systems: Towards creating artificial cells.
Interface Focus, 8(5): 2018.

[249] M. Booth, V. Schild, A. Graham, S. Ofof, H. Bayley.
Light-activated communication in synthetic tissues.
Science Advances, 2(4): 2016.

[250] A. Samanta, M. Hörner, W. Liu, W. Weber, A. Walther.
Signal-processing and adaptive prototissue formation in metabolic DNA protocells.
Nature Communications, 13: 3968, 2022.

[251] N. Martin, J. Douliez, Y. Qiao, R. Booth, M. Li, S. Mann.
Antagonistic chemical coupling in self-reconfigurable host-guest protocells.
Nature Communications, 9: 3652, 2018.

CHAPTER 5: NEW CITATIONS

[252] T. Schwarz-Romond, S. Gorski.
Focus on special organization of signalling.
The EMBO Journal, 29(16): 2675, 2010.

[253] L. Bich, W. Bechtel.
Organization needs organization: Understanding integrated control in living organisms.
Studies in History and Philosophy of Science, 93: 96-106, 2022.

[254] A. Brooks, S. Turkarslan, K. Beer, F. Yin Lo, N. Baliga.
Adaptation of cells to new environments.
Systems Biology and Medicine, 3(5): 544, 2011.

[255] A. Oyler-Yaniv, J. Oyler-Yaniv, B. Whitlock, Z. Luiz, R. Germain, M. Huse, G. Altan-Bonnet, O. Krichevsky.
A tunable diffusion-consumption mechanism of cytokine propagation enables plasticity in cell-to-cell communication in the immune system.
Immunity, 46(4): 609-620, 2017.

[256] R. Stubbendieck, C. Vargas-Bautista, P. Straight.
Bacterial communities: Interactions to scale.
Frontiers in Microbiology, 7: 2016.

[257] X. Trepat, Z. Chen, K. Jacobson.
Cell migration.
Comprehensive Physiology, 2(4): 2369, 2012.

[258] A. Heidari, O. Sentürk, S. Yang, A. Joesaar, P. Gobbo, S. Mann, T. de Greef, S. Wegner.
Orthogonal light-dependent membrane adhesion induces social self-sorting and member-specific DNA communication in synthetic cell communities.
Small, 2206474, 2023.

[259] K. Roy, S. Kar, R. Das.
Background of QSAR and Historical Developments.
Understanding the Basics of QSAR for Applications in Pharmaceutical Sciences and Risk Assessment.
Elsevier, 1-46, 2015.

[260] M. Ahmed, E. Papaleo, K. Lindorff-Larsen.
How well do force fields capture the strength of salt bridges in proteins?
PeerJ, 6: 2016.

[261] S. Pylaeva, M. Brehm, D. Sebastiani.
Salt bridge in aqueous solution: Strong structural motifs but weak enthalpic effect.
Scientific Reports, 8(1): 1-7, 2018.

[262] M. Muhammad, A. Idris, X. Fan, Y. Guo, Y. Yu, X. Jin, J. Qiu, X. Guan, T, Huang.
Beyond risk: Bacterial biofilms and their regulating approaches.
Frontiers in Microbiology, 11: 2020.

[263] K. Bisht, C. Wakeman.
Discovery and therapeutic targeting of differentiated biofilm subpopulations.
Frontiers in Microbiology, 10: 2019.

[264] K. Szalewicz.
Hydrogen Bond.
Encyclopedia of Physical Science and Technology.
Academic Press, 505-538, 2002.

[265] L. Paoloni.
Nature of the hydrogen bond.
The Journal of Chemical Physics, 30(4): 1045, 2004.

[266] B. Alberts, A. Johnson, J. Lewis, M. Raff, K. Roberts, P. Walter.
The structure and function of DNA.
Molecular Biology of the Cell.
Garland Science, 4th edition, 2002.

[267] J. Balszczyk, Z. Lu, Y. li, H. Yan, X. Ji.
Crystallographic and molecular dynamics simulation analysis of Escherichia coli dihydroneopterin aldolase.
Cell and Bioscience, 4(1): 2014.

[268] E. Glowacki, M. Irimia-Vladu, S. Bauer, N. Sariciftci.
Hydrogen-bonds in molecular solids – from biological systems to organic electronics.
Journal of Materials Chemistry B, 1(31): 3742-3753, 2013.

[269] L. Pray.
Discovery of DNA structure and function: Watson and Crick.
Nature Education, 1: 2008.

[270] X. Huang, M. Li, S. Mann.
Membrane-mediated cascade reactions by enzyme-polymer proteinosomes.
Chemical Communications, 50(57): 6278-6280, 2014.

[271] G. Garden, A. La Spada.
Intercellular (mis)communication in neurodegenerative disease.
Neuron, 73(5): 886, 2012.

[272] G. Cooper.
Structure and organization of actin filaments.
The Cell: A Molecular Approach.
Sinauer Associates 2nd edition, 2000

[273] F. Harold.
Molecules into cells: Specifying spatial architecture.
Microbiology and Molecular Biology Reviews, 69(4): 544, 2005.

[274] N. Higashi, T. Ochiai, C. Kanazawa, T. Koga.
Site-specific adsorption of gold nanoparticles coated with thermo-responsive peptides.
Polymer Journal, 45(5): 523-528, 2013.

[275] K. Hamner, M. Maye.
Thermal aggregation properties of nanoparticles modified with temperature sensitive copolymers.
Langmuir, 29(49), 15217-15223, 2013.

[276] M. Valignat, O. Theodoly, J. Crocker, W. Russel, P. Chaikin.
Reversible self-assembly and directed assembly of DNA-linked micrometer-sized colloids.
Proceedings of the National Academy of Sciences of the United States of America, 102(12): 4225-4229, 2005.

[277] P. Kundu, D. Samanta, R. Leizrowice, B. Margulis, H. Zhao, M. Börner, T. Udayabhaskararao, D. Manna, R. Klajn.
Light-controlled self-assembly of non-photoresponsive nanoparticles.
Nature Chemistry, 7(8): 646-652, 2015.

[278] K. Han, D. Go, D. Hoenders, A. Kuehne, A. Walther.
Switchable supracolloidal coassembly of microgels mediated by host/guest interactions.
ACS Macro Letters, 6(3): 310-314, 2017.

[279] K. Han, D. Go, T. Tigges, K. Ahimi, A. Kuehne, A. Walther.
Social self-sorting of colloidal families in co-assembling microgel systems.
Angewandte Chemie - International Edition, 56(8): 2176-2182, 2017.

[280] X. Lu, G. Du, Z. Zhong, G. Gong, W. Cai, L. Wu, G. Zhao.
Fabrication of redox- and pH-sensitive self-assembled nano-micelles with pegylated β-cyclodextrin for codelivery of doxorubicin and cyclopalladated ferrocene.
European Journal of Inorganic Chemistry, 8: 2022.

[281] O. Sentürk, E. Chervyachkova, Y. Ji, S. Wegner.
Independent blue and red light triggered narcissistic self-sorting self-assembly of colloidal particles.
Small, 15(25): 2019.

[282] C. Sharma, A. Walther.
Self-regulating colloidal co-assemblies that accelerate their own destruction via chemo-structural feedback.
Angewandte Chemie - International Edition, 61(19): 2022.

[283] B. Buddingh, A. Llopis-Lorente, L. Abdelmohsen, J. Van Hest.
Dynamic spatial and structural organization in artificial cells regulates signal processing by protein scaffolding.
Chemical Science, 11(47): 12829-12834, 2020.

[284] J. Chuang, Y. Huang, S. Lo, T. Hsu, W. Huang, S. Huang, Y. Lin.
Effects of pH on the shape of alginate particles and its release behavior.
International Journal of Polymer Science, 3902704: 2017.

[285] N. Saïed, M. Aider.
Zeta potential and turbidimetry analyzes for the evaluation of chitosan/phytic acid complex formation.
Journal of Food Research, 3(2): 71, 2014.

[286] E. Nwoko, I. Okeke.
Bacteria autoaggregation: How and why bacteria stick together.
Biochemical Society Transactions, 49(3): 1147, 2021.